



Diese Dissertation haben begutachtet

.....

## Dissertation

### **Identification of Ultrafast Electronic and Thermal Processes during Femtosecond Laser Ablation by Means of Surface Topography Investigations**

ausgeführt zum Zwecke der Erlangung des akademischen Grades eines  
Doktors der technischen Wissenschaften unter der Leitung von

**Prof. Dr. Wolfgang Husinsky**

Institut für Angewandte Physik

134

eingereicht an der Technischen Universität Wien  
Fakultät für Physik

von

**M.Phil. Shazia Bashir**

Matrikelnummer 0626586

Wiedner Hauptstr. 8-10, 1040 Wien

Wien, Februar 2010

eigenhändige Unterschrift



This dissertation evaluated

.....

Dissertation

**Identification of Ultrafast Electronic and Thermal Processes  
during Femtosecond Laser Ablation by Means of Surface  
Topography Investigations**

Realized to obtain the title of Ph. D in technical science under the supervision of

**Prof. Dr. Wolfgang Husinsky**

Institute of Applied Physics

134

Submitted to Technical University Vienna

Faculty of Physics

By

**M.Phil. Shazia Bashir**

Matr. No. 0626586

Wiedner Hauptstr. 8-10, 1040 Vienna

Vienna, February 2010

Personal signature

## Abstract

Thema dieser Dissertation ist die Wechselwirkung ultrakurzer Laserstrahlung mit Festkörpern, wobei hier natürlich nur einige wichtige Aspekte behandelt werden können. Der Schwerpunkt der hier präsentierten Ergebnisse liegt auf dem Studium dabei auftretender fundamentaler Prozesse und soll zu einem bessern Verständnis dieser führen. Es zeigt sich dabei, dass es besonders wichtig ist wie die Energie der Laserstrahlung deponiert wird, und zwar vor allem auf welcher Zeitskala. Das hier hauptsächlich verwendete „Werkzeug“ dies zu erreichen ist hochauflösende Messung der dabei entstehenden topographischen Änderungen der Oberfläche.

Mittels „Atom Force Microscopy“ (Atomkraftmikroskopie, AFM) wurde dazu das Auftreten von verschiedenen Strukturen wie Nanohillocks (Nanohügel), Bumps, Nanopores oder Nanogitter auf Nichtleitern ( $\text{CaF}_2$ , CR-39), Halbleitern (Si) sowie Metallen (Al) als Funktion verschiedener Parameter studiert. Dazu wurden die Oberflächen mit der Strahlung von einem Ti:Saphir Laser (Pulse mit 25fs und 800nm zentraler Wellenlänge) bestrahlt. Die Fluenz wurde dabei zwischen  $0.06 \text{ Jcm}^{-2}$  und  $3.6 \text{ Jcm}^{-2}$  variiert. Außerdem wurden entsprechende Ergebnisse für Bestrahlung in Luft bzw. im Ultrahochvakuum miteinander verglichen. Die entstehenden Oberflächenstrukturen wurden mit einem AFM im Kontaktmodus an Luft bei Raumtemperatur vermessen. Diese neuen Ergebnisse wurden mit früheren Messungen, wo wir die Charakteristika der Teilchenemission bei der Laserablation (Massenzusammensetzung und Teilchenenergie) untersucht haben, korreliert. So konnten drei charakteristische Typen von Prozessen identifiziert werden: 1.) Sub 100fs elektronische Prozesse wie Coulombexplosion (CE) oder Feldionenemission durch Optische Gleichrichtung an Oberflächen (SOR); 2.) Prozesse ausgelöst durch die Ausbildung eines elektronischen Plasmas, typischerweise auf einer Zeitskala von einigen 100fs. 3.) Thermische Prozesse (TA), Zeitskala typisch einige ps.

Besonders interessant sind die unter geeigneten Bedingungen beobachteten sogenannten Nanohillocks, die einen Durchmesser  $<50\text{nm}$  und eine Höhe von einigen nm aufweisen. Diese charakteristischen Oberflächenstrukturen sind ein starker Hinweis auf eine extrem lokalisierte Energieübertragung an das elektronische System und das Auftreten von CE bzw. SOR Prozessen. Die Lokalisierung ist die Voraussetzung für die effiziente Möglichkeit elektronische Energie in kinetische Energie der Atome umzuwandeln. Bei einer größeren Laserfluenz werden thermische Prozesse immer wichtiger. Diese wiederum resultieren in Strukturen geringer Lokalisierung mit weitreichenden (20-200nm) Oberflächenstrukturen mit Höhen im Bereich von 100nm-3 $\mu\text{m}$ . Diese Hügel und Täler resultieren aus thermischen Verspannungen sowie aus der Agglomeration von Fehlstellen.

Ein weiterer wichtiger Schritt für die Identifikation der Prozesse stellt die Korrelation der Oberflächenstrukturen mit chemisch-strukturellen Veränderungen dar. Dazu wurde Ramanspektroskopie verwendet.

Ein wichtiger Fall für die Anwendung ultrakurzer Laserstrahlung ist z.B. die Zweiphotonenmodifikation von Materialien, die meist auf der

Zweiphotonenabsorption in transparenten Materialien beruht. Im Hinblick darauf wurden im Rahmen dieser Dissertation Untersuchungen an CR-39 durchgeführt.

Neben den oben erwähnten für spezielle Prozesse charakteristischen Strukturen können – vor allem bei Bestrahlung mit einer Vielzahl von Pulsen - verschiedenartigste sogenannte selbstorganisierte (self-organized) periodische Strukturen beobachtet werden. Im Rahmen dieser Dissertation werden einige teilweise neuartige solcher Strukturen beschrieben. Insbesondere ist die Abhängigkeit ihrer Periodizität von der Laserintensität festgestellt worden.

Zusammenfassend kann gesagt werden, dass diese Untersuchungen ein vertieftes Verständnis der Prozesse bei der Laser-Festkörperwechselwirkung mit ultrakurzer Laserstrahlung gebracht haben. Als wichtige zukünftige Untersuchungen seien vor allem die Abhängigkeit der Strukturen von der Laserpulsbreite bzw. allgemein der Laserpulsform erwähnt.



## Abstract

In this dissertation selected important aspects of interaction of ultra-short laser radiation with solids are discussed. It addresses and enhances the understanding of fundamental physical processes involved in the interaction mechanism. The main goal of the work is to obtain a better understanding of basic mechanisms of localized laser energy deposition in materials (insulators, semiconductors and metals) on the fs time scale and to explore their role in surface modification.

Phenomena of nanohillock like defect-formation, explosions, bumps, nanopores and nanogratings like features on surfaces like,  $\text{CaF}_2$ , CR-39 (insulators), Si (semiconductors) and Al (metals), by ultra short laser irradiation have been investigated by means of Atomic Force Microscopy (AFM). The surfaces were exposed to Ti: sapphire 25-fs laser pulses with a central wavelength at 800 nm. Samples were irradiated at different laser fluences ( $0.06 \text{ Jcm}^{-2}$  to  $3.6 \text{ Jcm}^{-2}$ ) in air as well as under UHV condition. Detailed surface topographical features of bombarded targets were characterized by atomic force microscopy in contact mode in air at room temperature. By combining new studies of the surface topography and the emission characteristics of particles during interaction of ultrashort-laser radiation with surfaces in particular during laser ablation, three different types of general processes (sub 100 fs electronic processes like Coulomb explosion (CE) or field ion emission by Surface Optical Rectification (SOR), processes related to electronic plasma (FEP) formation (typically a few hundred fs time scale) and thermal ablation (TA)) could be identified to explain ultrashort-laser ablation of matter at laser intensities around the ablation threshold. In particular, the identification of the unique appearance of individual, localized nanohillocks, typically a few nm in height and with a diameter below typically 50 nm, can be regarded as characteristic for a strong localized potential energy deposition to the electronic system resulting in CE or SOR. These nanostructures due to localization of laser energy deposition in small areas provide a possible pathway from dense electronic excitation to atomic motion causing permanent structural modification. For moderate fluence regime surface elevations in the range of 20-200 nm in height and 100 nm-3  $\mu\text{m}$  in diameter are observed. These larger elevations are called bumps and are attributed to ultrafast melting (plasma formation), buildup of thermal stresses, diffusion, transformation and aggregation of primary defects. For high fluence regime where thermal processes start, craters and island-like structures have been observed which are due to surface melting and resolidification.

Surface topographical features of irradiated materials are well correlated with the structural changes explored by Raman spectroscopy.

Ultrashort lasers have proven to be a powerful tool for many advanced technological applications e.g. two-photon material processing by evoking nonlinear processes in transparent materials. In this regards a practical example is presented in which nonlinear absorption properties are correlated with the surface and structural changes of an ultra short laser irradiated CR-39.

Apart from features mentioned above, self-organized subwavelength ripples and classical ripples on Al,  $\text{CaF}_2$  and Si induced by laser pulses have been investigated by AFM under different experimental conditions. These features are attributed to the excitation of surface plasmon polaritons to induce a periodic enhancement of local fields in the surface layers.

AFM investigations of the surface topography together with the characteristics of ejected particles observed with laser analytical methods yield coherent information and have widened the understanding of the processes involved. This is definitely a first step and has a large potential for further investigations: influence of the pulse-shape on the topography, identifying other possible processes by pump-probe shadowgraphy etc. This represents a challenge for the next years.

## Acknowledgement

*Without the support of God, supervisor, family, friends, and coworkers, it is never possible to finish the hectic and cumbersome job of my dissertation. As I am going to complete my doctorate soon, I would like to express my gratitude to all those personalities who really helped and supported me during the long way of my Ph.D.*

*First of all I would like to be highly grateful to my dearest and nearest God (Piarey Allah Mian Jee) the most beneficent and merciful, who always listens whenever I call Him whole heartedly. Then I would be highly grateful to my Holy Prophet Muhammad (peace be Upon Him) who is source of knowledge, guidance and good moral values.*

*I have no words to pay my thanks to my supervisor Professor Wolfgang Husinsky. He was a continuous source of inspiration during three years of my stay at TU Wien. He was always helpful, cooperative, supportive and accommodating for me. He always pushed me to work and gave me the full independence to work. He motivated me to precede my research on this topic and I learnt a lot from him on my research topic. Whenever I called him to come to lab for help or guideline, he was always ready to come and willing to help. He provided me good, comfortable and supportive research environment. Whenever there was a tough time, he was always ready to listen and understand the problem. His nice and encouraging attitude was blessing for me. He is a compassionate and kindhearted person.*

*I am also grateful to Prof. F. Aumayr (my group head), who was always cooperative and encouraging for me, especially for using AFM facility. I would like to thank A.S. El-Said for his help and suggestions concerning the AFM.*

*For SEM facility I am thankful to Ms. K. Whitemore and Prof. Wernish for assistance. For Raman Spectroscopy I am highly thankful to Dr. A. Hobro and Prof.B.Lendle from Institut für Chemische Technologien und Analytik for providing me this facility.*

*The person to whom I am really grateful for technical and electronics help in my institute is Mr. Paul Berlinger. His attitude was very much positive and welcoming in all three years. Whenever I went to him for help he was always willing to help out and to solve the problem sincerely and immediately.*

*I am thankful to technical staff of work shop for their help. I am also thankful to Ms. M. Marik, Ms. C. Toupal-printer and Mr. F. Beringer for their cooperation. I would be thankful to my all colleagues in the Lab. Special thanks goes to Ali Ajami who helped me a lot. I would like to say thank to my young colleagues Elizbeth, Martin, Johanes and others.*

*I would also like to say my heartiest thanks to my dearest and nearest husband Dr. Muhammamd Shahid Rafique. I am so lucky and blessed to have such a nice life partner who really provided me the practical and moral support. He visited Vienna five times for me at the cost of his career. Whenever there were hard and tough timings, he was always me. His encouraging, loving, kind and caring attitude always made my morals high. I discussed all the ups and downs of my Ph.D. with him and he is the person whose cooperation is a key of my success. He really sacrificed precious years of our life alone at the cost of my Ph.D. He is really a nice, considerate and cooperative person. Without his cooperation and continuous support I cannot fulfill my long lasting desire of becoming Dr. Shazia.*

*I do not how to pay my thanks to my loving and caring parents. They made me who I am today and all my successes can be attributed to them. My dearest father departed this world during my Ph.D. This was the biggest shock of my life because he was very polite, encouraging, thoughtful and generous towards me and my aim of studies. My sincere thanks goes to my most loving, thoughtful, caring and selfless mother who is really a source of prayers for me. During any difficulty of my work I always spoke to her on phone to pray for me. She prayed and I believe my problem was solved immediately. She always shows a serious concern towards my health, happiness and success.*

*I would pay my gratitude to my most caring and considerate elder brother Shahid Bhai jan who is always kind and loving to me and used to call me and say , try to come back as early as possible after completion your Ph.D as we are waiting for you anxiously. My kind sister Asia baji who always showed her serious concern towards my success, happiness and health and always used to say I am praying for your success. I am thankful to Zahid Bhai, Shazia Bhabi , Zakwan, Muaz , Talha, Huzaiifa, and Atika for best wishes. I would like to say thanks to my father-in-law, mother-in-law Tahira Baji and all other extended family member who supported me morally during my Ph.D.*

*At the last I would be highly thankful to my all Pakistani friends and colleagues at Vienna. Without their moral support and guidelines it was really difficult to stay in Vienna. I want to mention specially the name of Zahida Parveen, who was with me at last and difficult stages of my Ph.D. I can never forget to take night line (in harsh cold weather) with Zahida during my write-up. In the institute or at the home all weekends we spent together. Thank you Zahida.*

### ***Acknowledgements of Financial Support***

*I am highly grateful to Higher Education Commission of Pakistan (HEC) for providing me the financial support (scholarship) to stay in Vienna, Austria.*

# Thesis Contents

<i>Acknowledgments</i> .....	<i>i</i>
<i>Abstract</i> .....	<i>iii</i>
<b>Chapter 1 Introduction</b>	<b>4</b>
<b>1.1 Motivation and goals</b> .....	<b>4</b>
<b>1.2 Interaction of femtosecond laser radiation with matter</b>	<b>12</b>
1.2.1 Femtosecond laser radiation energy deposition mechanism .....	12
(a) Energy absorption.....	19
(b) Electron-electron collisions .....	20
(c) Electron-phonon collisions .....	20
(d) Phonon-phonons Collisions.....	20
(e) Electron impact ionization .....	21
(f) Strong-electric-field ionization .....	21
1.2.2 Processes governing the ultrashort laser radiation ablation .....	21
1.2.2.1 Nonthermal Processes .....	22
(a) Coulomb explosion (CE) .....	22
(b) Femtosecond Field Ion Emission by Surface Optical Rectification .....	31
(c) Ultrafast melting (UFM).....	33
1.2.2.2 Thermal processes.....	35
(a) Vaporization .....	37
(b) Boiling .....	37
(c) Phase explosion .....	37
1.2.2.3 Photomechanical Damage.....	38
1.2.3 Investigation and identification of femtosecond laser energy deposition mechanisms (ultrafast electronic and thermal processes) .....	39
1.2.3.1 Laser ablation mechanism probed by particle emission using time of flight mass spectrometry .....	40

1.2.3.2 Laser ablation mechanism probed by surface topography using atomic force microscopy.	40
<b>Chapter 2 Experimental set-up and Techniques</b>	<b>43</b>
<b>2.1 Femtosecond laser system</b>	<b>44</b>
2.1.1 Oscillator	44
2.1.2 Amplifier	45
(a) Specifications of Amplifier	46
(b) Pump Laser Specifications	47
Diode pumped Nd: YLF DM Series Specifications	47
Lamp-pumped Nd: YLF Specifications	47
2.1.3 Compressor	47
2.1.4 Laser pulse characterization	47
Laser Beam Profilometer	48
<b>2.2 Specific Experimental Details</b>	<b>48</b>
2.2.1 Targets Exposure in air	49
2.2.2 Target exposure under ultrahigh vacuum conditions	50
<b>2.3 Laser ablation analysis and characterization: Diagnostic tools for Surface topography, Structural analysis and Nonlinear absorption properties of ablated materials</b>	<b>51</b>
2.3.1 Atomic Force Microscopy (AFM)	52
Basic modes of AFM	54
(1) Contact Mode AFM	54
(2) Tapping Mode AFM	55
(3) Non-contact Mode AFM	55
2.3.2 Scanning Electron Microscopy (SEM)	56
2.3.3 Raman Spectroscopy	56
2.3.4 Z-scan Technique	58
<b>Chapter 3 Results and Discussion</b>	<b>60</b>
<b>3.1 Results and Discussion</b>	<b>60</b>
3.1.1 Calculations of Beam Radius, Rayleigh Length and Fluence	62

3.1.2 Energy Deposited per atom (eV/atom) .....	64
<b>3.2 Results for Dielectrics (CaF<sub>2</sub> (111)).....</b>	<b>66</b>
3.2.1 AFM Measurements.....	66
(a) Low fluence regime .....	66
(b) Moderate fluence regime .....	75
(c) High fluence regime .....	84
3.2.2 Raman Spectroscopy.....	87
<b>3.3 Results for Semiconductors (Si (111)) .....</b>	<b>90</b>
3.3.1 AFM Measurements.....	90
(a) Low fluence regime .....	90
(b) Moderate fluence regime .....	94
(c) High fluence regime .....	102
3.3.2 Raman Spectroscopy.....	108
<b>3.4 Results for Metals (Al).....</b>	<b>112</b>
3.4.1 AFM Measurements.....	112
(a) Low fluence regime .....	112
(b) Moderate fluence regime .....	121
(c) High fluence regime .....	128
<b>3.5. Results for Polymers (CR-39) .....</b>	<b>136</b>
3.5.1 AFM Measurements.....	136
(a) Low fluence regime .....	136
(b) Moderate fluence regime .....	141
(c) High fluence regime .....	143
3.5.2 Raman Spectroscopy.....	144
(a) Low fluence regime .....	145
(b) Moderate and high fluence regime .....	148
3.5.3 Z-Scan Measurements.....	151
<b>Chapter 4 Conclusions .....</b>	<b>155</b>
<b>References .....</b>	<b>160</b>

# Chapter 1

## Introduction

---

### 1.1 Motivation and goals

The rapid development of femtosecond lasers over the last decade has opened up a wide range of new applications in nanotechnology, industry, material science, and surgery. The interaction of laser radiation with different materials has been a subject of considerable interest for many years and has many applications in the field of pulsed laser deposition of thin films [1], laser-induced plasma [2], laser ablation chemical analysis, spectroscopy [3], micromachining [4] and medical [5]. With increasing availability of ultrashort pulses, their potential abilities are now implemented e.g. their capability to ablate materials very precisely by depositing energy extremely localized with little or no collateral damage to the remaining material. Therefore, ultra-short pulses with very high peak power render them a unique tool for machining a diverse range of materials. E.g., it has been shown, that femtosecond lasers can induce structural modification by nonlinear absorption [6] in transparent materials. This is used to fabricate optical data storage devices, waveguides, gratings, couplers, power splitters, wavelength conversion devices and optical amplifiers [7].

Recent advances in high-intensity femtosecond laser pulses have made it possible to induce various nanostructures inside versatile materials including dielectrics, semiconductors, metals and polymers. These femtosecond laser induced nanostructures have exceptional features and are widely discussed [8-10]. There has been a growing interest in these nanostructures because they suggest a promising approach to nano-processing of materials and can be used for fluidic, electronic, optic, and mechanical devices in various fields. It is well known, however, that the formation of this localized nanostructure with femtosecond laser pulses cannot be explained by the conventional models, and thus the physical mechanism creating such nanostructures is an important subject to study. In particular, the low threshold for particle removal is of special interest and has been the focus of recent investigations [8-10].

This thesis addresses fundamental physical processes involved in the interaction mechanism of ultrashort laser radiation with matter. The main goal of the work is to understand basic mechanisms of localized laser energy deposition in materials (insulators, semiconductors and

metals) and to explore their role in surface modification. In response to this deposited energy, nanostructures or nanohillocks appear on the surface of materials. These nanohillocks are regarded as a typical topographic feature associated with fast (sub 100 fs) electronic processes (correlated with the existence of hot electrons) resulting in Coulomb explosion (CE) or field ion emission by Surface Optical Rectification (SOR), in particular, demonstrating the efficient localization of energy in small volumes.

Modification of the surface structure of solid materials by laser radiation involves a complex chain of processes. The first step is the deposition of a certain amount of optical energy in the material. The material excitation is strongly dependent on the laser pulse duration. With the use of ultrashort laser pulses nonequilibrium energy distributions with large excess population in the excited states can be produced. The distinct physical processes which come into play in laser–solid interaction on the ultrafast time scale open new routes of modifying the structure and the morphology of materials and offer interesting perspectives in laser materials processing. Laser ablation and desorption [11] represent an important class of phenomena resulting from the interaction of laser light with materials. The interaction process leads to the emission of particles and transient or permanent modification of the material topography and/or material properties. Both, the particle emission and the change in material properties are clue to the specific processes resulting from the laser radiation.

The following scheme in figure 1.1 describes the basic approach to explain the interaction of ultrashort laser radiation with matter. When laser-matter interaction takes place it is of fundamental interest to have detailed understanding of different processes involved in ultra-short-laser ablation. Understanding the mechanism that lead to ablation in detail, remains a formidable challenge because of the complexity of the processes taking place, the variety of species involved, and the range of length and time scales covered. Ultra fast laser interaction with surfaces results in fast electronic and thermal ablation processes. The way the energy is deposited to electronic system, determines to a large extent, how efficiently the different processes contribute to laser-matter interaction. These different processes can be revealed either by surface topographical features or by particle emission. In this dissertation we have concentrated on the following method and ultrafast electronic and thermal processes are probed by Atomic Force Microscopy (AFM) which allows determining the surface topography after different stages of ultra-short laser-matter interaction and provides valuable information with respect to different ablation processes. It is well known that ultrafast electronic processes are dominant in the lower fluence regime. Therefore by starting from the ablation threshold three different fluence regimes have been chosen a lower fluence regime,



(0.06- 0.5 J.cm<sup>-2</sup> single shot irradiation under UHV condition) and 0.25-2.5 J.cm<sup>-2</sup> single shot irradiation in ambient condition, a moderate fluence regime (0.25-1.5 J.cm<sup>-2</sup> multiple shot irradiation ) (3) a high fluence regime 2.5- 8 J.cm<sup>-2</sup> multiple shot irradiation. After exposing targets at laser energies corresponding to these three different fluence regimes, the change in surface topography can provide a clue to differentiate between ultrafast electronic processes., CE or SOR (sub 100 fs) at a lower fluence regime), Ultrafast Melting (UFM) (hundreds of fs), at a moderate fluence regime and slow thermal processes (ps time scale) at a high fluence regime.

Laser analytical techniques or TOFMS (time of flight mass spectrometry) can help to identify the time behavior of the energy deposition, the composition and energy of the emitted particles. It is a promising approach to identify these processes by varying the time behavior of the energy deposition (pulse length, pump-probe experiments) and study the corresponding changes in the particle emission characteristics. It is essential to be able to vary the time (and as a result the amount) of the energy deposited in the electronic system. For ultra short pulses, in principle, two alternatives are feasible: *a*) changing the pulse length with a pulse-shaping device *or b*) using a two-pulse autocorrelation setup in which the differential yield of emitted particles is measured as a function of the temporal separation between a pair of ablation pulses with a reflectron-type time-of-flight (TOP) spectrometer. The intensity of each pulse has to be kept below the ablation threshold. Since most of the particles are neutrals, post-ionization of the particles by a laser is a requirement. In addition, the energy of the particles has to be measured.

A good correlation of both techniques can yield substantial information for better understanding of the physics involved.

This dissertation marks a significant step in gaining a coherent understanding of the physics involved in processes of deposition of a certain amount of laser energy for structural and surface modification of materials after ultrafast laser irradiation. Together with previous results [12-14] we could successfully address the questions with regard to the validity of ultra fast electronic (sub 100 fs electronic processes like Coulomb explosion (CE) or field ion emission by surface optical rectification (SOR), processes related to electronic plasma (FEP) formation (typically a few hundred fs time scale) and thermal ablation (TA)) processes, which have recently been identified via the time behavior of the energy deposition, the composition and energy of the emitted particles [12-14]. The relevance of studying the surface topography as a clue for electronic processes is not restricted to laser–matter interaction, but is of much

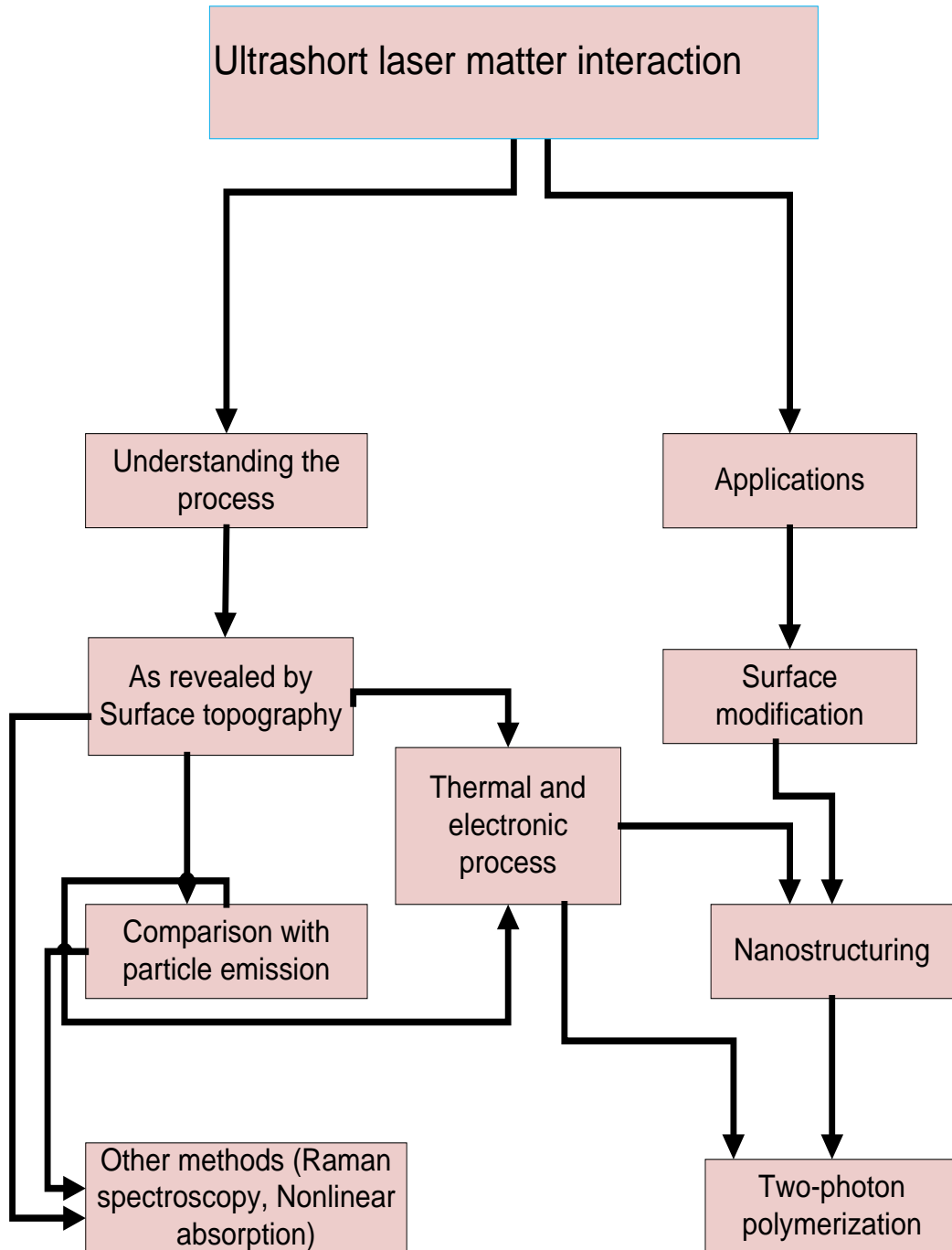


Figure 1.1: A schematic approach of ultrashort laser-matter interaction with two main aspects (fundamental and application) emphasizing that the correlation of two different techniques (surface topography and particle emission) provides possible pathways for detailed understanding of different (ultrafast electronic and slow thermal) processes involved in ultrashort-laser ablation.

more general interest. In fact, it has been recently shown, that the formation of nano-sized hillocks characterized by a sharp and well-defined threshold for the potential energy[15].

The first step of how energy of an ultra-short-laser pulse is transferred to a solid results in the creation of hot electrons in the conduction band [16]. In the case of dielectrics or represents a strong indication for the existence of electronic processes during ion bombardment of solids. semiconductors however, in a very first step electrons have to be promoted to the conduction band [11]. Following the excitation an avalanche process leads to hot electrons. Already three decades ago [17], it was proposed that ion bombardment and the ion sputtering process of insulators can be dominated by electronic processes. This fact has been established and proven since then on many occasions and by many groups.

Formation of nanohillocks for sputtering with highly charged ions [15] results in structures strikingly similar to the ones we have observed for ultra-short-laser irradiation and which are the major issue of this dissertation. It is, therefore, evident that one can speculate that these hillocks can be linked to similar fast electronic (potential energy) processes. Even if the details of the processes might be different, the creation of hot, fast electrons seems to result in a situation very similar to the one encountered for highly charged ion interaction with surfaces. The appearance of nano-sized hillocks under specific conditions should, therefore, be regarded as an additional and convincing argument for the physics of the various processes presented and discussed in [12-14]. Therefore, it is of fundamental interest to study the surface topography as it develops under ultra-short-laser radiation, in particular, close to the ablation threshold. Atomic Force Microscopy (AFM) is an ideal method to obtain this information.

The experimental data presented in [12-14] will be used for explaining the topographical results obtained by AFM. It is also important to mention, that in particular with respect to the sub 100 fs processes an alternative explanation (field ion emission by surface optical rectification (SOR)) avoiding some of the problems associated with Coulomb explosion (CE) for metals has been recently proposed by Vella et al [18]. Besides the fundamental, a more applied interest exists in studying the resulting surface topography, in particular the growth of nano-sized hillocks. Together with the fast development of practicable ultra-short-lasers over the last decade the controlled creation of nanohillocks might open a wide range of new applications for material science, in particular nano-science and technology and possibly medicine.

Ultrashort laser interaction mechanism can be different for different materials. In order to have a good correlation or comparison of different energy deposition mechanisms for

different materials insulators, semiconductors and metals are selected. The materials investigated are single crystals ( $\text{CaF}_2$  (111), Si (111)), polycrystalline (Al) and a polymer CR-39 (Allyldiglycol carbonate).

$\text{CaF}_2$  (dielectric) and CR-39 (polymer) have been selected for the investigations as representative examples.  $\text{CaF}_2$  is a dielectric material which has been recently investigated with regard to highly charged ions bombardment [15]. The appearance and formation of nano-sized hillocks has been found and it is characterized by a sharp and well-defined threshold for the potential energy. This represents a strong indication for the existence of electronic processes during ion bombardment of solids. The choice of  $\text{CaF}_2$  therefore makes it possible to have a good comparison of nanostructures developed after ultra-short-laser irradiation and ion bombardment and these structures can be linked and attributed to similar fast electronic (potential energy) processes. A second reason for selecting a dielectric material is, that CE with fs pulses in dielectrics is less controversial as compared to other materials [19, 20]. According to Bulgakova et al [20, 21] for near-infrared femtosecond irradiation charging of a dielectric surfaces causes a sub-picosecond electrostatic rupture of the superficial layers, alternatively called Coulomb explosion (CE), while this effect is strongly inhibited for metals and semiconductors as a consequence of superior carrier transport properties. If the surface topographical features obtained after near infrared (800 nm) femtosecond pulses for dielectric material are similar to a semiconductor and a metal, then a comparison can give a clue that similar kind of nonthermal (electronic processes either CE or SOR) ablation mechanism is responsible for energy deposition for all three kind of materials insulators, semiconductors and metals.

CR-39 (Allyldiglycol Carbonate) is an important polymer and is one of the most popular solid state nuclear track detector. It is known as an excellent material for a number of industrial, medical and optical applications. It has good optical transparency and structural stability. It is extensively used in various experiments in fusion research, nuclear science and astrophysics.

Si and Al are selected for several reasons: We have data from time of flight measurements available for these materials. This is helpful to obtain detailed information about the velocity distribution, the time behavior of the energy deposition (pulse width dependence studies), the composition and energy of the emitted particles and two-pulse correlation measurements. Through this information it is possible to identify the occurrence of ultrafast electronic (Coulomb explosion (CE), field ion emission by surface optical rectification (SOR), Ultrafast melting (UFM)) and thermal ablation. A comparison of surface topography with TOF

measurements can yield substantial information for better understanding of different processes involved in ultrashort laser matter interaction.

In addition, Raman spectroscopy is used for structural and crystallographic changes, which go hand in hand with surface topography changes. These structural, crystallographic and chemical changes, like amorphization, polycrystallization, stress distribution, bond breaking, bond weakening, crosslinking, polymerization, appearance of new disorder bands revealed by Raman spectroscopy measurements can be well correlated with the AFM surface analysis exhibiting the transition from electronic processes (nanoablation) to thermal processes with an appearance of a more disturbed target surface with increasing laser fluence.

Two-Photon Absorption (TPA) in molecular systems has attracted much attention of researchers due to its potential applicability in the field of future photonics such as 3D optical data storage, photonic crystals, photodynamic therapy, two-photon induced photopolymerization (TPIP) and many more. In order to obtain information how laser radiation is nonlinearly absorbed by a transparent material (CR-39) an open aperture Z-Scan technique is employed. As a practical example using Z-scan technique, nonlinear absorption properties of the polymer material have been investigated. The purpose of this study is to correlate surface, structural and chemical changes with nonlinear absorption properties induced by femtosecond laser irradiation at different fluences.

The first chapter introduces fundamental processes governing the interaction of ultrashort laser radiation with various materials (metals, semiconductors and insulators). The objective is to present the recent progress in understanding of the basic mechanism of laser- energy deposition in solids occurring on ultrashort time scales. This chapter presents an overview that how by choosing proper time windows and appropriate fluences, the various (ultrafast electronic and slow thermal) processes can be distinguished and investigated.

The second chapter deals with the basic layout, specifications and characterization of the laser system, and the main experimental set-up used to expose targets in air and UHV (ultrahigh vacuum) condition. The various diagnostic techniques employed for the surface and structural analyses of these ablated materials are discussed in the second chapter.

The third chapter is composed of experimental results concerning the surface modification of (dielectric, semiconducting, metallic and polymeric) materials after laser irradiation probed by AFM. This chapter explores and discusses the possibility of occurrence of localized laser energy deposition in different materials (insulators, semiconductors and metals) and to understand corresponding physical (ultrafast electronic and slow thermal) mechanism responsible for the development of different topographical features addressing the influence

of three different (a low, a moderate and a high) fluence regimes. Correlation of surface topographical features with time of flight mass spectrometry technique (the time behavior of the energy deposition, the composition and energy of the emitted particle) can yield substantial information for better understanding of the physics involved. Observed changes in surface topography are also correlated with Raman spectroscopy. In the last section surface and structural changes induced by laser irradiation are also correlated with nonlinear absorption properties of CR-39 as a practical example.

In the final section, general conclusions and a possible outlook of this work is presented.

## **1.2 Interaction of femtosecond laser radiation with matter**

### **1.2.1 Femtosecond laser radiation energy deposition mechanism**

The interaction of ultrashort laser pulses with materials involves a number of special features that are different from laser–matter interaction for longer pulse durations. With femtosecond laser excitation, it is possible to study fundamental physical processes (energy deposition mechanisms) in solids occurring on ultrashort time scales. By choosing proper time windows and appropriate fluences the various processes can be distinguished and investigated.

The initial step of how energy of an ultra short laser pulse is transferred to a solid results in the creation of hot electrons in the conduction band [22]. In the case of dielectrics or semiconductors, in a first step, however, electrons have to be promoted to the conduction band [23] . The creation of hot and fast electrons represents a situation very similar to the one encountered for highly charged ions interaction with surfaces [15].

When a laser pulse irradiates the surface of a solid, the laser energy may be absorbed. In metals the optical absorption is usually dominated by free carrier absorption, i.e. electrons in the conduction band absorb photons and gain higher energy. In semiconductors electrons are excited from the occupied valence bands to empty conduction bands, provided that the photon energy exceeds the band gap. In dielectrics with band gaps larger than the photon energy multiphoton transitions are necessary to promote electrons from the valence band to the conduction band. Multiphoton absorption is a nonlinear process i.e., the transition probability increases sharply with the laser intensity. In all these cases the timescale of the energy deposition is determined by the laser pulse duration. Following absorption, the optical energy is transferred from electrons to phonons and consequently lattice heating occurs.

Many theoretical investigations have been performed on NIR fs laser-induced ablation of dielectrics [23]. It has been proposed that the valence band electrons are excited to the conduction band (CB) via photoionization (PI) which includes multiphoton ionization and tunneling ionization. Ionization processes may lead to a rather high free electron density, which can explain the metal-like behavior of dielectrics under ultrashort laser pulse irradiation [24]. The conduction band electrons (CBEs) absorb laser energy via inverse Bremsstrahlung. When kinetic energy of CBEs is larger than the band gap, it impacts with another valence band electron, and excites the latter to CB. This impact ionization would induce CBEs numerical density to increase exponentially. Obviously, the process for CBEs absorbing laser energy played a very important role in impact ionization and laser energy deposition in samples. The processes responsible for the formation of a free-electron gas are illustrated in

Figure 1.2. According to Gamaly et al [25], if an intense ( $10^{13}$ – $10^{14}$  W/cm<sup>2</sup>), femtosecond pulse interacts with a dielectric, almost full single ionization of the target occurs at the beginning of the laser pulse. Following ionization, the laser energy is absorbed by free electrons due to Inverse Brehmstrahlung and resonance absorption mechanisms and does not depend on the initial state of the target. Consequently, the interaction with both metals and dielectrics proceeds in a similar way, which contrasts to the situation with a long pulse where ablation of metals occurs at a relatively low intensity compared with that for a transparent dielectric whose absorption is negligibly small. For dielectrics and semiconductors photoionization and electron–electron impact ionization are two competing processes which may lead to avalanche (free electron gas of comparably high density). In this regards the multiple rate equation (MRE) consisting of a set of coupled ordinary differential equations have been introduced by Rethfeld [23] . The transient free electron density in this regards is a fundamental parameter and is described by simple rate equation, combining the rate of photoionization  $\tilde{n}_{pi}$  with the rate of impact ionization, assumed to depend on the total free-electron density [23].

$$\frac{dn_{total}}{dt} = \tilde{n}_{pi}(E_L) + \alpha(E_L)n_{total} \quad 1.1$$

Where  $n_{total}$  is the total electron density,  $\tilde{n}_{pi}$  is the rate of photoionization,  $E_L$  is the amplitude of the electric laser field,  $\alpha$  is the avalanche coefficient.

Because of photoionization, depending directly on the amplitude of the electric laser field  $E_L$ , electrons are shifted from the valence band into the conduction band. In contrast, electron–electron impact ionization is caused by a free electron already existing in the conduction band. If its kinetic energy is sufficiently large, it may transfer part of it to an electron in the valence band, such that the latter is enabled to overcome the ionization potential. The avalanche coefficient depends on the effective energy gain of the free electron in the electric laser field  $E_L$ . One basic assumption of equation (1.1) is that impact ionization depends directly on the total density of the free electrons. However, also the energy of a particular electron plays an important role. Photoionization generates electrons with low kinetic energy in the conduction band while impact ionization requires electrons of high kinetic energy. This additional energy is absorbed from the laser light by intraband absorption. Figure 1.3 illustrates processes responsible for changing energy and density of free electrons in the conduction band (CB) of a dielectric, together with the processes involved in the generation of free electrons marked by arrows at the corresponding energies. Basically, the cycle of ionization is as follows:



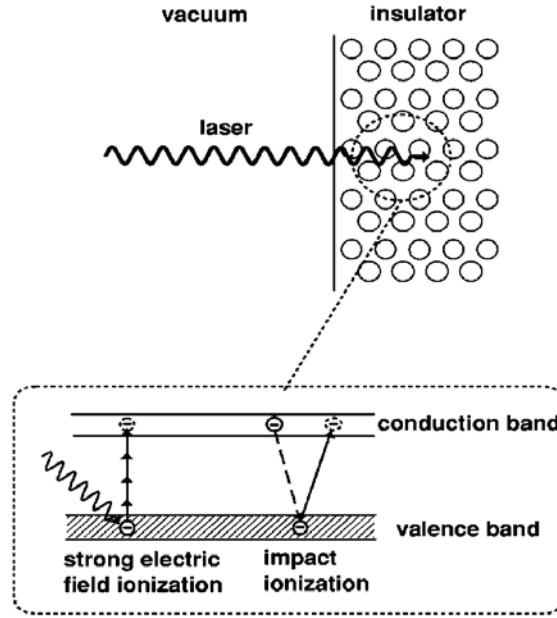


Figure 1.2: Processes for generation of free electron gas of an insulator [24].

Photoionization generates electrons with a certain ionization rate  $\tilde{n}_{pi}$  at the lower edge of the conduction band, i.e., with energy  $\varepsilon_o = 0$ . An electron at energy  $\varepsilon_o$  may absorb a single photon from the laser light with probability  $W_{1pt}(\varepsilon_o)$ . The resulting kinetic energy of the electron reads  $\varepsilon_1 = \varepsilon_o + \frac{\hbar}{2\pi}\omega_L$  where  $\omega_L$  is the laser frequency. In the same manner, further discrete energy levels  $\varepsilon_{j+1} = \varepsilon_j + \frac{\hbar}{2\pi}\omega_L$  are defined. When  $k = \left\lceil \frac{\varepsilon_{crit}}{\frac{\hbar}{2\pi}\omega_L} \right\rceil$ , where  $\varepsilon_{crit}$  is the critical energy for impact ionization, photons have been absorbed. The electrons energy  $\varepsilon_k = \varepsilon_o + k \frac{\hbar}{2\pi}\omega_L$  exceeds the critical energy for impact ionization  $\varepsilon_{crit}$ . For electrons with  $\varepsilon$

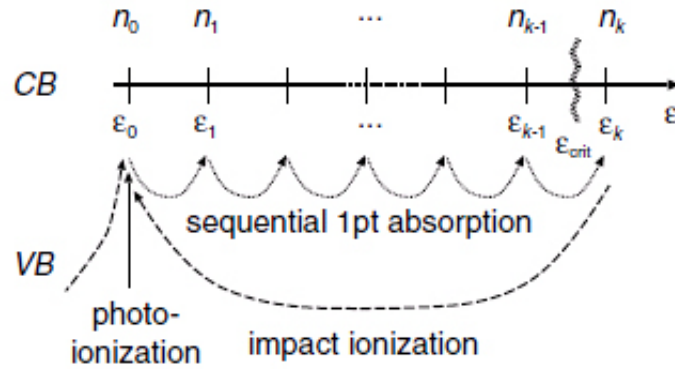


Figure 1.3: Illustration of the processes providing changes in the density and the energy, respectively, of free electrons in the conduction band of a dielectric [23].

$> \varepsilon_{crit}$  impact ionization occurs with a probability  $\alpha$ . Through this process, the kinetic energy will be reduced and a second electron is shifted from the valence band (VB) into the conduction band. Both electrons will then have a small kinetic energy, which is assumed to be comparable to  $\varepsilon_o$ . Defining the density  $n_j$  as the density of electrons at energy  $\varepsilon_j$  one can describe this process representing the multiple rate equation (MRE).

$$\frac{dn_{total}}{dt} = \tilde{n}_{pi}(E_L) + \alpha(E_L)n_k \quad 1.2$$

with  $n_{total} = \sum_{j=1}^k n_j$ . The difference in the last term of Eq. (1.2) compared to Eq. (1.1) is substantial. In Eq. (1.1) the impact ionization is assumed to depend on the total free-electron density  $n_{total}$ , while Eq. (1.2) considers the fact that only those electrons which bear sufficiently high energy may produce impact ionization.

A single laser pulse of femtosecond duration demonstrates the high-nonequilibrium state of the electron and phonon gas during and after laser irradiation. The free-electron gas is formed mainly by strong-electric-field ionization, whereas, impact ionization is of minor importance for laser pulses below 100 fs. Only with pulses of 200 fs the contribution to free electron density by impact ionization becomes as important as strong electric-field ionization.

Figure 1.4 [24] shows the transient behavior of the occupation number of free electrons in the conduction band as a function of kinetic energy  $\varepsilon_k$ . The applied laser pulse has a length of 100

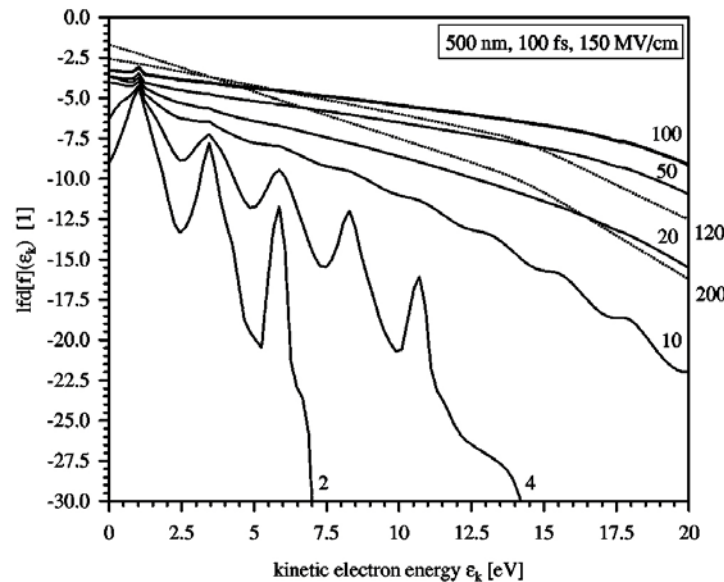


Figure 1.4: Transient behavior of electron occupation number, represented by the function Deviation from a straight line indicates disturbance of thermal equilibrium; the value represents the number of electrons in the corresponding energy state. The numbers at the curves are the time in femtoseconds from the beginning of laser pulse irradiation. For the calculation a laser beam with 100 fs pulse length applied on SiO<sub>2</sub> [24].

fs and an electric field of 150 MV/cm. The numbers at the curves denote the time in femtoseconds from the beginning of the pulse. A function  $lfd[f]$  is plotted, which is defined as

$$lfd[f] = -\log\left(\frac{1}{f(\varepsilon_k)} - 1\right) \quad 1.3$$

In thermal equilibrium, when electrons obey a Fermi-Dirac distribution,  $lfd[f]$  equals  $(\varepsilon_k + \varepsilon_{fermi}) / 2 / k_B T$ . In this case  $lfd[f]$  is a linear function of electron energy  $\varepsilon_k$  with a

slope proportional to the inverse electron temperature. Values of  $lfd[f]$  increase monotonically with  $f$  values. The deviation of  $lfd[f]$  from a straight line indicates the deviation of the electron gas from thermal equilibrium. Immediately after the beginning of irradiation, the occupation number in the conduction band starts to grow, as electrons are shifted from the valence band into the conduction band by strong-electric-field ionization, and thermal equilibrium is strongly disturbed.

As can be seen in Fig. 1.4, the free-electron occupation number distribution function changes its shape within the femtosecond regime. *The values of  $lfd[f]$  for  $t=4$  fs show a series of equally spaced peaks.* The peak at the lowest energy results from electrons excited by strong-electric-field ionization. Some of these free electrons absorb further photons, resulting in an increased occupation number at energies larger by multiples of the photon energy. This leads to the formation of an equally spaced peak structure.

In the further course, more and more electrons are promoted to the conduction band where they continue absorbing energy from laser irradiation. The peak like structure, formed at the beginning of laser irradiation, is smeared out due to internal relaxation processes like electron-electron collisions. Also phonon heating by electron-phonon collisions leads to a relaxation of the electron gas. Already 50 fs after beginning of the laser pulse, no distinct peaks are visible except the lowest one caused by strong-electric-field ionization. At the end of and after the laser pulse ( $t \geq 100$  fs) the high-energy part of the occupation number decreases while for low kinetic energies, the number of free electrons increases. This is an effect of impact ionization, where high energy electrons partially transfer their energy to valence electrons. In such a collision, one high-energy electron disappears while two low-energy electrons emerge. After irradiation, strong-electric-field ionization disappears whereas,

impact ionization still continues. Except for the high-energy tail, the free-electron occupation number resembles an equilibrium distribution  $lfd[f]$  –curve by that time. The slope of the  $lfd[f]$  – curve decreases with time since the hot electron gas transfers energy to the lattice.

In metals the energy transfer from hot electrons to the initially cold lattice is usually described by a two-temperature model (TTM) [26]. The TTM is generally accepted model for electron-phonon energy relaxation (the experimental effective electron-phonon relaxation time is 710-530 fs and 830-530 fs for Ag and Au respectively, for 300 -10K lattice temperature [27] ) and is based on the assumption that electron and lattice can be described by two different time-dependent temperatures. In other words, the energy distributions of both electrons and phonons are thermal distributions, each characterized by a temperature, the electron temperature and the lattice temperature, respectively. This model is particularly applicable on the system which can be described by time scales larger than the electron–electron collision time. A Fermi distribution is established in the electron system by electron–electron collisions. However, for times shorter than the electronic thermalization time (on femtosecond time scale) , and for low excitations non-thermalized electron gas may be observed [28]. Shorter time scales events (taking place in fs time regime) are nonthermal in nature and cannot be dealt with TTM model. A nonthermal electron model is developed by Groeneveld et al [27], in which electron-electron and electron-phonon dynamics is accounted simultaneously. It is demonstrated by this model that incomplete electron thermalization yields a slower electron-phonon energy relaxation in comparison to the thermalized limit.

The transient behavior of electrons and phonons in metals has been studied by Rethfeld et al. [29, 30]. A microscopic approach was used that took into account the temporal evolution of the electron and phonon distribution functions and their changes due to laser absorption, electron–electron, and electron–phonon collisions. This approach allowed a detailed investigation of the influence of the individual collision processes even for highly nonequilibrium conditions. On femtosecond time scales, non-thermalized electron gas may be observed. For low excitations, a non-thermalized electron gas may affect observable characteristics like electron–phonon coupling. According to [29, 30] the system of Boltzmann equations for the calculation of distribution functions of electron gas and phonon gas can be expressed as

$$\partial f(k)/\partial t = \partial f(k)/\partial t|_{el-el} + \partial f(k)/\partial t|_{el-phon} + \partial f(k)/\partial t|_{absorb} \quad 1.4$$

$$\partial g(q)/\partial t = \partial g(q)/\partial t|_{phon-el} \quad 1.5$$

Where  $f(k)$  and  $g(q)$  are distribution functions of electrons and phonons depending on the modulus of wave vector  $k$  and  $q$  respectively. Before irradiation,  $f(k)$  and  $g(q)$  are assumed

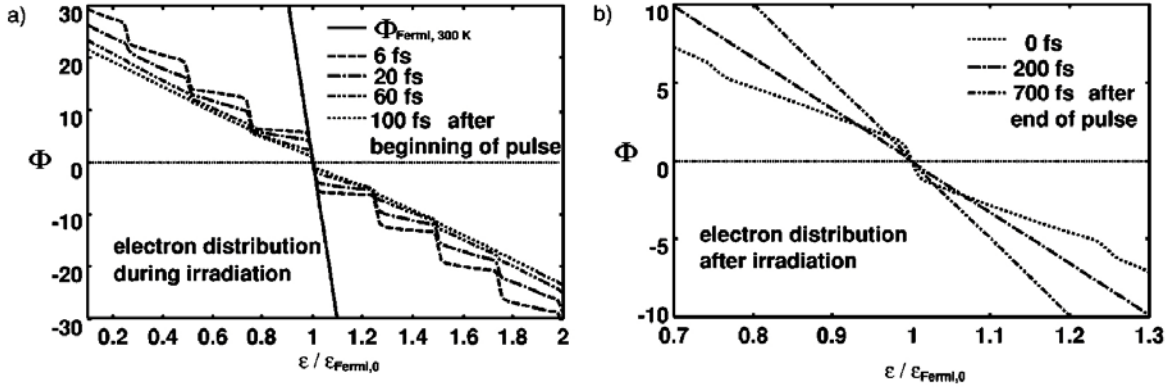


Figure 1.5: Distribution function of free electrons in aluminium during (a) and after irradiation (b). The quantity  $\Phi$  defined by equation (1.3) is shown as a function of electron energy. A laser pulse of 100 fs duration and rectangular intensity profile was assumed, with  $\lambda = 630$  nm, electric laser field corresponding to an intensity of an absorbed fluence of (b) shows a section of about the energy scale [30].

to Fermi-Dirac distribution and Bose-Einstein distribution respectively, both at room temperature.

As soon as an electron is excited to energy  $\varepsilon$  above Fermi energy it will decay after a time  $\tau_{ee} \propto (\varepsilon - \varepsilon_{Fermi})$ . However, the distribution function of electrons is in nonequilibrium for a much longer time because secondary electrons are created. Thus, many electron-electron collisions are needed to establish finally a Fermi distribution. It was shown experimentally [30] that the electron distribution function, after excitation with a femtosecond laser pulse, is not in thermal equilibrium for a few 100 fs up to the picosecond regime. Thus, the description of the electron gas with a temperature  $T_e$  as done in the two-temperature model is questionable for time scales below 1 ps.

Figure 1.5 shows the transient behavior of the occupation number of free electrons for an electric laser field of amplitude  $E_L = 1.4 \times 10^8 \text{ V/m}$  corresponding to an intensity of  $I_L = 7 \times 10^9 \text{ W/cm}^2$  and an absorbed fluence of  $F_{abs} = 0.7 \text{ mJ/cm}^2$ . A function  $\Phi$  is defined as

$$\Phi(\varepsilon) = -\ln\left(\frac{1}{f(\varepsilon)} - 1\right) \quad 1.6$$

is shown as a function electron energy  $\varepsilon/\varepsilon_{fermi}$ . This function increases monotonically with increasing occupation number  $f(\varepsilon)$  and is particularly suitable to visualize the perturbation of

the electron gas. In thermal equilibrium, when electrons obey a Fermi–Dirac distribution,  $\Phi(\varepsilon)$  equals  $(\varepsilon_{fermi} - \varepsilon) / k_B T_e$ . In this case,  $\Phi(\varepsilon)$  is a linear function with a slope proportional to

the inverse electron temperature  $1/T_e$ . Values of  $\Phi(\varepsilon)$  increase monotonously with increasing occupation number  $f(\varepsilon)$ . A deviation of  $\Phi(\varepsilon)$  from a straight line indicates a deviation of the electron gas from thermal equilibrium. Figure 1.5 (a) shows a strong perturbation of the electron gas immediately after the beginning of irradiation in comparison with the straight solid line representing the initial Fermi distribution at 300 K, the absorption of photons leads to a step-like distribution function.

Figure 1.5 (b) shows energy distribution function of free electrons in aluminum during and after irradiation for energies of about  $\pm \frac{\hbar}{2\pi} \omega_L$  around the Fermi edge. A straight line  $\Phi(\varepsilon)$  corresponding to a Fermi distribution  $f_{Fermi}(\varepsilon)$ , is reached about 200 fs, after irradiation has ended. Its slope, however, is still much smaller than those for the Fermi distribution at 300 K. Thus, the electron gas is heated significantly. Later on, the effect of electron-phonon interaction is also visible. The cooling of the hot electron gas leads to an increasing slope of  $\Phi(\varepsilon)$  corresponding to lower electron temperatures.

When studying electron emission, for example, one is only interested in high-energy electrons. Then it is sufficient to focus on the high-energy tail of the distribution function and on the lifetime of one electron. Since the electron-electron collision time depends on the electron energy, this lifetime is much shorter than the collision time of an electron in the low-energy region. However, low-energy electrons are essential when investigating the time needed to establish a Fermi distribution, which is important for the collective behavior of the free-electron gas. The transient evolution of the electron distribution in metals after laser excitation is thus of fundamental interest for a wide field of research [30].

### **(a) Energy absorption**

Energy absorption from the laser occurs in metals [30] and dielectrics [24] mainly through free electrons. In the classical picture, a free electron oscillates in the electromagnetic field of the laser and absorbs energy only when it is changing its momentum parallel to the oscillation direction. This can happen through a third collision partner, which disturbs the oscillation of the electron. The kinetic oscillation energy is  $\langle \varepsilon_{kin} \rangle = \frac{e^2 E_L^2}{4m_e \omega_L^2}$  on average, where  $\omega_L$

is the angular frequency of the laser light,  $e$  is the electron charge,  $m_e$  is the electron mass, and

$E_L$  is amplitude of its electric field. Collisions of electrons with fixed ions change solely the momentum of free electrons, while the energy of a free electron changes in collisions with ion vibrations, which are represented by phonons. Thus, electron-ion collisions mediate the energy absorption of laser light by free electrons, while energy transfer between the electron gas and lattice occurs through electron-phonon interaction.

#### ***(b) Electron-electron collisions***

Electron-electron collisions lead to an energy relaxation within the electron gas called (electron) thermalization. Through this process the absorbed energy is distributed among the free electrons so that the electron gas tends towards a thermal equilibrium and thus to a Fermi distribution [24, 30].

#### ***(c) Electron-phonon collisions***

The main effect of electron-phonon collisions is to transfer energy from the laser-heated electron gas to the cold lattice. By emission of phonons the electron gas cools down. Since the maximum phonon energy is small compared to the kinetic electron energy, one electron-phonon collision changes the energy of the electron gas slightly. Thus, many electron-phonon collisions are necessary to decrease the amount of kinetic energy stored in the electron gas. In addition, electron-phonon interactions have an equilibration effect on the electron gas. Phonon emission and absorption occur in such a way that the electron gas tends to establish a Fermi distribution (at phonon temperature). In metals, not only the interaction of one electron with the lattice deformation has to be taken into account but also the screening of the lattice deformation by free electrons and the interaction of that electron with the screening electrons [30].

The interaction between the free electron gas and a nonpolar phonon gas is described with deformation potential theory, which is a valid approximation for long phonon wavelengths. This expression is, however, also applied to phonons with short wavelength. As a result, the free electrons interact only with longitudinal phonons [24].

#### ***(d) Phonon-phonons Collisions***

The phonon distribution function is assumed to change only due to phonon-electron collisions. Direct absorption of the laser energy is neglected. Thus, phonon-phonon collisions are neglected as well. Phonon-electron interaction leads to heating of the phonon gas, analogously to the cooling of the electron gas by electron-phonon collisions. It was found that

for weak excitations the energy transfer from the electrons to the lattice is delayed when the energy distribution of the laser-excited electrons is nonthermal. On the other hand, for stronger excitations (leading to melting or ablation) thermalization occurs more rapidly [30].

***(e) Electron impact ionization***

In dielectrics impact ionization takes place by free electrons of high kinetic energy, which may transfer sufficient energy to valence electrons to overcome the ionization potential. Impact ionization leads to an increased electron density in the conduction band. For this process a minimum kinetic energy of the colliding free electron is needed to fulfill energy and momentum conservation. A common treatment for impact ionization is the application of the so-called Keldysh's impact ionization formula

$$W_{imp}(\varepsilon) = P \cdot \left[ \frac{(\varepsilon - \varepsilon_c)}{\varepsilon_c} \right]^2 \quad 1.7$$

where P is constant. This expression gives the impact ionization for a free electron with kinetic energy  $\varepsilon$  above the critical energy  $\varepsilon_c$  shifting an electron from valence band into conduction band [24].

***(f) Strong-electric-field ionization***

In strong electric laser fields, an electron in the valence band (in case of dielectrics) may absorb several photons in one step and gain enough energy to overcome the ionization potential. This process is called multiphoton ionization, its probability, of course, increases with laser intensity. For very high electric laser fields, the potential well formed by the band gap is distorted and photo-induced tunneling may occur.

Keldysh examined strong-electric-field ionization, and obtained a general expression for the ionization rate and approximate expressions for both limiting cases [24].

## **1.2.2 Processes governing the ultrashort laser radiation ablation**

The nature of processes which govern the interaction of ultrashort laser radiation ablation of materials can be a complex interplay between ultrafast processes and processes on time scales which one traditionally calls the thermal regime. The way (magnitude, timescale etc.), in which the energy is deposited to the electronic system, determines to a large extent, how efficient these different processes contribute. Therefore, a promising approach to identify these processes is to vary the time behavior of the energy deposition (pulse length, pump-probe experiments) and study the corresponding changes in particle emission characteristics.



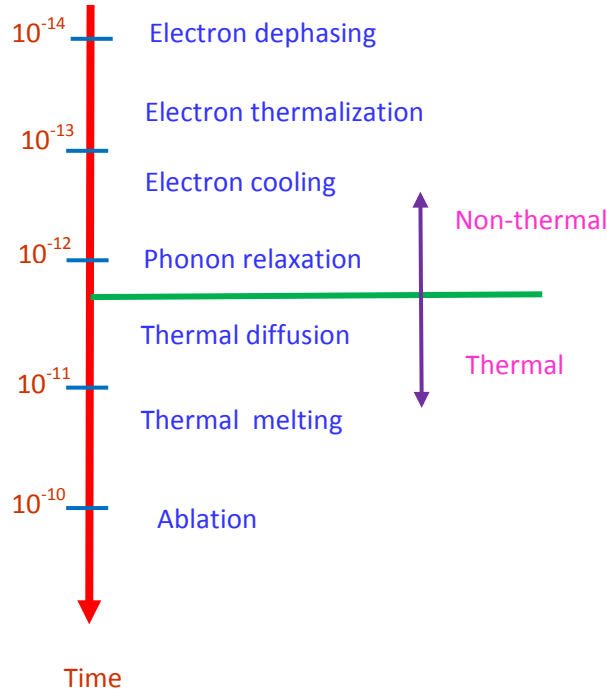


Figure 1.6: The time scale of various processes governing the interaction of ultrashort laser radiation with matter [31].

Ultrafast processes occur before the thermalization process between the atoms and the hot electrons. The chain of events governing the interaction of ultrashort laser radiation with matter can be crudely classified according to the time as shown in figure 1.6 [31].

#### 1.2.2.1 Nonthermal Processes

##### (a) Coulomb explosion (CE)

Coulomb explosion is an ultrafast nonthermal process responsible for particle emission of several eV within 100 fs and can be observed experimentally around the ablation threshold. CE can occur when parts of the lattice become charged due to fast electronic processes and as a consequence the lattice disintegrates through the repulsive forces between the charged lattice sites. As far as ultrashort laser ablation is concerned, CE is of particular interest. Under conditions where this mechanism is dominant, the irradiated surface appears smooth and material removal can be accurately controlled on the nm scale. This has been termed the gentle ablation phase. The velocities of charged particles following disintegration are determined by the repulsive Coulomb forces, while neutral particles can obtain their velocities by collisions with fast ions or can be formed from neutralized ions. Experimental studies have lead to the conclusion that a significant fraction of the ions emitted from a surface after short-

pulse laser irradiation can show the fingerprints of Coulomb explosion (CE) in dielectrics [32-36], semiconductors [12, 37] and even in metals [13, 14, 38, 39].

Positive charges are generated on the surface by photoexcitation, and CE occurs wherever the charge density exceeds a certain threshold level, i.e., the electrostatic repulsion overcomes the bond energy. The emitted positive ions (typically clusters) accelerated in the electrostatic field possess high kinetic energies, ranging from a few eV up to a few hundred eV.

Besides positive ions, high-energy neutral clusters have also been observed, [13] indicating a high probability for collision and neutralization.

Pros and cons of CE are discussed below. The occurrence of the surface Coulomb explosion generating macroscopic material removal and high ion kinetic energies has been demonstrated for dielectrics and other insulating materials [32-36], while for semiconductors and metals [20, 25, 40] the subject remains controversial [41]. The occurrence of CE in semiconductors has already been debated [12, 13, 20, 37, 42].

According to Bulgakova et al [20, 21], for near-infrared femtosecond irradiation charging of dielectric surfaces causes a sub-picosecond electrostatic rupture of the superficial layers, alternatively called Coulomb explosion, while this effect is inhibited for metals and semiconductors as a consequence of superior carrier transport properties.

According to Stoian et al [42], sufficient charge can be accumulated at the dielectric surface to initiate CE on the 100 fs time scale. With semiconductors and metals, the higher electron mobility and higher density of available free electrons ensure effective screening and a much smaller net positive charge accumulation during the laser pulse. This is not sufficient, by orders of magnitude, to induce a macroscopic electrostatic breakup of the outer layers of the substrate. Coulomb explosion modeling involves description of free electron generation, their heating and photo-emission, and, as a result, generation of the self-consistent electric field and electric current in the targets. Under ultrashort pulsed laser irradiation different interrelated processes are demonstrated in a simplified scheme shown in figure 1.7 [40] for the case of dielectrics and semiconductors. Two kinds of processes are taking place: one starting from photoionization (with the order of the process depending on the relation between the photon energy and the material bandgap) and another starting from photo-emission (with the order of nonlinearity determined by the ratio of the work function to the photon energy). Dependences between different processes are shown by arrows. Most of the processes are interconnected, which is shown by double-sided arrows. Dependences of the processes within a branch are stronger (solid lines) than between the branches (broken lines). The electrons excited to the conduction band absorb laser radiation and can produce secondary electrons by collisional

ionization. As soon as electronic avalanche is developed, absorption and reflection dynamics vary dramatically. A drastic consequence of electron photoemission is the violation of the target quasi-neutrality that results in positive charging of the target as a whole and thus in generation of an ambipolar electric field. The electric field forces the charge carriers to relocate in order to neutralize the excess positive charge. The charge-carrier current is a superposition of drift and diffusion. Redistribution of the charge carriers (free electrons and, in the case of semiconductors, holes) affects electron photoemission and the avalanche multiplication process. Photoemission depletes a superficial target layer and, avalanche in turn regulates photo-emission through its influence on the available free-electron density.

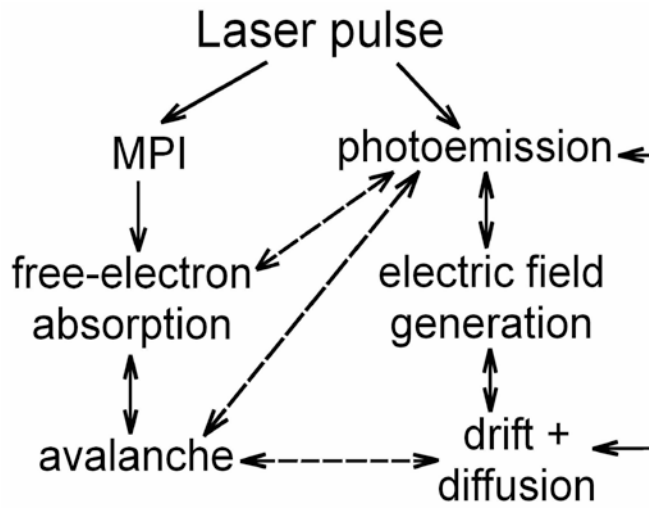


Figure 1.7: A scheme of major interconnections between different interrelated laser-matter interaction processes [40].

The continuity equations for electrons and holes (ions) can be written in a general form as [40]

$$\frac{\partial n_x}{\partial t} + \frac{1}{e} \frac{\partial J_x}{\partial x} = S_x + L_x \quad 1.8$$

where  $S_x$  and  $L_x$  are the source and loss terms describing the free carrier populations,  $n_x$  denotes the carrier densities with subscript  $x = e, i$  representing electrons and ions respectively,  $J_x$  is electric current consisting of the drift and diffusion terms.

The source term accounts for free electron generation (one- or multiphoton ionization depending on the material band gap and avalanche). In the loss term, free-carrier recombination is taken into account as well as loss of electrons in volume photo-emission

from the electronic escape depth. In metals and semiconductors, photo-emission is considered as a surface process and the PE term is set as a boundary condition for electric current through the sample surface. For metals, Equation 1.8 has a net value zero on the RHS. Electric field generation resulting from PE is described by the Poisson equation. It should be noted that, even in absence of PE, the internal electric field can be found in dielectrics and semiconductors due to strong density and temperature gradients of charge carrier population (with preserving quasineutrality of the target as a whole). On the other hand, the PE and surface charging can have influence on the energy balance which justifies to use a wide variety of models describing laser light absorption and heating of different materials [21]. The strong charging of sapphire shown in figure 1.8 (a) [21] is not a result of higher photoemission as compared to silicon and gold. Accordingly, the sapphire target loses approximately  $6.8 \times 10^8$  electrons over the entire laser pulse duration from an irradiated spot of  $470 \mu\text{m}^2$ , whereas  $6.2 \times 10^{11}$  and  $3.5 \times 10^{11}$  electrons are removed for Si and Au targets, respectively. At the same time the largest electric field is generated in the sapphire target. Figure 1.8 (b) shows the temporal behavior of the electric field values developed at the sapphire surface in comparison with the field values induced in other types of materials. The negative value implies that the field is directed away from the target, streaming from the sub-surface layers to the vacuum. It is observed that the electric field exceeds the critical value and reaches a value of  $8.4 \times 10^{10} \text{ V/m}$  beneath the surface. The above-threshold electric field exists for a few tens of fs and can induce the electrostatic rupture of a surface layer approximately  $40 \text{ \AA}$  wide, in excellent agreement with the experimental estimation of the Coulomb exploded region.

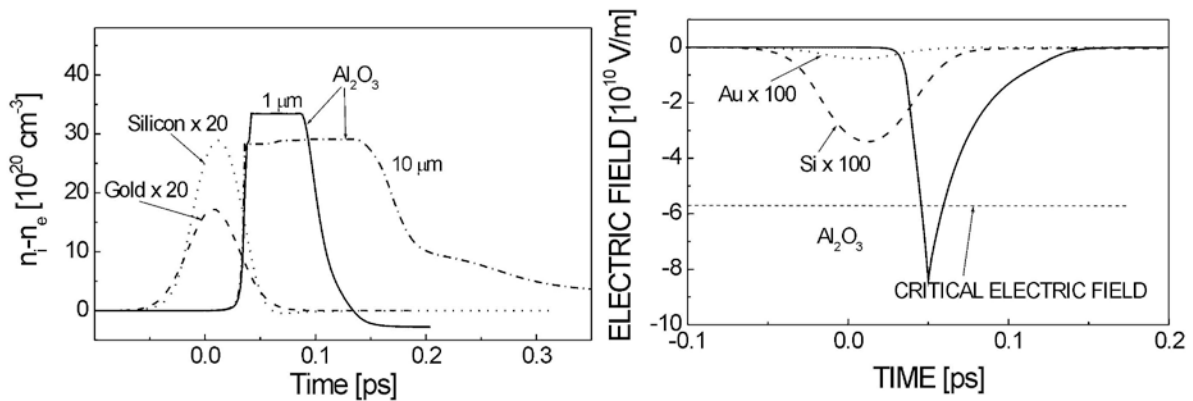


Figure 1.8: (a) Temporal behavior of the net surface charge density (the difference between the hole and the electron populations) for different classes of materials. Laser fluences are chosen to be above the ion emission threshold for each material ( $4 \text{ J/cm}^2$ ,  $0.8 \text{ J/cm}^2$ , and  $1.2 \text{ J/cm}^2$  for Al<sub>2</sub>O<sub>3</sub>, Si, and Au, respectively). The laser pulse of 100 fs duration is centered at  $t = 0$  (b) Temporal profiles of the laser-induced electric field in the surface region of targets [21].

What happens when a target is subjected to laser irradiation, loses electrons due to photoemission? The conditions for optical breakdown occur within a skin layer with a near-exponential decay towards the target depth. Because of photoemission, the target quasi-neutrality is broken. According to the Gauss's law, the target, which starts to behave like a metal upon strong excitation, accumulates excess positive charge on the surface (figure 1.9). The electric field in this thin surface layer is “negative” (directed to the vacuum), that means that the electrons are forced towards the target depth to a region with lower field, while in the deeper region electron drift is directed toward the surface. It should be observed that, in a region with “negative” electric field, the holes drift toward the surface, thus favoring positive charge accumulation. As noted above, for nanosecond laser pulses with low fluence, the electrons cannot gain a high average energy because of efficient electron-lattice relaxation [21]. So, in contrast to NIR femtosecond laser pulses, where electron diffusion toward the surface closes the positive area, withstanding the electric force because of high electron energy, for UV nanosecond laser pulses the outer target layer is charged positively to a high value. The most important consequence inherent to ns laser pulses is that in the charged outer layer one-photon ionization is continuing during the laser pulse, whereas the Auger recombination is strongly suppressed because of the lack of electrons. Under fs NIR laser irradiation with  $0.8 \text{ J/cm}^2$  the hole density has a maximum shift from the surface toward the bulk, which is caused by the suppression of the avalanche process in the surface layer depleted of electrons due to photoemission. In this case, a free-carrier “pool” is formed in a certain depth in the target, on the order of several tens of micrometers, resulting in a strong electron supply to the charged target layers. On the contrary, under UV laser irradiation the hole density profiles are strongly limited by the characteristic absorption width, so that in a depth of  $0.2 \text{ }\mu\text{m}$  the charge carrier density corresponds to the intrinsic one ( $1.5 \times 10^{10} \text{ cm}^{-3}$ ). For UV ns laser pulses, this provides the conditions for CE, cutting down the electronic supply from the bulk, while for UV fs laser pulses this leads to a localization of the laser energy in a thin target layer, resulting in an extremely low melting threshold and in the occurrence of phase explosion as the most probable consequence [21].

Conditions for Coulomb explosion can be reached when the energy of the electric field generated in the target or applied from outside exceeds the binding energy of atoms (or larger pieces composing matter like molecules or clusters) in the bulk material. For surface atoms the binding energy can be evaluated from the latent heat of vaporization corresponding to one atom  $\Lambda_{\text{at}}$ . Comparing the value of the binding energy with the energy of the electric field

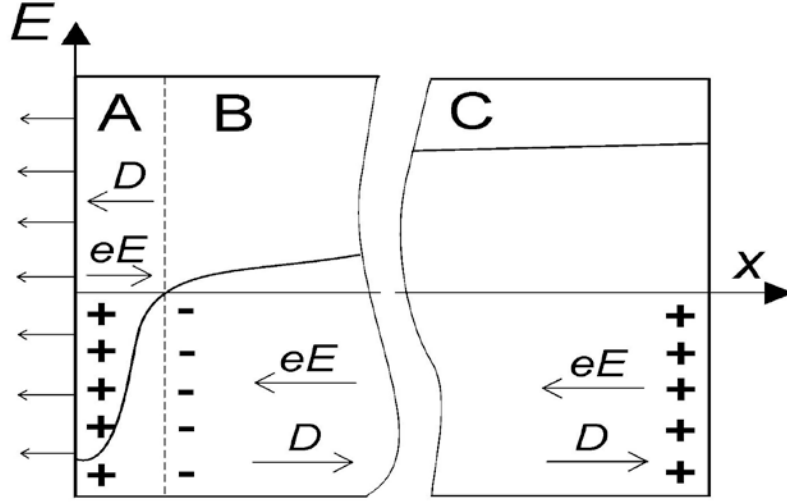


Figure 1.9: A schematic representation of a target irradiated by a laser pulse. A denotes a surface region depleted of electrons, where the electric drag force  $eE$  dominates the electron diffusion  $D$  toward the depleted region. This results in the accumulation of a high positive charge at the target surface. In zone B where the electric field is small, a region with negative charging is formed. Further to the target depth (region C), a new zone arises with a reduced positive charge [21].

corresponding to the volume occupied by one atom, the threshold electric field with respect to CE [40] is given as

$$E_{th}|_{x=0} = \sqrt{2\Lambda_{at}n_0/\epsilon\epsilon_0} \quad 1.9$$

where  $n_0$  is the number density of the target material,  $\epsilon$  is the permittivity of the medium and  $\epsilon_0$  is permittivity of free space. The heated surface atoms having a definite energy of vibrations can escape from the surface with higher probability than the cold ones, a fact which should decrease the above threshold value. Also the surface adatoms having lower binding energy with the surface as compared to usual surface atoms can be emitted at even lower electric fields. However, for macroscopic CE when at least several monolayers of material are ablated, equation (1.9) represents a reasonable criterion.

It is important that for the Coulomb explosion regimes, conditions may be created where ion emission can be initiated below the thermodynamic melting threshold, due to the different nature of the corresponding mechanisms. With increasing laser fluence beyond the onset of thermal mechanisms involving melting and vapor transformation, the additional mechanisms of rather thermal nature are superimposed on CE and can substantially mask the latter. The main difference of the electronic and thermal mechanisms is in scaling of the velocity distribution of species which is momentum scaling for the first and energy scaling for the

second [37]. On the one hand, higher laser fluence induces stronger electron photo-emission, thus enhancing CE probability. But on the other hand, the particles abundantly emitted during phase explosion have a wide velocity distribution with a high-energy tail masking the electronically ablated energetic particles. Another masking factor can be charge separation in the gas phase that leads to appearance of a high-energy ion peak in the front of the plume with momentum scaling in the velocity distribution. Observations of CE at high laser fluences well above the ablation threshold are thus contradictory as it can involve a number of the superimposed mechanisms leading to the same effect of fast particle generation [40].

At laser intensities well below the single shot damage threshold, Coulomb explosion upon multiphoton surface ionization has been established as the principal origin of positive ion emission from dielectrics[35, 36]. This process occurs on a femtosecond time scale, resulting in a positive surface charge. The generated holes cannot be filled again immediately, and at a sufficient hole density, the surface becomes electrostatically unstable and explodes. Typical features in this regime are an evident dependence of the kinetic energies on the ion charge, as well as only a very weak dependence of the ion generation rate on their electronegativity, indicating that most of the ablated material is in form of positive ions. In this regime, the density of excited electrons which do not leave the surface is not sufficient to transfer enough energy via hot electron phonon collisions to the lattice to provoke substantial heating[43].

The situation changes with increasing excitation energy. First, the density of conduction band electrons inside the crystal becomes larger. Second, the surface ionization rate starts to saturate since a significant space charge builds up near the surface because of the high surface hole density. This leads to an additional increase of the electron density in the conduction band. These electrons can then be heated by free carrier absorption and impact processes to produce a hot electron gas, which subsequently relaxes to the lattice by electron phonon collisions. Since typical time constants for this process are in the sub-picosecond to picosecond range [18, 19], the surface region can be rapidly heated to very high temperatures (far above the melting temperature). This temperature rise and even the critical temperature without any significant volume expansion (limited by the speed of sound), should occur on a time scale of several picoseconds, and almost immediately (on a sub-picosecond timescale) results in lattice destabilization [17, 20].

The existence of CE for ultra-short laser ablation of Si, even though questioned, at least has been claimed by other groups [37]. Results of [14] are shown in figure 1.10 that indicate the existence of CE in Si ( with the appearance of first sharp peak within 50 fs time scale) From this figure it can be deduced that CE is more dominant mechanism for lower fluence regime

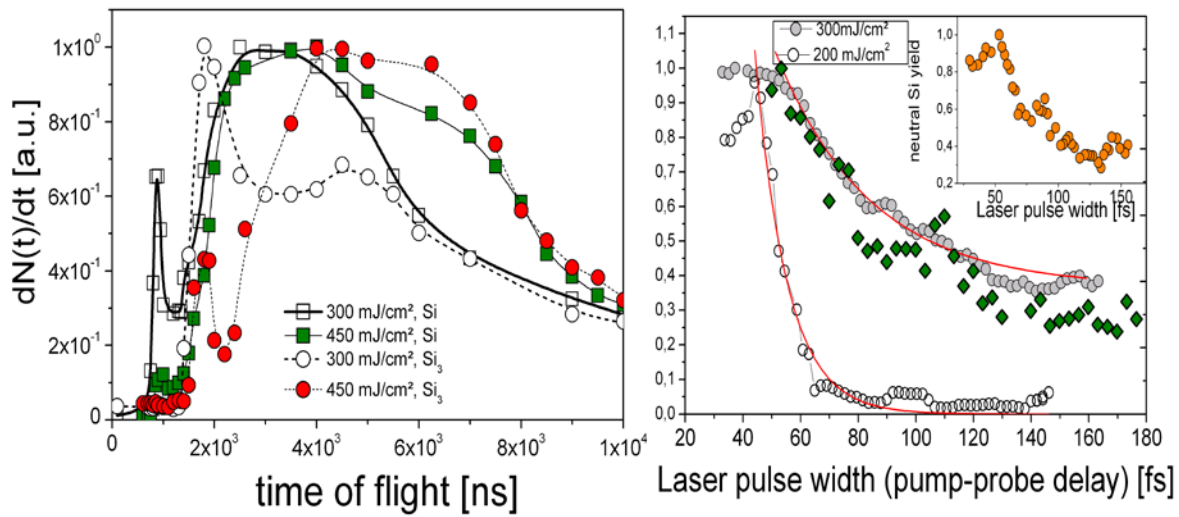


Figure 1.10: (a) TOF (velocity) spectra of ablated neutral Si and Si trimers for two different laser intensities. The spectra have been normalized for better visualization. For orientation: in the spectra at increased laser intensities the fast peak remains constant and the yield of thermal particles increases correspondingly (b) Pulse width dependence of the total Si ion and neutral (inset) yield. For comparison also the ion yield for a pump-probe experiment with two equal intensity subthreshold beams (squares) is shown (pump-probe delay shown on the horizontal axis) [14].

(around the ablation threshold) and is responsible for the emission of particles of high energies (several eV). Thermal processes taking place in ps time regime, play a leading role in ablation for higher fluences with the appearance of broad band energy distribution and responsible for the emission of low energy particles (fractions of eV).

As described in the previous section that when a high-power femtosecond laser pulse interacts with a metal, the optical absorption is usually dominated by free carrier absorption, i.e. electrons in the conduction band absorb photons and gain higher energy. The typical electron-lattice relaxation times are of the order of several ps, while the actual laser pulse has a length of less than hundred fs. Hence a material exposed to a sub picosecond laser pulses gets excited into a highly non-equilibrium state in which the electron temperature can be much higher than the lattice temperature [30]. The energy transport process in ultrafast laser heating of metals consists of two stages. The first stage is the absorption of the laser energy through photon-electron interactions within the ultrashort pulse duration. It takes a few femtoseconds for electrons to re-establish the Fermi distribution. This characteristic time scale, the mean time for electrons to restore their states, is called the electron relaxation time. In spite of nonequilibrium states of the electrons within this characteristic time, the temperature of the electrons is still numerically valid in the limit when the pulse duration is much longer than the electron relaxation time, which is proven by a model using the full



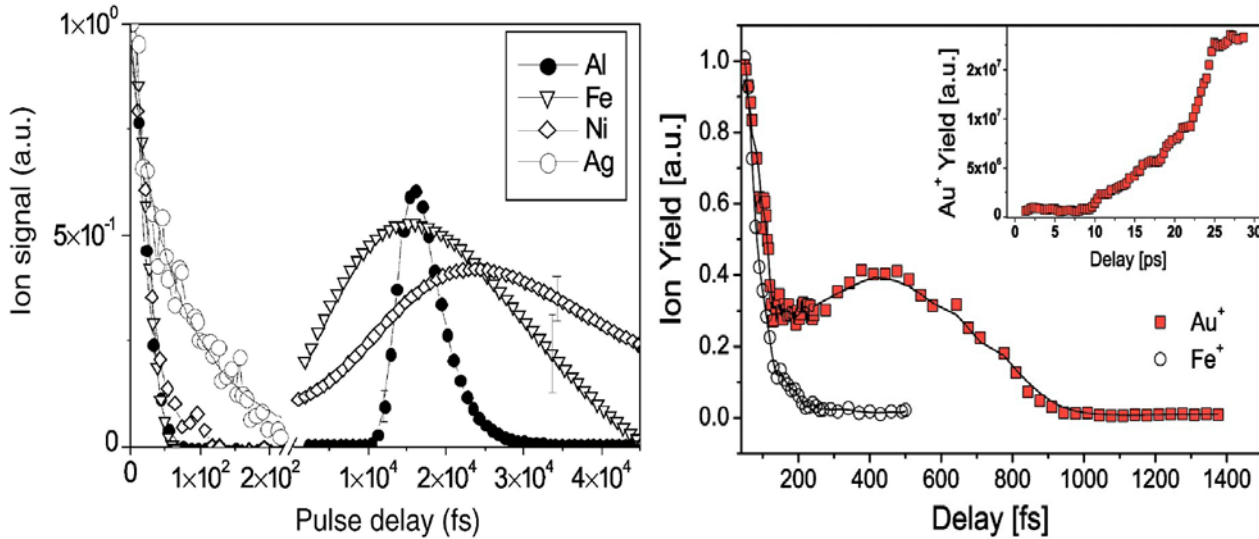


Figure 1.11: Normalized ion yield as a function of the pump–probe separation. (a) Shown are the best fits to the data for all investigated targets Al, Fe, Ni and Ag. Error bars indicate the reproducibility of the data. Note the change of the scale before and after the break. On the LHS of the break the envelope of the interferometric signal during pulse overlap is shown. Except for Ag the signal drops to zero when the pulses are separated in time. Only Ag shows a decay like behavior up to 200 fs. On the RHS of the break the ablation dynamics is shown in the picosecond range. Here the Ag signal is not depicted since it is under the detection limit. All other metals exhibit a further peak at a pulse separation of approximately 15–25 ps [44]. (b) Ion yield of Au<sup>+</sup> (Fe<sup>+</sup>) for pump-probe delays between 60 and 1.5 ps (pulse width = 25 fs). The inset shows the Au-signal time delays  $t > 2$  ps. Full lines are drawn to guide the eyes [13].

Boltzmann transport theory [30]. Within the duration of a single ultrashort pulse, the change of lattice temperature is generally negligible [44].

Figure 1.11 shows the results for pump-probe ablation measurements of different metals (Al, Fe, Ni and Ag) in (a) [44] and for Au and Fe in (b) [13]. According to these findings the observed decrease within the first 150 fs (for Fe, and Au) and 100 fs (for Al) is an indication of nonthermal processes in metals and can be attributed to Coulomb explosion.

Coulomb explosion of a metal exposed to an intense picosecond laser pulse is numerically simulated by Rukhadze et al [38] using a plasma layer as an example. For metals an analytic model is proposed by Bychenkov et al [39] that describes the generation of a monoenergetic beam of light ions during the Coulomb explosion of a stratified target irradiated by an ultrashort high-power laser pulse. It is proposed in this model that when the laser intensity is so high that all the target electrons escape into a vacuum, the ions are accelerated due to a Coulomb explosion. For a foil made of a high-Z material, the time scale on which the ions of the light coating are accelerated is too short for the ions to expand appreciably [39].

The few examples regarding ultrafast electronic (nonthermal) processes in metals on fs timescale are given below. Gamaly [25] proposed that the minimum energy that an electron needs to escape the solid (metals surface) equals the work function. In order to drag the ion

out of the target the electron must have an additional energy equal to or larger than the ion binding energy.

$$T_e = \varepsilon_{esc} + \varepsilon_b = \text{work function} + \text{binding energy} \quad 1.10$$

The free electrons in the skin layer can gain the energy exceeding the threshold energy required to leave a solid target during the pulse time. The energetic electrons escape the solid and create a strong electric field due to charge separation with the parent ions. The magnitude of this field depends directly on the electron kinetic energy and on the gradient of the electron density. The field pulls the ions out of the solid target if the electron energy is larger than the binding energy  $\varepsilon_b$  of ions in the lattice. According to Gamaly [25] the maximum electron temperature at the surface of a copper target under the fluence  $1 \text{ J.cm}^{-2}$  reaches a value of 7eV which is close to its Fermi energy. The calculated ion acceleration time, i.e., the time required for the ion to acquire the energy of  $\varepsilon_e = T_e - \varepsilon_{esc} - \varepsilon_b$  is 40 fs for Cu [25], where  $T_e$  is the electron temperature,  $\varepsilon_{esc}$  is the work function and  $\varepsilon_b$  is the binding energy.

Another example was reported by Lech et al [9], who demonstrated a strongly anisotropic ablation of suspended gold nanoparticles induced by 100 fs laser pulses, which stopped completely if the pulse duration was stretched to 1 ps, and this was attributed to some yet unidentified nonlinear optical effect.

Guo et al [45, 46] indicated a disordered lattice due to electronic heating and suggest that a nonthermal component exists in the heat-induced structural deformation and phase transition in Au and Al

CE in metals is still under discussion and debatable and needs more evidence for definite proof.

Another explanation (phenomenon) of surface optical rectification is considered to be responsible for removal of atoms from a metal surface within a time as short as few hundreds of femtosecond where thermal effects are probably not dominant. This issue is discussed in the following section

### ***(b) Femtosecond Field Ion Emission by Surface Optical Rectification***

Femtosecond field ion emission by surface optical rectification represents a relatively new idea proposed by Vella et al [18] to explain ultrafast nonthermal (electronic) processes taking place in metals by ultrashort laser irradiation.

THz "optical rectification" occurs by nearly-degenerate difference frequency mixing between the frequency components of an ultra-short pulse in a 2nd order nonlinear optical medium. This process is capable of producing very broadband THz pulses (generation of a (quasi) DC

polarization) at the passage of an intense optical beam. When the applied electric field is delivered by a femtosecond laser, the spectral bandwidth associated with such short pulses is very large. The mixing of different frequency components produces a beating polarization, which results in the emission of electromagnetic waves in the terahertz regime. In a nonlinear optical material, the polarization induced by an electric field will not reverse its sign at the same time as the driving field, leading to a nonlinear polarization and thus frequency mixing. This is the optical analog of the audible beat frequency generated by two struck tuning forks. The emitted field is related to the polarization,  $P$ , by [18]

$$E_{THz} \propto \partial^2 P / \partial t^2 \quad 1.11$$

The efficiency of THz generation depends on the second order nonlinear susceptibility of the medium. This is the analogue of the electric rectification effect, where an AC signal is converted ("rectified") to DC and is based on the inverse process of the electro-optic effect. Optical rectification (OR) is a classical second-order nonlinear optical process taking place in non-centrosymmetric materials [18]. However, a direct detection of surface OR is very difficult and an undisputable evidence of its occurrence is still lacking, although some possible confirmations have been reported [18]. The surface gradients of electronic density

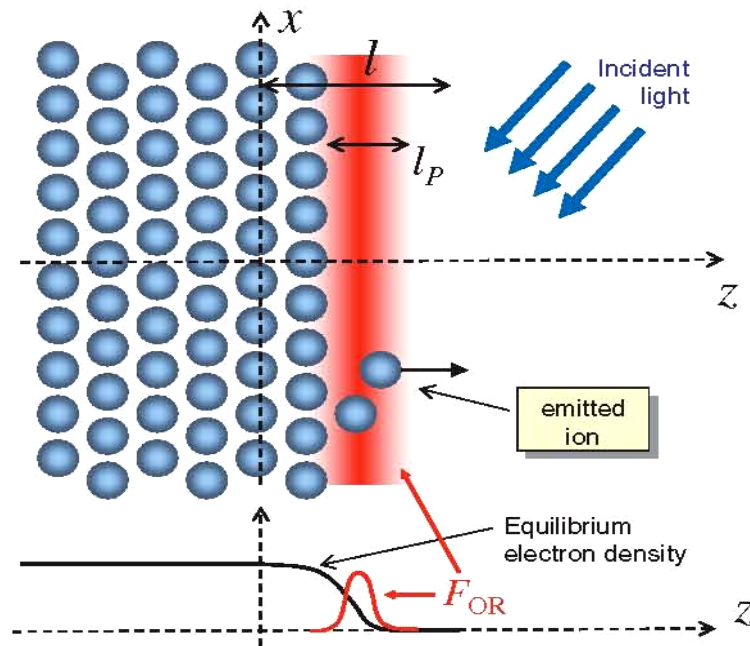


Figure 1.12: Pictorial representation of the surface optical rectification process and ensuing laser-assisted field-ion emission (LAFIE). The red shaded area is the region where the rectified field is induced (the red curve shows its qualitative profile, as obtained by density-functional calculations [18]).

and of all other material properties are then assumed to be comprised between  $z = 0$  and  $z = l$  where  $l$  is the total thickness of the interfacial region, or “selvedge.” For an input optical wave of frequency  $\omega$  and wavelength  $\lambda$ , the resulting surface OR may be characterized by a second order nonlinear (electrostatic) polarization. The density-functional calculations reported in [47] also show that this OR field (as well as the second-order polarization) is located in a interfacial layer (of thickness  $l_p$ ) which is centered at about  $2\text{\AA}$  (i.e., one atomic-plane spacing) outside the outermost surface plane of ions (see Fig. 1.12). This implies that the OR field will be most effective on the isolated atoms adsorbed on the surface and on the atoms belonging to step edges at the surface terraces, which are also the most weakly bonded ones and therefore the easiest to be emitted. Then, at small enough light intensities, atoms should be emitted preferentially from the edge of terraces.

Vella [18] proposed an explanation of ultrafast LAFIE as a result of the quasi dc (THz) electric field generated by the electronic nonlinear optical response of the metal surface: the so-called optical rectification (OR) effect for explaining the results of pump-probe experiments which indicates that the ion emission is actually taking place on a femtosecond time scale. In another example of pump-probe experiments it is argued that the ion emission from metals is actually taking place on a femtosecond time scale [48]. According to Vella, the ablation thresholds (a nonthermal ablation regime) reported in [13, 14] for particle emission on the femtosecond time scale can also be explained by OR model.

### ***(c) Ultrafast melting (UFM)***

In semiconductors an additional non-thermal pathway of phase transformation has been described, which allows melting within a few femtosecond [49]. This so called non-thermal melting is ascribed to the massive excitation of charge carriers into the conduction band, converting the interatomic forces into antibonding states. It has indeed been observed that after rapid femtosecond excitation of silicon or germanium the lattice order disappears within about a hundred femtoseconds [50], which has been interpreted as an initial ballistic atom disordering due to the lack of remaining binding forces or anharmonicity. This so-called ultrafast melting is considered as one important aspect in the ablation mechanisms of semiconductors as well [51].

For UFM the photoexcited high density electron-hole plasma causes destabilization of the lattice, and the material melts in a time less than 1 ps [12]. This electronically induced solid-to-liquid transition in semiconductors, or nonthermal melting process is triggered by interband excitation of a dense electron-hole plasma ( $10^{22} \text{ cm}^{-3}$ ) leading to ultrafast disordering of the

semiconductor crystal and the formation of a hot liquid at high pressure. A complex chain of phenomena follows on a picosecond time scale, including strong density perturbations propagating away from the molten layer, and the ablation of macroscopic amounts of material at higher laser fluences. Nonthermal melting is observed to take place within 300–500 fs in case of Ge [50] and around 200 fs in case of Si [12]. From the ultrashort transition time a non-thermal physical mechanism is playing dominant role in ablation, because such a short melting time cannot be explained by classical thermal melting. For a high concentration of carriers the crystal lattice becomes unstable. Under these conditions structural transformations on a time scale of less than one picosecond are possible.

As in semiconductors photoionization and electron–electron impact ionization can produce a free electron gas of comparably high density, therefore a solid material exposed to laser intensity of about  $10^{14} \text{W/cm}^2$  or higher is fully ionized and a hot plasma of approximately solid density is produced. In this case the electrons acquire energy much larger than the cohesive energy, and one can speak of a direct transition from the solid state to the plasma state. For femtosecond laser excitation around  $10^{12} \text{W/cm}^2$  a rapid transition to the liquid state is known to occur in covalent semiconductors. The absorption coefficient of Si under femtosecond laser irradiation increases significantly due to a generation of carriers by photo-excitation. The photo-excited high density electron hole plasma occurs only at fluences above  $1 \text{ J/cm}^2$  ( $F > 5F_{\text{abl}}$ ) [52] leads to a lattice instability resulting in a disordering of the lattice on a timescale of approximately 100 fs. Since the disordering occurs faster than lattice heating, this process is often called non-thermal melting. Ultrafast melting within less than one picosecond was demonstrated by many authors [12, 14, 50]. Thus, the threshold for ablation is much smaller than that of nanosecond lasers making femtosecond laser a suitable source for material processing and surface photochemistry.

The simulation results of Jeschke et al [53] with a laser pulse of Gaussian shape,  $\tau=20$  fs,  $E_0=4$  eV per atom,  $N=64$  atoms for Si show that bond breaking fluctuations are functions of time. Moderate expansion takes place during 100 fs. After 200 fs strong bond breaking with enhanced expansion takes place. After 500 fs the lattice structure suffers an irreversible damage and ablation starts to take place.

UFM is not only observed in semiconductors [12, 14, 50, 54] but also in metals (Au)[13]. A large lifetime of nonthermal electrons in Au can offer a particular interesting situation, where ultrafast processes should be observed. The velocity (energy, TOF) distribution of the ejected particles represents one of the most informative quantities accessible for experiments with regard to obtain a clue for the nature of the involved physical processes. Figure 1.13 (a) shows

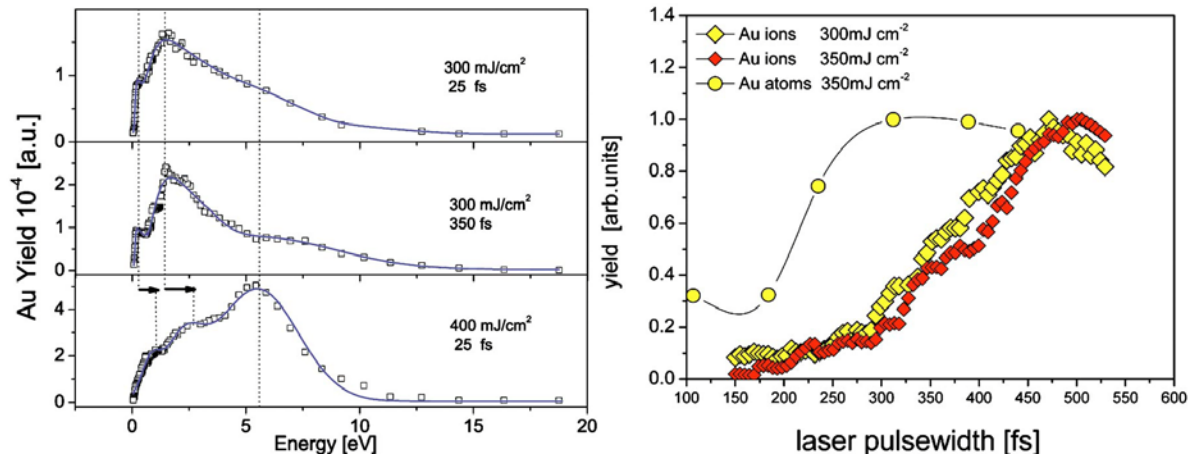


Figure 1.13: (a) Yield of neutral Au atoms (measured as TOF distribution) as a function of particle energy for different fluences and pulse widths. Full lines are drawn to guide the eyes (b) Ablation yield of Au ions and neutrals as a function of the laser pulse length (for two different laser fluences) [13].

signal of ablated neutral Au atoms as a function of particle energy for two characteristic laser pulse lengths of the ablation laser (25 and 350 fs) and for two different laser fluences (0.3 and 0.4 J.cm<sup>-2</sup>). The dependence of the neutral and ionic Au yields as a function of the pulse length at 300 mJ/cm<sup>2</sup> is shown in Figure 1.13 (b). These figures present evidences for existence of ultrafast melting (nonthermal process) in metals (Au), which appears to develop on few hundred femtosecond time scale at relatively low fluences, slightly higher than the ablation threshold. UFM is responsible for the emission of particles of few eV.

### 1.2.2.2 Thermal processes

At a fluence considerably higher than the damage threshold, an irradiated target surface reaches the melting and evaporation point giving rise to thermal ablation and a large amount of low velocity ions and neutrals exit forming a crater on the surface, a phenomenon, usually, called strong ablation. Strong ablation proceeds through the hydrodynamic expansion of the evaporated material and characterized by ablated volumes, which is several orders of magnitude larger than the ablated volumes produced by gentle ablation. Thus, thermal evaporation is considered to be the dominant ablation mechanism above this threshold [55]. These processes have been extensively discussed.

Thermal ablation processes are characterized by a transfer of the deposited energy to the phonon bath through electron-phonon interactions, typically on the order of tens of picoseconds and a description of the equation of state by means of defined temperature and pressure. Although the electron-phonon collision time may be comparable to the electron-

electron collision time, it takes much longer to transfer energy from free electrons to phonons, because the phonon mass is much larger than the electron mass. The characteristic time for the free electrons and the lattice to reach thermal equilibrium is called the thermalization time. The generally accepted picture for damage of defect-free dielectrics involves the heating of conduction-band electrons by the incident radiation and transfer of this energy to the lattice in the time domain of few tens of picoseconds.

Damage occurs through conventional heat deposition (heating of the lattice), resulting in melting, boiling, or fracture of the dielectric material. Thermal processes predicts a  $\tau^{1/2}$  dependence of the threshold fluence on pulse duration [56].

In this process, the phonon temperature is used to characterize the Bose- Einstein distribution. The concept of two-temperature model (TTM) for dealing with the heated electron gas, interacting with the lattice was proposed more than 30 years ago [26]. This model describes the energy transfer inside a metal with two coupled generalized heat conduction equations for the temperatures of the electrons and the lattice. Noble metals (Au, Cu etc) have a relatively weak strength of the electron–phonon coupling those results in quite high values of the electronic temperatures upon a laser light absorption. Transitional metals (Al, Ni etc) , on the other hand, exhibit much stronger electron–phonon coupling and much lower electronic temperatures are reached during the laser–matter interaction process [57].

Generally, the electron-lattice relaxation time in metals amounts to 1-10 ps. Therefore, the mechanism of femtosecond laser ablation is different from laser ablation with longer pulses. Thermal ablation occurs when the laser pulsewidth is exceeds the electron-lattice relaxation time or it can represent the dominant mechanism with femtosecond laser pulses in the higher fluence regime. The importance of the pulsewidth compared to the electron-lattice scattering time and the thermal diffusion time corresponding to the skin depth was pointed out by Stuart et al.[56, 58].

In the thermal regime different mechanisms have been proposed to explain the ablation. Three kinds of thermal processes may lead to material loss from a laser-irradiated surface: 1) vaporization, 2) boiling, and 3) explosive boiling (phase explosion). By excluding “subsurface heating”, the relevance of the three processes depends on the laser pulse duration as well as on the temperature attained in the irradiated zone. At laser fluences above the threshold, a collective multilayer ejection occurs in which large liquid droplets are ejected and the total yield of the ablated material follows a critical volume density of the deposited energy. These thermal processes play an important role for the removal of the materials from irradiated surface.

### **(a) Vaporization**

By *normal vaporization* we refer to the transition from a condensed phase (solid or liquid) to vapor by virtue of the emission of particles (atoms or molecules) from the extreme outer surface under conditions of electron–phonon coupling. Obviously “vaporization”, as we use the term, includes “sublimation” and “evaporation”.

### **(b) Boiling**

This process involves heterogeneous nucleation and occurs at a temperature only minimally higher than the boiling temperature. These are vapor bubbles, which in the case of liquids initiate heterogeneously from a variety of disturbances such as gas or solid impurities, or defects, or an underlying or enclosing solid surface. Once bubbles are formed, they tend to diffuse and if, given enough time, escape from the outer surface of the liquid. Bubbles may be formed in either solids (as in nuclear fuel together with the disproportion) or liquids, but due to the problem of mobility only liquids need to be considered for short time scale processes.

### **(c) Phase explosion**

There is the possibility of phase explosion under femtosecond laser ablation in vacuum or low-pressure background after electron–lattice temperature equilibrium is reached (10–100 ps, depending on the target material). If a target surface layer is heated below the critical temperature but above the melting one ( $T_m$ ), the matter inevitably enters the region of a metastable state. It may stay there until (i) the pressure above the surface reaches the saturation value due to target vaporization hypothetical time is 1–10 ns (ii) cooling and then solidification takes place due to thermal conductivity, or (iii) the matter returns to the binodal due to phase explosion (explosive boiling) [59].

If superheating occurs and the temperature lies sufficiently near  $T_{tc}$ , phase explosion (*explosive boiling*) occurs by homogeneous nucleation. As a result the hot region near the surface breaks down in a very short times into vapor plus equilibrium liquid droplets [60].

A phase diagram of Cs in the neighborhood of  $T_{tc}$  is shown in figure 1.14 [60]. The curve marked “equilibrium vaporization” that corresponds to liquid Cs in equilibrium with saturated Cs vapor, at vapor pressure.



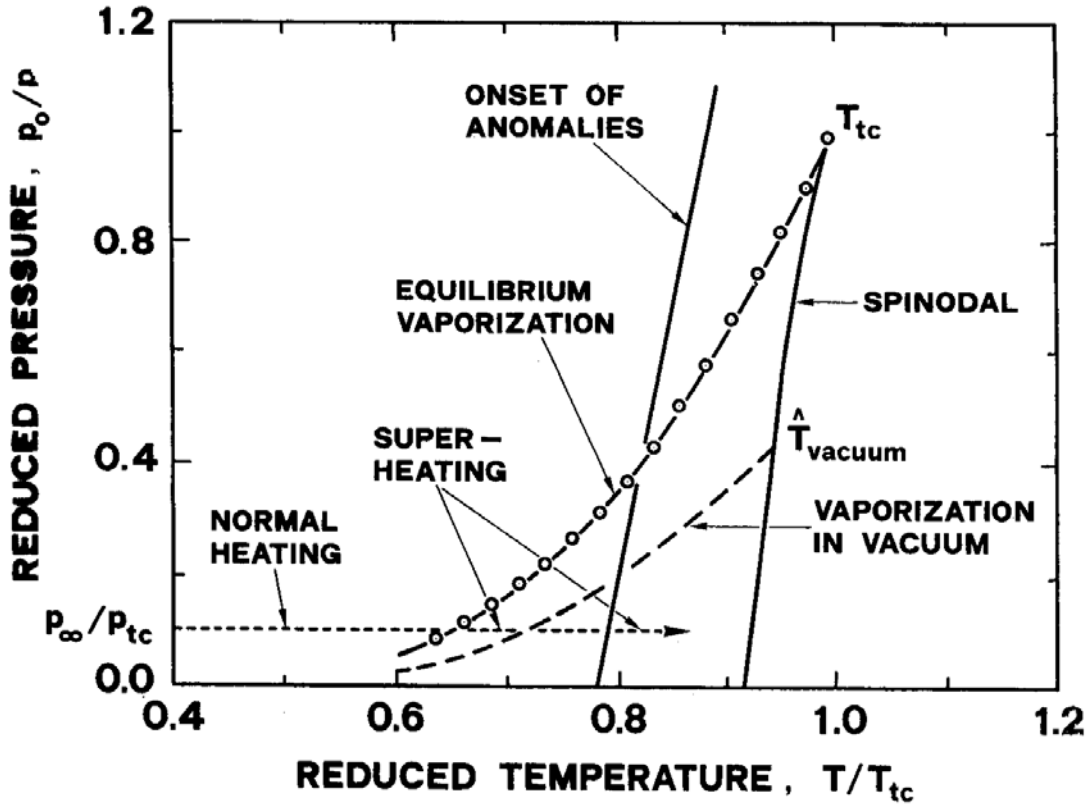


Figure 1.14 : A  $p$ - $T$  phase diagram of a metal in the neighborhood of  $T_c$  [60].

### 1.2.2.3 Photomechanical Damage

Thermomechanical and photomechanical effects can also play a role in laser ablation. Perez and Lewis [15] pointed out that ablation can also be induced by a mechanical effect, rather than a thermal phase transition. In that case the rapidly released thermoelastic stress can surpass the physical strength of the material during stress confinement, which leads to rupture and material ejection.

Multiphoton generation [61] of free carriers and relaxation of conduction band electrons (CBE) in insulators play a major role leading to damage in the material. With ultrashort laser pulses ( $\tau \leq 30$  fs) the probability for the formation of defects (electron-hole pairs) due to multiphoton absorption is very high [62] and this multiphoton ionization (MPI) alone can provide critical density of electrons (approx.  $10^{21} \text{ cm}^{-3}$  [61]). MPI dominates the production of ions (and hence conduction band “free” electrons) during the first stages of a fs laser pulse [63]. After several femtoseconds, the avalanche process dominates, which leads to drastic change in the optical properties of the material and is instrumental in the final surface modification [64].  $\text{CaF}_2$  is a material with very strong electron-phonon coupling which

implies a high rate for self-trapping of excitons and/or holes after laser excitation [65]. The electronic excitation and relaxation [66] in  $\text{CaF}_2$  crystal have been studied by means of femtosecond time-resolved spectroscopy [66]. It was found that if the CBE relaxes rapidly (decay time is about 700 fs) [66], it will be trapped by a hole and form a self-trapped exciton (STE), on a time range of about 1 ps. The lifetime of these STE is a few  $\mu\text{s}$  [65]. It means for very short pulses (fs), the self-trapped excitons will be formed after the pulse. There is no remaining laser pulse to produce rapid heating of the crystal via single photon absorption from the defect states. After the laser pulse all the energy stored in the STEs will contribute to bond weakening interactions via electron-lattice coupling [67] and strongly deform the lattice. If they have been produced with sufficient density without being thermally removed, the lattice deformation will cause immense stresses.

The maximum temperature on the surface is defined by the pulse duration equal to the electron–phonon relaxation time, the rate of the lattice temperature growth is nevertheless higher for pulses shorter than  $t_{\text{e-ph}}$ . This implies that if there is enough space for the temperature gradient to be established [1, 20, 21], the shorter pulses will induce higher stresses upon the laser heating, until the conditions called the inertial stress confinement [22] are realized, when  $\tau_{\text{heating}} < L/C_s$  (where  $L$  is geometrical size of the system and  $C_s$  is the speed of sound). Physically, it means that the rate of temperature gradient growth exceeds the rate of thermal expansion of the solid in response to that heating. The relaxation of overheated solid, apparently, is attributed with a propagation of a strong pressure wave that in turn may cause the mechanical damage. Therefore, the shorter the pulse, the stronger will be laser-induced stresses, with the more photomechanical damage. Contrary, the pulses longer than  $t_{\text{e-ph}}$  result in establishing of temperature gradients in a longer time and any damage therefore can be rather addressed with photo-thermal effects, like melting or boiling processes.

### **1.2.3 Investigation and identification of femtosecond laser energy deposition mechanisms (ultrafast electronic and thermal processes)**

The aim of the work is to probe and identify ultrafast electronic and thermal processes during femtosecond laser ablation by means of surface topography investigations. This is possible only by a combination of complementary in-situ and ex-situ diagnostic methods which can allow reliable measurements for all relevant physical parameters involved in the ablation process (fluence, pulse width etc) and corresponding phenomena taking place after laser interaction with material. For this purpose, targets are irradiated under UHV conditions. AFM analysis of irradiated targets provides information about the changes in surface topography

due to localized energy deposition addressing the influence of different laser fluences. These AFM surface topographical investigations can then be compared with in-situ measurements of particle emission using time of flight mass spectrometry providing detailed information about energy- (TOF-) distributions and composition of emitted particles and energy deposition time. A good correlation of these two diagnostic techniques can be useful to explore and distinguish different ultrafast electronic and slow thermal processes.

#### ***1.2.3.1 Laser ablation mechanism probed by particle emission using time of flight mass spectrometry***

Time of flight mass spectrometry is an important technique for probing the laser ablation mechanism. It yields information for identifying fast electronic and thermal processes. The way (magnitude, timescale etc.) in which the energy is deposited to the electronic system, determines to a large extent, how efficiently these different processes contribute. Therefore, a promising approach to identify these processes is to vary the time behavior of the energy deposition (pulse length, pump-probe experiments) to study the corresponding changes in particle emission characteristics [12, 13, 44, 68]. It is essential to be able to vary the time (and as a result the amount) of the energy deposited in the electronic system. For ultra short pulses, in principle, two alternatives are feasible: a) changing the pulse length with a pulse-shaping device or b) using a two-pulse autocorrelation setup in which the differential yield of emitted particles is measured as a function of the temporal separation between a pair of ablation pulses with a reflectron-type time-of-flight (TOP) spectrometer. The intensity of each pulse has to be kept below the ablation threshold [68]. Since most of the particles are neutrals, post-ionization of the particles by a laser is a basic requirement. In addition, the energy of the particles has to be measured.

#### ***1.2.3.2 Laser ablation mechanism probed by surface topography using atomic force microscopy.***

With ultrashort pulse-irradiation, different surface irregularities (protrusions and pits) are expected to emerge progressively with different geometrical sizes depending upon the laser fluence.

To control the development of surface topography, surfaces of targets should initially be irradiated with single shots using laser fluence around the ablation threshold (starting from lowest possible fluence) where particle emission starts (to minimize changes induced in surface topography by thermal ablation). In this way the involved physical phenomena can be better and more accurately studied. In order to investigate surface topographical changes

induced by thermal processes, targets were irradiated with higher fluences or with multiple shot-irradiations. If the laser energy deposited (eV/atom) exceeds the melting threshold localized and isolated defects are expected at a low fluence (around ablation threshold) for a single pulse irradiation. On the other hand, larger bumps, nanopores and nanoripple-like structures are expected due to ultrafast melting and surface plasmons at a moderate fluence and multiple-shot-irradiation. Classical (micro) laser-induced periodic surface structures (LIPSS), larger humps, islands (thermal ablation) and craters are expected at higher fluences (significantly above the threshold) with multiple-shot-irradiation due to thermal ablation. The different sizes of structures can be explained on the basis of marked differences in energy deposition and material ejection mechanism.

The relevance of studying the surface topography as a clue for electronic processes is not restricted to laser–matter interaction, but is of much more general interest. In fact, it has been recently shown, that the formation of nano-sized hillocks [15], characterized by a sharp and well-defined threshold for the potential energy, represents a strong indication for the existence of electronic processes during ion bombardment of solids. Formation of a typical nano-sized (few nm diameter and height) localized hillock at the ion impact site and with a sharp and well defined threshold of potential energy carried into the collision of about 14 keV for hillock formation on CaF<sub>2</sub> surfaces [15] results in structures which we are expecting for ultra-short-laser irradiation and are the major issue of this dissertation. It is, therefore, evident that one can speculate that these hillocks can be linked to similar fast electronic (potential energy) processes. Even if the details of the processes might be different, the creation of hot, fast electrons seems to result in a situation very similar to the one encountered for highly charged ion interaction with surfaces.

These very specific topographic features can, therefore, be interpreted as characteristic for a large localized potential energy transfer to the electronic system. It should be stated that both the emission characteristic as well as topographic features represent very valuable information with respect to the physics of the ablation process. In our opinion it is even more helpful with regard to understand the processes, if a correlation between both can be established, in particular if we can associate specific topographic features with particular particle energies etc.

It seems quite evident that e.g. the energy of an emitted particle reflects the process, which led to their emission. We can expect quite different energies for particles ejected by Coulomb Explosion, ultrafast melting or thermally evaporated atoms. Whether the surface topography after irradiation gives us a clue as to which processes took place during laser-matter

interaction is not so obvious. For sure, we can expect a substantially modified surface after heating the surface and ablation of substantial amount of material. An originally flat surface will exhibit a lot of surface topographical features after laser irradiation and results into melting, evaporation etc. In a typical "violent" thermal process, craters, large bumps, explosions etc. will be left and might give us a hint on the relevant processes. However, it is not so obvious, whether we can obtain more detailed information on specific processes like Coulomb explosion, hot electron plasmas etc. Do they leave a specific footprint which will help us to identify such processes? In general, the difficulty (not surprisingly this is also the case for studying the particle emission characteristics) is mainly due to the fact that there is only a relatively small range of laser intensities (close to the ablation threshold), for which different possible processes contribute with a comparable strength to leave distinguishable tracks. At higher laser intensities thermal footprints left behind are usually overwhelming (e.g. craters, micro periodic surface structures, islands or mountains on the surface, thermal energies of particles, typical picoseconds timescales for the energy deposition).

Some good examples in which different surface topographical feature are associated with different processes responsible for laser energy deposition are described below.

To explore the role of Coulomb explosion for nanostructuring of material surfaces is the subject of considerable interest. Some good examples in which surface modification of different materials by femtosecond laser irradiation is explained on the basis of CE are: the hillock-shaped damage, formed on a glass surface by femtosecond pulses of 180 fs with energy of 5 nJ/pulse at 800 nm wavelength is reported by Vanagas et al [69]. The lateral cross section of the hillocks observed was 115–155 nm with a height of 40-70 nm. According to the authors the formation of hillocks without obvious melting and crater pitting proves that material starts to leave the surface before melting or vaporizing and is attributed to a Coulomb explosion of the exposed material. In another example ultrafast melting of graphite is observed by Raman spectroscopy, atomic force microscopy as well as time of flight mass spectrometry. A displacive motion between the topmost surface layers is attributed to Coulomb explosion [70]. The formation of microbump and nanojet formation on nanosize gold films under femtosecond laser irradiation is explained in the framework of the elastoplastic model [71]. The relaxation of the compressive stresses generated by the fast laser heating is identified as the main driving force responsible for the separation of the metal film from the substrate and formation of the nanobumps in femtosecond pulse laser nanostructuring of thin metal films [16]. Bump-formation in  $\text{CaF}_2$  is explained on the basis of surface instability supported by self organized phenomena and Coulomb explosion [72].

# Chapter 2

## Experimental Setup and Techniques

---

The main aim of the project was to identify ultrafast electronic and thermal processes during femtosecond laser ablation by means of surface topography investigations. For this purpose, the surface and structural characterization of the various materials after irradiation by an ultrashort laser around the ablation threshold and for higher fluences has been performed.

The first section of this chapter briefly describes the introduction of the laser system with its specifications. The second section deals with specific experimental setups used for exposing targets in air and UHV condition exactly under the same conditions where times of flight measurements have been performed. Various diagnostic techniques like AFM, SEM, and Raman Spectroscopy have been employed to investigate the surface topography and structural changes of laser ablated materials. The third section deals with the description of these diagnostic techniques. For measurements of nonlinear optical properties of transparent samples, Z-scan technique is employed which is briefly discussed in the last section of this chapter.

## 2.1 Femtosecond laser system

The ultrashort laser system used in experiments is a Ti: sapphire femtosecond multipass amplifier system (FEMTOPOWER<sup>™</sup> COMPACT<sup>™</sup> PRO Femtolasers Productions GmbH Austria). This system delivers ultra short laser pulses with a maximum average power of approximately 1 mJ at a repetition rate of 1000 Hz. The pulse duration, estimated as the FWHM of a Gaussian temporal profile, is typically 25 fs and the spectrum is centered at 800 nm. The system consists of three parts (1) Oscillator (2) Amplifier and (3) Compressor. The basic layout of these three parts is presented in figures 2.1, 2.2 and 2.3.

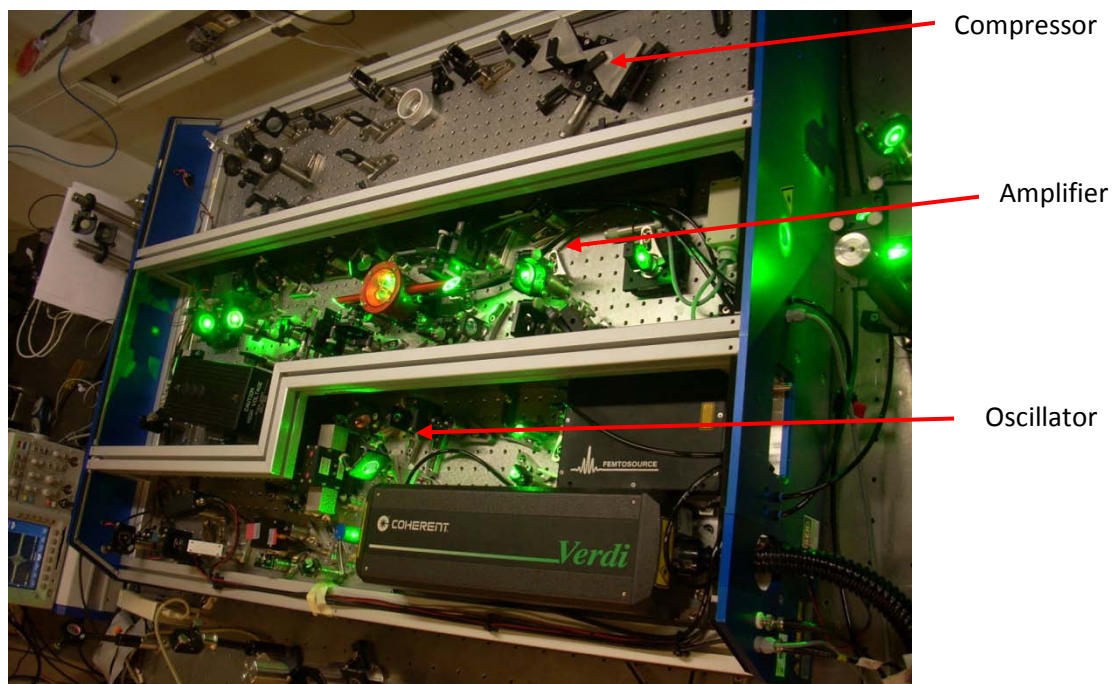


Figure 2.1: The Ti: Sapphire laser system with an oscillator, an amplifier and a compressor.

### 2.1.1 Oscillator

The seed beam is produced by a mirror dispersion- controlled Ti:sapphire oscillator (FemtoSource Pro; FemtoLasers GmbH). It is pumped by a diode-pumped (809 nm) frequency- doubled Nd:YVO<sub>4</sub> laser 522nm (Coherent, Inc. Santa Clara, CA ) and delivers sub-20 fs pulses of few hundred nJ energy at a repetition rate of 75MHz with an output power of more than 800 mW and a spectral width greater than 100nm. It is a Kerr-lens mode





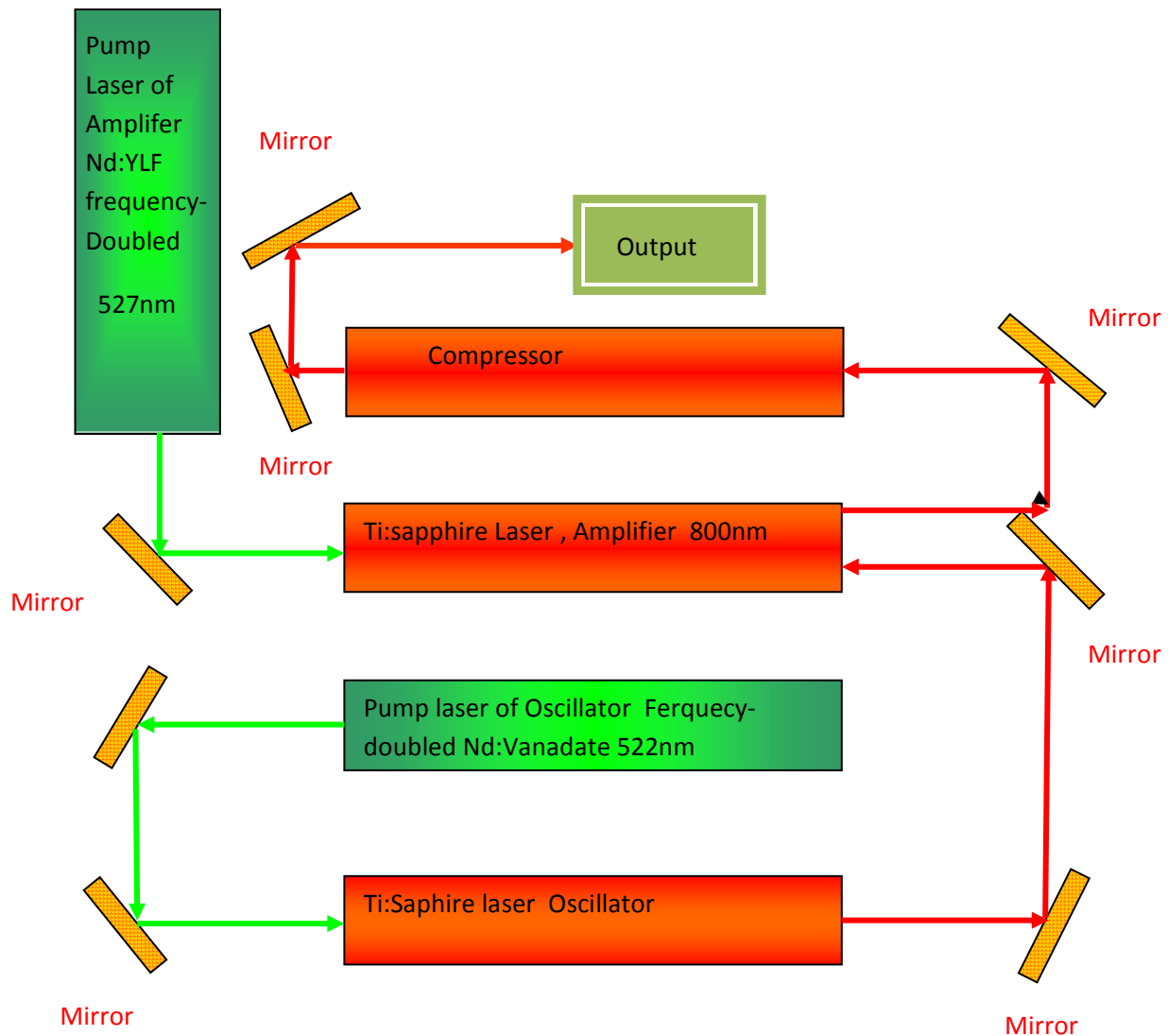


Figure 2.3: A basic layout of femtosecond laser system

Pulse stretching before amplification is accomplished by a comparatively small amount of dispersion introduced by a 10-cm-long block of heavy flintglass (SF57) and other system components (e.g. Faraday isolators, Pockels cell, and polarizers) to a duration of ps.

The pulse propagates nine times along slightly different paths through the gain region of amplifier medium. After first four passes through the crystal, a single pulse is selected out of the pulse train with a Pockel cell. The selected single pulse is re-injected and amplified in another five passes.

#### ***(a) Specifications of Amplifier***

The amplifier has a pulse duration  $< 20$  fs, spectral width  $> 40$  nm FWHM, output power (average)  $> 800$  mW, output energy  $> 800$   $\mu$ J, repetition rate of 1 kHz and pump beam diameter  $\approx 10$  mm

### ***(b) Pump Laser Specifications***

The pump laser is frequency doubled Nd: YLF BMI621 D/2 laser or equivalent emitting at 527 nm. Pulses with energies  $> 12\text{ mJ}$  and a duration between 100 ns and 500 ns are required. The beam must be horizontally polarized. Both lamp-pumped, intra-cavity doubled, Q-switched Nd: YLF lasers (Model GM-20-527) and Diode pumped Nd: YLF Lasers (Model DM Series) (Photonic Industries International, Inc. Bohemia NY, USA)) were used as a pumping source.

#### ***Diode pumped Nd: YLF DM Series Specifications***

Nd: YLF (Model DM 10-527) with a wavelength of 527 nm, a rep rate of 1 KHz, an average power of 10 W, a pulse energy of 10 mJ, and a pulse width of 220 ns is used.

#### ***Lamp-pumped Nd: YLF Specifications***

Lamp-pumped Nd: YLF (Model GM-20-527) with a wavelength of 527 nm, a rep rate of 1 KHz, an average power of 20W, a pulse energy of 20 mJ, a pulse width 200 ns and pumped by an arc lamp is used.

### **2.1.3 Compressor**

A pulse compression technique is used to obtain the ultrashort amplified pulses. Two chirped mirrors and a prism pair were used for dispersion compensation. Each time the laser pulse travels through the optical components inside the laser cavity, it becomes stretched. A prism compressor inside the cavity is designed such that it exactly compensates this inter-cavity dispersion.

Alignment for ultrashort pulses is obtained by moving prism in and out. The duration of the pulse was about 25 fs (FWHM) and spectral width was approximately 40 nm (FWHM) as measured by ocean optics spectrometer. If prism is moved from its optimum position it will introduce dispersion. By moving the prism more in, we introduce more positive dispersion and by moving the prism out, negative, dispersion was introduced.

### **2.1.4 Laser pulse characterization**

The pulses were characterized with respect to their temporal, spectral and spatial parameters. The spectral width and wavelength was measured with a spectrometer S2000 (Ocean Optics). The energy of the laser beam was controlled by neutral density filters or a half wave plate polarizer and was measured with a calibrated Piezoelectric detector (Power Energy meter

Coherent 210). The pulse width could be controlled by a combination of Acoustic Optic Programmable Dispersion filter and prism pairs and their temporal evolution was measured with an autocorrelator. The beam quality has been monitored by a beam profiler and CCD camera.

### ***Laser Beam Profilometer***

In many laser-matter interaction applications, precise measurements of laser beam profiles are essential for estimating laser performance. In general, the analysis of laser beam is based on pulse energy, the intensity distribution, divergence and beam waist for fluence measurement. A typical Gaussian beam with a circular symmetry and intensity smoothness is very important for measurements. Figure 2.4 is a pseudo colored intensity profile of a typical Gaussian beam taken by a laser beam profilometer Laser Cam –HR (Coherent). The colors represent the variation in the intensity from the central maxima (red) to the edges of the profile with minimum intensity (blue).

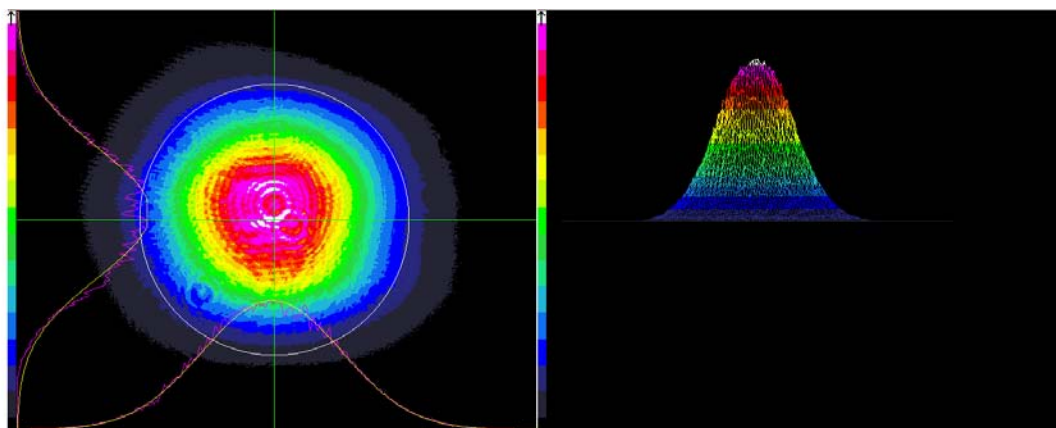


Figure 2.4: A typical Gaussian beam profile.

## **2.2 Specific Experimental Details**

Experiments have been performed on a single crystal freshly cleaved  $\text{CaF}_2$  (111), Si (111), polycrystalline Al (99.99%) and a polymer CR-39. The dimensions of targets used were;  $\text{CaF}_2$  (15mm×15mm×1mm), Si (20mm×20mm×1mm), Al (15mm×15mm×2mm), and CR-39 target (20 mm × 20 mm × 1 mm). The metallic samples were polished with a mechanical polisher using SiC papers of grades 120, 220, 500, 1000, 1200, 2400 and 4800, respectively. Mirror like surfaces were achieved after final polishing with diamond powder. The samples were cleaned in ultrasonic bath before irradiation.

### 2.2.1 Targets Exposure in air

An experimental set-up used to expose targets in air is shown in figure 2.5. Figure 2.6 is a schematic of the set up. Targets were mounted on a motorized translational stage. The purpose of the stage was to attain a precise position of the target for each exposure maintaining a constant separation distance between consecutive exposures. This translation stage consists of two perpendicularly mounted piezo motors (AG-LS25 Linear Stage (Newport)). A precise positioning of the target in XY-plane was made possible by controlling the movement of the motor with the help of a Lab VIEW program. This programmable motorized translational stage enabled us to move the target on each axis with a total distance of 12 mm with a minimum achievable step size of 50 nm.

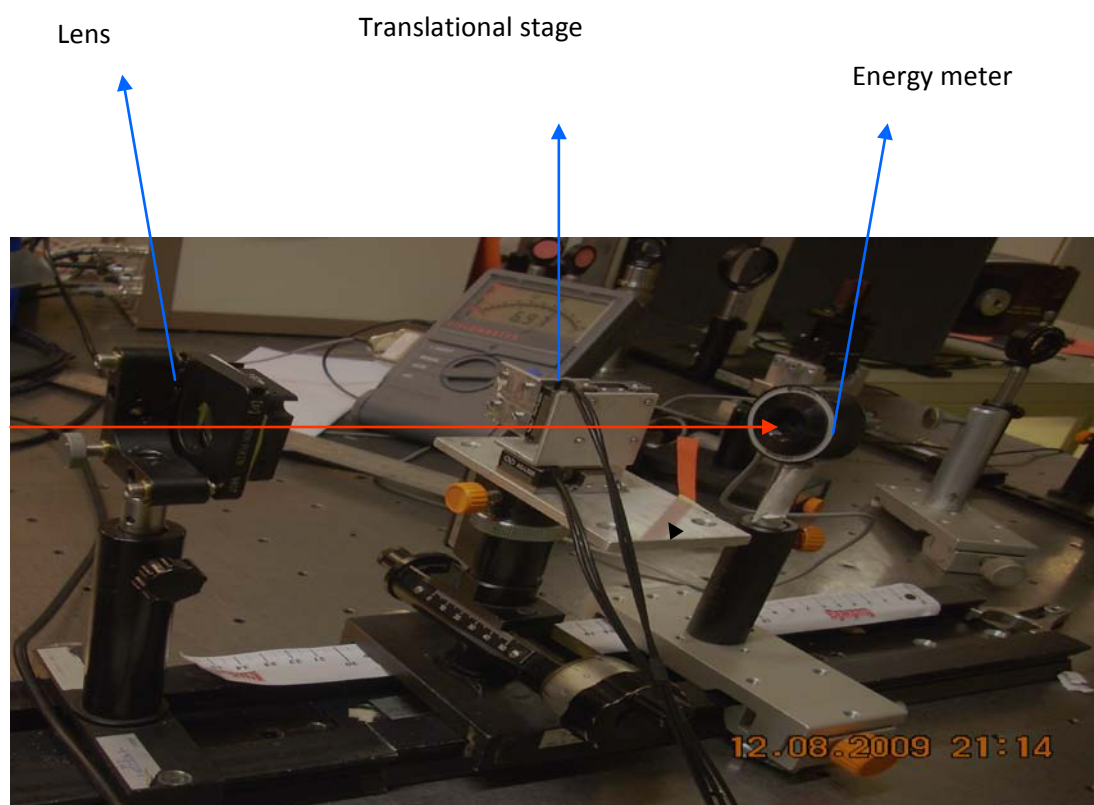


Figure 2.5: A computer controlled translational stage for the target exposure in air.

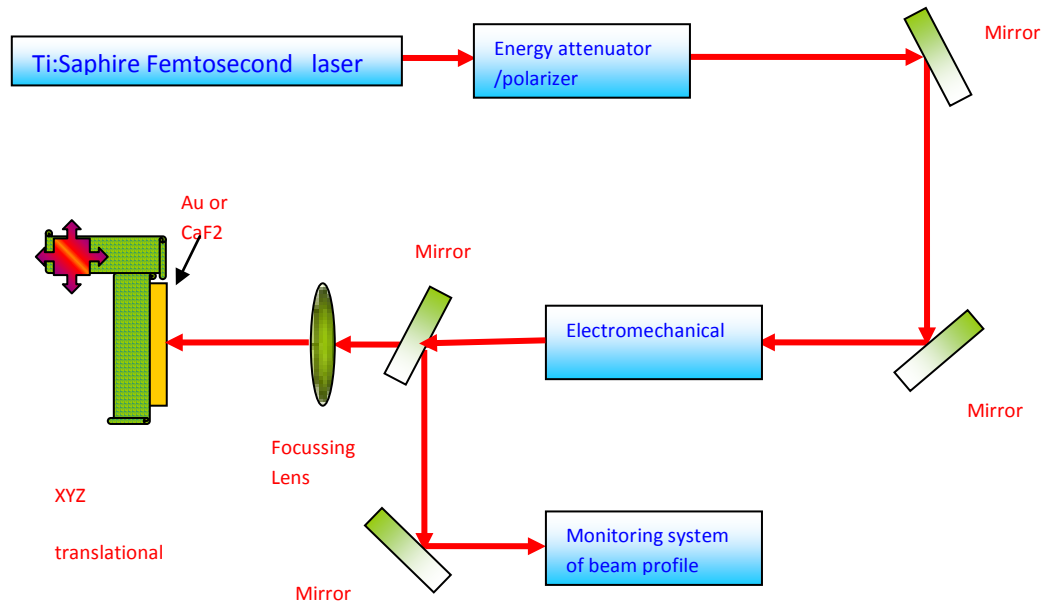


Figure 2.6: Schematic of experimental set-up for femtosecond laser ablation of various targets in air.

In order to perform AFM measurements, a surface area of approximately  $1\text{ mm} \times 1\text{ mm}$  was irradiated by overlapping individual laser spots with a spatial resolution of  $5\text{ }\mu\text{m}$  (400000 exposures). The number of laser shots was controlled by an electronic counter working with Lab VIEW program after triggering it through a green beam signal via photodiode and giving its output to the pockel cell driver

### 2.2.2 Target exposure under ultrahigh vacuum conditions

The various targets were irradiated with laser pulses in UHV ( $10^{-9}$  torr) condition. The targets were mounted on an xyz-manipulator with a spatial resolution of  $5\text{ }\mu\text{m}$  in each direction for a precise positioning of sample for each exposure. The laser beam, after focusing through a 36 cm focal length lens, was incident perpendicular to the surface of the target placed 5 mm away from focus giving a spot diameter of  $100\text{ }\mu\text{m}$ .

The irradiation fluence was varied from  $0.06\text{ Jcm}^{-2}$  to  $8\text{ Jcm}^{-2}$  (in case of and UHV condition both). In order to perform AFM measurements, a surface area of approximately  $1\text{ mm} \times 1\text{ mm}$  was irradiated by overlapping individual laser spots. A beam profiler (Laser Cam –HR Coherent) was used to monitor the laser beam (intensity) profile. A schematic of the experimental set-up used to expose targets in UHV is shown in figure 2.7.

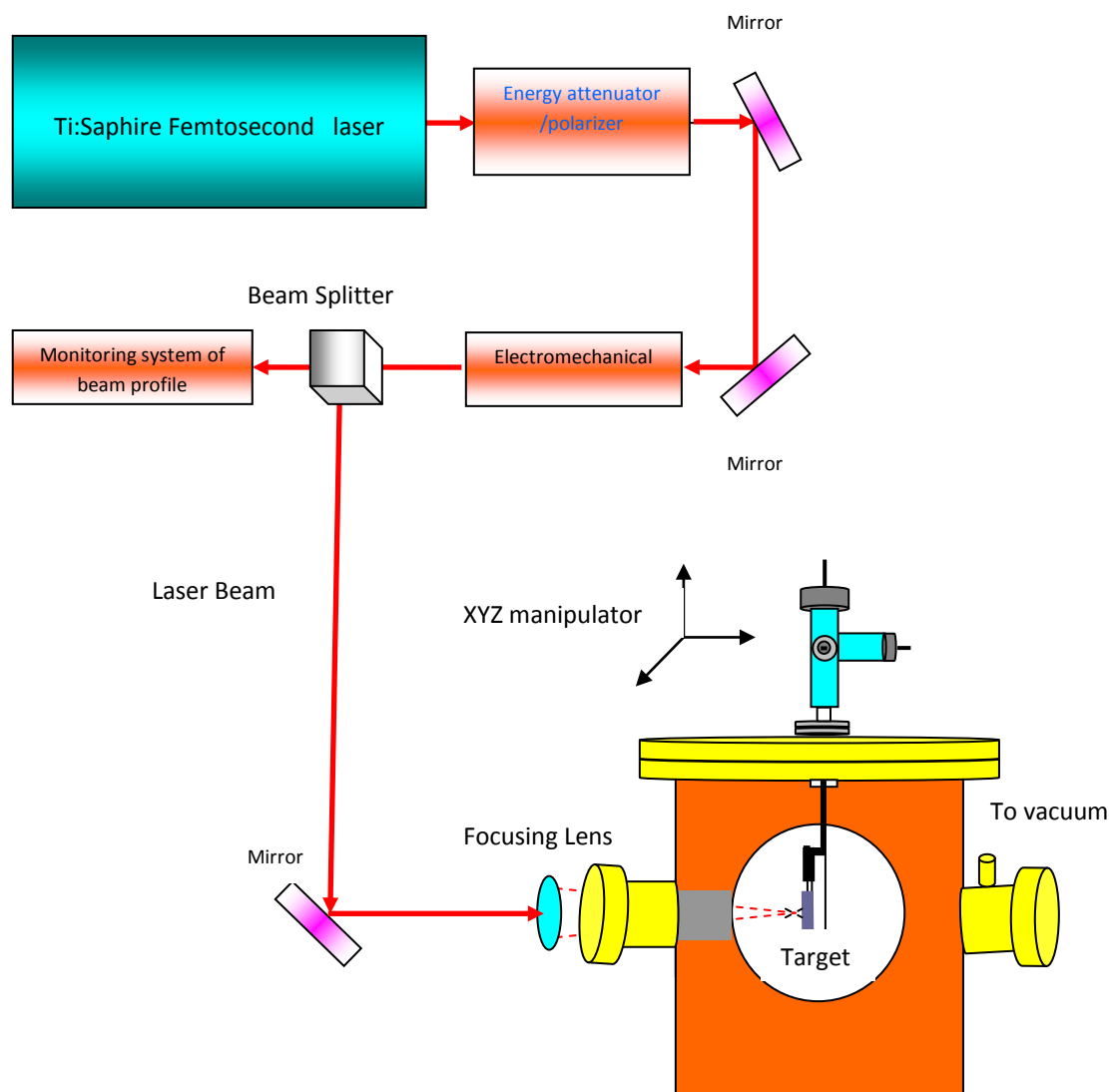


Figure 2.7: An experimental set-up for the growth of micro- and nanostructures by a femtosecond laser on different targets under UHV condition.

### 2.3 Laser ablation analysis and characterization: Diagnostic tools for Surface topography, Structural analysis and Nonlinear absorption properties of ablated materials

The following section will concentrate on practical aspects of different techniques employed for laser ablation analysis and characterization. The technique employed as a major tool for surface analysis of laser ablated materials is Atomic Force Microscopy (AFM). The scanning electron microscopy is also employed for investigation of surface morphology in certain conditions (for a material irradiated with a very high fluence where the depth of ablation crater is so high that the cantilever of an AFM does not work). Raman spectroscopy is

performed for the structural analysis. The Z-scan technique is used for nonlinear absorption measurements.

### 2.3.1 Atomic Force Microscopy (AFM)

For surface characterization of laser irradiated targets, an AFM was employed as a major tool. The purpose of the surface analysis is to identify and investigate topographical changes induced by localized laser energy deposition around the ablation threshold on various target surfaces for better understanding of possible physical mechanism responsible for these topographical changes. Atomic force microscopy is one of the best, powerful and invaluable surface analysis techniques to image surfaces with unprecedented

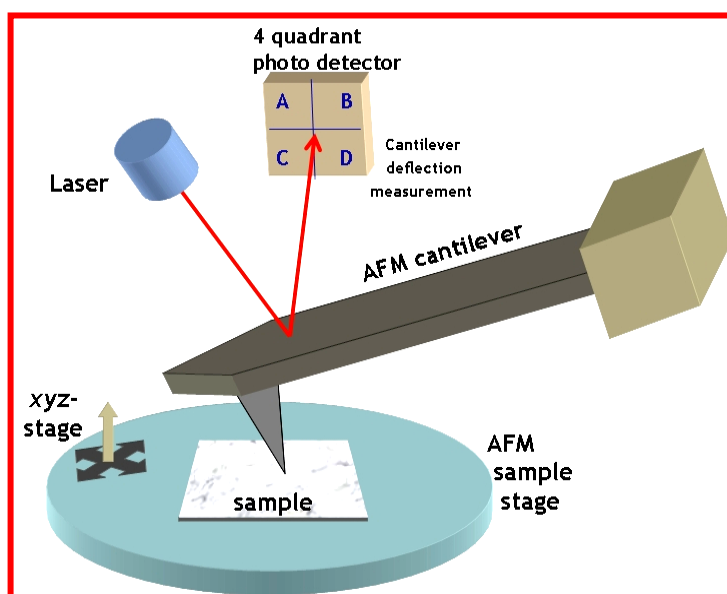


Figure 2.8: A typical AFM setup. The deflection of a cantilever with a sharp tip is measured by reflecting a laser beam off the backside of the cantilever while it is scanning over the surface of the sample.

vertical and lateral resolution on micro- and nanoscale and even on atomic and molecular scale. The resolution of AFM is not limited by diffraction, but only by the size of the probe-sample interaction volume. Hence the ability to measure smaller structures laterally (10nm) and small differences in object height (picometre) is possible. The other main advantage of AFM is that there is no need of special sample preparation and both conducting and non conducting samples can be analyzed. Unlike electron microscope methods, the specimens do not require a partial vacuum but can be observed in air at standard temperature and pressure or while submerged in a liquid reaction vessel. The aim of the surface analysis was also the quantitative characterization of topographical features e.g. diameters and heights of hillocks and bumps, depths and heights of nanocraters, heights and spacings of nanogratings as a function of laser fluence.

MFP-3D scanning force microscopy (Asylum Research, Santa Barbara USA) in contact mode (see later for detailed description) under ambient conditions was employed. The measurements were performed at constant loading force of 6nN, using nonconductive silicon

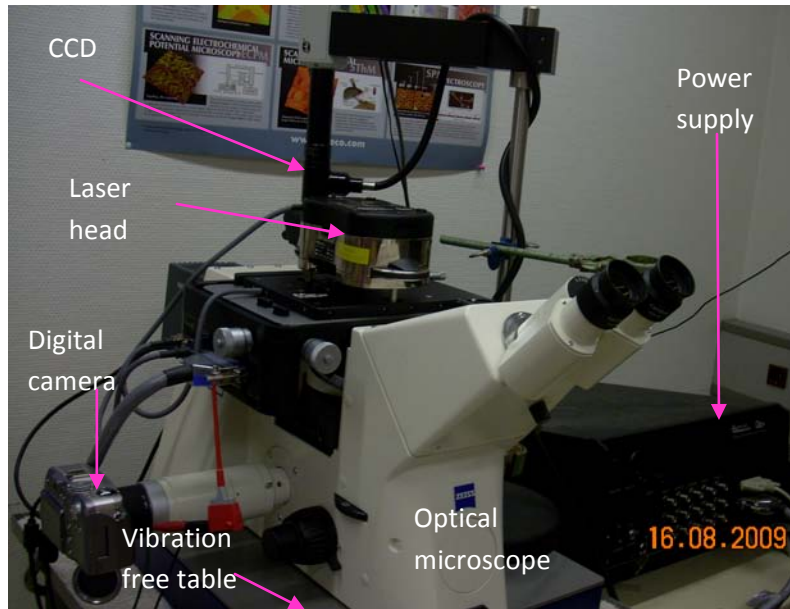


Figure 2.9: An Atomic Force Microscope

nitride sensors (Veeco Instruments, France). The resonant frequencies of cantilevers which have been typically used are around 26- 50 KHz and force constant is 0.1 N/m, having tip diameter 10nm.

$$f_o = \frac{1}{2\pi} \sqrt{\frac{k}{m}} \quad 2.1$$

Where  $f_o$  is resonance frequency and  $k$  is spring constant. For optimal AFM imaging, scan rates less than 1Hz (as low as 0.2 Hz ) set point voltages of less than 1.0 V, and amplitude set point voltages of around 600-700 mV have been employed.

Since the discovery of Atomic Force Microscopy in 1986 by G.Binnig and Coworkers [73], an AFM has rapidly developed into a powerful and invaluable surface analysis technique on micro- and nanoscale and even on atomic and molecular scale.

Atomic force microscopy (AFM) is a method of measuring surface topography on a scale from angstroms to 100 microns. The basic imaging principle is very simple: a sample attached to a piezoelectric positioner is rastered beneath a sharp tip (with a radius of 10-20 nm) attached to a sensitive cantilever spring. Undulations in the surface lead to deflection of the spring, which is monitored optically. The tip is held several nanometers above the surface and usually, an employed feedback loop holds the spring deflection constant, and the corresponding movement of the piezoelectric thus generates the image. A schematic representation of the technique is shown in figure 2.8. A photographic view of an AFM is shown in figure 2.9. It is clear, that the scanning AFM has all the attributes necessary for the



determination of surface and adhesion forces; a sensitive spring to determine the force, a piezoelectric crystal to alter the separation of the tip and surface, which if sufficiently well-calibrated also allows the relative separation of the tip and surface to be calculated [74].

Variations in tip height are recorded while the tip is scanned repeatedly across the sample, producing a topographic image of the surface. However, cantilevers can also be used for sensing applications. These so-called nanosensors show features of extreme sensitivity for the detection of chemical vapors or adsorption of molecules. Upon adsorption to the cantilever surface, the molecules cause the cantilever to bend. Thus physical, chemical or biochemical processes are directly transduced into nanomechanical motion.

### ***Basic modes of AFM***

There are three basic modes of AFM

1. Contact mode (static)
2. Non-contact mode (dynamic)
3. Tapping Mode (dynamic)

#### ***(1) Contact Mode AFM***

In contact mode, the force between the tip and the surface is kept constant during scanning by maintaining a constant deflection. The tip scans the sample in close contact with the surface. The cantilever is pushed against the sample surface with a piezoelectric positioning element. During the scanning process, the deflection of the cantilever is permanently sensed and compared in a DC feedback amplifier to a preset value of deflection (set point). The higher the chosen value of the set point, the stronger the tip pushes into the surface. Therefore, one practically starts with small deflections and increases the set point slowly. Forces range from nano to micro Newton in ambient conditions and even lower (0.1 nN or less) in liquids. If the measured deflection is different from the desired value, the feedback amplifier applies a voltage to the piezo to raise or lower the sample relative to the cantilever in order to restore the present value of deflection. The voltage applied to the piezo is directly correlated to the piezo movement and therefore to the height of features on the sample surface. It is displayed as a function of the lateral position of the sample.

For topographic investigations of laser ablated targets, an AFM in contact mode was employed. Its advantage over other modes is that it is a highly stable technique, with high

scan speeds. It is the only mode that can obtain “atomic resolution” images. Rough samples with extreme changes in topography can sometimes be scanned more easily. Its disadvantages are that the lateral (shear) forces can distort features in the image. The forces normal to the tip-sample interaction can be high in air due to capillary forces from the adsorbed fluid layer on the sample surface. The combination of lateral forces and high normal forces can result in reduced spatial resolution and may damage soft samples (i.e. biological samples, polymers, silicon) due to scraping.

## ***(2) Tapping Mode AFM***

A cantilever with attached tip is oscillated at its resonant frequency and scanned across the sample surface. A constant oscillation amplitude (and thus a constant tip-sample interaction) is maintained during scanning. Typical amplitudes are 20-100 nm. Forces can be 200 pN or less. The amplitude of the oscillations changes when the tip scans over bumps or depressions on a surface. This technique is ideal for imaging sample surfaces that are easily damaged, loosely attached to their substrate or difficult to image by other AFM techniques. The tip is alternately brought in contact with the surface to provide high resolution and then moved away from the surface to avoid scratching over the surface. In tapping mode the cantilever is oscillated at or near its resonant frequency using a piezoelectric crystal. The cantilever oscillates with a high amplitude (typically greater than 20 nm), when the tip is not in contact with the surface. The tip is approached to the surface until it begins to lightly touch or tap the surface.

## ***(3) Non-contact Mode AFM***

The cantilever oscillates slightly above its resonant frequency with oscillations of amplitude <10nm. The tip does not touch the sample and hovers 50 - 150 Angstrom above the sample surface. A constant oscillation amplitude is maintained. The resonant frequency of the cantilever is decreased by the Van der Waals forces which extend from 1-10 nm above the adsorbed fluid layer. This in turn changes the amplitude of oscillation.

The disadvantages of AFM are that the detailed shape of the scanning tip is sometimes difficult to determine. Its effect on the resulting data is particularly noticeable if the specimen varies greatly in height over lateral distances of 10 nm or less. The scanning techniques are generally slower in acquiring images, due to the scanning process. The maximum image size

is generally smaller. Scanning probe microscopy is often not useful for examining buried solid-solid or liquid-liquid interfaces [5].

### **2.3.2 Scanning Electron Microscopy (SEM)**

The irradiated targets were also analyzed by a (FEI-QUANTA 200F, Netherlands) Scanning Electron Microscope (SEM). A scanning electron microscope can scan the surface of a sample with a finely focused high energy electron beam to produce an image from the beam-specimen interactions and contain information about the sample's surface composition and other properties and is detected by a wide array of detectors. A variety of detectors are available, from secondary electron detectors to provide surface information, to backscattered detectors for compositional information in both high and low vacuum modes. A SEM with the following specifications was employed for measurements with accelerating voltage 200-20KV, continuously adjustable probe current up to 2 $\mu$ A, magnifications 20  $\times$  to 1000000 $\times$ , Chamber size 284 mm-279 mm (inner diameter) and resolution 2 nm-10 nm, depending upon modes of operation i.e. high vacuum or low vacuum.

### **2.3.3 Raman Spectroscopy**

The purpose of Raman spectroscopy is to reveal the structural, crystallographical and chemical changes, like crystallization, amorphization [75], bond breaking, bond weakening, cross linking, polymerization, appearance of new disorder bands for irradiated targets [76] and to correlate them with surface analysis obtained by AFM. It is also important technique to investigate laser-induced stress distribution of processed materials [77].

The Raman spectroscopy is performed by a Raman spectrometer Lab Ram HR-800 (Horiba Jobin-Yvon). A He-Ne laser is used as an excitation source with 8 mW power, at 632.8 nm. A 20  $\times$  objective lens is used for laser focusing, resulting in a spot size of  $\sim$ 20  $\mu$ m. The spectral data were accumulated at a fixed grating position and collected using an air-cooled CCD camera. It is a non-destructive, non-invasive technique without the requirement of sample prepartion and provides qualitative and quantitative data.

When a laser interacts with materials most of the photons are elastically scattered, a process which is called Rayleigh scattering. In Rayleigh scattering, the emitted photon has the same wavelength as the primary absorbed photon. Raman Spectroscopy is based on the Raman effect, which is the inelastic scattering of photons by molecules. The Raman effect comprises a very small fraction ( $1: 10^7$ ), of the incident photons. In Raman scattering, the energies of the incident and scattered photons are different. A simplified energy diagram that

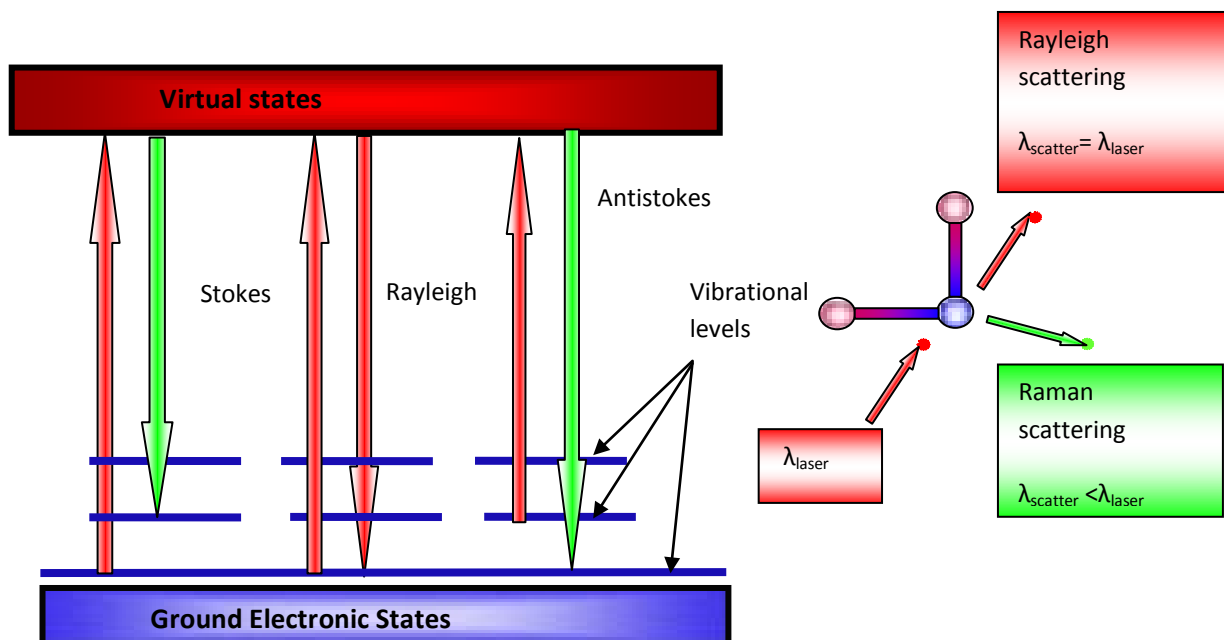


Figure 2.10: A simplified energy diagram that illustrates concepts of Raman Scattering: Rayleigh scattering (of same wavelength as the incident light) and Raman scattering (of new wavelength)

illustrates these concepts is depicted in figure 2.10. The energy of the scattered radiation is less than the incident radiation for the Stokes line and the energy of the scattered radiation is more than the incident radiation for the anti-Stokes line. The energy increase or decrease from the excitation is related to the vibrational energy spacing in the ground electronic state of the molecule and therefore, the wavenumber of the Stokes and anti-Stokes lines are a direct measure of the vibrational energies of the molecule. Raman spectroscopy measures the vibrational energies of molecules therefore for a transition to be Raman active there must be a change in polarizability of the molecule. A

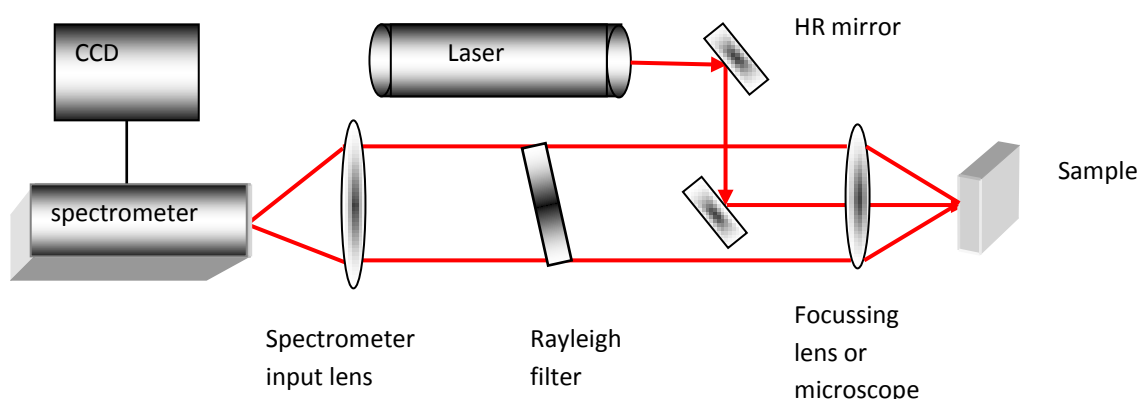


Figure 2.11: Schematic of Raman spectroscopy

schematic of Raman spectroscopy is illustrated in figure 2.11

### 2.3.4 Z-scan Technique

In order to measure non-linear absorption properties of transparent materials the Z-scan Technique has been employed. The main aim is to correlate the surface; structural and chemical changes (probed by AFM and Raman Spectroscopy) induced by femtosecond laser irradiation at different fluences with non linear absorption properties of irradiated materials.

For this purpose, an open aperture Z-Scan technique [78] has been employed and is illustrated in figure 2.12 . This technique allows to determine the nonlinear absorption coefficients (Two Photon Absorption (TPA) or Three Photon Absorption (ThPA)) of the material [79] ). In this technique, ultrashort pulses were obtained from the same system as have been used for ablation (section 2.1) . The irradiated target was scanned by a laser at a scanning energy of 100 nJ. The beam splits in two orthogonal directions, one being used as intensity reference (detected at the reference diode  $D_r$ ). The other is directed to a focusing lens (20 cm focal

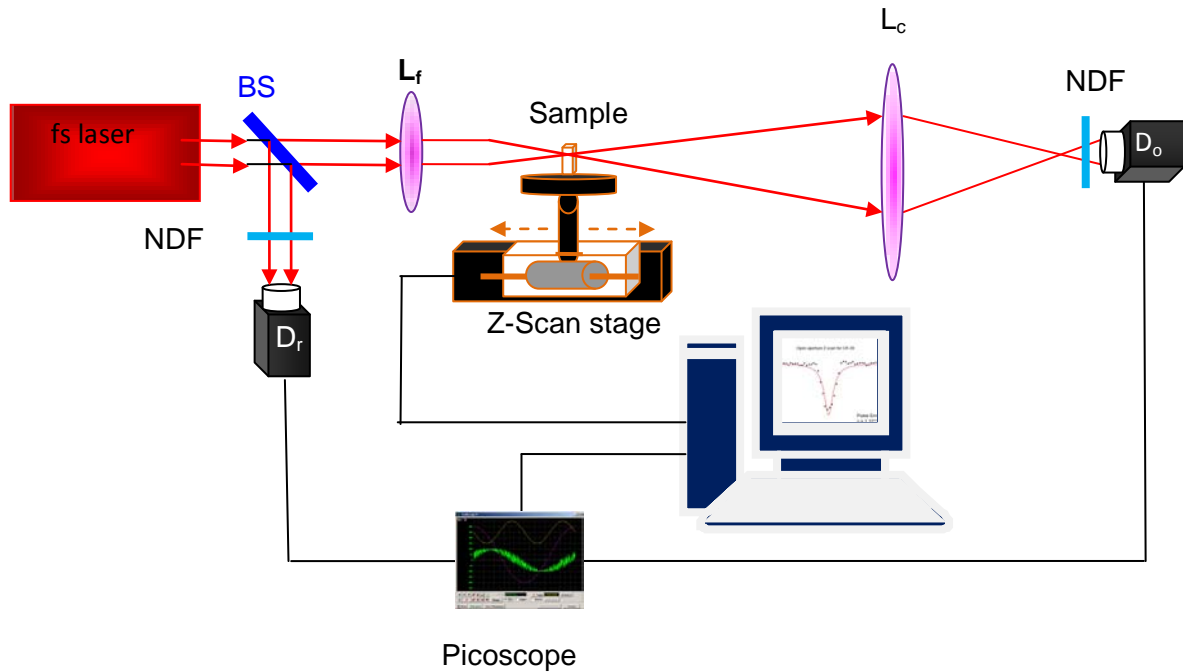


Figure 2.12: Schematic lay out of an open aperture Z-scan technique, where BS: Beam Splitter,  $L_f$ : Focussing lens,  $L_c$ : Collecting lens, NDF: Neutral Density Filter, A: Aperture,  $D_o$ : Open aperture collecting Diode,  $D_c$ : Close aperture collection Diode,  $D_r$ : Reference Diode

length) and then after passing through the sample gives beam waist  $14\mu\text{m}$  and a Rayleigh length of 0.8 mm. The targets were mounted on a translating stage that can be moved across 25 mm through the beam focus. The transmitted intensity is then collected by a lens (10 cm

focal length) and directed to the diode *Do* (open aperture configuration). This requires adjustment of the absolute intensity at the diodes (Neutral Density Filters NDF) to fall into the dynamic range of the diodes. The signal at the diodes is recorded with a low-cost two-channel PC Oscilloscope (Picoscope). The computer software analyzes the intensity of individual laser pulses (including averaging over several laser shots) and also handles the movement of the translation stage as well as the entire data acquisition process (Lab View). A schematic of the setup in Fig. 2.12 shows an open aperture Z-scan technique, which yields the TP (and/or three photon-) absorption coefficients of transparent materials.

# Chapter 3

## Results and Discussion

---

### 3.1 Results and Discussion

The experimental results obtained by exploring the surface of the laser irradiated dielectric, semiconducting, metallic and polymeric materials by AFM has been discussed in this main chapter of the thesis. Observed changes in surface topography are correlated with Raman spectroscopy. The main goal of the work is to identify and understand basic mechanisms of localized laser energy deposition in different materials (insulators, semiconductors and metals) as well as the corresponding physical (ultrafast electronic and slow thermal) processes leading to ablation by ultrashort laser radiation. In the last section surface and structural changes induced by laser irradiation are also correlated with nonlinear absorption properties of CR-39 as a practical example.

In order to obtain more detailed information on specific processes, like ultrafast electronic processes e.g. Coulomb explosion (CE), Surface Optical Rectification (SOR), hot electron plasmas or ultrafast melting (UFM)) and extended class of thermal processes, it is a very important fact that there is only a relatively small range of laser intensities (close to the ablation threshold), for which different possible processes contribute with a comparable strength to leave distinguishable features. For obtaining specific footprints, which can help us to identify different processes, laser fluence is the major parameter, which has been varied during most experiments. All other parameters such as repetition rate, pulse duration, target position from focus point, distance between overlapping pulses to hit the target, and angle of incidence were kept constant. It is a well-known fact from time of flight measurements [14] that ultrafast electronic processes are dominant for lower intensities. Therefore, the starting point for performing experiments is chosen to be single shot irradiation at lower fluence regime (around the ablation threshold where particle emission starts). Targets were also exposed for moderate and high fluence regimes for single as well as multiple shots.

All experimental results are organized in such a way that one can clearly distinguish between three fluence regimes (with regards to the dominating processes).

- A very low fluence regime (around the ablation threshold)
- A moderate fluence regime (slightly higher than the ablation threshold)

- A high fluence regime (significantly higher than the ablation threshold).

The corresponding topographical changes represent an overall picture of the occurrence of

- Ultrafast Coulomb Explosion (sub 100 fs ) or Surface Optical Rectification (SOR) in the low fluence regime (around the ablation threshold);
- Ultrafast Melting (few hundred fs) as a dominant mechanism at moderate fluence regime (slightly higher than ablation threshold);
- A transition from ultrafast electronic processes or gentle ablation to large class of thermal processes (in ps time regime) at a high fluence regime (significantly higher than ablation threshold).

With increasing laser fluence, beyond the onset of thermal mechanisms involving melting and vapor transformation, these mechanisms of thermal nature are superimposed on CE and can substantially mask the latter. Higher laser fluences can cause high rate of electron photo-emission, thus enhancing CE probability. On the other hand, the particles abundantly emitted during phase explosion have a wide velocity distribution with a high-energy tail masking the electronically ablated energetic particles.

It is of fundamental interest to study the surface topography as it develops under ultrashort laser radiation, in particular, close to the ablation threshold. The appearance of nano-sized hillocks on the surfaces of different materials (dielectric, semiconducting, metallic and polymeric) around ablation threshold (in the lower fluence regime) can be correlated with ultrafast electronic processes (Coulomb explosion) corresponding to sub 100 fs time regime and particle emission of energies several eV which have been presented and discussed in [12-14].

In order to investigate surface topographical changes induced by ultrafast melting (plasma formation) corresponding to time regime of 100,s of fs and particle emission of few eV targets were irradiated with fluence slightly higher than the damage threshold. Bumps, nanopores and micro and nanoripples like structures have been observed due to ultrafast melting, surface plasmon and photomechanical effects (inertial stress confinement) at a moderate fluence of single or multiple-shot-irradiation. We call a micro-bump a cone-like extrusion of material, typically 200 nm-3 $\mu$ m in diameter and 10-50 nm in height.

In order to investigate surface topographical changes induced by thermal processes targets were irradiated with fluence significantly higher than the damage threshold, and with multiple-shot-irradiation. These higher fluences cause slower ion emission typically on the order of tens of picoseconds with the emission of a large amount of low velocity ions and neutrals. This slower particle emission is a consequence of electron-phonon coupling in the



material leading to thermal excitation of the lattice followed by a thermal particle removal. Due to strong ablation or phase explosion the surface of an irradiated target reaches the melting and evaporation temperature. The footprint left behind after this strong thermal ablation is usually overwhelming (e.g. craters, islands, larger humps and bumps, chaotic and highly disturbed surface). The different sizes of structures can be explained on the basis of marked differences in energy deposition and material ejection mechanism.

### 3.1.1 Calculations of Beam Radius, Rayleigh Length and Fluence

The laser fluence has been observed to affect strongly the resulting surface topographical changes. Therefore, it is important to mention how the laser spot size 5 mm away from focus point and the laser fluence has been determined.

The laser beam radius ( $\omega_f$ ) after focusing through a 36 cm focal length lens is calculated by using following formula.

$$\omega_f = \frac{\lambda f}{\pi \omega_o} = \frac{800 \text{ nm} \times 36 \text{ cm}}{3.14 \times 0.75 \text{ cm}} = 12.229 \mu\text{m} [12.229 \mu\text{m} \times M^2] \quad 3.1$$

where  $\lambda$  is the laser wavelength,  $f$  is focal length of the lens,  $\omega_o$  is the beam radius without focusing and

$$M^2 = \theta / \frac{\lambda}{\pi \omega_o} = 2 \text{ is the beam quality factor or beam propagation factor}$$

Therefore,  $\omega_f = 24.5 \mu\text{m}$  (focused beam radius)

Rayleigh Length ( $Z_R$ ) is calculated as follows

$$Z_R = \frac{\pi}{\lambda} \omega_o^2 = \frac{3.14 \times 24.5 \times 24.5}{800 \text{ nm}} = 2.45 \text{ mm} \quad 3.2$$

For irradiation, targets were placed at an optimized distance of 5 mm from the focus point.

Therefore, the beam radius  $\omega(z)$  at 5 mm from the focal point is

$$\omega(z) = \omega_f \left[ 1 + \frac{z^2}{z_R^2} \right] = 24.5 \left[ 1 + \left( \frac{5}{2.45} \right)^2 \right]^{\frac{1}{2}} = 55 \mu\text{m} \quad 3.3$$

where  $Z$  = distance of the target from focus point,  $Z_R$  = Rayleigh length

The laser fluence is calculated by using a relation

$$\text{Fluence} = \frac{E_{\text{pulse}}}{\pi (\omega(z))^2} \quad 3.4$$

where  $E_{\text{pulse}}$  is the laser pulsed energy.

The laser pulse energies have been varied from 6  $\mu\text{J}$  – 800  $\mu\text{J}$ . The corresponding irradiation fluences are in the range of 0.06  $\text{Jcm}^{-2}$  to 8  $\text{Jcm}^{-2}$ . In order to perform AFM measurements, a

surface area of approximately  $1\text{ mm} \times 1\text{ mm}$  was irradiated by overlapping individual laser spots with an average spacing of  $5\text{ }\mu\text{m}$ .

Ultrashort laser interaction mechanism can be different for different materials. In order to have a good correlation or comparison of different energy deposition mechanisms for different materials, insulators, semiconductors and metals are selected. Materials investigated are single crystals  $\text{CaF}_2$  (111), Si (111), a polycrystalline Al, and a polymer CR-39 (Allyldiglycol carbonate).

$\text{CaF}_2$  as a dielectric material has been recently investigated for highly charged ions bombardment [15] for the formation of nano-sized hillocks and is characterized by a sharp and well-defined threshold for the potential energy, representing a strong indication for the existence of electronic processes during ion bombardment of solids. With  $\text{CaF}_2$  it was the only possibility to have a good comparison of nanostructures developed after ultra-short-laser irradiation and ion bombardment and these structures can be linked and attributed to similar fast electronic (potential energy) processes. The second important reason for the choice of this material is that for low laser intensities Coulomb explosion upon multiphoton surface ionization is already considered as a noncontroversial dominant process, yielding electrons and fast positive ions by Reif et al [36, 72]. A substantial work is reported on the production of conduction band electrons, their diffusion, laser energy deposition and formation of self-trapped excitons after fs laser irradiation [80, 81].

CR-39 (Allyldiglycol Carbonate) is an important polymer and is one of the most popular solid state nuclear track detector [82]. It is known as an excellent material for a number of industrial, medical and optical applications. It has good optical transparency and structural stability. It is extensively used in various experiments in fusion research, nuclear science and astrophysics [83, 84]. A CR-39 nuclear track detector has been well demonstrated to have an excellent track registration property and used widely in various fields by many authors [83, 85, 86]. Very few studies, however, have been performed to obtain the fundamental information on laser irradiation effects on this detector [82, 87].

Si and Al are selected, since time of flight measurements for these materials are helpful to obtain detailed information about the velocity distribution, the time behavior of the energy deposition (pulse width dependence studies), the composition and energy of the emitted particles and two-pulse correlation measurements. This information serves as a starting point for identifying the occurrence of ultrafast electronic (Coulomb explosion (CE), field ion emission by surface optical rectification (SOR), Ultrafast melting (UFM)) and thermal

ablation. A comparison of surface topography with TOF measurements can yield substantial information for better understanding of different processes involved in ultrashort laser matter interaction.

### 3.1.2 Energy deposited per atom (eV/atom)

With ultrashort pulse-irradiation, different surface irregularities (protrusions and pits) emerge progressively with different geometrical sizes depending upon the laser fluence and the target selection. If the laser energy deposited (eV/atom) exceeds the heat of melting (threshold) per atom for a corresponding irradiated target then localized and isolated defects can be observed at a lower fluence (around ablation threshold) for a single pulse irradiation.

Therefore, it is important to calculate the deposited energy per atom for different irradiated targets for a fluence in the range of  $0.06 \text{ Jcm}^{-2}$  to  $3.5 \text{ Jcm}^{-2}$ .

The deposited energy per atom is calculated using following steps:

Energy per pulse  $E$  (J) can be converted into energy in  $\text{eV/nm}^2$ , i.e., for  $\omega(z) = 55 \mu\text{m}$  and using  $1\text{eV} = 1.6 \times 10^{-19}\text{J}$

$$\text{Energy} \left( \frac{\text{eV}}{\text{nm}^2} \right) = \frac{E \times 10^{-6}}{1.6 \times 10^{-19}} \left\{ \frac{1}{3.14 \times (55 \times 10^3)^2} \right\} \quad 3.5$$

$$= E \times 0.657 \times 10^3 \quad 3.6$$

In order to calculate energy per unit area ( $\text{eV/nm}^2$ ), pulse energy (J) is multiplied by a factor  $0.657 \times 10^3$ .

Therefore the energy deposited per unit volume ( $\text{eV/nm}^3$ ) in a skin layer ( $l_s$ ) excited by fs-laser is defined by following relation [25]

$$E_{abs} \cong E \left( \frac{\text{eV}}{\text{nm}^2} \right) / l_s \quad 3.7$$

A laser beam with 800 nm excites Al in the skin layer  $l_s = 15 \text{ nm}$  [67], Si ( $l_s$ ) = 42 nm [88], and transparent materials (CaF<sub>2</sub> and CR-39) with  $l_s = \left( \lambda / 4\pi \right) \cong 65 \text{ nm}$  [25] 3.8

where  $\lambda$  is the laser wavelength.

The optical properties of the material (reflection or absorption at 800 nm) affect the energy deposition to specific material. An absorption coefficient  $A=(1-R)$  at 800 nm for Al is 0.15 [89], for Si is 0.66 [89] and for transparent materials (20% ) with overlapping pulses[79, 90].

The real value of energy deposited ( $\text{eV/nm}^3$ ) is calculated by multiplying equation 3.7 with an absorption coefficient of the corresponding material as


$$E_{abs} \cong A E \left( \frac{eV}{nm^3} \right)$$

3.9

In order to calculate the energy deposited per atom (eV/atom), the number of atoms per unit volume (atom/nm<sup>3</sup>) must be known. As number of atoms per cm<sup>3</sup> is known 6.02 x 10<sup>22</sup> for Al and 5 x 10<sup>22</sup> for Si [91]. The number of atoms per nm<sup>3</sup> is 50-60. By dividing energy deposited per unit volume (eV/nm<sup>3</sup>) by number of atoms (50-60 atoms /nm<sup>3</sup>), energy deposited per atom have been calculated.

Real values of energy deposited per atom have been listed in the table 3.1.

Table 3.1: Energy deposited per atom for different materials after ultrashort laser irradiation in the fluence regime 0.06- 4.5 J.cm<sup>-2</sup>

Material	Al	Si	CaF <sub>2</sub>	CR-39
Reflection and Absorption	R=0.85 A=0.15 [89],	R=0.34 A=0.66 [89]	T=80%-90% A= 20%	T=80%-90% A= 20% [25]
Heat of melting per atom E <sub>m</sub> ( eV/atom )	0.3 eV/atom [92]	0.53 eV/atom [93]	0.55 eV /atom [94]	
Skin depth , l <sub>s</sub>	15 [67]	42	65	65
Pulsed Energy (μJ)	Dep. Energy (eV/atom)			
6	0.645	1.18	0.24	0.24
12	1.305	2.4	0.5	0.5
25	2.7	5	1.04	1.04
50	5.7	10	2.06	2.06
100	10.8	20	4	4
150	15	30	6.	6.
200	21	50	8	8
250	27	51	10	10
300	32	61	12	12
350	37	71	15	15
400	43	81	16	16
450	49	92	19	19

In the following at first results for dielectric ( $\text{CaF}_2$ ) are presented because CE with fs pulses in dielectric materials is noncontroversial [19, 20]. Then results for a semiconductor (Si) are discussed. The existence of CE for ultra-short laser ablation of Si, even though questioned, at least has been argued by Roeterdink et al [37]. Results for a metal (Al) are presented in the next step. CE in metals is still under discussion and controversial and needs some more evidences for its existence.

A comparison of similarities and differences in surface topographical features of a dielectric with a semiconductor and a metal after irradiating their surfaces with femtosecond pulses provides a clue that similar kind of nonthermal (electronic processes either CE or SOR) processes is responsible for energy deposition for all three kind of materials. All results are compared and correlated with particle emission studies with detailed information about the velocity distribution, the time behavior of the energy deposition, the composition and energy of the emitted particles.

The next part comprises of: AFM results of a polymer CR-39 and the surface topography of  $\text{CaF}_2$ , Si and CR-39 correlated with Raman Spectroscopy.

In the last section a practical example is presented, in which nonlinear absorption properties are correlated with the surface and structural changes of laser irradiated CR-39.

## **3.2 Results for Dielectrics ( $\text{CaF}_2$ (111))**

### **3.2.1 AFM Measurements**

Results presented in this section are classified into three categories depending upon the irradiation fluence regimes as: (a) Low fluence regime (b) Moderate fluence regime and (c) High fluence regime. AFM micrographs have been presented in such a way that for a low fluence regime, images are shown with a higher magnification (or scan area  $500 \text{ nm} \times 500 \text{ nm}$ ) for all materials. Whereas, in case of moderate and high fluence regimes, the images are presented with lower magnification or larger scan area (ranging from  $1 \text{ }\mu\text{m} \times 1 \text{ }\mu\text{m}$  to  $20 \text{ }\mu\text{m} \times 20 \text{ }\mu\text{m}$ ).

#### ***(a) Low fluence regime***

When the laser intensity is slightly higher than the ablation threshold, the major characteristic feature observed as shown in figure 3.1 is the appearance of nanohillocks, which are visible as small protrusions with typical diameter of 25-60 nm and a height of 2-5 nm. We, therefore, in accordance with observations of other group [15] define a nanohillock as a clearly identified and isolated surface bump, with height typically from 1 nm up to 20 nm and diameter from 10

nm up to 100 nm. The appearance of nanohillocks on a  $\text{CaF}_2$  surface with increasing laser fluences is shown in figure 3.1 (under UHV condition) and figure 3.2 (under ambient condition). These figures show AFM surface topography of scan area  $500 \text{ nm} \times 500 \text{ nm}$ . The energy range from  $0.06$  to  $0.5 \text{ J.cm}^{-2}$  (figure 3.1) corresponds to the regime, where the transition from ultra fast electronic processes to thermal dominated ablation has been

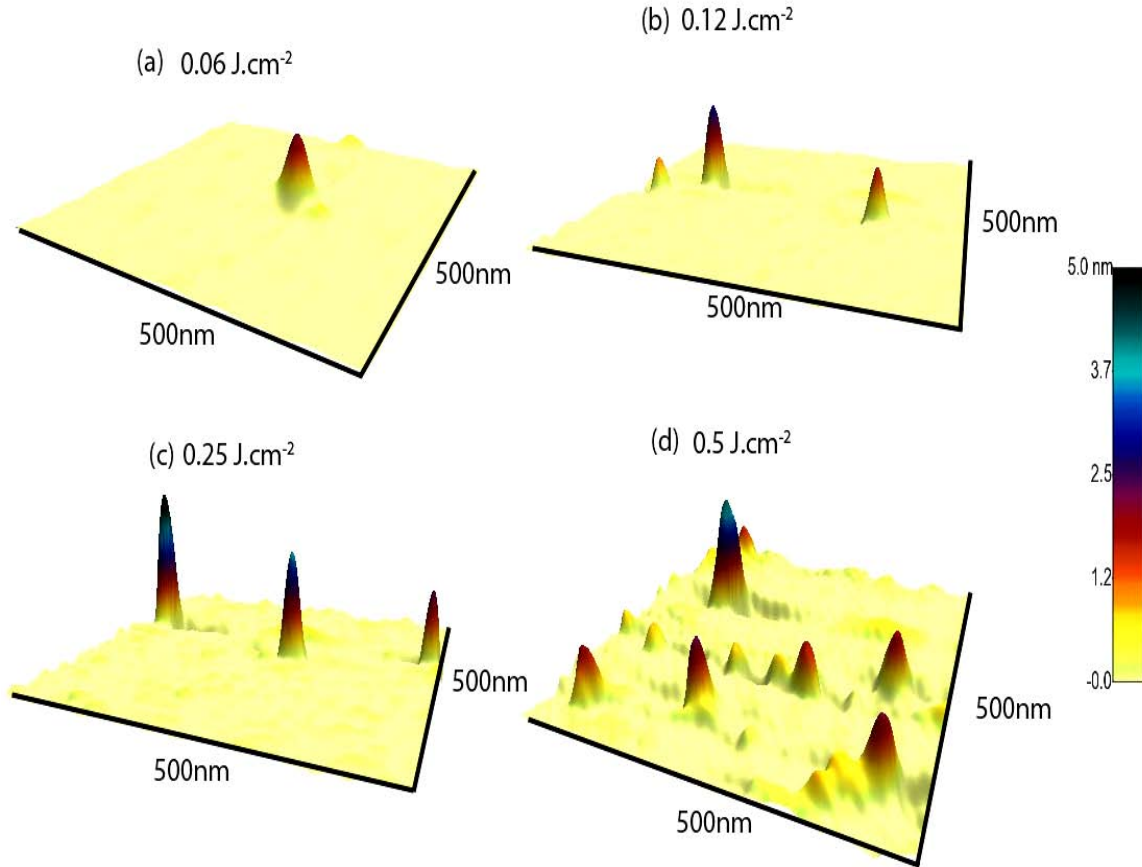


Figure 3.1: AFM Topographic images of nanohillock-formation on the  $\text{CaF}_2$  surface (scan area  $500 \text{ nm} \times 500 \text{ nm}$ ) as a result of single shot of  $25 \text{ fs}$  laser irradiation under UHV condition at fluences (a)  $0.06 \text{ J.cm}^{-2}$  (b)  $0.12 \text{ J.cm}^{-2}$  (c)  $0.25 \text{ J.cm}^{-2}$  (d)  $0.5 \text{ J.cm}^{-2}$

previously observed. [12-14]. Furthermore, at  $0.12 \text{ J.cm}^{-2}$  energy of approximately  $0.5 \text{ eV/atom}$  is deposited in  $\text{CaF}_2$  under the exposure condition in our setup. Interestingly, this corresponds very well with the deposited energies, for which nano-sized hillocks are observed under highly charged ion bombardment [15] and is slightly higher than the ablation threshold reported by Reif et al [36] for  $\text{CaF}_2$ . Below  $0.12 \text{ J/cm}^2$  only very few single nanohillocks are found in the exposed area (Figure 3.1a). Starting at the threshold for particle ejection (we

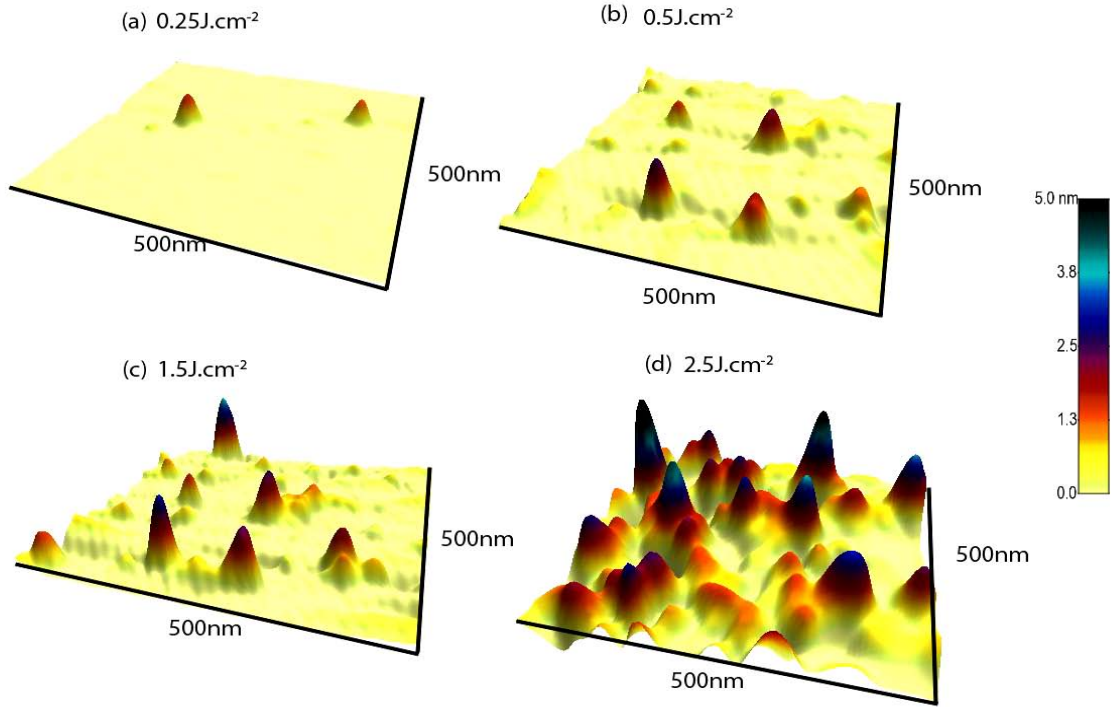


Figure 3.2: AFM Topographic images of nanohillock-formation on the  $\text{CaF}_2$  surface (scan area  $500 \text{ nm} \times 500 \text{ nm}$ ) as a result of single shot of 25fs laser irradiation in air at fluences (a)  $0.25 \text{ J.cm}^{-2}$  (b)  $0.5 \text{ J.cm}^{-2}$  (c)  $1.5 \text{ J.cm}^{-2}$  (d)  $2.5 \text{ J.cm}^{-2}$

could call it the ablation threshold) an increasing number of hillocks are observed (figure 3.1 b). The height of the hillocks remains more or less unchanged at 1–3 nm. The number of hillocks, but in particular their height, increases up to 5 nm as the laser fluence is further raised (Figure 3. 1c). Finally, if the fluence increases above  $0.4\text{--}0.5 \text{ J.cm}^{-2}$  the hillocks become broader (figure 3.1d) and the surface is rendered highly disturbed. It makes no sense to speak of localized, isolated nanohillocks anymore, even though the AFM pictures might perhaps imply their existence. Since they are now superimposed on large scale, non-localized disturbances, quantification (number and size) is not useful. The appearance of nanohillocks with a typical diameter of 25 nm and an average height of 2 nm are shown in figure 3.2 (a). Figure 3.2(b) presents the appearance of several numbers of nanohillocks with an average height of 3 nm and an average diameter of 40 nm, when the target was exposed to a fluence of  $0.5 \text{ J.cm}^{-2}$ . Further increasing the incident fluence to  $1.5 \text{ J.cm}^{-2}$ , the average number and the height of nanohillocks has been increased. The average height of 4 nm and an average diameter of 50 nm are observed for this fluence. If the laser fluence is further increased to  $2.5 \text{ J.cm}^{-2}$ , the entire surface is severely disturbed with no identifiable localized nanostructures as shown in figure 3.2(d).

The observations shown in Figure 3.1(a-d) and 3.2(a-d) are characterized by features which are attributed to a localized energy deposition mechanism in the crystal around the ablation

threshold. Nanohillock-formation reveals that this energy deposition is confined to spots localized within 100 nm in diameter in spite of the fact that the laser spot diameter is approximately 100  $\mu\text{m}$ .

The energy deposition into the electronic system by ultrashort- laser pulses seems to initiate

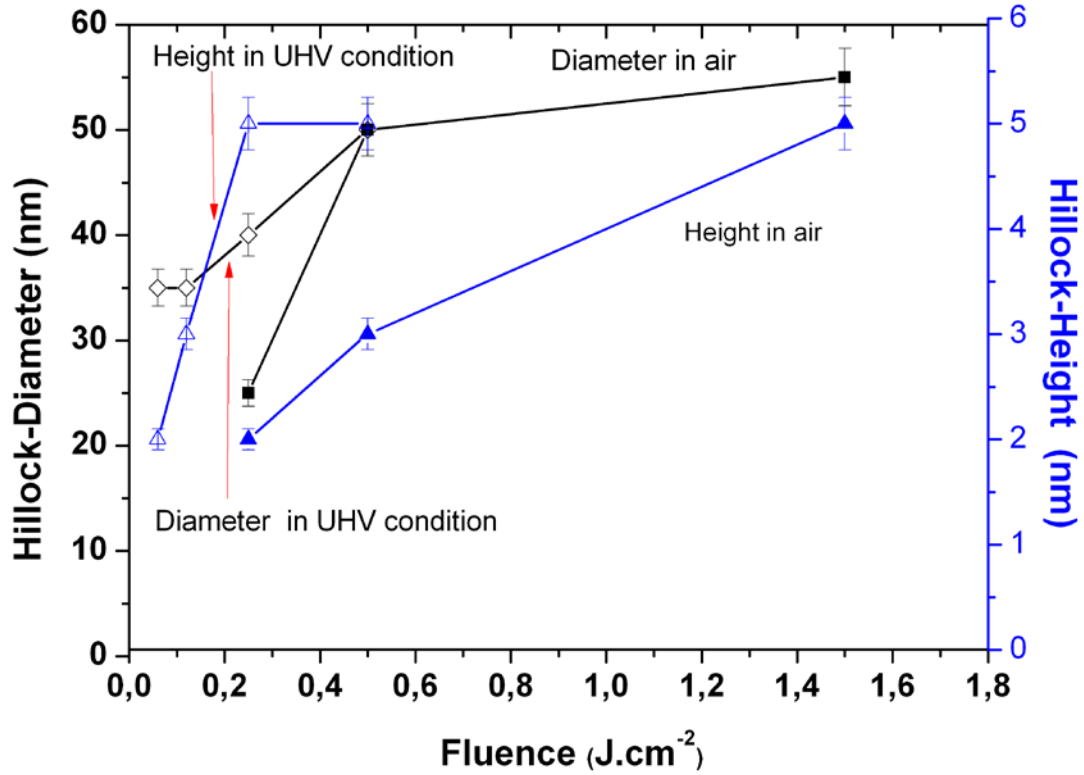


Figure 3.3: Average diameter and height of nanohillocks formed on the  $\text{CaF}_2$  surface versus laser fluence as a result of its exposure to 25fs laser radiation in air and under UHV condition

similar or identical processes observed for bombardment with highly charged ions, where a substantial part of the kinetic energy of the ions is deposited as inelastic energy [15]. Depending upon the ionization density and charge neutralization time the mutual repulsion of the target ions may convert a significant amount of an electronic potential energy into an atomic motion. In case of ion bombardment this conversion mechanism has been explained by Coulomb explosion by some authors [95-97].

Coulomb explosion in dielectrics is well accepted [20, 21, 36, 72]. At laser intensities around the single shot damage threshold, Coulomb explosion upon multiphoton surface ionization has been established as the principal origin of positive ion emission [12, 13, 36]. The transfer of energy stored in the hot electrons into kinetic energy of ablated particles or dislocated target surface atoms is a complicated process. Femtosecond laser radiation initially transfers



its energy to the electronic system of the target, leading to a region of strong electronic excitation. As the laser pulse is shorter than the electron-phonon energy transfer time, only electrons are heated during the pulse [98]. The explosive emission of positive ions from dielectrics under intensive femtosecond irradiation is due to Coulomb explosion of the surface, preceded by appreciable ionization. The principle action of the laser pulse is to ionize the target surface. Because of the very short interaction time, this ionization may be considered to be almost instantaneous with a kinetic energy of the electrons which is sufficiently high for immediate escape from the target. Therefore, no space charge shielding of the sample should occur. Consequently, the dielectric target is left behind with a corresponding density of localized positive holes. Once a sufficient density of holes is achieved, the target surface becomes electrostatically unstable, resulting in a Coulomb explosion of positive ions [36]. Since many mechanisms can and will contribute, a conclusive answer, which one is actually taking place, is difficult to answer. Based on experimental observations we postulated Coulomb explosion as a highly probable and possible explanation for particles emission [12, 14, 36], caused by excitations on fs timescale. The laser energies per pulse and the pulse width of 25 fs are sufficient to create the charging required for CE. In particular, the localized hillocks might imply that a large area (laser spot) is charged due to loss of hot electrons, but only a few localized spots surrounded by an electron deficient area become sufficiently charged for a time long enough to experience Coulomb explosion. This explosion has been suggested to be a responsible mechanism to cause localized surface modification and particle ejection, leaving a nanohillock like structures on the irradiated surface. There are some examples in which CE has been considered as the underlying mechanism of femtosecond laser-induced gentle ablation (ultrafast nonthermal melting ) for the formation of nanostructures [33, 99].

From the results by El-Said et al [15] for highly charged ions, the correlation between the potential energy deposited in the electronic system and the appearance of nanohillocks seems to be evident. However, in the case of highly charged ion bombardment, the energy is deposited in a clearly defined localized manner at the impact positions of the individual ions. On the other hand, in the present situation of laser irradiation, the laser energy is more or less uniformly distributed over the exposed area. Furthermore, the laser energy is deposited in extremely short times resulting in high peak intensities of the electric field. Therefore, multiphoton processes are highly probable. They are required to create free electrons in the conduction band of insulators and semiconductors. The characteristic development of individual hillocks suggests that the energy is absorbed favorably at these localized sites. This

may be due to voids, inhomogeneities and/or non-linear absorption of the laser energy concentrating the energy on localized sites. The underlying assumption is that a flat homogeneous surface initially sputters (gently ablates) homogeneously, i.e. some significant disturbance must be created before observable structures may occur. This significant disturbance can appear in the form of radiation-induced defects and nucleation. It is well known fact that both, structural defects (cracks, roughness etc.) as well as electronic defects (e.g. color centers, self trapped excitons), may enhance the ablation process [100]. In the case of overlapping pulses, it appears that structural defects are produced, that lead via local field enhancement to an increasing ionization cross-section. This scheme may also be responsible for localized features as observed in figures 3.1 and 3.2.

The effect of laser fluence on the geometrical size (diameter and height) of these nanohillocks after exposing the target in air and vacuum is plotted in figure 3.3. For air and vacuum, both the average diameter and height of hillocks increase with increasing laser energy and this is attributed to an increased energy deposition.

The results reported above indicate that similar kind of nanostructures has appeared in UHV as well as for ambient conditions. One difference, however, has been found: in case of UHV condition, the characteristic surface nanostructures (nanohillocks) are observed for fluences ranging from  $0.06 \text{ Jcm}^{-2}$  to  $0.5 \text{ Jcm}^{-2}$  whereas, in case of air these nanostructures are observed for fluences ranging from  $0.25 \text{ Jcm}^{-2}$  to  $2.5 \text{ Jcm}^{-2}$ . Under an ambient condition, the threshold for the appearance of nanohillocks has been found to be  $0.25 \text{ J.cm}^{-2}$ , which is higher than in UHV condition. It should be noted that the fluence values quoted here are the actual, measured energy densities at the 5mm away from focus point (the laser beam is de-focused). Therefore, low ablation threshold for UHV condition can be attributed to the rapid lateral heat diffusion or substantial increased energy absorption by air molecules.

After laser irradiation  $\text{CaF}_2$  crystal can decompose into metallic clusters on its surface, and in a near-surface layer. The formation of nanohillocks with a lateral extension of 50 nm can be attributed to laser-induced calcium colloid-formation. Colloid formation results from the aggregate of F-centers. Such small structures with lateral extension of 50 nm are also reported after electron irradiation on a  $\text{CaF}_2$  and are attributed to the formation of metallic clusters [101].

In order to compare a low fluence with moderate and high fluence regimes, results have also been presented with larger scan area ( $5 \mu\text{m} \times 5 \mu\text{m}$ ). Figure 3.4 presents 2D and the corresponding 3D-AFM topographic images (scan area  $5 \mu\text{m} \times 5 \mu\text{m}$ ) of a  $\text{CaF}_2$ . Figure 3.4 show an unexposed target surface (a & d), exposed for single shot at a lower laser fluence of

0.25 J.cm<sup>-2</sup> with the appearance of nanohillocks (b & e) and for a fluence of 0.5 J.cm<sup>-2</sup> with a single shot irradiation, where the appearance of nanohillocks is almost vanished with the formation of bumps (c & f).

Another important feature observed in the lower fluence regime is the formation of nanoripples. A detailed view of nanoripples (scan area 500 nm×500 nm) appearing on a CaF<sub>2</sub> surface after its exposure to a laser fluence of 0.5 J.cm<sup>-2</sup> with single shot irradiation is shown in figure 3.5 (a) (an enlarged view of figure 3.4(c)). This fluence is slightly higher than the ablation threshold, a fluence regime where nanohillock formation due to CE is already negligible and bump formation starts due to plasma formation (UFM). Two kinds of features are apparent simultaneously. In addition to isolated bumps, the appearance of nanoripples on the entire surface is also evident. The average periodicity of 70±5 nm and an average height of 1nm have been evaluated from the section profile in figure 3.5 (b).

Regarding laser induced periodic surface structures (LIPSS), it has been observed that this kind of structures has been observed at a fluence slightly higher than threshold. This femtosecond laser-induced-surface-ripple-generation is attributed to self-organized instabilities [72]. The dependence for direction of nanoripples (either parallel or perpendicular to laser polarization) has not been accounted for in our measurements. However, it is reported by other groups [72, 102] that the polarization-dependent ripple-formation takes place only long after the end of the laser pulse because a material anisotropy and diffusion processes at the target surface memorize the laser electric field [103].

The formation of periodic structures can be attributed to the excitation of Surface Plasmon Polaritons (SPP) to induce the periodic enhancement of local fields in the surface layer. SPPs result from the coherent interaction of the incident laser field with free electrons created in the material [104]. With this irradiation condition, in an ultra-short time scale, abundant electrons are excited and high density plasmas are produced, which will change the surface physical properties significantly (especially optical properties). Such change in optical properties will, in turn, intensively affect the laser-matter interactions by modulating the electromagnetic intensity distribution, inducing localized strong fields. The occurrence of CE is dependent on the local charge density in an ultrashort time scale. The condition of fs timescale and enhancement of localized strong field can induce CE as a result of exciting plentiful localized transient charges, which are responsible for the nonthermal ultrafast laser ablation mechanism [33].

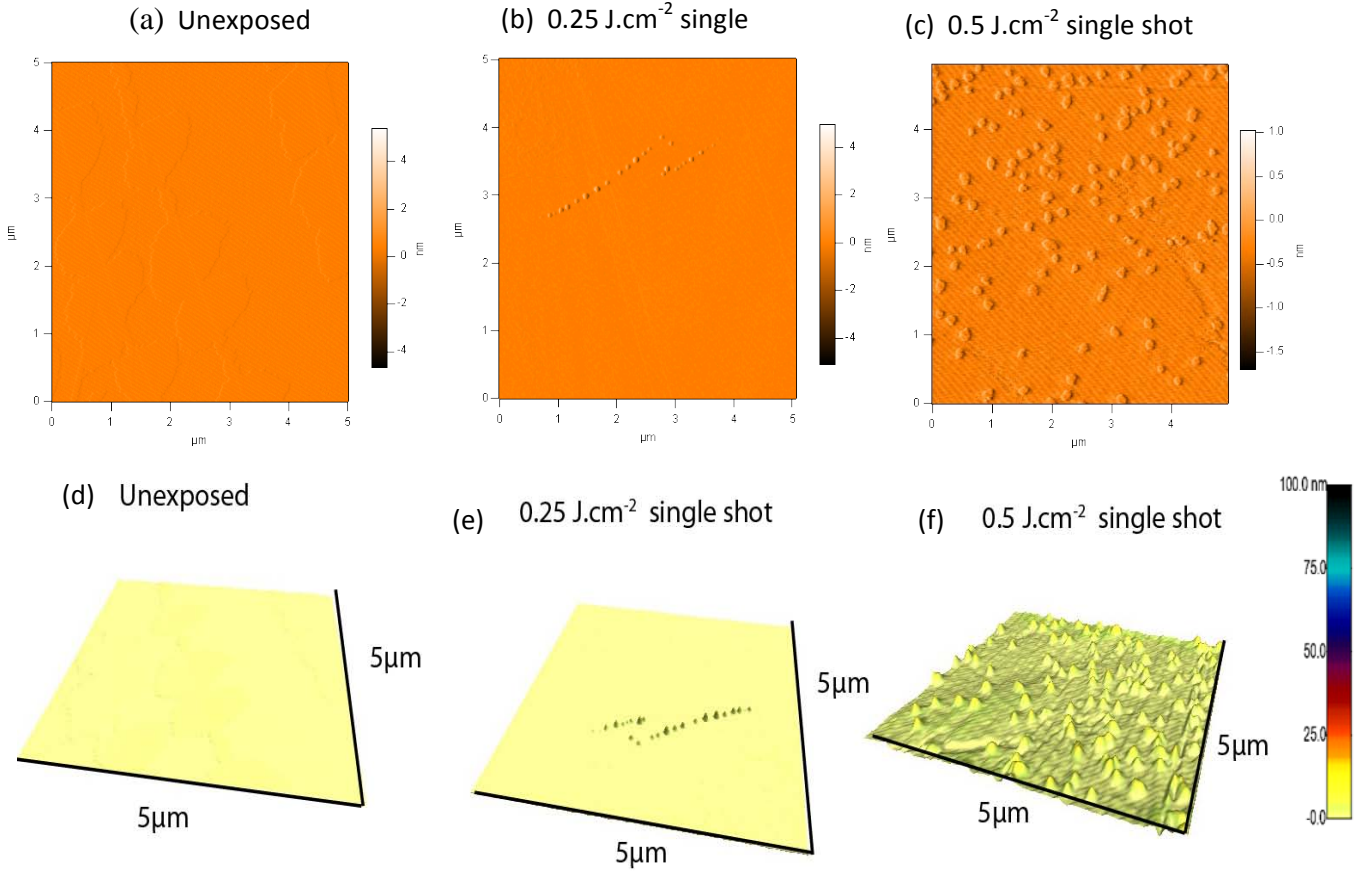


Figure 3.4: 2D and corresponding 3D-AFM topographic images (scan area  $5\mu\text{m}\times 5\mu\text{m}$ ) for a lower fluence (around the ablation threshold) modification regime of  $\text{CaF}_2$  produced as a result of different applied laser fluences under UHV condition (a) unexposed (b)  $0.25\text{ J.cm}^{-2}$  single shot, nanohillocks (c)  $0.5\text{ J.cm}^{-2}$  single shot, nanohillocks almost vanished and bumps-formation starts with surface ripples.

Ultrashort laser pulses can induce morphological features on the nanometer scale at the surfaces of various targets. These nanostructures much smaller than  $\lambda$  allow the incident  $E$ -field to coherently couple with the collective oscillations of free electrons to excite SPPs in the surface layer. The SPP will initiate the nanoscale ablation [105]. Once the ablation is locally induced, self-organized structures of nanometer periodicity are created on the surface. Since the field enhancement should be larger in narrower spaces and valleys, subsequent laser pulses are able to extend the length of ablation traces to combine [104]. In a theoretical work dealing with optical breakdown of dielectrics, it is reported [106] that a coherent plasma oscillation persists for tens of femtosecond, which may be useful to understand the dynamic process of laser-induced plasma and to get some clues for the origin of nanogratings.

These periodic structures are attributed to an inhomogeneous distribution of energy on the surface due to interaction between the incident light and surface scattered waves or radiation remnant field structures. Thus, in response to spatial modulation of the energy, the modulated modifications on the surface of the materials are formed. The question is how the modulated

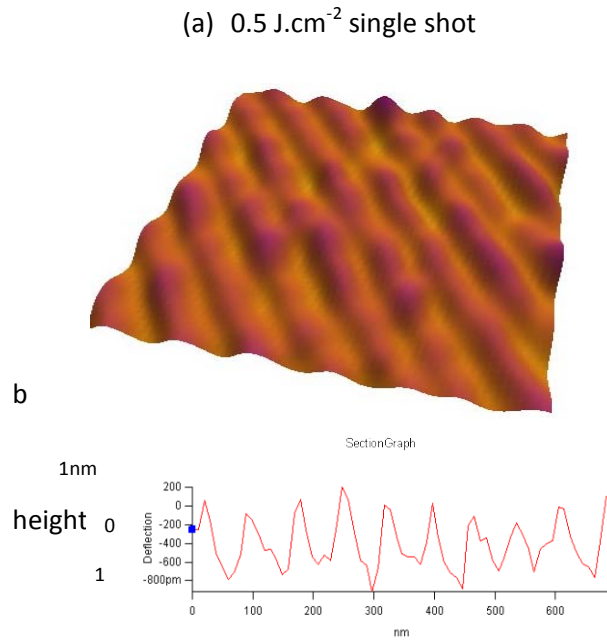


Figure 3.5: A detailed view of nanoripples (scan area  $500\text{nm} \times 500\text{nm}$ ) appearing on a  $\text{CaF}_2$  surface after its exposure to a laser fluence of  $0.5 \text{ J.cm}^{-2}$  single shot (b) Corresponding section-profile.

irradiance is physically transformed into a persisting variation of surface geometry. The basic sequence is that the material melts, undergoes deformation and finally re-solidifies making the deformation permanent. This surface deformations or irregularities act to scatter a small amount of light from the incident laser beam. This scattered light may propagate as a surface wave above or within the irradiated material and interferes with the incident beam producing an intensity distribution across the surface. The intensity distribution acts as a diffraction grating, scattering additional light into the surface wave, therefore creating a positive feedback effect [107].

An alternative explanation for nanogratings can also arise from local field enhancements that occur during inhomogeneous breakdown in dielectric materials [90]. This is based on ideas arising from nanoplasmonics. The existence of nanogratings that develop over many laser shots requires that there is a memory in the material that can feed back to the breakdown. Such a memory could arise from metastable color centers or permanent changes in electronic structure. The internal electric field inside an under dense plasma exceeds the laser field. This enhances the local nature of the breakdown. There is positive feedback since the rate of plasma formation increases as the density increases. Shot to shot memory allows the feedback to work over many pulses. Thus nanoplasmas may grow even from thermal noise. It is possible that the breakdown is inhomogeneous even on the first shot for two reasons. Natural inhomogeneties in the dielectric such as color centers and defects might form nucleation

centers for nanoplasmas. In addition, the multiphoton and avalanche ionization model could form highly inhomogeneous plasmas [90]. Intense fs laser pulses will excite dense plasma on the sample surface, and change rapidly the lattice structure. The orientation of the surface structure was found to change during the interaction between fs laser and irradiated targets. Thus, the periodic nanostructure is not sensitive to the initial crystal orientation.

### ***(b) Moderate fluence regime***

Representative AFM results for a moderate fluence regime for increasing laser fluences under UHV condition are shown in figure 3.6 (for better illustration 2D and corresponding 3D graphs are shown in many cases). In this fluence regime, the characteristic nanohillocks become less and less obvious and the occurrence of larger bumps and explosions is the most prominent feature when targets were exposed to same fluence as in figure 3.4 ( $0.25 \text{ J.cm}^{-2}$  and  $0.5 \text{ J.cm}^{-2}$  respectively) but with 20 succeeding pulses ( see figure 3.6 a-d) . The lateral size of these bumps is typically in the range of  $500 \text{ nm}$ - $1 \mu\text{m}$  with an average height of  $50 \text{ nm}$ . The image in figure 3.6 (a) reveals appearance of bumps having an average height of  $80 \text{ nm}$ . When a  $\text{CaF}_2$  is exposed to a fluence of  $0.5 \text{ J.cm}^{-2}$  for 20 shots both bumps and explosions are clearly seen in figure 3.6 (b and d). The height of bumps is reduced to  $50 \text{ nm}$  as the major part of laser energy is consumed for direct removal of material by evaporation resulting in nanocrater-formation (explosions) along bumps.

Figure 3.7 (a-b) shows 3-D AFM images (each representing a  $20 \mu\text{m} \times 20 \mu\text{m}$  area,  $150 \text{ nm}$  height) of  $\text{CaF}_2$  irradiated in air with single shot exposure at two different laser fluences i.e. (a)  $1 \text{ J/cm}^2$  single shot (b)  $1.5 \text{ J/cm}^2$  single shot (c)  $1 \text{ J/cm}^2$  20 shots (d)  $1.5 \text{ J/cm}^2$  20 shots. These images illustrate that at moderate fluences (slightly higher than ablation threshold) both nanohillocks and bumps are present. This can be attributed to the fact that particle emission due to both nonthermal processes (Coulomb Explosion and Ultrafast Melting) is superimposed. Furthermore, it becomes clear, that the appearance of bumps strongly depends on the laser fluence. The number, diameter and height of bumps increase with increasing laser fluence.

The second important feature evident in figure 3.7 is caused by applying several lasers shots to the same spot. At  $1 \text{ J/cm}^2$  (Figure 3.7 c) fluence, the area around the bump created by the first shot is modified and finally, at higher laser fluences material in the center of the bump is removed resulting in typical craters (figure 3.7 c). In the following we call these features as explosions. They appear when  $\text{CaF}_2$  is irradiated with 20 shots for same fluences as in (figure 3.7 a and 3.7 b). In particular, it seems justified to interpret the feature in figure 3.7 (c) as the

onset of the explosions (laser fluence of  $1 \text{ J/cm}^2$ ), whereas in figure 3.7 (d), the situation at a laser fluence of  $1.5 \text{ J/cm}^2$  is shown after 20 shots. Figure 3.8 shows an enlarged view ( $4 \mu\text{m} \times 4 \mu\text{m}$ ) of the figure 3.7 (c). A deflection trace (Figure 3.8 a), 3D-image (3.8 b) and the corresponding cross-section profile (3.8 c) are shown. The affected zone is characterized by a diameter of  $3 \mu\text{m}$  and a typical height of  $1 \text{ nm}$  with respect to the unexposed surface. A bump of diameter  $450 \text{ nm}$  and height  $40 \text{ nm}$  is clearly seen in this affected region. This bump appears to be ruptured at the centre with a dip of diameter  $60 \text{ nm}$  and depth of  $1 \text{ nm}$  as can clearly be seen from line profile in figure 3.8 (c).

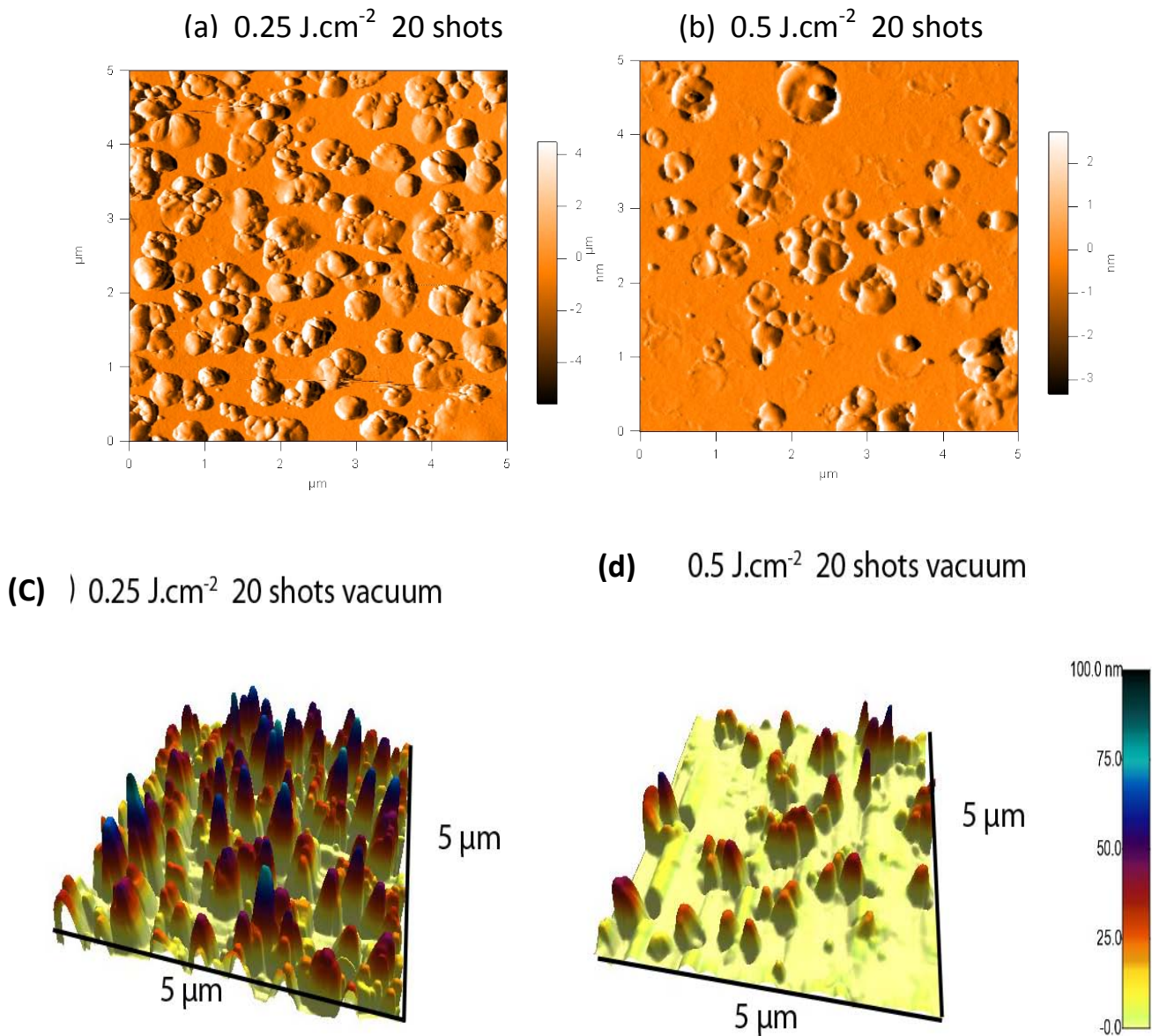


Figure 3.6: 2D and corresponding 3D-AFM topographic images of  $\text{CaF}_2$  (scan area  $5 \mu\text{m} \times 5 \mu\text{m}$ ) as a result of two different applied laser fluences in a moderate fluence (slightly higher than the ablation threshold) regime under UHV condition (a and c)  $0.25 \text{ J.cm}^{-2}$  20 shots, bump-formation (b and d)  $0.5 \text{ J.cm}^{-2}$  20 shots, bumps and explosions (nanocraters).



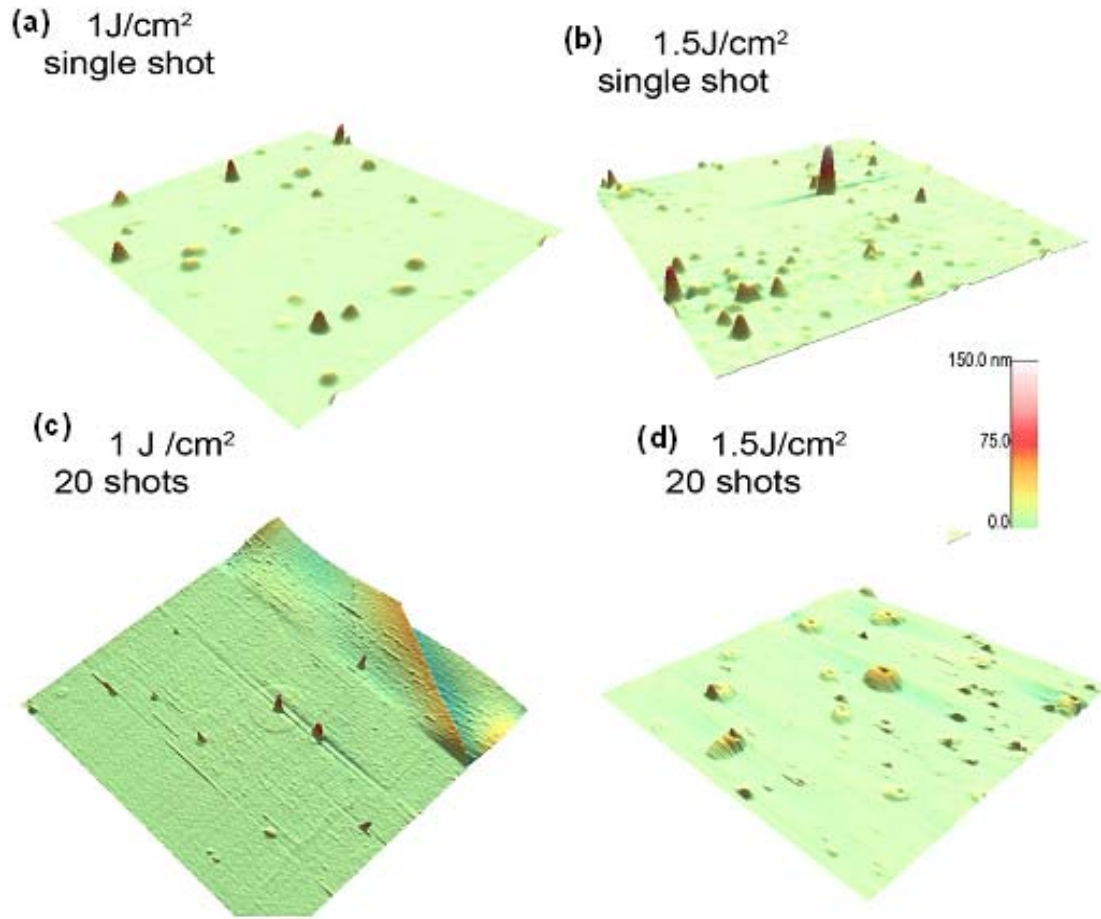


Figure 3.7: AFM surface topography of a  $\text{CaF}_2$  ( $20\text{ }\mu\text{m}\times 20\text{ }\mu\text{m}$ ) irradiated with 25 fs laser pulses in air for increasing fluences (a)  $1\text{ J}/\text{cm}^2$  single shot (b)  $1.5\text{ J}/\text{cm}^2$  single shot (c)  $1\text{ J}/\text{cm}^2$  20 shots (d)  $1.5\text{ J}/\text{cm}^2$  20 shots.

Further increase in the fluence up to  $1.5\text{ J}/\text{cm}^2$  results in the explosive removal of material. Figure 3.9 (b) shows a 3D image ( $12\text{ }\mu\text{m}\times 12\text{ }\mu\text{m}\times 50\text{ nm}$ ) of the explosions in the final stage. The corresponding deflection trace and cross-section are shown in figure 3.9 (a) and 3.9 (c), respectively. Explosions with two characteristic sizes can be identified in the figure: (i) larger protrusions of an average diameter  $3\text{ }\mu\text{m}$  and a height 30-40 nm with central cavities of diameter 700-800 nm and depth in the range of 20-30 nm. (ii) smaller protrusions with a typical diameter 800 nm-1  $\mu\text{m}$  and 5-20 nm of height, characterized by nanocavities of diameter 200-400 nm and depth 1-10 nm (figure 3.9 c). Figure 3.9 (e) is an enlarged 3D-image ( $4\text{ }\mu\text{m}\times 4\text{ }\mu\text{m}\times 25\text{ nm}$ ) exhibiting one of explosions from figure 3.9 (b). Figure 3.9 (d) is its corresponding deflection trace. This micro protrusion has a diameter of about  $2\text{ }\mu\text{m}$  and a height of 40 nm. In the center of the protrusion material is popped off and creates a



$$F=1\text{J/cm}^2$$

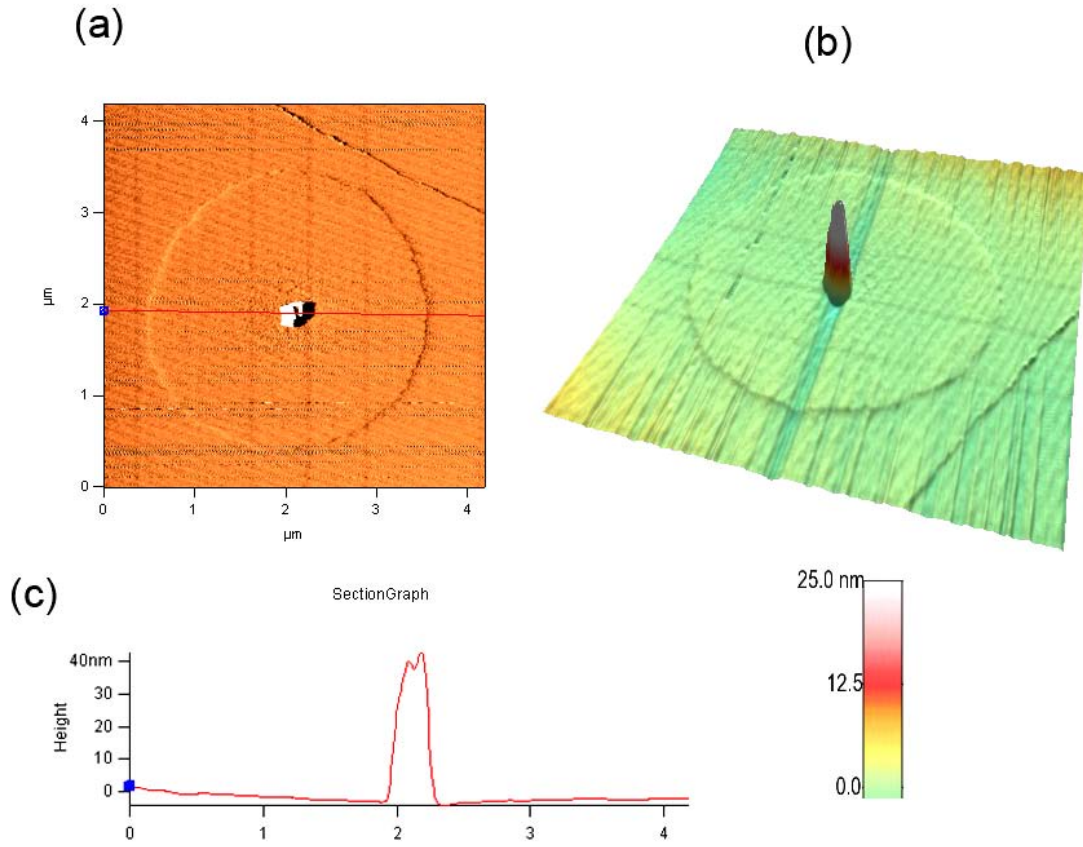


Figure 3.8: AFM surface topography of  $\text{CaF}_2$  ( $4\mu\text{m}\times 4\mu\text{m}$ ) irradiated with 20 shots of fs laser at a fluence of  $1\text{ J/cm}^2$  in air (a) Deflection trace (b) 3-D image (c) Line profile.

nanocavity of  $700\text{ nm}$  diameter with  $25\text{ nm}$  depth (figure 3.9 f). After the laser irradiation, the single crystal  $\text{CaF}_2$  can decompose and some of fluorine can diffuse out from exposed area and can migrate out to form  $\text{F}_2$  bubbles at the adjacent area. These bubbles which are produced by fluorine diffusion process into the bulk leads to the development of a high internal pressure, which yield a surface deformation in the form of a micron-sized surface elevations in the scanning force microscopy images and is very much similar to a low-energy electron induced decomposition processes of  $\text{CaF}_2$  [101]. Therefore the irradiation on the  $\text{CaF}_2$  crystal not only creates color centers, but also generates tiny  $\text{F}_2$  bubbles at locations with and without structural defects. Those bubbles can move inside the crystal and have the tendency to stick on structural defects and can generate larger bumps at the irradiated surface and can also appear in the form of a bulged  $\text{CaF}_2$  surface (figure 3.6 & 3.9).

In the moderate fluence regime the appearance of bumps or larger structures (lateral dimensions of greater than  $100\text{ nm}$ ) can be attributed to either ultrafast melting (plasma formation taking place on a time regime of hundreds of fs) or to the development of surface

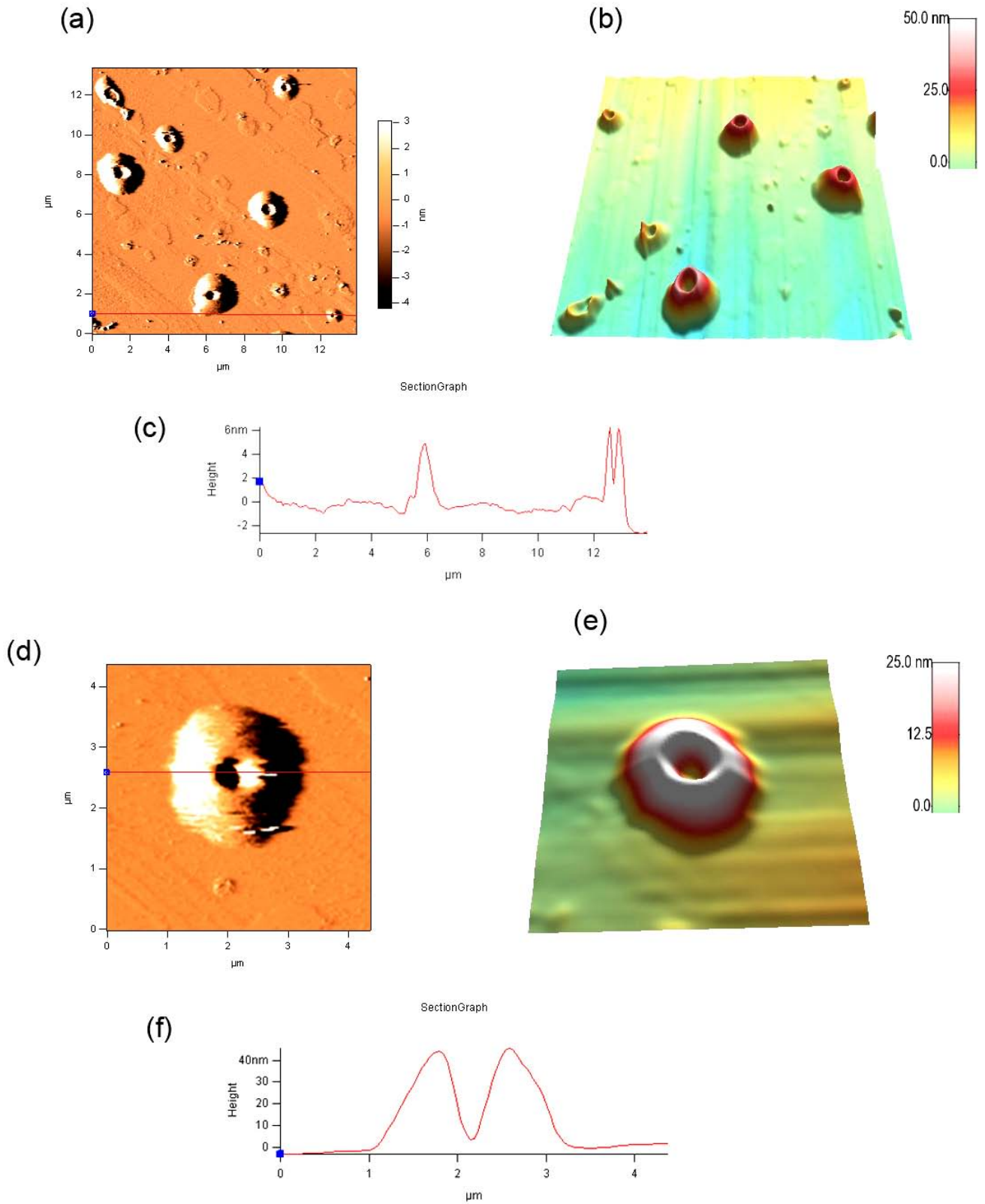


Figure 3.9: AFM surface topography of  $\text{CaF}_2$  irradiated with 20 shots of fs laser in air at a fluence of  $1.5 \text{ J/cm}^2$  (a) Deflection trace ( $12\mu\text{m} \times 12\mu\text{m}$ ) (b) 3-D image ( $12\mu\text{m} \times 12\mu\text{m}$ ) (c) Line profile ( $12\mu\text{m} \times 12\mu\text{m}$ ) (d) Deflection trace ( $4\mu\text{m} \times 4\mu\text{m}$ ) (e) 3-D image ( $4\mu\text{m} \times 4\mu\text{m}$ ) (f) Line profile ( $4\mu\text{m} \times 4\mu\text{m}$ ).

tension and diffusion [24] (See figures 3.6 -3.9). If there is a modulation in the height of these bumps, then desorption from this modulated surface will not be homogeneous: an ion sitting in a valley will encounter more charged neighbors than an ion on a crest, resulting in a correspondingly higher desorption probability. Thus, the desorption process starts to amplify the modulation by preferentially deepening the “valleys”. On the other hand, an atomic self-diffusion tends to smooth the surface by filling the valleys with diffused crest-atoms. Hence, in the unstable layer the particle on the crest will feel a higher surface tension than in the valley, the general tendency being to pull the particles downhill and equilibrate the surface spacing. This situation is close to well-known hydrodynamic instabilities [11].

It is evident from our observations that localized and isolated defects observed in a  $\text{CaF}_2$  at a low fluence from  $0.06\text{-}1.5\text{ J.cm}^{-2}$  for single pulse irradiation can be regarded as a consequence of charging of defects due to Coulomb explosion (gentle ablation) whereas larger defects (bumps) observed for multiple-pulse irradiation (20 succeeding pulses in our case) can be attributed to plasma formation, diffusion, aggregation and stress distribution processes. After the first pulse, subsequent pulses are incident on a material with potentially modified chemical, structural, and optical properties. The modification threshold fluence decreases with increasing number of pulses, and has been reported for various crystalline materials [108, 109] and is called incubation effect. In dielectric materials this effects is greatly influenced by the excitation and generation of conduction-band electrons, which eventually leads to an accumulation of defect sites. The multi-photon excitation will lead to a production of electron-hole pairs on a sub-100-fs time scale. These states typically have a lifetime between 150 fs and several ps before forming self-trapped exctions and Frenckle pairs [110]. A small fraction of these Frenckle pairs may not recombine and stabilize to F centers, introducing additional energy levels and excitation routes for the next laser shot [110].

The different sizes of protrusions can be explained on the basis of marked differences in the energy deposition and the material ejection mechanism. During an expansion of laser-induced vapor/plasma, the density of vapor phase species is significantly non-uniform due to the plasma composition and various processes involved such as absorption of laser radiation, ultrafast melting, ionization, recombination, condensation and clustering. At the early stage a single atom is sputtered. This single atom diffuses by interstitial paths whereas two atoms attract each other and form a stable dimer, which can push further atoms off from their original lattice sites and occupies the vacancy. This dimer has ability to attach another atom to form a trimer causing lattice deformation. Consequently, there is occurrence of variation in the rate of nucleation and growth of clusters (dimers, trimers etc). This variation marks a

significant difference in the sizes of bumps, which are discrete localized aggregates of atoms (agglomerates), which cannot escape from the surface and are frozen in place in the form of protrusions. Other significant differences arise in considering optical reflection coefficients, momentum transfer from plasma ions and existence of a fluence threshold for optical vaporization.

The formation of bumps can also be caused by a local volume increase due to buildup of stresses [16, 89] by fast laser heating. The relaxation of these compressive stresses, diffusion, transformation and aggregation of primary defects can be responsible for the formation of these micro-bumps [16]. Strong electron temperature gradients established in the radial direction following the initial localized laser energy deposition result in a fast cooling of electrons and the lattice. If such a strong under-cooling takes place, a rapid solidification of the surface results in bump-formation.

A substantial work is reported on the development of thermal stresses in transparent materials [111-113] by laser irradiation. However, no work is reported in which thermal stresses can be considered as the major cause of bumps formation in transparent materials. The possible reason for considering thermo elastic stresses as a major cause for bump formation is that in literature it is reported that the sudden laser heating of the target can induce the generation and propagation of a thermo elastic wave [113]. This phenomenon is more prominent when the laser pulse duration is smaller than or of the order of the characteristic time for a stress wave to propagate across the heated volume [111]. In femtosecond optical breakdown, the laser pulse duration (25fs in our case) and time for thermalization of the energy of the free electrons (thermalization times typically in the 10–500 fs range [14, 29]) are much shorter than the acoustic transit time from the center of the focus to its periphery. The characteristic propagation time of the stress wave through the heated volume is defined as  $t_m = 1/(\alpha_{\text{eff}}c_s)$  [113] where  $\alpha_{\text{eff}}$  is the effective absorption coefficient and  $c_s$  the sound propagation velocity = 1600 m/s [114]. Thus, the condition for confinement of thermo elastic stresses  $t_p/t_m < 1$ , with  $t_p$  the pulse duration, is established, indicating that photomechanical effects play an important role in the modification of materials [113].

The features in figures 3.7 (c & d), 3.8 and 3.9 are typical features observed only for transparent materials ( $\text{CaF}_2$ ) after exposure to ultrashort pulses in air. Femtosecond laser pulses which are non-linearly absorbed in the focal volume by the dielectric can lead to permanent changes in the material as seen in figures 3.7 (d) and 3.8. These permanent changes can be attributed to changes of the refractive index [115] after stress-induced densification [112] due to the high pressures generated in the focal region. The absorbed

energy of femtosecond laser radiation within the skin depth of the ionized volume generates pressures, which in turn, generates shock waves [116, 117]. The distance at which the shock front effectively stops defines the shock-affected volume [116, 117]. This stopping distance,  $r_{\text{stop}}$ , can be estimated from the condition that the internal energy in the volume inside the shock front is comparable to the absorbed pulse energy. The radius of a shock-affected region,  $r_{\text{sh}}$ , is given by [116, 118]

$$r_{sh} = \sqrt[3]{\frac{E_{abs}}{4\pi Y/3}} \quad 3.10$$

Where,  $E_{\text{abs}}$  is the absorbed energy and  $Y$  is the Young modulus. By substituting the values of absorbed energies and Young modulus of  $\text{CaF}_2$  (75.86 GPa) the diameter of the shock-affected region turns out to be 2-7  $\mu\text{m}$ . As the value of shock affected zone deduced from the AFM measurement is 3  $\mu\text{m}$  (in diameter) and lies within the range of calculated value, therefore, can be identified as the shock affected region. When the material is irradiated with multiple femtosecond laser pulses, the nonlinear absorption is enhanced due a refractive index change [115, 119] (induced by first few i.e. one or two laser pulses) and leads to explosion-type features in the irradiated target. It is a well known fact, that the first few (one or two) pulses of a laser can induce stress distributions [112], structural changes [120], densification [121], bond breaking [111], bumps formation [122] and local melting in transparent materials. All these phenomena are responsible for a change in the refractive index [123] of the irradiated material. Easily ionized defect states, surface states and broken bonds can also cause optical breakdown [124] and enhanced laser absorption of the subsequent laser pulses. Nonlinear absorption of the laser energy by the material through multi-photon [63] and avalanche [43] photoionization process, resulting in optical breakdown and the formation of a high-density plasma. This hot plasma explosively expands into the surrounding material [124] with a velocity exceeding the speed of sound [125]. An explosion occurs inside the material and results in a permanently damaged region (popped off see figure 3.8d and 3.9). This explosion triggers shock and rarefaction waves [126]. This shock wave becomes an acoustic wave for a large propagation radius, while the rarefaction (compression) wave expands which produces central, low density region, i.e. the cavity [127]. At higher fluences ( $>1.5 \text{ J.cm}^{-2}$ ) the evidence of such micro explosions is less visible, but a large number of bumps with higher diameters and heights develop. This can be caused by the fact, that during the explosion, the phase of relaxation is less effective and shock-liquidized material refills the cavities initially formed by explosion [118]. It is also speculated [128] that the effect of shock wave may lead to migration of a part of the atoms and may result in the disappearance of some dislocations.

As discussed earlier, that for ultrashort laser radiation [111, 113] no acoustic relaxation is possible during the thermalization time. Therefore, thermo-elastic stresses caused by the temperature rise stay confined in the focal volume, which result into a maximum pressure rise. This maximum pressure rise and the deposited energy (eV/atom) can be calculated by considering the volumetric energy absorbed, the focal volume and the skin depth [117, 118]. The graph in figure 3.10 shows the calculated value of the energy deposited (eV/atom) and the corresponding pressure caused (GPa) at different laser fluences for CaF<sub>2</sub>, both for single and 20 shot exposure. Since both, the pressure and the deposited energy increase linearly with

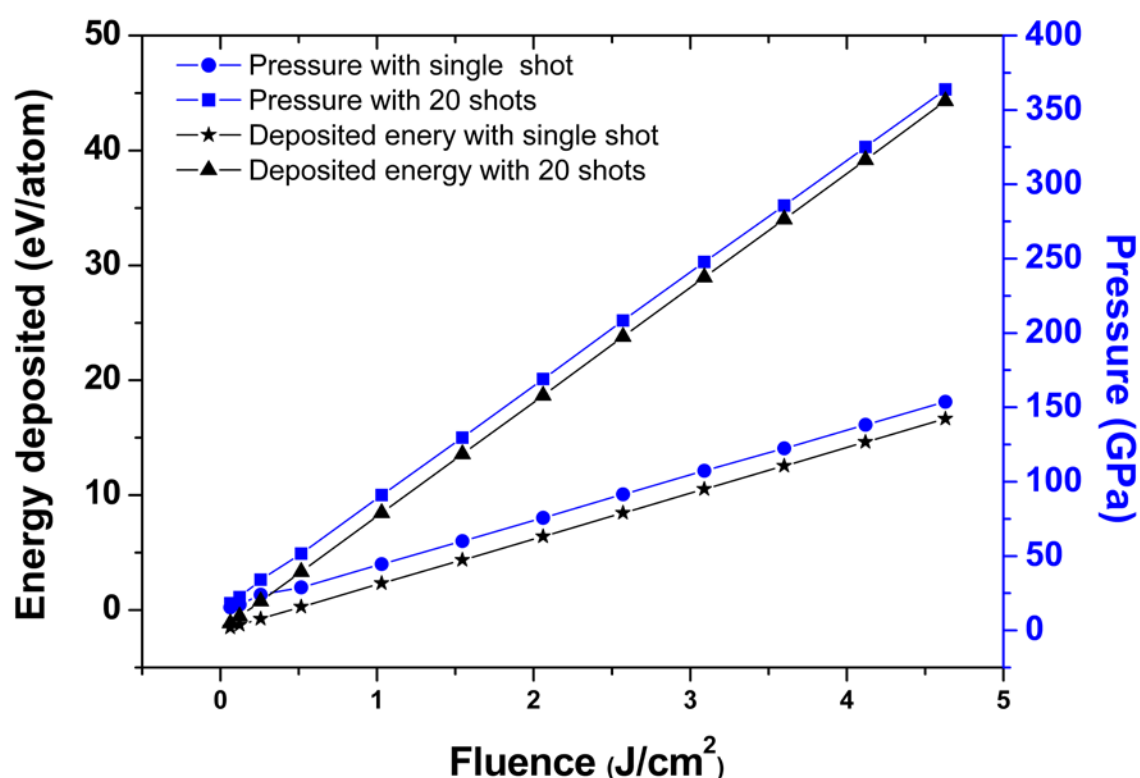


Figure 3.10: Energy deposited (eV/atom) and developed pressure (GPa) Vs different laser fluences for single and 20 shots irradiated CaF<sub>2</sub>.

laser fluence, the pressure for single pulses reaches values of 30 and 50 GPa at laser fluences of 1 J/cm<sup>2</sup> and 1.5 J/cm<sup>2</sup> respectively, which are smaller than the Young modulus of CaF<sub>2</sub>. From our experimental observations it can be concluded that the pressure reached with one pulse on the other hand, is sufficient to produce bumps at the surface. For 20 succeeding pulses the pressure increases (due to more laser energy absorption) up to 120 GPa at laser fluences of 1.5 J/cm<sup>2</sup>. This pressure is capable of producing bumps (figure 3.7 c) as well as

explosions resulting in the characteristic nanocavities shown in figure 3.7 d. The formation of a nanocavities due to rupturing of material are observed when the absorbed energy density (i.e. the pressure  $J/m^3 = N/m^2 \equiv Pa$ ) exceeds the Young modulus (75.79GPa) of  $CaF_2$  [117] (see figures 3.8 a-d).

Femtosecond laser induced bumps are formed on a bulk  $CaF_2$  when irradiated with either single or multiple shots for some appropriate incident laser fluences. Compressive stresses induced by laser heating are responsible for formation of these bumps. Multiple femtosecond laser pulses due to no-linear absorption result in an explosive expansion of the ionized material by forming nanocavities (permanently popped off material) at the central top of the bumps. These typical features are called explosions and have been reported at a laser fluence of  $1.5 Jcm^{-2}$  with 20 overlapping pulses. The pressure at this fluence (120 GPa) is much higher than the Young's modulus of  $CaF_2$  (75GPa). At lower fluences ( $<1.5 Jcm^{-2}$ ), explosions were not observed, because the pressure values were not sufficient to rupture the surface. Explosions are due to high-density plasma generated shock and rarefaction waves which expand explosively into the surrounding materials.

### ***(c) High fluence regime***

Further increase of the input laser fluence to the regime of approximately  $1.5 J.cm^{-2}$  to  $8 J.cm^{-2}$  (a fluence significantly higher than the threshold) resulted in footprints of ablation corresponding to thermal ablation regime with an appearance of microstructures and is shown in figure 3.11. The highly disturbed crystalline surface can be seen in the surface topographic image of figure 3.11 (a &b) after its exposure to a fluence of  $1.5 J.cm^{-2}$  for 20 shots. Due to thermal processes and melting, nonsymmetrical and exploded bumps, swelling and bulges at the ablated surface are observed. An appearance of very huge hump (protrusion) with an aggregation of large amount of material of a typical diameter of  $5 \mu m$  is encountered in figure 3.11 (c-e) representing enhanced thermal processes at a fluence of  $3.5 J.cm^{-2}$ . At the periphery of this hump, where the laser fluence is smaller than the centre due to Gaussian



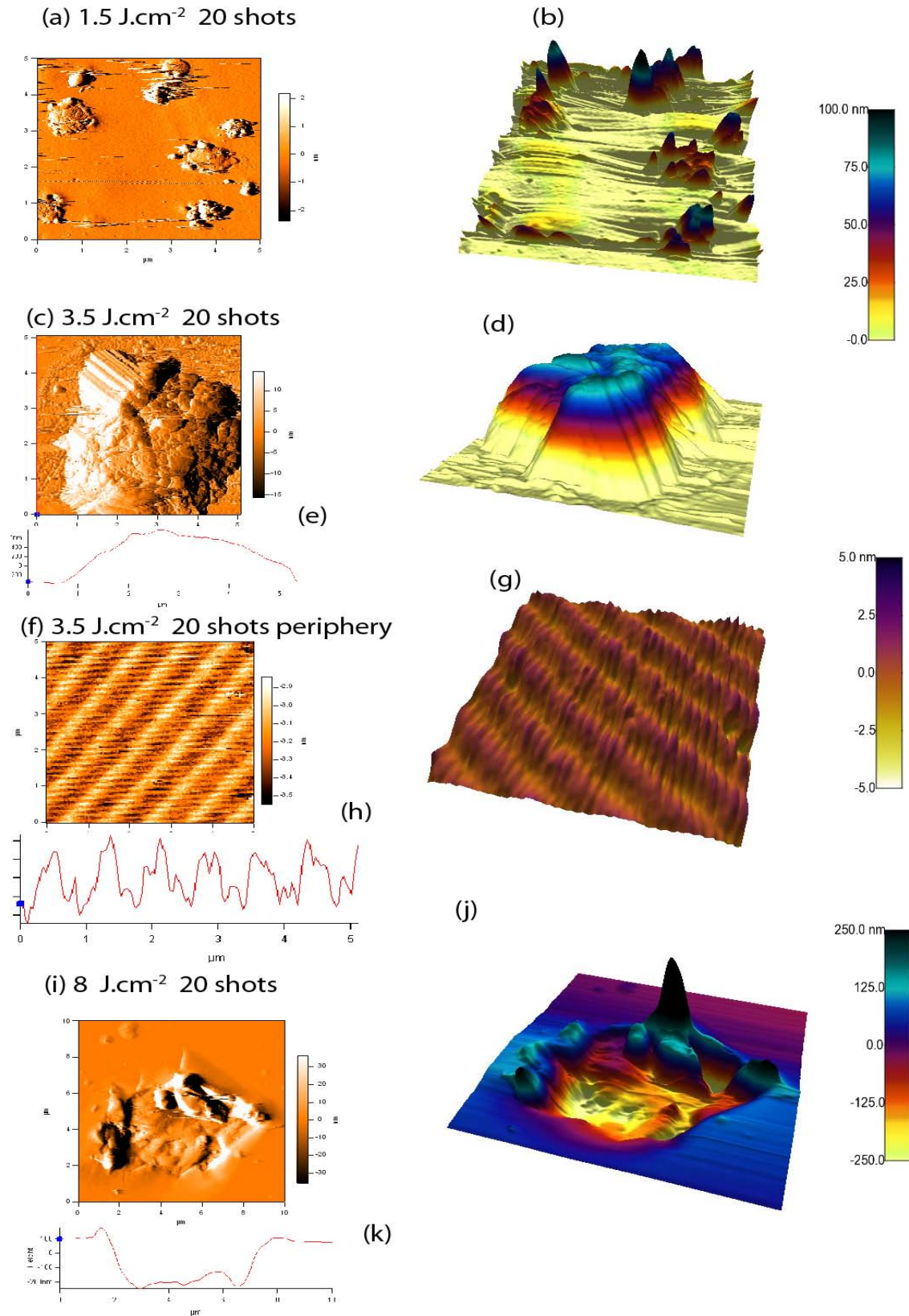


Figure 3.11: 2D and corresponding 3D-AFM topographic images of  $\text{CaF}_2$  as a result of different applied laser fluences in a high fluence (significantly higher than the ablation threshold) regime under UHV condition (a and b)  $1.5 \text{ J.cm}^{-2}$  20 shots, Bumps, explosions and swelling (c, d and e)  $3.5 \text{ J.cm}^{-2}$  20 shots, huge hump (f, g, h) Ripples formation (i, j and k)  $8 \text{ J.cm}^{-2}$  20 shots, a huge crater.



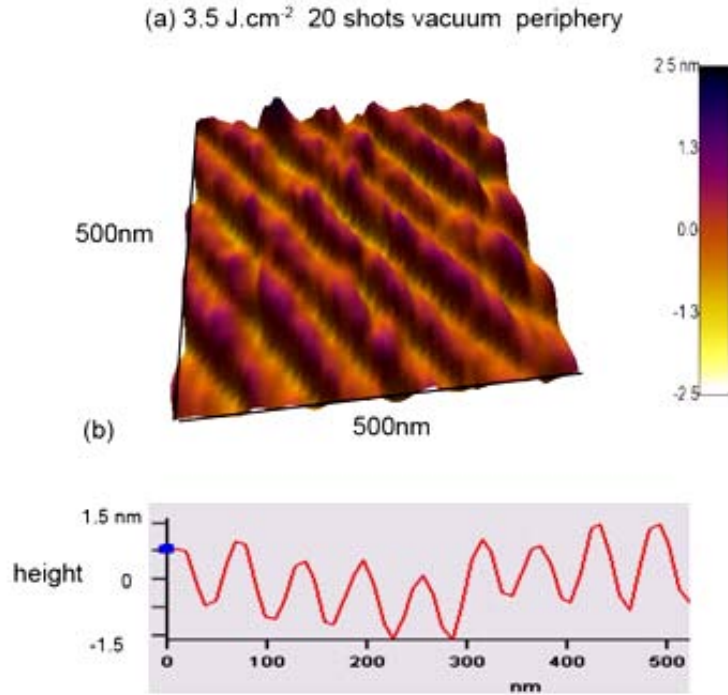


Figure 3.12: A detailed view of nanoripples (scan area 500 nm×500 nm) appearing on a CaF<sub>2</sub> surface after its exposure to a laser fluence of 3.5 J.cm<sup>-2</sup> (20 shots) at the periphery of ablated area (b) section-profile of (a).

beam distribution, laser induced periodic surface structures are formed (figure 3.11 (f-g) with its corresponding cross-section- profile (figure 3.11h). Two kinds of LIPSS are observed: bigger ones with an average periodicity of  $625 \pm 10$  nm and with an average height of 2nm and smaller ripples on the top of bigger ones are perpendicularly aligned with an average spacing of 250 nm and of height 1nm. Due to appearance of these smaller ripples at the top of larger ripples, undulating behavior of cross-section profile is evidently observed in figure 3.11 (h). When the fluence was further increased to 8 J.cm<sup>-2</sup> as shown in figures 3.11 (i and j), an important feature which is frequently observed in conventional ablation, has been characterized by the formation of an extremely large crater with a typical diameter of 8  $\mu$ m and of a typical depth 300 nm. Its corresponding section profile is shown in figure 3.11 (k). This crater is representing a massive ejection of material due to enhanced and vigorous thermal processes after melting and evaporation.

A detailed view of nanoripples (scan area 500 nm×500 nm) appearing on a CaF<sub>2</sub> surface after its exposure to a laser fluence significantly higher than ablation threshold is shown in figure 3.12. It is important to note that such kind of nanoripples (in case of higher fluence regime) are only observed at the outskirts of the ablated area (the more detailed view of figure 3.11(f

and g) at a fluence of  $3.5 \text{ J.cm}^{-2}$  for 20 succeeding pulses) where the laser fluence due to Gaussian energy distribution is slightly higher than the ablation threshold. At the boundary (from more intense to less intense part of the laser spot), the observed features have been changed from a huge hump (figure 3.11 c-e) to ripples of periodicity 625 nm (figure 3.11 (f-g)). At an extreme outer edge of an ablated area, the periodic surface structures (figure 3.12) with an average periodicity of  $60 \pm 10 \text{ nm}$  with an average height of 1.5 nm have been observed (evaluated from cross-section figure 3.12b). These nanoripples are more or less similar to features observed in figure 3.5 (at a fluence slightly higher than ablation threshold).

### 3.2.2 Raman Spectroscopy

In order to characterize single- and multishot femtosecond laser ablation of  $\text{CaF}_2$ , Raman spectroscopy measurements have been performed with the primary intention to correlate the different structural and chemical changes (colloid formation, compressive stresses, appearance of new disordered bands for representing carbonates, calcium oxides,  $\text{F}^+$  and  $\text{H}^{-2}$  centers) with features observed on the irradiated surface by AFM measurements. The development of nanostructures for different laser fluences, for which the transition from electronic processes (nanoablation) to thermal processes takes place (characterized by an appearance of a more and more disturbed dielectric surface), can be compared to the results of a structural characterization performed by Raman spectroscopy.

Figure 3.13 shows Raman spectra of the pristine, single -and multi- pulse irradiated  $\text{CaF}_2$  for different laser fluences in ultra high vacuum. The strongest Raman band of  $\text{CaF}_2$  occurs at  $322 \text{ cm}^{-1}$  and represents its Raman active  $\text{T}_{2g}$  vibration mode in which the anion sublattice vibrates in antiphase and the cations are stationary [129, 130].

For a lower fluence regime ( $0.06\text{-}0.25 \text{ J.cm}^{-2}$ ) with single-pulse-irradiation, where nanohillocks on irradiated  $\text{CaF}_2$  are observed by AFM measurements and are ascribed to CE, the only detectable change observed in the Raman spectra is an enhanced Raman signal. This is attributed to enhanced surface roughness induced by laser radiation [131]. As the fluence increases, more F aggregates agglomerate yielding more Ca clusters which in turn cause pronounced phonon scattering for Raman probe wavelength. At a fluence of  $0.5 \text{ J.cm}^{-2}$  a Raman Shift of ( $4 \text{ cm}^{-1}$ ) from  $322 \text{ cm}^{-1}$  to  $318 \text{ cm}^{-1}$  is observed in the peak  $\text{T}_{2g}$ . This line shift is observed at a fluence where a transition from nanohillock-formation to bump-formation (due to ultrafast CE to ultrafast melting or plasma formation) takes place and signifies the stresses in the  $\text{CaF}_2$ , due to the presence of the calcium colloids [132] and can be interpreted as defect scattering induced by anion vacancies and interstitials [130]. Further increase in the

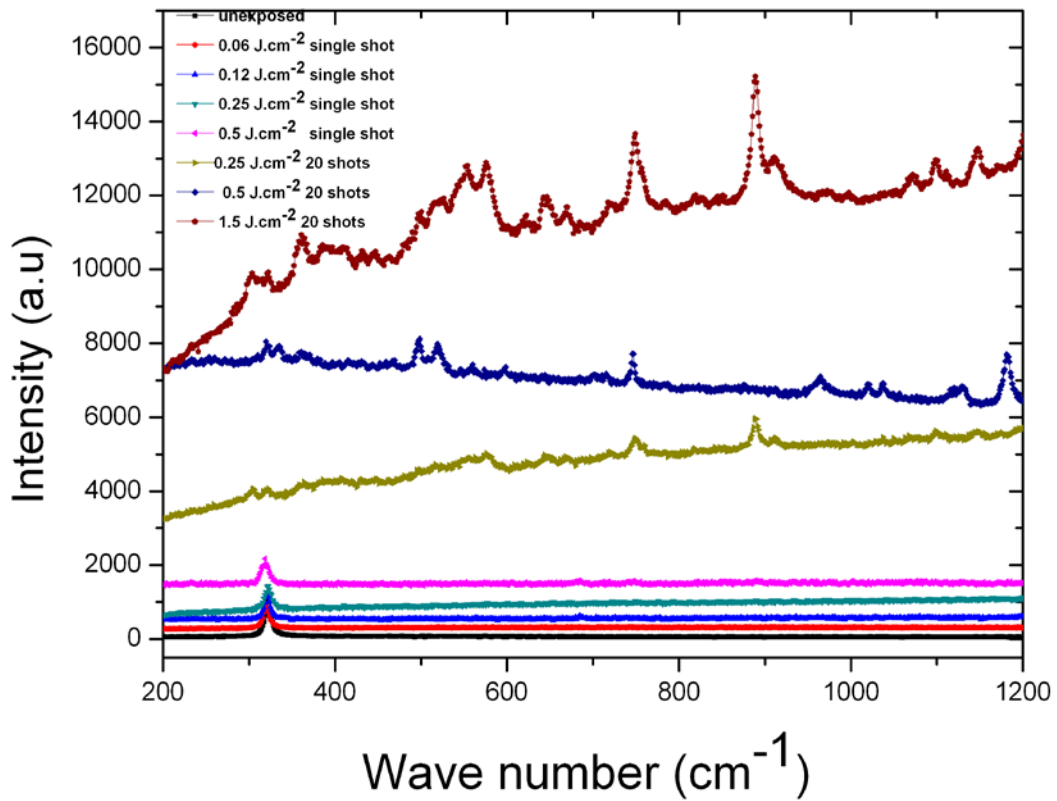
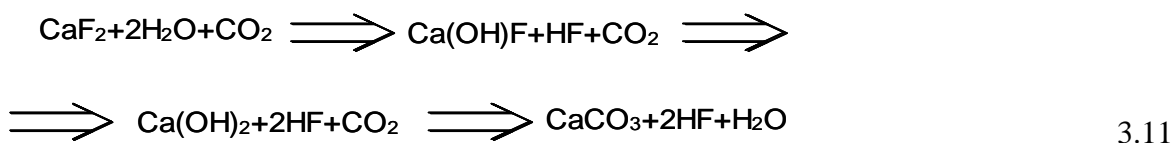


Figure 3.13 Raman spectra of the pristine, single and multipulse (20 shots) irradiated  $\text{CaF}_2$  in UHV for different fluences (a) pristine (b)  $0.06 \text{ J.cm}^{-2}$  single shot (c)  $0.12 \text{ J.cm}^{-2}$  single shot (d)  $0.25 \text{ J.cm}^{-2}$  single shot (e)  $0.5 \text{ J.cm}^{-2}$  single shot (f)  $0.25 \text{ J.cm}^{-2}$  20 shots (g)  $0.5 \text{ J.cm}^{-2}$  20 shots (h)  $1.5 \text{ J.cm}^{-2}$  20 shots.

laser fluence (or a laser doze) in terms of number of pulses (from  $0.25 \text{ J.cm}^{-2}$  to  $1.5 \text{ J.cm}^{-2}$  with 20 shots), it is observed that the intensity of this band reduces after exposure and splits up into two peaks. For a fluence of  $0.25 \text{ J.cm}^{-2}$  two closely spaced lines are identified at  $322 \text{ cm}^{-1}$  and  $304 \text{ cm}^{-1}$  (One original peak and one shifted peak to lower frequency). For a fluence of  $0.5 \text{ J.cm}^{-2}$  two lines at  $320 \text{ cm}^{-1}$  and  $334 \text{ cm}^{-1}$  have been identified. For a fluence of  $1.5 \text{ J.cm}^{-2}$  two lines at  $322 \text{ cm}^{-1}$  and  $338 \text{ cm}^{-1}$  (One original peak and one shifted peak to higher frequency) have been observed. Under compressive stresses the peak is shifted to higher frequency of Raman Spectrum, while for tensile stress the peak is shifted to lower frequency [77]. These two closely spaced lines are representing compressive and tensile stresses.

For fluences in the range of  $0.25$  to  $1.5 \text{ J.cm}^{-2}$  (for 20 pulses), additional peaks are identified indicating that the underlying material has accumulated a larger number of defect aggregates. For a fluence of  $1.5 \text{ J.cm}^{-2}$ , the intensity of these peaks is higher as compared to the peaks for fluences ranging from  $0.25$  to  $0.5 \text{ J.cm}^{-2}$ . This indicates a “strong” or thermal ablation as it is clear from the surface topography images in figure 3.11 (a & b) which present a highly

disturbed surface. Thus, from results obtained by the topographic images of figure 3.1-3.2, 3.6 and 3.7, in which the appearance of both nanohillocks and bumps is clear, one can easily visualize the decomposition of  $\text{CaF}_2$  into fluorine gas and calcium metal. Additional Raman peaks are assumed to be due to vibration modes from F-interstitials and vacancies, and are in well agreement with results reported previously [131, 133]. Additional peaks observed at  $364\text{ cm}^{-1}$ ,  $717\text{ cm}^{-1}$ ,  $888\text{ cm}^{-1}$  and  $1066\text{ cm}^{-1}$  were only found for targets irradiated in moderate and high fluence regimes and correspond to development of calcite (crystalline  $\text{CaCO}_3$ ) on the surface [134, 135]. These peaks are attributed to photochemical or photo thermal decomposition of  $\text{CaF}_2$  (equation 3.11). This process takes place mainly in the presence of water vapors, contaminants and defects which are induced by the laser elevated temperatures.



Ca from reaction 3.11 after mixing with  $\text{CO}_2$  and  $\text{H}_2\text{O}$  forms calcium carbonate  $\text{CaCO}_3$ . From the precipitation of  $\text{CaCO}_3$ , hydrated calcium carbonate (hexa and mono hydrate) is formed. This is indicated by an appearance of peaks at wavenumbers  $718\text{ cm}^{-1}$  and  $1066\text{ cm}^{-1}$  corresponding to the formation of  $\text{CaCO}_3$  hexahydrate ( $\text{CaCO}_3 \cdot 6\text{H}_2\text{O}$ ) and calcium carbonate monohydrate ( $\text{CaCO}_3 \cdot \text{H}_2\text{O}$ ), respectively [136].

Raman peaks ranging from  $400$  to  $600\text{ cm}^{-1}$  (appearing at  $497\text{ cm}^{-1}$ ,  $522\text{ cm}^{-1}$ ,  $554\text{ cm}^{-1}$ ,  $575\text{ cm}^{-1}$ ,  $597\text{ cm}^{-1}$  and  $622\text{ cm}^{-1}$  wavenumbers) can be attributed to  $\text{COO}^-$  vibration and are representing surfactants. These peaks correspond to lattice vibrational bands of F and  $\text{F}^+$  centers. These centers consist of a proton surrounded by either two or three electrons and occupy an oxygen vacancy. With two electrons in the vacancy, a region of local positive charge exists, which can act as traps for electrons photoexcited from F centers, resulting in  $\text{F}^+$  and  $\text{H}^-$  centers. The sharp and intense peak at  $1048\text{ cm}^{-1}$  corresponds to the localized vibrational mode of  $\text{H}_2$  ion in CaO [137].

The remaining peaks appearing at  $1110\text{ cm}^{-1}$ ,  $1147\text{ cm}^{-1}$  and  $1180\text{ cm}^{-1}$  can be attributed to monofluoro derivatives (C-F stretching) and C-O stretching modes [138].

This structural characterization clearly indicates that for the lower fluence regime (corresponding to nanohillock-like defect formation) only an enhanced surface roughness is observed. When the laser fluence is increased (in terms of multiple- pulse- irradiation) and a transition from nanohillocks to larger bumps and nanocraters occurs, additional peaks are identified. These additional Raman peaks appear due to diffusion, transformation and

aggregation of defects and can be regarded as typical features representing a transition from CE to UFM. The identification of enhanced intensity of these additional peaks appear where crystalline surface is totally disturbed (melting and evaporation) with an appearance of large bulges and swelling with a transition from electronic processes to thermal processes.

### 3.3 Results for Semiconductors (Si (111))

#### 3.3.1 AFM Measurements

##### *(a) Low fluence regime*

As a next step, the analogous development of the surface topography for Si has been investigated. In this case, the localization of the deposited energy is expected to be less stringent as compared to a non-conducting dielectric.

Surprisingly, the energy distribution of ejected particles and the pulse shape dependence for ultra-short-laser ablation have been found to be very similar [12, 13], implying the same mechanisms to work. As demonstrated in figure 3.14 and figure 3.15, this is also true for the surface topography, i.e. the appearance of nanohillocks on a Si surface around the ablation threshold (in a low fluence regime). An appearance of nanohillocks on a Si (111) surface with increasing laser fluences is shown for AFM surface topography images under UHV condition (figure 3.14) and in air (figure 3.15). In case of UHV conditions, the structures are observed for lower fluences ranging from  $0.06 \text{ Jcm}^{-2}$  to  $0.5 \text{ Jcm}^{-2}$  whereas, in case of air, surface structures are observed for fluences ranging from  $0.25 \text{ Jcm}^{-2}$  to  $2.5 \text{ Jcm}^{-2}$ . The laser energies in figure 3.14 and figure 3.15 are the same as used in figure 3.1 and 3.2 respectively, but the deposited energy/atom is 4–5 times higher for Si due to the different penetration depth and reflection coefficient. A value of 2.4 eV/atom is estimated for  $0.12 \text{ J.cm}^{-2}$  incident laser fluence. Similar kind of nanostructures have been observed for Si as have been observed and discussed for  $\text{CaF}_2$  (in section 3.2) with the only difference that the average height of nanohillocks for a Si (6–8 nm) is significantly higher than  $\text{CaF}_2$ . This can be attributed to larger values for the deposited energy/atom for Si as compared to a  $\text{CaF}_2$  in spite of the fact that the same laser energies are used for irradiation.

Under UHV condition again, below  $0.12 \text{ J.cm}^{-2}$  very few single nanohillocks are found in the exposed area (Figure 3.14 a). Starting at the threshold for particle ejection an increasing number of hillocks is observed (Figure 3.14 b). The height of hillocks is in the range of 3–6 nm. The number of hillocks, but in particular their height increases up to 8 nm as the laser fluence is further raised (Figure 3.14 c). Finally, if the laser fluence increases above  $0.5 \text{ J.cm}^{-2}$

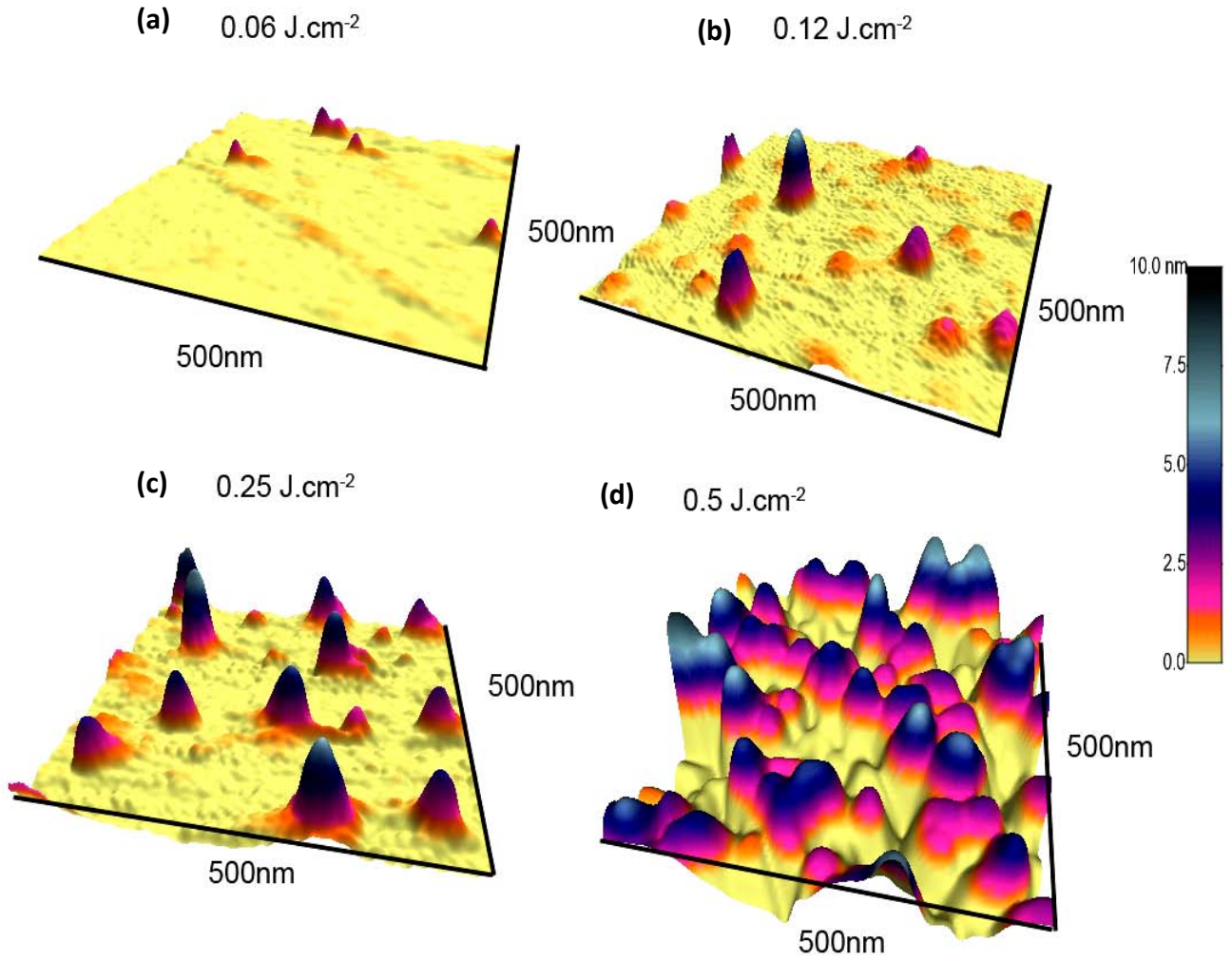


Figure 3.14: AFM topographic images of nanohillock-formation on the Si surface (scan area 500 nm×500 nm) as result of 25fs laser irradiation (around the threshold for particle removal) under UHV condition for increasing laser fluences of (a) 0.06 J.cm<sup>-2</sup> (b) 0.12 J.cm<sup>-2</sup> (c) 0.25 J.cm<sup>-2</sup> (d) 0.5 J.cm<sup>-2</sup>.

the hillocks become broader (Figure 3.14 d) and the surface turns out to be highly disturbed.

The onset of these non-localized surface changes are more pronounced in Si than for CaF<sub>2</sub>.

The appearance of nanohillocks under an ambient condition is presented in figure 3.15. Under an ambient condition, the threshold value of the fluence for appearance of nanohillocks is found to be 0.25 J.cm<sup>-2</sup> as shown in figure 3.15 (a). Figure 3.14 (b) shows the appearance of several numbers of nanohillocks with an average height of 6 nm and an average diameter of 50 nm, when the target was exposed to a fluence of 0.5 J.cm<sup>-2</sup>. Figure 3.14 (c) shows that the average number and height of nanohillocks are significantly enhanced when Si is exposed to a fluence of 1.5 J.cm<sup>-2</sup>. The average height of 8 nm and an average diameter of 55 nm are observed for this fluence. If the laser fluence is further increased to 2.5 J.cm<sup>-2</sup>, larger surface



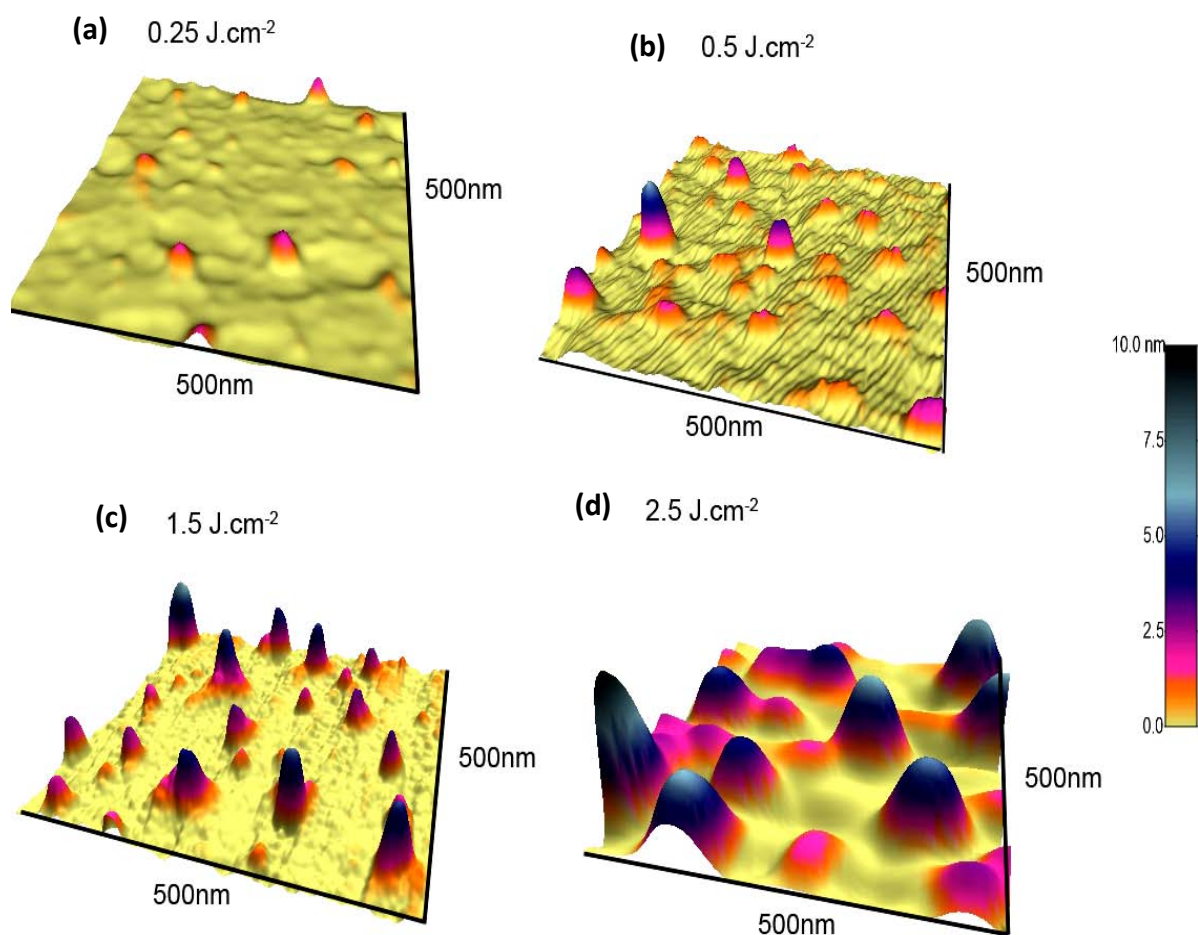


Figure 3.15: AFM topographic images of nanohillock-formation on the Si surface (scan area 500 nm×500 nm) as result of 25fs laser irradiation in air for increasing laser fluences of (a) 0.25 J.cm<sup>-2</sup> (b) 0.5 J.cm<sup>-2</sup> (c) 1.5 J.cm<sup>-2</sup> (d) 2.5 J.cm<sup>-2</sup>.

structures are observed as shown in Figure 3.14 (d). It makes no sense to speak of localized, isolated nanohillocks anymore.

The observations of figures (3.1 & 3.2) and figure (3.14 & 3.15) suggest that the similar kind of nanostructures have been observed for semiconductors as well as for dielectrics. The appearance of these localized features around the ablation threshold provides a clue that laser energy deposition mechanism in both dielectrics and semiconductor is identical. Therefore, Coulomb Explosion has been suggested to be a highly probable mechanism to cause localized surface modification and particle ejection, leaving a nanohillock like structures on the irradiated surface. Femtosecond laser radiation initially transfers its energy to the electronic system of the target, leading to a region of strong electronic excitation. As the laser pulse is shorter than the electron-phonon energy transfer time, only electrons are heated during the pulse [98]. In Ref. [12-14], a wealth of experimental evidence is provided to justify the assumption that the energies per pulse and the pulse width of 25 fs are sufficient to create the charging required for CE. Therefore, CE is a possible and probable explanation. Together

with previous results [12-14] one could successfully address the questions with regard to the validity of ultra fast electronic (sub 100 fs) processes like Coulomb explosion in semiconductors. From the results by El-Said et al.[15] on highly charged ions the correlation between the potential energy deposited in the electronic system and the appearance of nano-sized hillocks seems to be evident.

The deposited energy per atom is converted to a temperature according to [93]

$$E = \rho cVT + E_m \text{ For } E > \rho cVT_m + E_m \quad 3.12$$

$$E = \rho cVT \text{ For } E < \rho cVT_m \quad 3.13$$

$$T = T_m \text{ For } \rho cVT_m < E < \rho cVT_m + E_m \quad 3.14$$

where  $\rho$  denotes the mass density of ( $\text{kg/m}^3$ ) material,  $c$  the specific heat ( $\text{J/kgK}$ ),  $V$  the atomic volume ( $\sim 10^{-29} \text{m}^3$ ),  $T_m$  the melting temperature (K), and  $E_m$  the heat of melting per atom (eV/atom).

For Si  $E = \rho cVT_m = 0.42 \text{eV}$ ,  $E_m = 0.52 \text{eV}$  according to [93],

Therefore,  $E + E_m = 0.92 \text{eV}$

If we take into account the initially deposited energy distribution in space, an atom may be

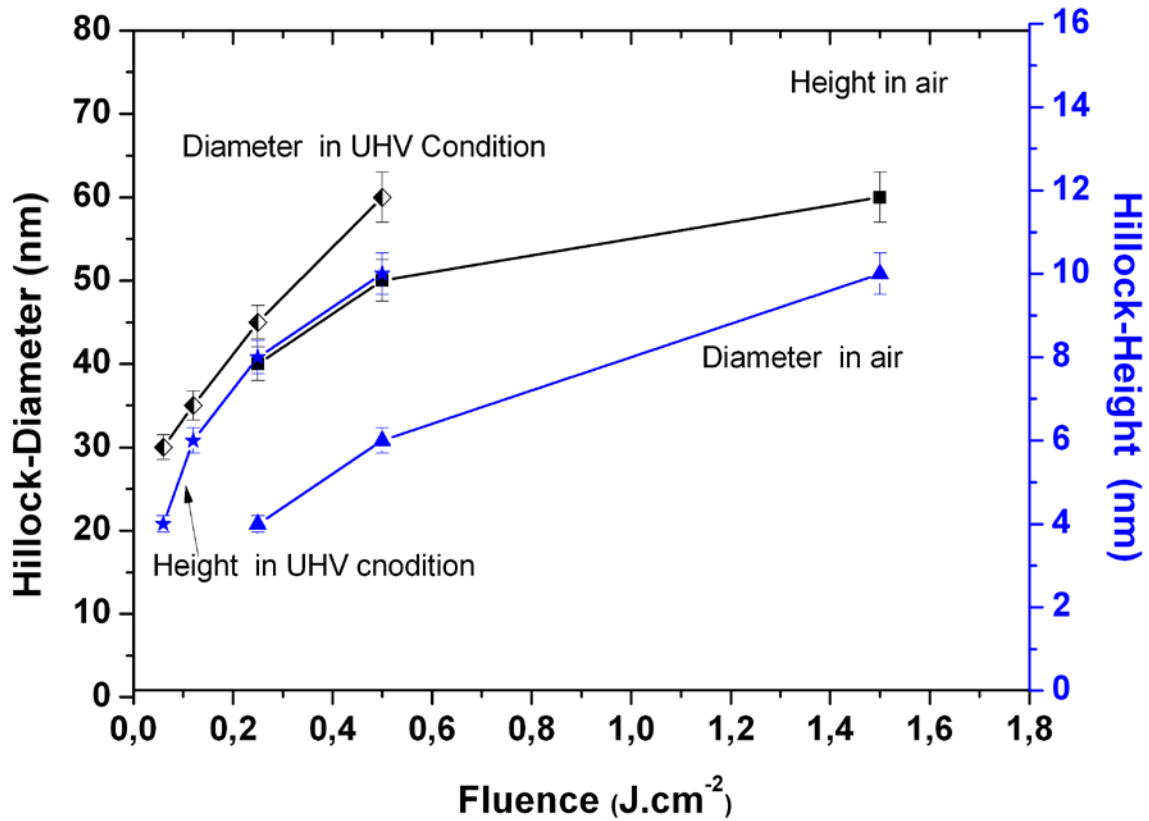


Figure 3.16: Average diameter and height of nanohillocks formed on the Si surface versus laser fluence as a result of its exposure to 25fs laser radiation under UHV condition and in air.



labeled “molten” when its temperature exceeds the melting temperature  $T_m$ . The calculated value of the energy deposited (eV/atom) to Si for a fluence of  $0.06 \text{ J.cm}^{-2}$  is  $1.8 \text{ eV/atom}$  which is higher than  $E+E_m= 0.92 \text{ eV}$  and is sufficient to induce nanodefects in Si (as can be observed from figure 3.14a).

The effect of the laser fluence on the geometrical size (diameter and height) of these nanohillocks after exposing the target in air and vacuum is plotted in Figure 3.16. For air and vacuum, both the average diameter and height of hillocks increase with increasing laser energy and can be ascribed to an increased energy deposition.

### ***(b) Moderate fluence regime***

In Figure 3.17 (a-b) (scan area  $20 \mu\text{m} \times 20 \mu\text{m}$ ) topographical images of Si after its exposure to increasing laser fluences (at a moderate fluence regime) under UHV condition are presented. The image in Figure 3.17 (a) shows the surface topography for conditions where an existence of nanohillocks vanishes and bump-formation is observed at a fluence of  $0.5 \text{ J.cm}^{-2}$  for single shot irradiation. When Si is exposed to  $0.5 \text{ J.cm}^{-2}$  for 20 shots, three different structures can be observed within the ablated area. The first prominent observed feature is an irregular ring shaped ablation pattern ( $3\mu\text{m}$  in diameter) with distinct and uplifted ( $20 \text{ nm}$  high) border. In the central zone of these rings larger bumps are observed with a typical diameter of  $1\mu\text{m}$  and a height of  $200 \text{ nm}$ . These observed characteristic circular symmetrical features can be attributed to the Gaussian distribution of the laser beam [75]. The second prominent features are larger bumps outside the ablated rings. Typical heights of these bumps

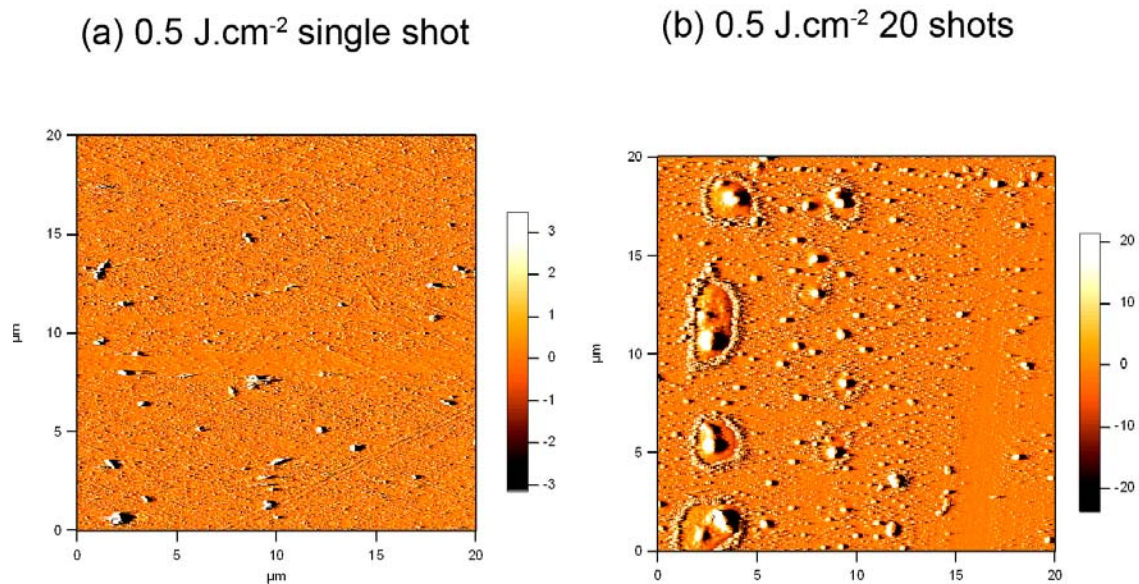


Figure 3.17: AFM Topographic images of the Si surface (scan area  $20 \mu\text{m} \times 20 \mu\text{m}$ ) as result of laser irradiation in a moderate fluence regime in UHV condition at the fluence of (a)  $0.5 \text{ J.cm}^{-2}$  single shot (b)  $0.5 \text{ J.cm}^{-2}$  20 shots.

are 200 nm with a diameter ranging from 800 nm to 1  $\mu\text{m}$ . The appearance of such characteristic features can be attributed to ultrafast melting (correlated with existence of electron-hole plasma) in nonthermally melted silicon, showing again the efficient localization of energy due to the occurrence of plasma. In the low fluence regime with single shots, where the laser fluence of each pulse is around the ablation threshold, only the appearance of nanohillocks is observed which has already been attributed to ultrafast Coulomb Explosion (Figure 3.14 (a-d)). No noticeable ablation due to ultrafast melting for single shot irradiation is observed because the free-electron density generated by the first pulse is still well below the critical density of ultrafast melting. The ultrafast melting occurs with overlapping laser pulses, because nanodefects produced by the first shots increase the absorption of succeeding pulses. This may lead to a free-electron density well above the critical density for ultrafast melting. This UFM may cause further processes resulting in even more pronounced ablation [12, 14]. In addition to these bumps, nanohillocks of diameter less than 100 nm and of typical heights 10 nm are also seen in the outer zone of irradiated area where laser fluence is around the ablation threshold. As already described for  $\text{CaF}_2$ , these (micro-) bumps are related to

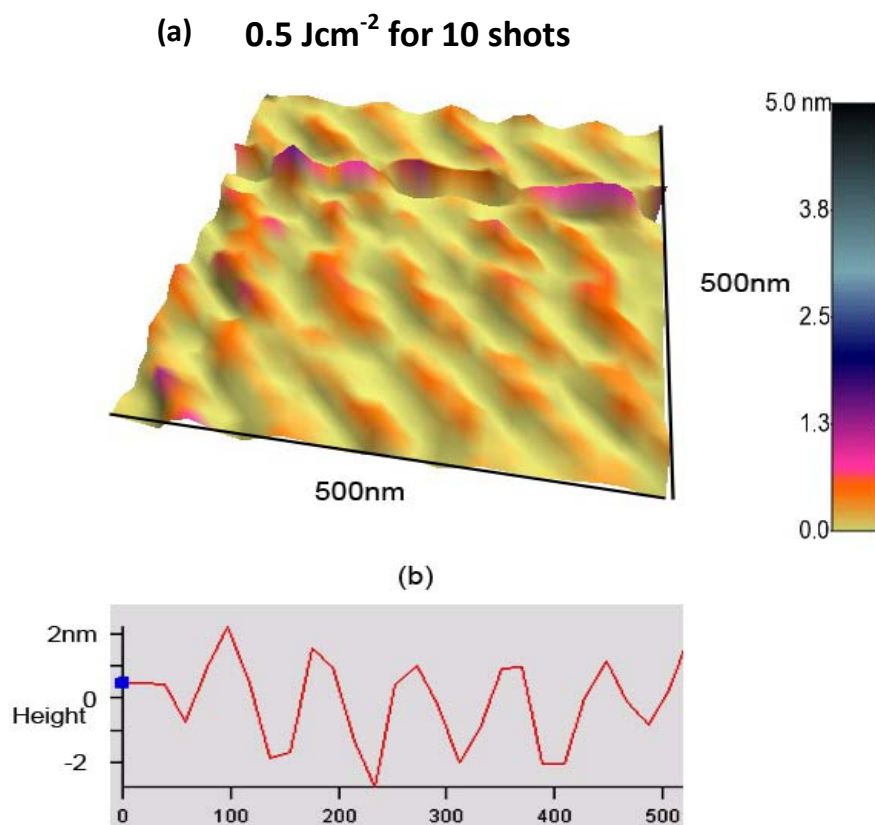


Figure 3.18 : An AFM topography representing nanoripple-formation on the Si surface as result of laser irradiation in a moderate fluence regime in UHV condition (a) Nanoripples at a fluence of  $0.5 \text{ Jcm}^{-2}$  for 10 shots (scan area  $500\text{nm} \times 500\text{nm}$ ) (b) Cross-section profile of figure a.

compressive stresses due to a pressure built-up induced by fast laser heating. Relaxation of these compressive stresses is responsible for the formation of these micro-bumps [16]. Nevertheless for Si, after irradiation by ns-laser pulses, another mechanism of bump-formation is described: the volume of silicon increases during liquid solid phase transition. As a consequence, during the resolidification the liquid silicon is squeezed radially to the center and forms a protrusion [139]. This mechanism is also valid in the case of fs-laser pulse induced melting of silicon [75].

Figure 3.18 (a) is an AFM view of nanoripple-formation on a Si surface (scan area 500 nm×500 nm) with a corresponding cross section profile shown in figure 3.18 (b). Nanoripples of typical height of 2 nm and an average periodicity of  $100\pm10$  nm are observed after exposing the target in UHV conditions with a fluence of  $0.5 \text{ J.cm}^{-2}$  for 10 shots. The only, but very pronounced, difference compared to structures produced on  $\text{CaF}_2$  approximately at the same fluence (but for single shot irradiation), is an interesting “bifurcation feature” in the ripples formation.

Figure 3.19 (a, b and c ) shows an AFM image of an exposed Si surface (scan area  $20 \mu\text{m} \times 20 \mu\text{m}$ ) at a fluence of  $1.5 \text{ J/cm}^2$  for 20 succeeding pulses. AFM analysis yields direct evidence that two kinds of ripples are formed on the irradiated Si surface: a) microstructures at the centre of the laser spot and b) nanostructures in the periphery of microstructures where the intensity of the laser beam is near damage threshold. The appearance of periodic structures parallel to the surface can clearly be identified in the 3D image (3.19 a) and in the deflection trace (3.19 b). The formation of similar “parallel lines” on Si in a femtosecond laser irradiated area has been reported previously [53, 140, 141]. The periodicity of the structures can be obtained from a section graph (1c) and is found to be  $1.064 \mu\text{m}$  with height 200 nm, In the literature, the periodicity of such structures in some cases is reported to exhibit a direct correlation with the incident wavelength [53, 109, 140, 142]. However, in our case the observed periodicity has no relation with the incident wavelength as evidenced in [141, 143, 144]. Generally, these periodic structures are attributed to an inhomogeneous distribution of energy on the surface due to interaction between the incident light and surface scattered waves or radiation remnant field structures. Thus, in response to spatial modulation of the energy, the modulated modifications on the surface of the materials are formed.

The question is how the modulated irradiance is physically transformed into a persisting variation of surface geometry. The basic sequence is that the material melts (may be ultrafast melting), undergoes deformation and finally after irradiation re-solidifies making the deformation permanent. This surface deformations or irregularities act to scatter a small

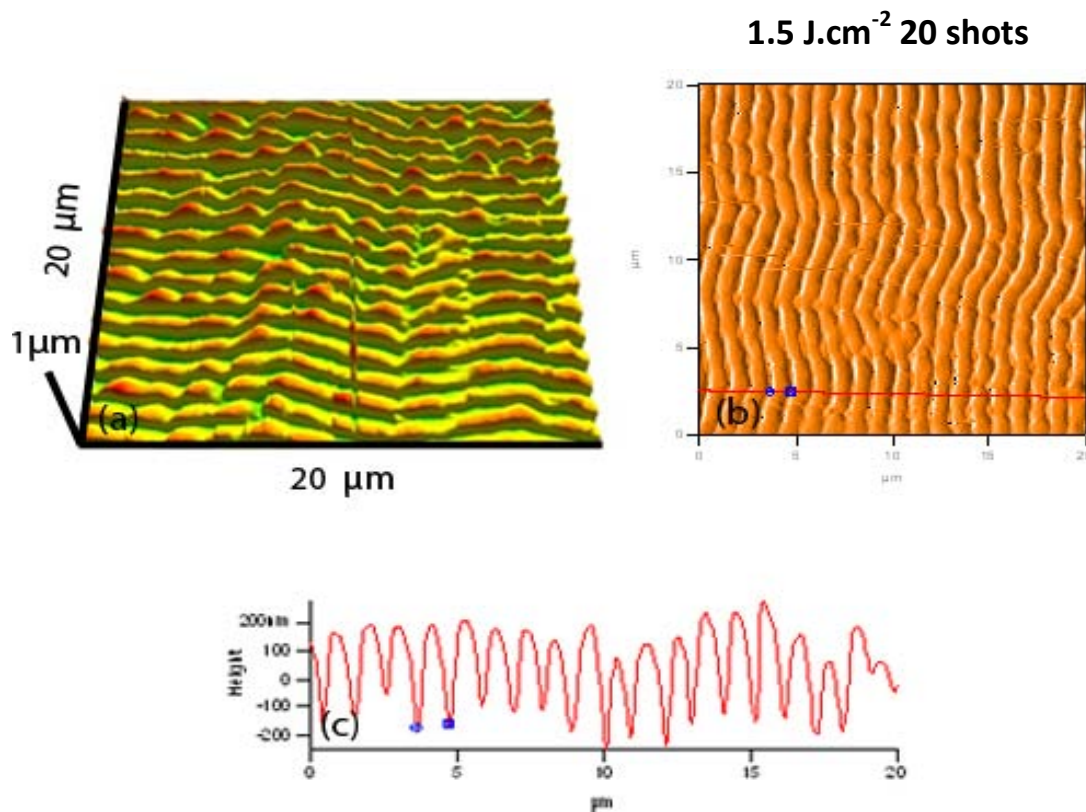


Figure 3.19: AFM micrographs exhibiting periodic micro structures on Si (111) as result of laser irradiation at a fluence of 1.5 Jcm<sup>-2</sup> for 20 shots under UHV condition (a) 3-D image (b) deflection trace and (c) line scan on the deflection trace

amount of light from the incident laser beam. This scattered light may propagate as a surface wave above or within the irradiated material, and interferes with the incident beam producing an intensity distribution across the surface. The intensity distribution acts as a diffraction grating, scattering additional light into the surface wave, therefore creating a positive feedback effect [107]. The ripple-formation has also been attributed to scattering from surface roughness and to re-radiation from surface defect sites [140, 145]. Surface deformations are the most common and most efficient scatterers, but latent patterns such as lateral variations in lattice temperature or in free-carrier density [146], result in some scattering even on geometrically smooth surfaces. Whatever is the origin, scattered fields from different scattering features interact and diffraction at ripples gives rise to secondary ripples. The resulting patterns contain Fourier components at several frequencies. Thus, once a fringe pattern has been physically imprinted on a surface, it can perpetuate itself coherently in subsequent fully or partially overlapping laser shots [142]. This may explain the gradual build-up of periodic damage patterns that is frequently observed during the repeated irradiation by pulses too weak to cause any conspicuous damage individually [147]. Figure 3.20 (a) gives the AFM topographic image for scan area of 5μm×5μm. The periodicity of the



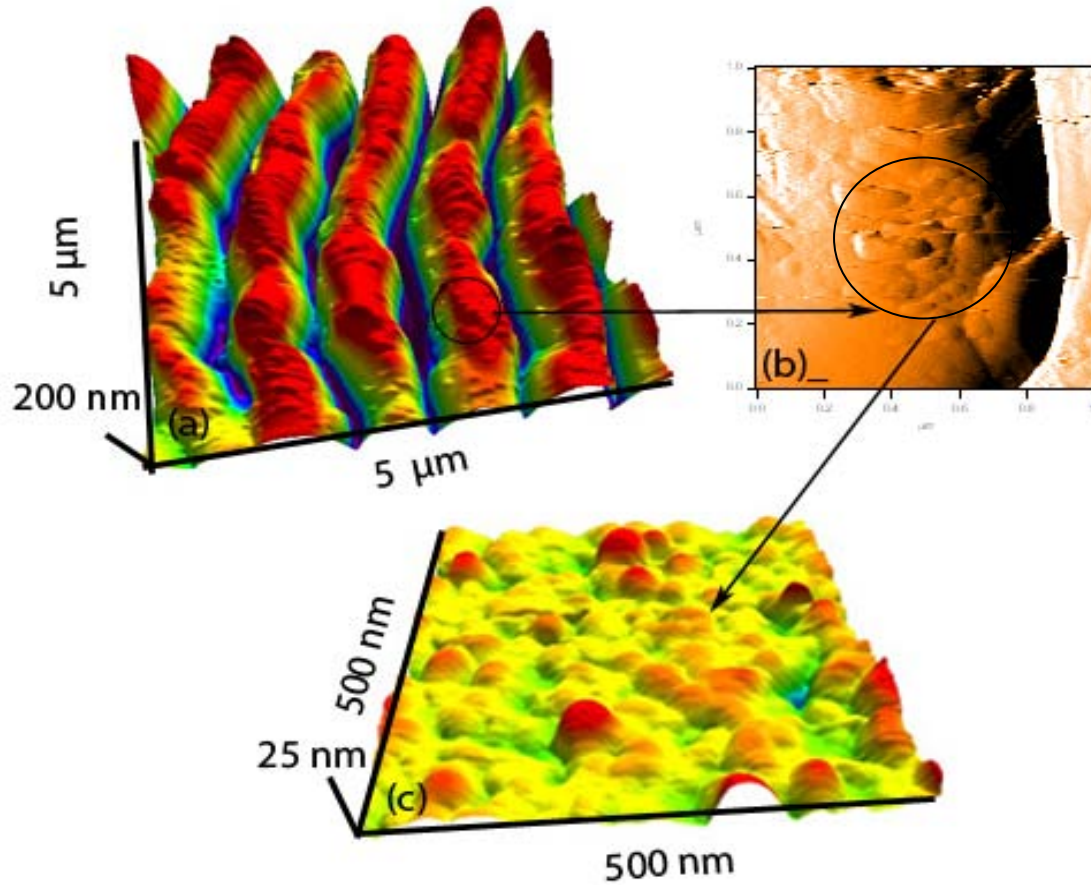


Figure 3.20: An enlarged view of the periodic micro surface structure induced on the Si surface as result of laser irradiation at  $1.5 \text{ J.cm}^{-2}$  for 20 shots (a) 3-D image (b) deflection trace of an encircled area on the top of a microstructure of figure a. (c) 3D image of the encircled area in (b).

pattern is perfectly regular with humps and pits typically with an average height of 200 nm. A deflection trace of a hump of one of this periodic microstructure (encircled area) is magnified (scan area  $1 \mu\text{m} \times 1 \mu\text{m}$ ) in figure 3.20 (b). This microstructure is further magnified in a 3D image (scan area  $500 \text{ nm} \times 500 \text{ nm}$ ) in figure 3.20 (c). This topographic image shows that the top of the surface of one microstructure is rough consisting of many nano-protrusions and nano-dots. There are no sub-periodic nanostructures found in the magnified images of a periodic microstructure. This is in agreement with the previous results [147].

In our experiment, in addition to the microstructures we have clear and conclusive evidences of the formation of nano structures with spacing as low as a few nanometers at the edges of the microstructures where the intensity of the laser beam is substantially lower than the value at the central area. Figure 3.21 (a) shows a 3D image (scan area  $6.4 \mu\text{m} \times 6.4 \mu\text{m}$ ) of the periphery of the micro-periodic structures. Figure 3.21 (b) presents a deflection trace of an enlarged area (scan area  $100 \text{ nm} \times 100 \text{ nm}$ ) encircled in (a). From the section graph in figure 3.21(c) the obtained average periodicity of self-organized nanostructures is 10 nm. Figure

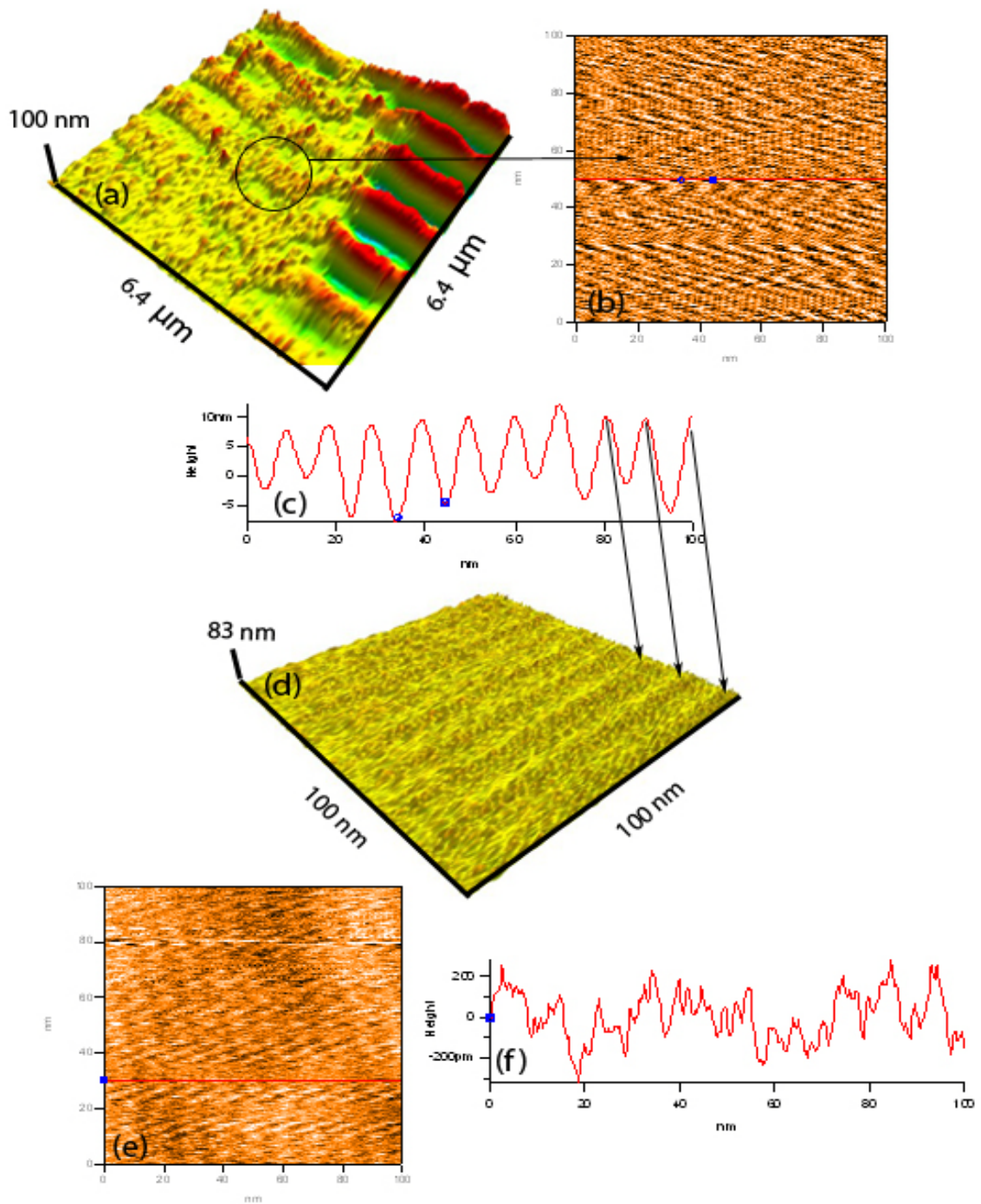


Figure 3.21: AFM micrographs of nano periodic structures grown in the periphery of the micro periodic structures (a) 3D image of the periphery of the microstructure. (b) deflection trace of the encircled area in (a). (c). line trace/section graph of the deflection trace in (b) (d) 3D image of the deflection trace in (b). (e) For reference a deflection traces of the unexposed area along with the (f) line trace /section graph.

3.21(d) is a 3D image of the deflection trace in (b) which exhibits the formation of self-organized nano ripples. The average height of these nanoripples is 8 nm. This AFM scan reveals an abrupt change in the spatial and size distribution of the nanoripples at the edges of the laser spot. For a reference a deflection trace (figure 3.21e) and a section graph (figure 3.21f) of an unexposed Si surface is also shown. The roughness of unexposed Si is in pm range with no known periodicity. The formation of the nanostructures at the edge of the central region of the spot has already been reported [145, 148-151]. However, a spacing of the periodic surface structures as low as a 10 nm induced by a femtosecond laser irradiation has not been found in literature so far.

Formation of such nanostructures do not depend on the wavelength but depends strongly on the laser fluence [152]. Different interpretations of these features can be given. The formation of periodicity can be attributed to the excitation of surface plasmon polariton to induce the periodic enhancement of local fields in the surface layer. Depending on the electron density, nanogratings as a result of the interaction of laser pulses with laser-produced surface plasma can be considered as one major reason for such kind of structures. The process of pattern formation is related to different relaxation processes resulting in the formation of nanostructures on the surface.

Another physical reason responsible for nanoripples formation becomes evident by considering the evolution of the electron and lattice temperatures. Generally, the energy is primarily absorbed by the electrons. The laser excitations result in a high electron temperature at the end of the pulse. In a next step, a sharp drop in the electron temperature due to energy transfer from the hot electrons to the lattice will take place. The corresponding energy transfer results in the increase of the lattice temperature, which eventually will exceed the melting temperature of Si and a melt pool is formed on the silicon surface. In the vicinity of the molten silicon, the temperature of the surface rises and is modulated periodically. Various processes in the melt pool can initiate irreversible features like periodic surface structures, ripples, which freeze after a very fast cooling process. Strong electron temperature gradients following the initially localized energy deposition result in a fast cooling of electrons ( $\sim 10$  ps) and the lattice at later times ( $\sim 50$  ps) [16] .

The lattice temperature at the periphery of the melted region drops below the equilibrium melting temperature starting a process of re-crystallization. Crystallization gives way to a massive homogeneous nucleation of multiple crystallites within the cooled liquid region resulting in a rapid solidification of the nanoripples [16] leading towards the growth of frozen

capillary waves characteristic for the molten silicon [153]. The density change between solid and liquid phases of silicon ( $2.53 \text{ g cm}^{-3}$  for the liquid and  $2.30 \text{ g cm}^{-3}$  for the solid) provides a driving force for the creation of capillary waves. Solidifying silicon expands and exerts a positive force on the adjacent melt causing propagation of capillary waves [154]. When the laser energy ( $\phi_0 = \text{heat flux}$ ) is absorbed by the melt pool, variation in the surface temperature can be estimated from the solution of heat diffusion equation in a pool of depth  $h$ . Since capillary waves are generated by the temperature gradients, there is a resulting surface tension distribution ( $\sigma$ ) [155]. The spatial period ( $d$ ) of capillary waves on the surface of molten silicon [151] can be calculated by the relation

$$d = \left[ \frac{\sigma h}{\rho} \right]^{\frac{1}{4}} (2\pi\tau_L)^{\frac{1}{2}} \quad 3.15$$

Where  $\sigma = 850 \text{ mNm}^{-1}$  is the surface tension coefficient of molten silicon

$\rho = 2.5 \text{ gcm}^{-3}$  is the liquid mass density,

$\tau_L$  the lifetime of the molten state

and  $h$  is the height of the molten layer which can be calculated by [39]

$$h = \frac{\phi_0(1-R)}{c_v T_m + L_m} \quad 3.16$$

where  $\phi_0$  is the laser fluence,  $R = 0.34$  at  $800 \text{ nm}$  is the reflectivity of silicon,  $c_v = 2 \text{ Jcm}^{-3}\text{K}^{-1}$  is the specific heat capacity  $T_m = 1685\text{K}$  is the melting temperature and  $L_m = 4130 \text{ Jcm}^{-3}$  is the specific heat of melting.

The ripples are formed at the periphery of the real damaged spot indicating where the fluence is around the ablation threshold [36]. The damage threshold fluence of silicon at  $800 \text{ nm}$  is  $0.6 \text{ J.cm}^{-2}$  [16].

Considering that the time of the molten state is much longer than the pulse duration (the thermal process lasts for ps [39] and (the molten lifetime  $\tau_L$  is assumed to be 1-5 ps) the calculated periodicity ranges from 9-20 nm.

The measured value of periodicity is  $10 \text{ nm}$  which is well within the calculated range. Therefore, it is convincing evidence that relaxation of deformation occurs as the molten silicon surface cools down and excites capillary waves. These capillary waves are most likely the instabilities that drive the formation of the periodic surface nanostructures.



**(c) High fluence regime**

Figure 3.22 (a & b) represents a change in surface topography of Si surface after its exposure to a higher fluence regime (a fluence significantly higher than ablation threshold) i.e.  $2.5 \text{ J.cm}^{-2}$  and  $3.5 \text{ J.cm}^{-2}$  for 20 succeeding pulses. The appearance of islands is encountered at the semiconductor surface. The size of each island is usually about  $3 \times 5 \text{ }\mu\text{m}$ . The heights of these projections vary from 600 nm-1.5  $\mu\text{m}$ . Thermal processes taking place in the higher fluence regime on the ps time scale are assumed to be responsible for the formation of these kind of island-like structures. Phase transformations and liquid disruptions occurring under strong conditions of superheating and high deformation rates are main cause of these frozen structures. Once the crystalline semiconductor has been melted crystal nuclei are created. These nuclei (dimers or trimers etc) act as condensation nucleus for further cluster growth. Early growth occurs by incorporation of atoms (molecules). Subsequently, collisions between smaller clusters can lead to coalescence and formation of larger clusters [156]. The irradiated surface is sequentially solidified from these nuclei, clusters and agglomerates. This surface consists of an amorphous as well as a polycrystalline phase (composed of many crystallites) (also revealed by Raman spectroscopy in the next section). The appearance of island-like structures on a Si surface can also be explained as follows: the crystalline silicon melts under the action of the laser pulse and resolidifies in an amorphous state without accompanying effects of ablation or melt flows. The crystalline silicon melts at a lower temperature than amorphous silicon dioxide ( $T_m(\text{c-Si}) = 1690\text{K} < T_m(\text{a-SiO}_2) = 1973$  [89]), this could arise

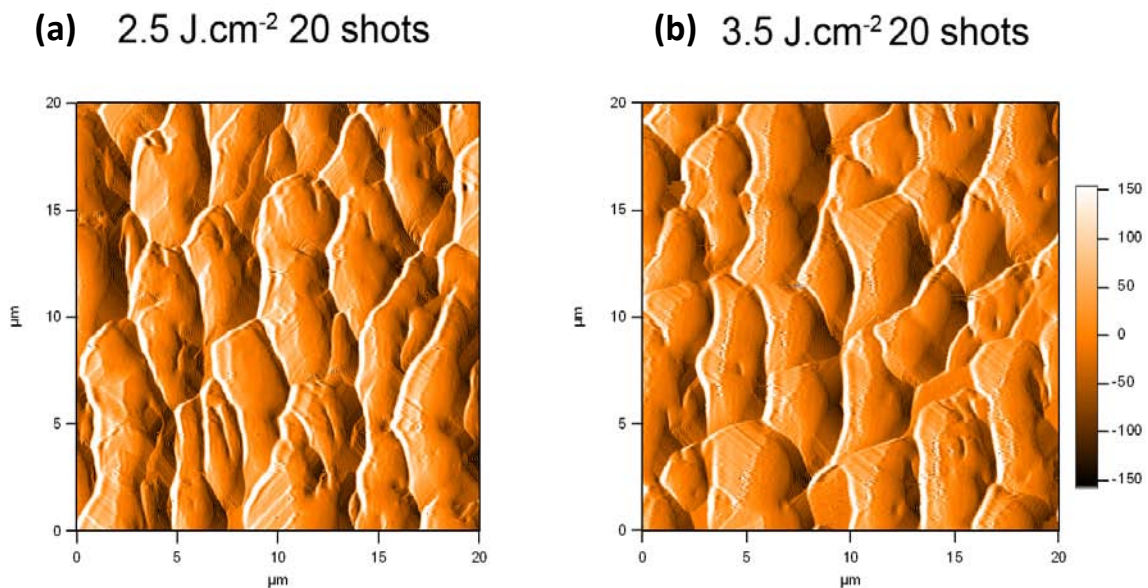


Figure 3.22: AFM Topographic images of the Si surface (scan area  $20 \mu\text{m} \times 20 \mu\text{m}$ ) as a result of laser irradiation in a high fluence regime in UHV condition at a fluence of (a)  $2.5 \text{ J.cm}^{-2}$  20 shots (b)  $3.5 \text{ J.cm}^{-2}$  20 shots.

from a local mechanical destruction due to melt flows or due to the volume contraction and expansion of the underlying silicon during melting and subsequent resolidification (mass densities of the solid and the liquid:  $\rho(\text{c-Si}) = 2.32 \text{ g/cm}^3$  and  $\rho(\text{l-Si}) = 2.52 \text{ g/cm}^3$ ) [89]. This volume contraction and expansion with the development of very high pressures (100, s of GPa) during ablation creates island like protrusion at the irradiated surface. Figure 3.23 (a) shows an AFM image (scan area  $5\mu\text{m} \times 5\mu\text{m}$  area) of Si irradiated with 20 shots in air at a laser fluence of  $2.5 \text{ J/cm}^2$ . Figure 3.23 (b) is enlarged view of figure 3.23 (a) (scan area  $1\mu\text{m} \times 1\mu\text{m}$ ). Explosion like features or nanocavities in the irradiated target are clearly seen. A laser pulse incident on a surface will produce a pressure wave which propagates into the material and can lead to lattice disorder. Very large magnitudes of transient pressures can be generated near the surface by femtosecond laser irradiation. It is estimated by Borowiec et al [157] that a pressure of a few gigapascals would be required to nucleate defects in semiconductors. It has already been discussed in section 3.2, that for ultrashort laser [111] radiation, no acoustic relaxation is possible during the thermalization time and thermo-elastic stresses caused by the temperature rise stay confined in the focal volume leading to a maximum pressure rise. This maximum pressure rise and deposited energy (eV/atom) can be calculated by considering the volumetric energy absorbed, the focal volume and the skin depth [117, 118].

The graph in Figure 3.24 shows the calculated values of the energy deposited (eV/atom) and

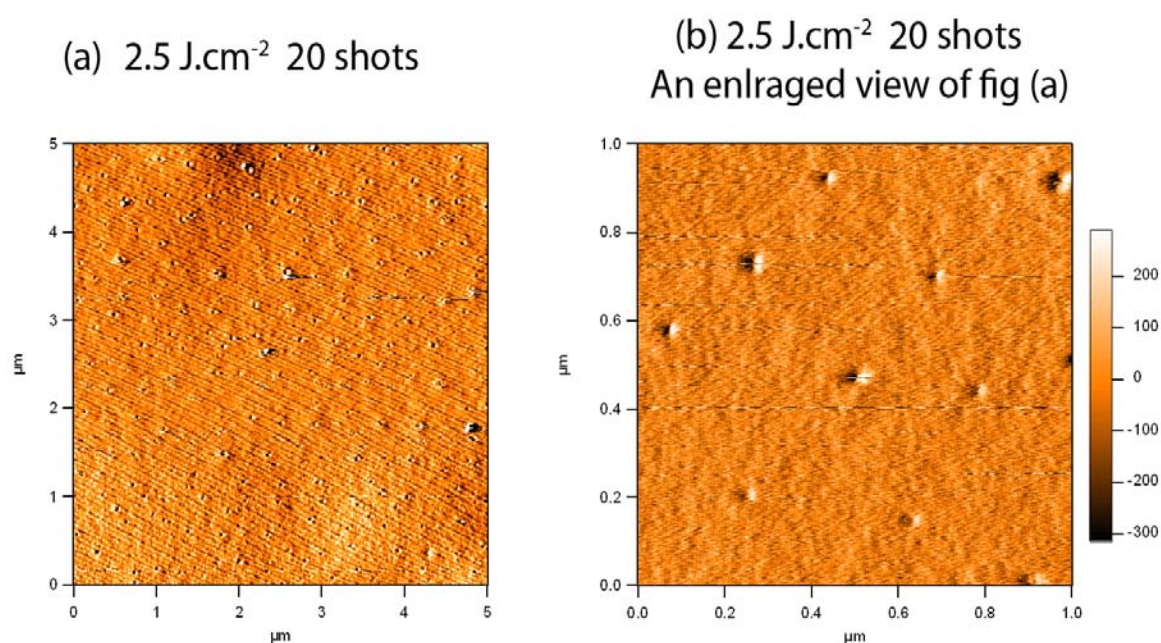


Figure 3.23: AFM Topographic images of the Si surface as a result of laser irradiation at a fluence of  $2.5 \text{ J/cm}^2$  in air (a) Explosions and nanocavities (scan area  $5\mu\text{m} \times 5\mu\text{m}$ ) (b) An enlarged view of figure 3.23 (a) (scan area  $1\mu\text{m} \times 1\mu\text{m}$ ).

the corresponding developed pressures (GPa) at different laser fluences for Si. Since both pressure and deposited energy increase linearly with laser fluence, the pressure developing for a fluence of  $0.5 \text{ J.cm}^{-2}$  reaches a value of 80 GPa, which is smaller than the Young modulus of Si (130 GPa). The pressure increases to 240 and 400 GPa for a laser fluence of 1.5 and  $2.5 \text{ J.cm}^{-2}$  respectively and is capable of producing periodic structures, in case of exposure in UHV condition and explosion like features in case of an exposure in air resulting in the characteristic nanocavities shown in figure 3.23 (a and b). The formation of a nanocavities due to rupturing of material are observed when the absorbed energy density exceeds the Young modulus (130 GPa) of Si [117] (see Figure 3.23 a-b). These small explosions or nanocavities have only been observed in air and can be explained on the basis of the destruction of the covering native oxide layer.

It is evident from our observations that multiple-pulse irradiation induces defects in silicon more effectively than single-pulse irradiation. Localized and isolated defects were observed at a low fluence from  $0.06 - 0.5 \text{ J.cm}^{-2}$  for a single pulse irradiation. While larger bumps with ring shaped ablation (ultrafast melting), LIPSS have been observed at moderate fluence

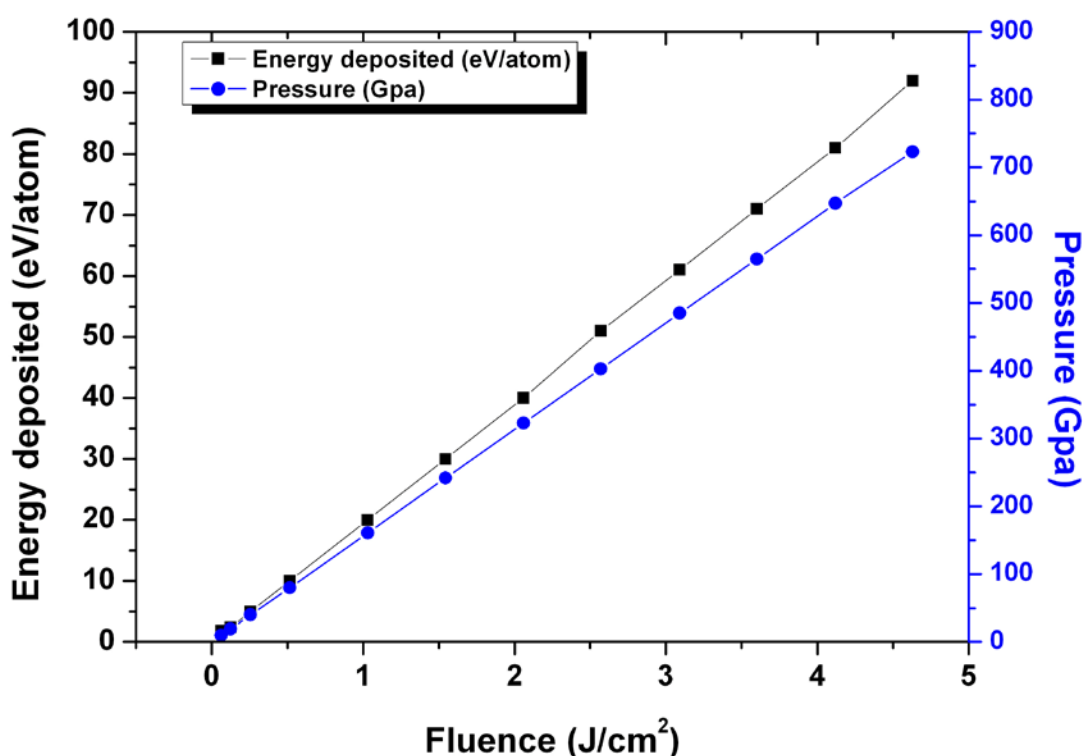


Figure 3.24: Energy deposited ( $\text{eV/atom}$ ) and developed pressure (GPa) Vs different laser fluences for Si.

regime ( $0.5 - 1.5 \text{ J.cm}^{-2}$ ) with 20 succeeding pulses. In case of exposing the target with succeeding laser pulses (20 in this case) in a high fluence regime ( $2.5-3.5 \text{ J.cm}^{-2}$ ), larger islands have been observed and are attributed to thermal ablation. After the first pulse, subsequent pulses are incident on a material with potentially different chemical, structural, and optical properties. An incubation effect, in which the modification threshold fluence decreases with increased number of pulses, has been reported for various crystalline materials including silicon. It has been proposed that incubation could arise from the storage of energy by changes of a mechanical (stress-strain), chemical, or crystallographic nature [108, 109].

Figure 3.25 (a-c) shows a SEM image of a Si irradiated with a fluence of  $8 \text{ J.cm}^{-2}$  which is significantly higher than ablation threshold. Figure 3.25 (a) is presenting a crater formation in the mainstream with sideline surface modification. Figure 3.25 (b) is enlarged view of border line of (a) and is presenting ripple-formation at the periphery of ablated crater. Figure 3.25(c) is enlarged view of (b) with a clear picture of fine ripples of an average periodicity of 500 nm.

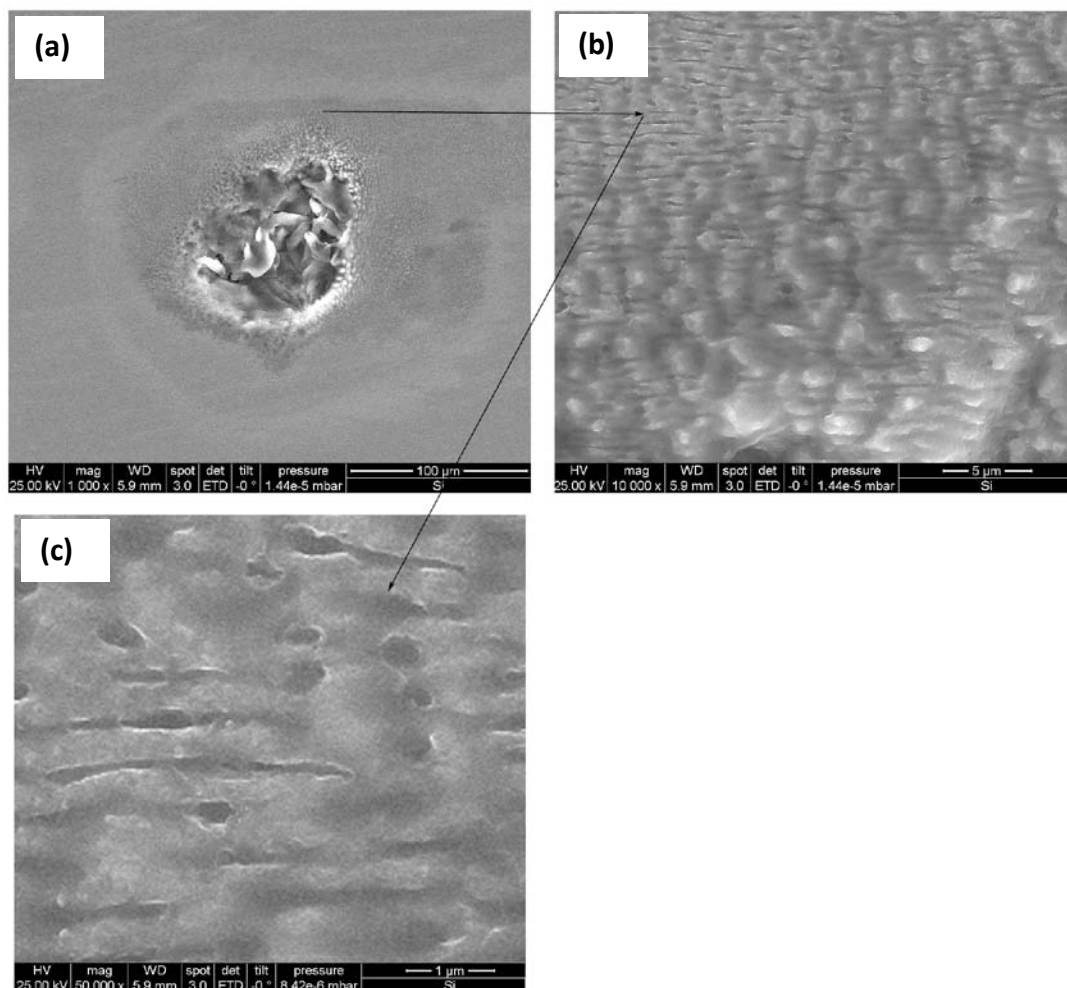


Figure 3.25: SEM images of Si irradiated with a fluence of  $8 \text{ J.cm}^{-2}$  with 10K shots (a) Crater formation (b) Ripples at the periphery of ablated crater (c) Enlarged view of fine ripples with an average periodicity of 500 nm.

These nanoripples are observed only at the periphery of ablated area for fluence well above the ablation threshold due to lower intensity of the laser beam in these regions.

From results discussed above, it is evaluated that at the fluence near the ablation threshold similar kind of nanostructures for a semiconductor and a dielectric material have been obtained, whereas for a moderate and a high fluence regime the physical properties of materials play a more dominant role after ultrafast laser irradiation. Common points are as follow. For both materials (semiconductors and dielectrics) we have observed bump formation and nanoripples of periodicity much smaller than the laser wavelength. These nanoripples are observed at a fluence slightly higher than the ablation threshold in the moderate fluence regime. Interspacing of ripples depend upon the material, laser fluence and ambient conditions. For fluences well above the ablation threshold, classical ripples of periodicity  $1\mu\text{m}$  or higher are observed. For lower laser fluences the spacing of the nanostructure pattern has the tendency to be shorter. For certain condition these nanoripples are observed at the periphery of ablated area for fluences well above the ablation threshold. Since the spatial laser beam profile is Gaussian, this suggests that in the off-center regions of the irradiated areas (for fluences higher than the material threshold), this nanoripple-formation is a consequence of the lower intensity of the laser beam in these regions. Island-like structures are only observed in Si and can be attributed to melting and resolidification of Si.

And last but not least, unique features of the Si surface topography can be correlated with specific particle energies. This is demonstrated in figure 3.26, where the time of flight (TOF) spectrum of ejected Si atoms is shown for two characteristic laser intensities separating the three time regimes: Ultrafast CE taking place in less than 100 fs (electronic processes) responsible for nanohillock-formation (fast particles emitted with several eV). Then ultrafast melting takes place in hundreds of fs (again electronic processes) responsible for ring-shaped ablation, and LIPSS (particles with a few eV). Then slow thermal ablation taking place in ps time regime is responsible for islands-like structures (particles with fractions of eV). It is remarkable, that hillocks have been observed (without other significant surface modification) for both semiconductor and dielectric materials investigated exactly under these conditions (laser energy) for which a substantial part of the ejected particles have kinetic energies of several eV (figure 3.26) which has been shown previously [14]. Even more importantly, it has shown with pump-probe techniques, that it is essential to deposit the energy on a time scale of typically 30–200 fs. Another fact, which becomes obvious from figure 3.26 (TOF measurement) is that ultrafast electronic processes or CE phenomenon (less than fs regime) are more dominant in the lower fluence regime. A very important experimental evidence,



which is obvious from figure 3.14 is that the formation of hillocks starts at the threshold laser energy. Their number increases from very few (about one or two) in an area of  $500 \text{ nm} \times 500 \text{ nm}$ , but saturates just above the threshold at typically 5-10 hillocks per  $500 \text{ nm} \times 500 \text{ nm}$  and remains constant for laser fluences up to  $0.300\text{-}0.4 \text{ J}\cdot\text{cm}^{-2}$ . This is in good accordance with the results shown in figure 3.26. Increasing the laser intensity enhances the thermal ablation, but the amount of fast particles remains constant. The transfer of energy stored in the hot electrons into kinetic energy of ablated particles or dislocated target surface atoms is a complicated process. Since many mechanisms can and will contribute, a conclusive answer, which one is actually taking place, is difficult. Based on several experimental observations we postulated Coulomb explosion as a highly probable explanation [14].

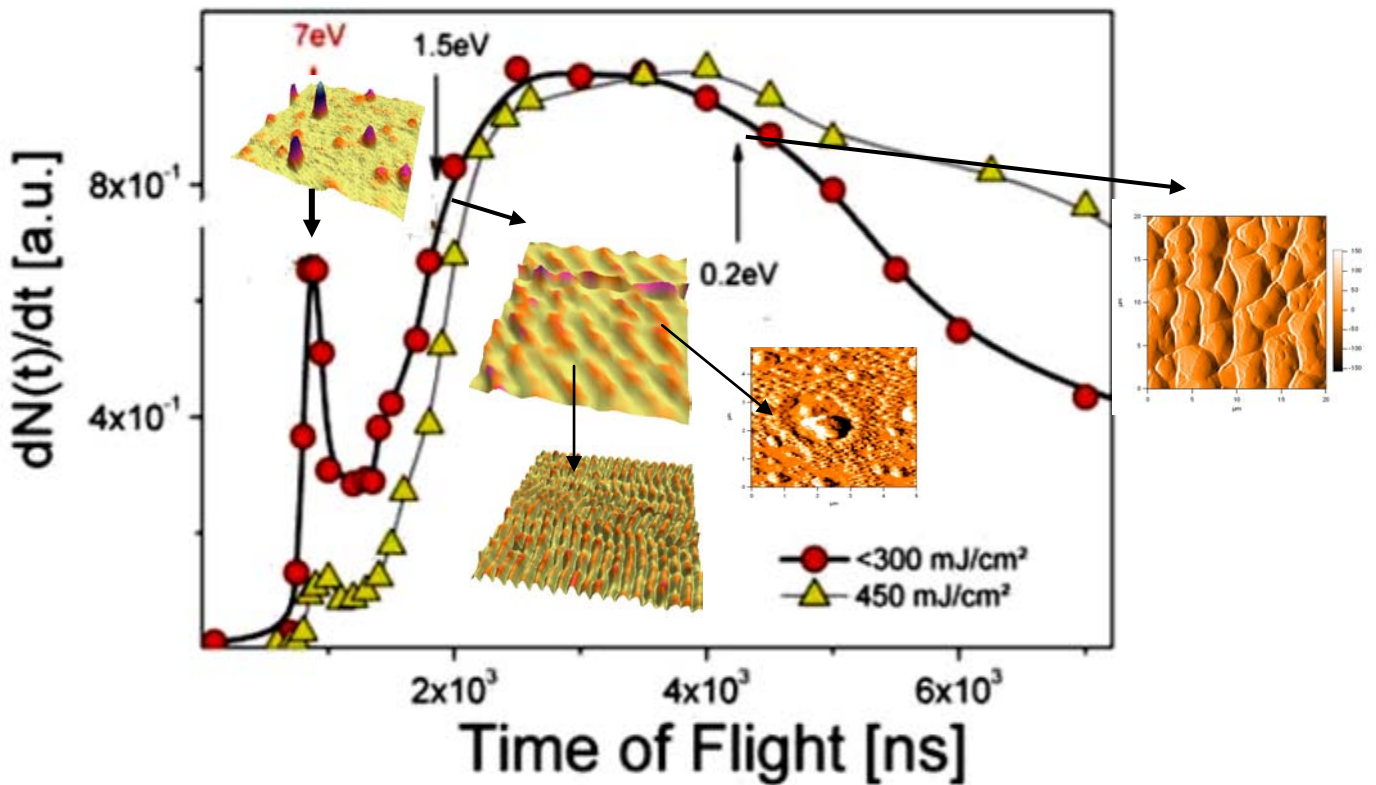


Figure 3.26: Correlation between observed surface topography and energy of ejected Si atoms. Up to  $300 \text{ mJ}/\text{cm}^2$  fast Si atoms contribute substantially. For higher laser intensities thermal particles become the dominant contribution. The curves shown are time of flight spectra of post-ionized neutral Si atoms. The time of flight represents the time the atoms need to reach the ionization volume from the target normalized to the thermal velocity peak [14].

### 3.3.2 Raman Spectroscopy

In order to investigate the changes in crystallographical properties of a Si wafer after the femtosecond laser irradiation for different fluence regimes, Raman spectroscopic measurements were performed. The structural and chemical changes appear as an identification of crystalline and polycrystalline phase and an appearance of new disorder band which is related to an amorphous phase of a Si. The main purpose of these investigations is to correlate Raman spectroscopy measurements with the surface analysis performed by an AFM exhibiting the transition from electronic processes (Coulomb Explosion and ultrafast melting) to thermal processes with an appearance of a more disturbed Si surface with increasing laser fluence. Figure 3.27 and 3.28 show Raman spectra of the pristine and single pulse irradiated Si for different laser fluences exposed under UHV condition and ambient condition, respectively. In the pristine Si the single and sharp peak is identified at  $520\text{ cm}^{-1}$ . It arises from the first-order Raman scattering of the longitudinal optical (LO) and the transverse optical (TO) phonon modes which are degenerated at the G-point (phonon wave vector  $q \sim 0$  near the center of the Brillion zone) [75]. No Raman shift is observed in these modes in case of ablation in air and under UHV condition for all laser fluences.

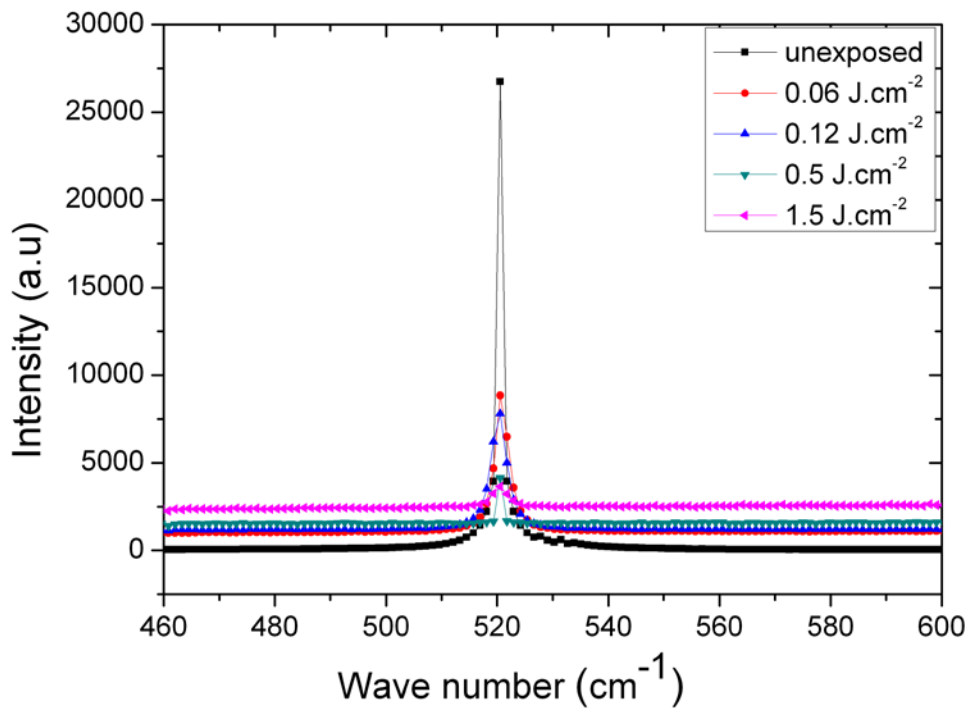


Figure 3.27: Raman spectra of the pristine and single pulse irradiated Si under UHV condition for different fluences  $0.06\text{ J.cm}^{-2}$ ,  $0.12\text{ J.cm}^{-2}$ ,  $0.25\text{ J.cm}^{-2}$  and  $0.5\text{ J.cm}^{-2}$ .

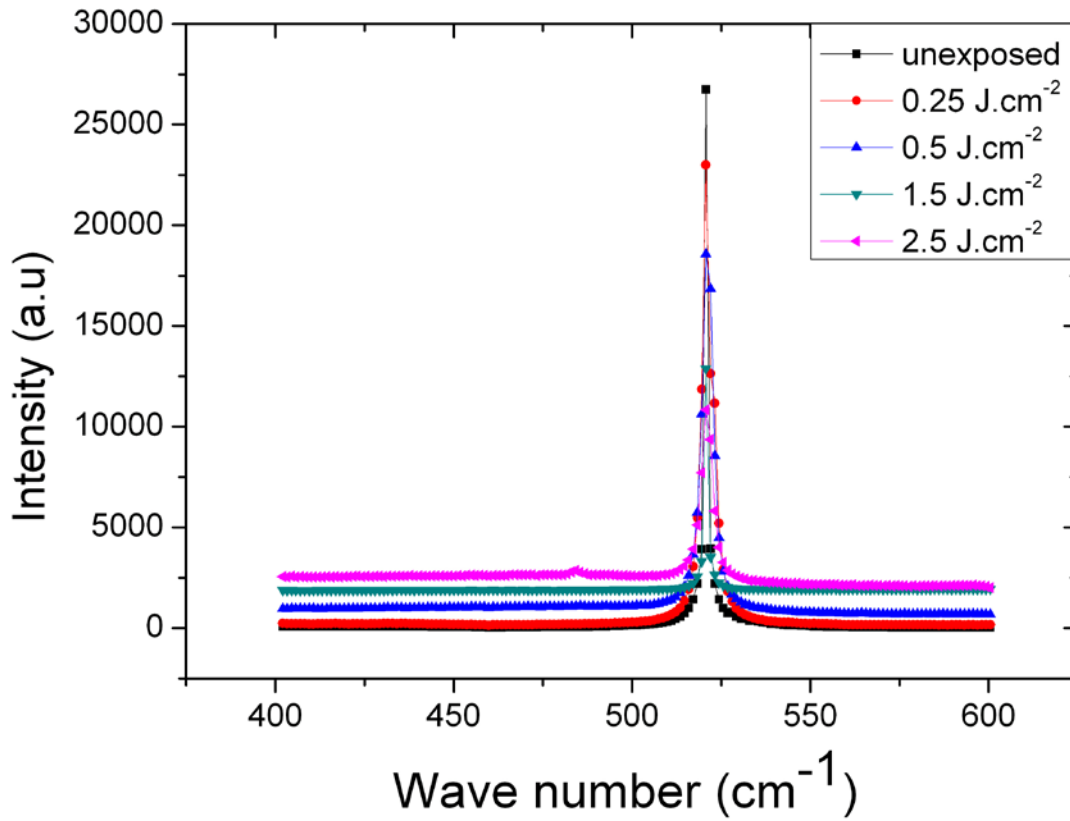


Figure 3.28: Raman spectra of the pristine and single pulse irradiated Si in air for different fluences  $0.25 \text{ J.cm}^{-2}$ ,  $0.5 \text{ J.cm}^{-2}$ ,  $1.5 \text{ J.cm}^{-2}$  and  $2.5 \text{ J.cm}^{-2}$ .

However, a TO-peak with a significantly reduced intensity is observed. This can be attributed to localized defects without bulk melting and thermal gradients. The observations of Figure 3.14 and 3.15 (regarding nanohillock-formation) along with figure 3.27 and 3.28 (Raman measurements) imply that for energies around the ablation threshold, a mechanism takes place, which is extremely localized (in spite of the fact that the laser spot is typically  $100 \mu\text{m}$  and more in diameter). As revealed by particle ejection and surface modification through the nanohillock formation, it is confined to very much localized spots. Together with this information CE seems to be an appropriate explanation for particles emitted with several eV, caused by excitations with a fs timescale and a strong geometric localization. For higher fluence ( $2.5 \text{ Jcm}^{-2}$ ) in case of air, the significantly reduced intensity in TO-band with an appearance of a small new disorder band at  $473\text{cm}^{-1}$  is observed. This disorder band appears where a transition from electronic processes (nanoablation) to thermal processes takes place with the appearance of more disturbed Si surface.

Figure 3.29 shows Raman spectra of the pristine and 20 pulse irradiated Si for different laser fluences (ranging  $0.5\text{-}3.5 \text{ J.cm}^{-2}$ ) after its exposure in UHV condition. This behavior (along with AFM topography shown in Figure 3.17, 3.19 and 3.22) for higher fluences represents the



transition from localized electronic processes (ultrafast melting) to a large class of thermal processes, which eventually result in the total loss of localization, if the entire lattice is heated. For a fluence of  $0.5 \text{ J.cm}^{-2}$  only a reduced intensity in TO band is observed. The structural disordering of the Si is observed for a fluence of  $1.5 \text{ J.cm}^{-2}$  and above. A Raman spectrum reveals a broadening in the TO-peak which is attributed to the formation of polycrystalline silicon (pc-Si) with small traces of amorphization. The target exposed to higher fluences  $2.5 \text{ J.cm}^{-2}$  and  $3.5 \text{ J.cm}^{-2}$  shows a relatively broadened and low intensity peak centered around  $520 \text{ cm}^{-1}$  with one additional shifted peak at  $514 \text{ cm}^{-1}$  and appearance of an additional peak with very small intensity with maxima at  $480 \text{ cm}^{-1}$ . This band represents an amorphization of a Si. For these fluences both the behaviors of polycrystallization and amorphization phases are observed which are related to surface melting and resolidification [75, 108, 158]. The resolidification times and velocities are strongly affected by the temperature gradient and the amount of latent heat stored in the remaining liquid layer of varying thickness (dependent on the laser fluence). Thus, the release of latent heat of crystallization can retard the solidification process at moderate-fluence multipulse-irradiation. This leads to the formation of (poly-) crystalline material. At high fluences with multipulse-irradiation enhanced thermal processes are observed. This will lead to steep lateral temperature gradients induced high cooling rates. Thus, the time for resolidification is too small for the formation of crystallites. Consequently, the surface solidifies into an amorphous state. The presence of *a*-Si implies the presence of liquid silicon (*l*-Si). Amorphous-Si formed by the rapid solidification of the molten region (*l*-Si). The existence of very high pressure up to 500 GPa (evaluated from a graph of Figure 3.24 ) during ablation will push out the molten material and force it to form protrusions, mountains and islands [158]. The generation of bumps and islands as revealed by surface topography is attributable to the generation of thermal stresses, which is revealed by a corresponding Raman shift ( $7 \text{ cm}^{-1}$ ). Their sizes depend on stresses, i.e., on the density of generated defects. Relaxation of these stresses can be considered as the possible cause of the formation of micrometer-sized structures (figure 3.22 a and b).

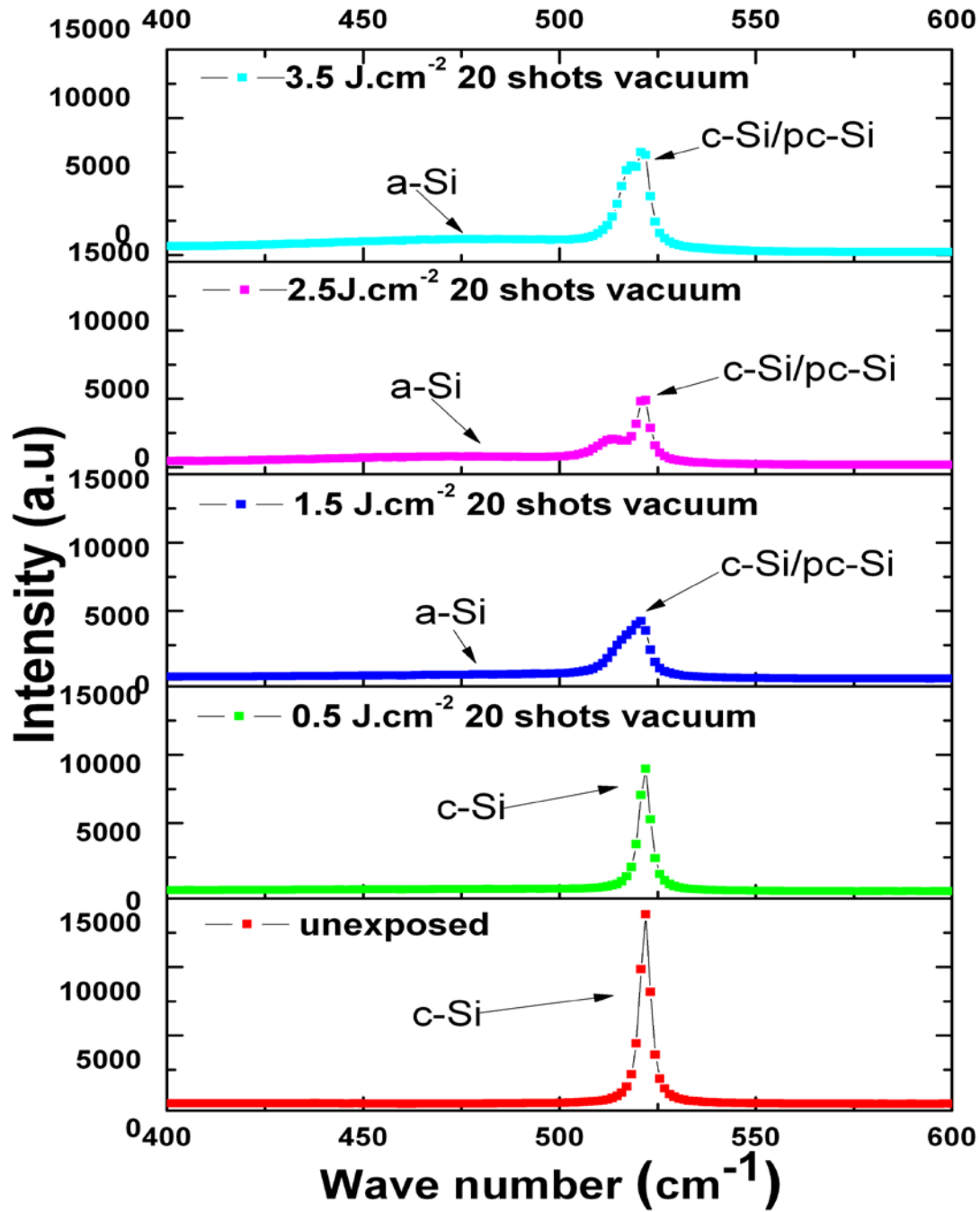


Figure 3.29: Raman spectra of the pristine and irradiated Si in UHV for 20 shots at different laser fluences 0.5 J.cm<sup>-2</sup>, 1.5 J.cm<sup>-2</sup>, 2.5 J.cm<sup>-2</sup>, and 3.5 J.cm<sup>-2</sup>.

### 3.4 Results for metal (Al)

#### 3.4.1 AFM Measurements

##### *(a) Low fluence regime*

An interesting and challenging question is, whether nanohillocks can also be observed on metal surfaces. As shown in the previous sections, the appearance of nano-sized hillocks under specific conditions can be regarded as a strong argument for a class of mechanisms, which involve charging of the irradiated volume and a subsequent disintegration of the volume. This requires that the potential energy is transferred into kinetic energy fast enough, in particular, this time has to be shorter than the time for neutralization of the charged volume. In metals this is questionable because of the high number of non-localized electrons. On the other hand, this assumption does not take into account, that the electronic structure of the material exposed to ultra short laser light might be totally different from the initial metallic structure. Therefore, it is of fundamental interest to study the surface topography as it develops under ultra-short-laser radiation for metals, in particular, close to the ablation threshold.

CE for fs irradiation of dielectric materials is, already discussed in detail, debated but accepted. In case of metals it is still controversial. If the surface topographical features obtained after near infrared femtosecond pulses for a dielectric and a semiconductor material are similar to a metal, then a comparison can give a clue that similar kind of nonthermal (electronic processes either Coulomb Explosion or Surface Optical Rectification (SOR)) ablation is responsible for energy deposition for all three kind of materials insulators, semiconductors and metals.

Previously Coulomb explosion is proposed as one possible mechanism for ultra-short-laser ablation [13, 14, 68], even on metals. In summary, it is argued that Coulomb explosion (or a related process) is observed, if the laser energy is deposited in a very short time (i.e. 20-200 fs depending on the material), as identified by pump-probe experiments. The particles emitted via this mechanism are characterized by a few eV kinetic energy. Furthermore, if the laser fluence is increased above a few hundred  $\text{mJ.cm}^{-2}$ , thermal processes start to dominate, masking ultra fast Coulomb explosion effects. For this purpose, the surface topography with respect to nanohillocks for an Al polycrystalline target has been investigated. The vacuum conditions ( $10^{-9}$  mbar) and the average number of laser shots of approximately 50-100 hitting the surface under the conditions of the experiment guarantee an oxide free surface. The results for Al under UHV condition are summarized in figure 3.30. The estimated value for the

deposited energy per atom amounts to 1.3 eV/atom for Al at a laser fluence of  $0.12 \text{ J.cm}^{-2}$ . Comparing the results in figure 3.30 with the results shown in figure 3.1 and 3.14, the same trends are observed. However, the transition from the hillock to the ultrafast melting or thermal dominated regime is shifted to lower laser energies. This can be attributed to a lower melting threshold energy /atom ( $E_m$  in eV/atom ) for Al (0.3 eV/atom) [92] as compared to Si (0.53 eV/atom ) [93] and  $\text{CaF}_2$  (0.55 eV/atom) [94]. But the important evidence of nanohillocks is clearly visible.

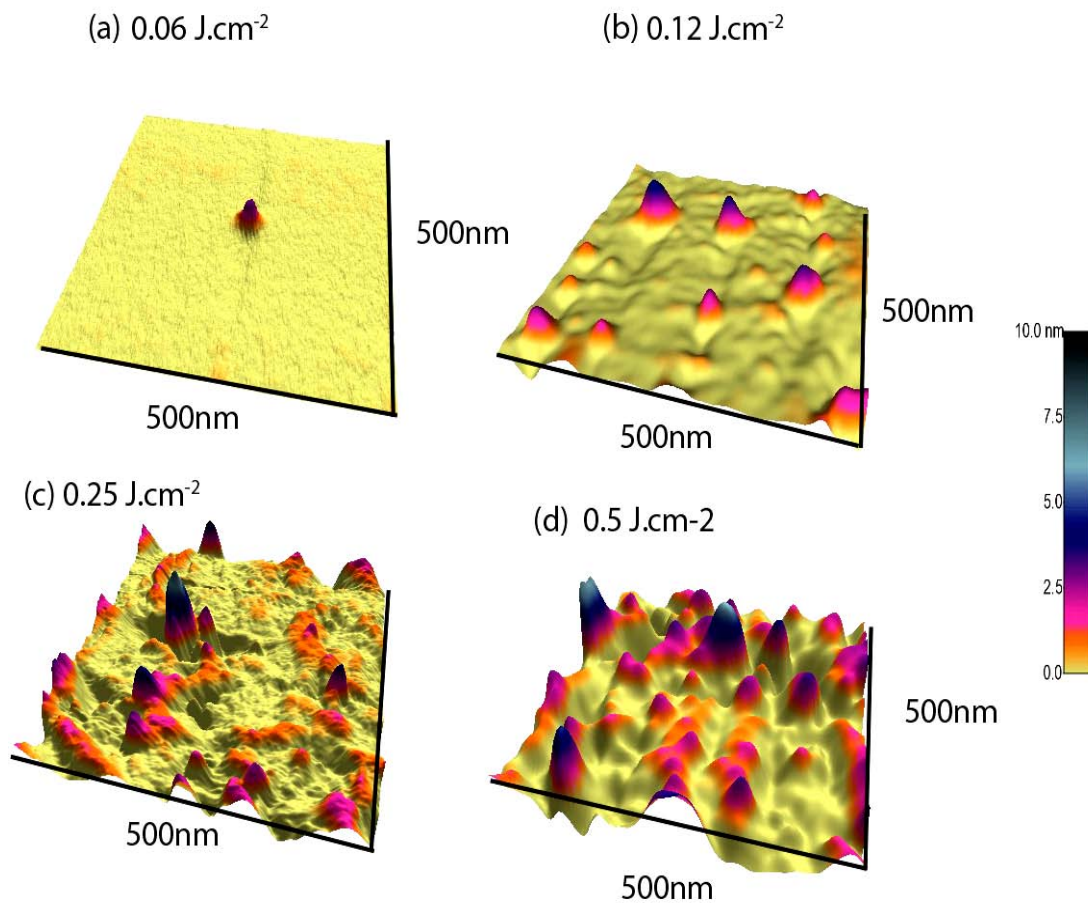


Figure 3.30: AFM Topographic images of nanohillock-formation on an Al surface (scan area  $500\text{nm} \times 500 \text{ nm}$ ) as a result of 25fs laser irradiation in UHV condition at the fluence (a)  $0.06 \text{ J.cm}^{-2}$  (b)  $0.12 \text{ J.cm}^{-2}$  (c)  $0.25 \text{ J.cm}^{-2}$  (d)  $0.5 \text{ J.cm}^{-2}$ .

The appearance of nanohillocks on an Al surface with increasing laser fluences under ambient condition is shown by the AFM surface topographical images in figure 3.31. The general

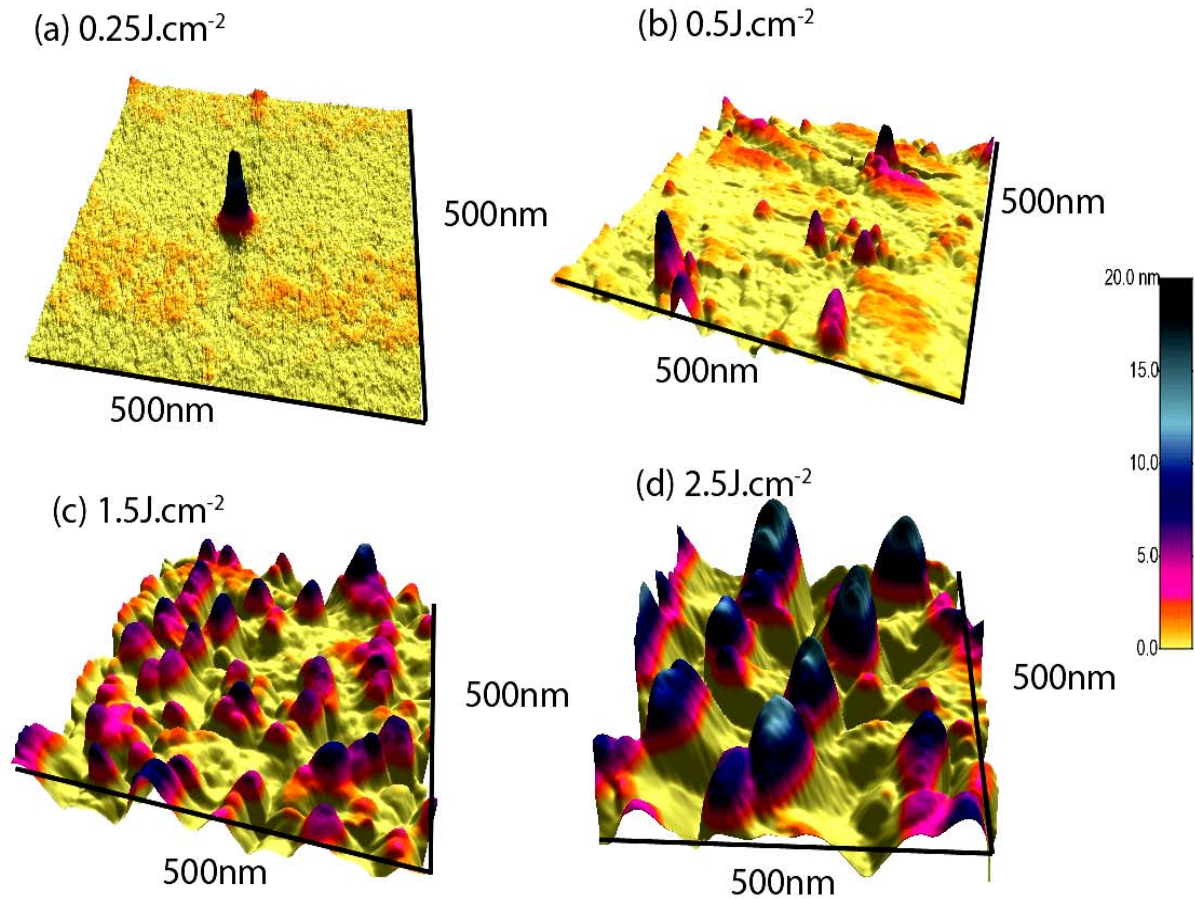


Figure 3.31: AFM Topographic images of nanohillock-formation on an Al surface (scan area 500 nm×500 nm) as a result of laser irradiation in air at fluences (a)  $0.25 \text{ J.cm}^{-2}$  (b)  $0.5 \text{ J.cm}^{-2}$  (c)  $1.5 \text{ J.cm}^{-2}$  (d)  $2.5 \text{ J.cm}^{-2}$ .

tendency as found, going from  $\text{CaF}_2$  to Si, has been further verified for Al (both in case of UHV and ambient condition) with the only difference that nanoprotusion are of larger heights in case of Al than Si and  $\text{CaF}_2$ . If the laser fluence is further increased to  $2.5 \text{ J.cm}^{-2}$  in case of air, the entire surface is severely disturbed with no localized nanohillocks but with an appearance of bumps with an average diameter greater than 100 nm and of height 20-25 nm, as shown in figure 3.31 (d). Further increase of laser fluence makes the surface more disturbed and no localized and isolated nanohillocks could be observed for higher fluences.

To understand the experimental results described above, three important observations can serve as a starting point: firstly, the characteristic features of the observed material in particular ultra-short-laser ablations of dielectrics, semiconductors and metals have a lot in common. Secondly, energy deposition into the electronic system by ultrashort-laser pulses seems to initiate similar or identical processes observed for bombardment with highly charged ions, where a substantial part of the kinetic energy of the ions is deposited as inelastic energy.

These unique features of the surface topography can be correlated with specific particle energies already shown and discussed in figure 3.26.

Coulomb explosion model is considered as more adequate description of track formation in metals irradiated by heavy ions as compared to the T-spike model [159]. It also seems to be an appropriate explanation for particles emission [13, 44], caused by excitations on fs timescale. In localized nanometer sized areas within the laser spot the energy deposition and creation of a hot electron density is developed. These hot electrons drift out resulting in positively charged small volumes, where the charging can lead to Coulomb explosion.

The effect of laser fluence on the geometrical size (diameter and height) of these nanohillocks after exposing the target in air and vacuum is shown in figure 3.32. For air and vacuum, both the average diameter and height of hillocks increase with increasing laser energy and are ascribed to an increased energy deposition.

Finally, the issue of CE, which is well accepted in dielectrics [72, 103] and is still a source

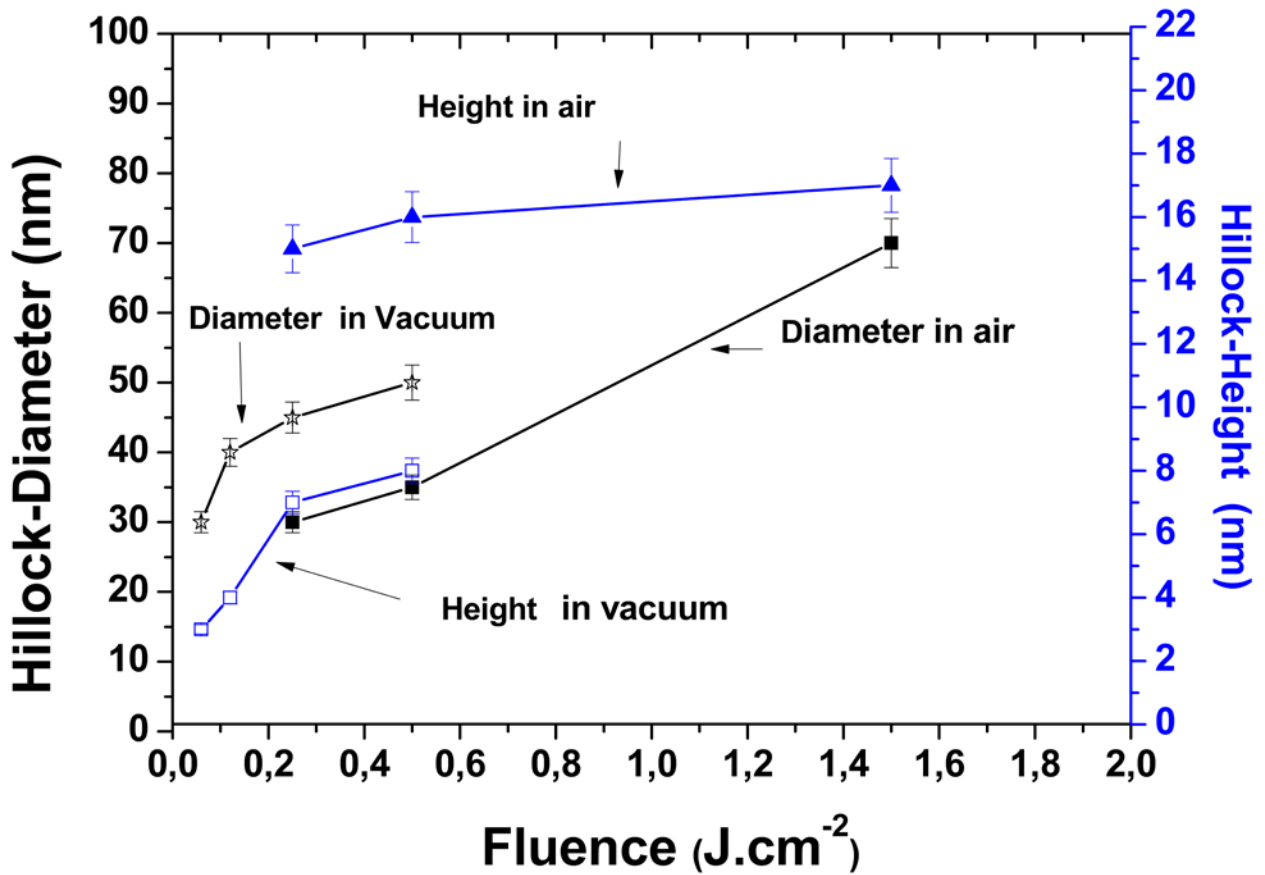


Figure 3.32: Average diameter and height of nanohillocks formed on an Al surface versus laser fluence as result of 25fs laser irradiation in air and under UHV condition.

of debate for metals, is once more addressed here. Coulomb explosion of a metal exposed to an intense picoseconds laser pulse has been simulated by Rukhadze et al [38] assuming a plasma layer. It is shown that plasma electrons leave the plasma layer under the action of the ponderomotive force opposing the laser radiation field gradient, whereas plasma ions are ejected away in the field of the self-space charge. For metals an analytic model is proposed by Bychenkov et al [39] that describes the generation of a monoenergetic beam of light ions during the Coulomb explosion of a stratified target irradiated by an ultrashort high-power laser pulse. It is proposed in this model that when the laser intensity is so high that all the target electrons escape into a vacuum, the ions are accelerated due to a Coulomb explosion. For a foil made of a high-Z material, the time scale on which the ions of the light coating are accelerated is too short for the ions to expand appreciably [39]. A basic condition (equation 3.17) for Coulomb explosion has been formulated in such a way, that irrespective of how the energy is applied to the metal, the laser pulse duration ( $\tau$ ) should be smaller than the time required by metal ions to obtain sufficient energy to be ejected from the target surface [39].

$$\tau < (\delta \nu_e)^{-1} \quad 3.17$$

Where  $\tau$  is the pulse duration,  $\nu_e$  is the electron–electron elastic collision rate ( $\nu_e = 10^{15} \text{s}^{-1}$ ) and  $\delta$  is the fraction of the energy that is transferred to the crystal lattice. For metals,  $\delta = 10^{-4} - 10^{-3}$  and  $\tau = 10^{-11} - 10^{-10}$  [38]. Dachraoui and Husinsky [12-14] provided a wealth of experimental evidence, that CE is a possible and probable explanation. Therefore, it is justified to explain the results presented here in the context of CE. The laser energies per pulse and the pulse width of 25 fs are sufficient to create the charging required for CE. In particular, the localized hillocks might imply that a large area (laser spot) is charged due to loss of hot electrons, but only a few localized spots surrounded by an electron deficient area become sufficiently charged for a time long enough to experience Coulomb explosion. Thus it can be understood, why even in a metal the charging can be maintained in the actual place, where the CE takes place. Results of a numerical calculation by Rethfeld et al [30] for Al (100 fs pulses;  $h\nu = 2 \text{ eV}$ ) show that the laser-excited electron energy distribution thermalizes within 100 fs for sufficiently high excitations [22].

An alternative and interesting option is surface optical rectification (SOR) proposed by Vella et al. [160]. It can be considered as a responsible mechanism for the removal of atoms from a metal surface within a time as short as few hundreds of femtosecond where thermal effects are probably not dominant. Optical Rectification (OR) is a classical second-order nonlinear optical process taking place in non-centrosymmetric materials [160, 161]. It is also predicted to occur at the surfaces of all materials, where inversion symmetry is broken by the strong

material gradients. Vella [18] proposed an interpretation of ultrafast LAFIE (Laser Assisted Field Ion Emission) as resulting from the action of the quasi dc (THz) electric field generated by the electronic nonlinear optical response of the metal surface: the so-called optical rectification effect for explaining the results of pump-probe experiments which indicate that the ion emission is actually taking place on a femtosecond time scale [48]. According to Vella [18], the ablation thresholds (a nonthermal ablation regime) reported in [13, 14] developing on the femtosecond time scale can also be explained by the OR model. In this case, however, the striking similarities between highly charged ion and laser irradiation cannot be explained.

Of course, one puzzle still exists: Why does a particle emission process like CE or SOR result in hillock formation and not the creation of nano-sized craters, as one would expect? This question cannot definitely be answered yet, but preliminary MD simulations [162] indicate the emission of particles from a highly localized spot can result in particle extrusions (hillocks) as “leftovers”.

It is remarkable, that an appearance of hillocks for all materials have been investigated exactly under these conditions (laser energy) for which a substantial part of the ejected particles have kinetic energies of several eV (figure 3.26) and for which Coulomb explosion has been postulated as a highly probable explanation [14]. Another model has been suggested for highly charged ions [15]. Computer simulations of the formation of nano-bumps on thin Ni films [16] yield a similar overall picture for the hillock formation. However, in particular the short timescale, in which the energy has to be deposited favors a Coulomb-like process. Nanohillock formation together with fast particle emission is observed exactly in this case, where the laser energy is deposited within less than 50 fs (except 200 fs for Au). Processes where the electron-phonon coupling comes into play, exhibit less stringent requirements on the timescale of the energy deposition. They start to dominate at higher laser intensities (above 300 mJ/cm<sup>2</sup>) for all materials (figures 3.1-3.14 and 3.30). Characteristic for these processes are the much lower particle energies (200 meV at 300 mJ/cm<sup>2</sup> laser energy) and the optimal energy deposition time (pulse shape) [12].

These results confirm and support the idea that different materials behave roughly in the same manner when they are irradiated by femtosecond pulses at intensities around the ablation threshold. In this condition, the very general mechanisms responsible for the ejection of matter always seem to lead to similar characteristic features, regardless of the specific nature of the target material (dielectric, semiconductor or metal).



In addition to an appearance of nanohillocks on an Al surface, additional remarkable features in the low fluence regime (around ablation threshold) is the formation of nanoripples under specific conditions. Figure 3.33 (a-c) (scan area  $20\ \mu\text{m} \times 20\ \mu\text{m}$ ) shows topographical images of an Al surface. Figure 3.33 (a) is the image for a pristine surface and figure 3.33 (b-f) are images of irradiated surface after exposure to a laser fluence of  $0.25\ \text{J.cm}^{-2}$  with a single shot. Figure 3.33 (c) (scan area  $20\ \mu\text{m} \times 20\ \mu\text{m}$ ) is the 3D image of (b) and reveals the surface topography where a coexistence of nanohillocks as well as nanoripples is encountered on an Al surface. A Magnified view of figure 3.33 (b) with nanohillock- formation (scan area  $500\ \text{nm} \times 500\ \text{nm}$ ) is shown in figure 3.33 (d) whereas a magnified view of figure 3.33 (b) with nanoripple-formation (scan area  $500\ \text{nm} \times 500\ \text{nm}$ ) is presented in figure 3.33 (e). Ripple structures with spacing significantly smaller than the irradiation wavelength are observed. The corresponding 2-D image and cross-section profile are also shown in of 3.33 (f) and 3.33 (g) respectively. It is evident that these periodic surface structures have very clear contours and sharp edges with an average spatial periodicity of 20 nm and an average height of 2 nm. Figure 3.34 shows AFM topographic images of the Al surface after single shot irradiation, but at a fluence higher than in figure 3.33 i.e.  $0.5\ \text{J.cm}^{-2}$ . Figure 3.34 (a) is a 2D image and figure 3.34 (b) is its corresponding 3D (scan area  $20\ \mu\text{m} \times 20\ \mu\text{m}$ ). These two images, once more reveal a coexistence of nanohillocks with nanoripples at the surface. A magnified view of the results of figure 3.34 (a) for nanohillock- formation (scan area  $500\ \text{nm} \times 500\ \text{nm}$ ) is shown in figure 3.34 (c), whereas a magnified view of figure 3.34 (a & b) with nanoripple-formation (scan area  $500\ \text{nm} \times 500\ \text{nm}$ ) is presented in figure 3.34 (d). In Figure 3.34 (e), a section profile of figure 3.34 (d) is shown. The results reveal that the periodicity of ripples is enhanced from 20 to 100 nm, but the average height of the ripples remains more or less the same after increasing the fluence from  $0.25\ \text{J.cm}^{-2}$  to  $0.5\ \text{J.cm}^{-2}$ . It should be noted here that this fluence regime ( $0.25\text{-}0.5\ \text{J.cm}^{-2}$ ) is the same where we have observed nanohillock-like structures on an Al and is close to the single pulse modification threshold of Al  $0.3\ \text{J.cm}^{-2}$  (experimental) [163] and  $0.5\ \text{J.cm}^{-2}$  (numerical) [164].

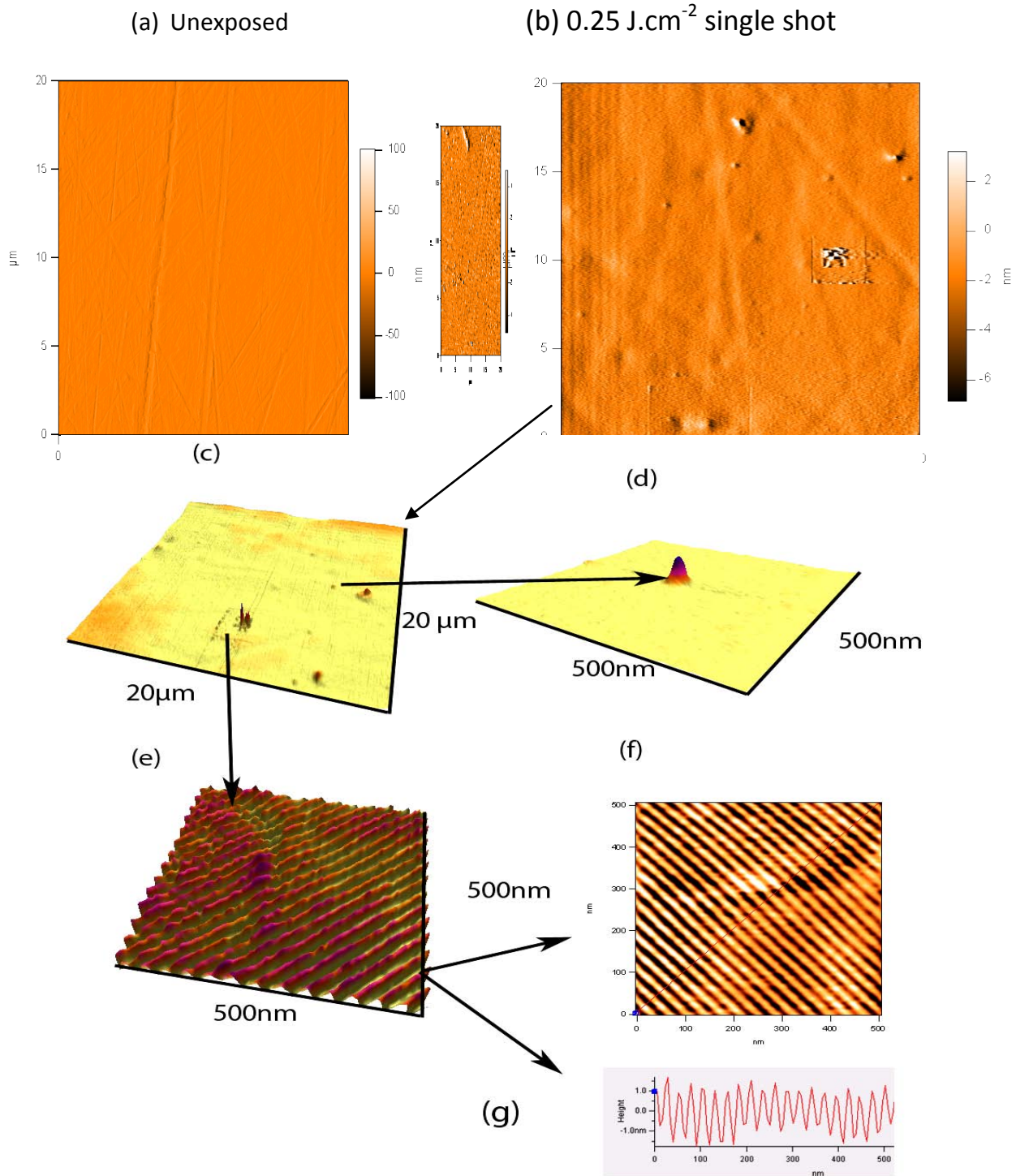


Figure 3.33: AFM Topographic images of the Al surface (a) unexposed surface, (b-g) Images as a result of single shot irradiation at a fluence of  $0.25 \text{ J.cm}^{-2}$  (b) 2D image, (c) 3D image of figure b, (d) Magnified view of c with nanohillock-formation (scan area  $500 \text{ nm} \times 500 \text{ nm}$ ), (e) Magnified view of c with nanoripple-formation (scan area  $500 \text{ nm} \times 500 \text{ nm}$ ), (f) 2D image of e, (g) A section profile of f.

The formation of periodic surface structures can be attributed to the excitation of surface plasmon polaritons (SPP). They can induce the periodic enhancement of local fields in the

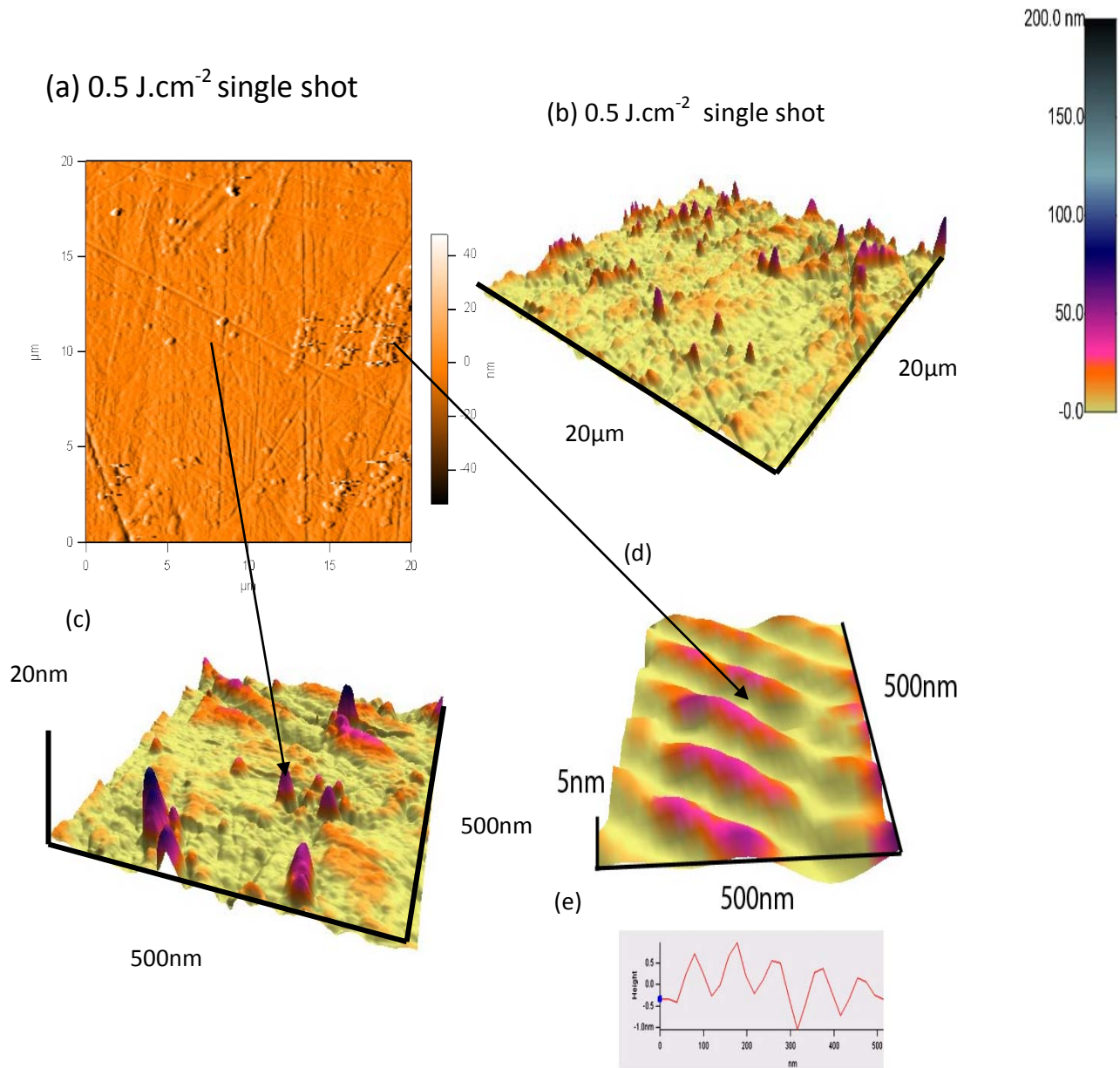


Figure 3.34: AFM Topographic images of the Al surface as a result of single shot of laser irradiation at a fluence of  $0.5 \text{ J.cm}^{-2}$  (a) 2D image (scan area  $20 \mu\text{m} \times 20 \mu\text{m}$ ), (b) 3D image of (a) (c) Magnified view of (a) & (b) with nanohillock-formation (scan area  $500 \text{ nm} \times 500 \text{ nm}$ ), (d) Magnified view of (a) & (b) with nanoripple-formation (scan area  $500 \text{ nm} \times 500 \text{ nm}$ ), (e) A section profile of figure d.

surface layer. SPPs result from the coherent interaction of the incident laser field with free electrons created in the material [104]. When the photon intensity is sufficiently high, as a general rule  $nh\nu > \Phi$  ( $\Phi$  is work function), the multiphoton ionization (photoemission (nPPE)) process can be plasmon-mediated. It has a much higher transition probability and photons are “saved” for several fs in the plasmon state, leading to high concentration of electromagnetic energy in the nanoparticle. This, in turn, leads to a higher local intensity due to the plasmon near field and thus to a higher photon density [165]. In the case of irradiation of metal clusters

by intense lasers one observes, not surprisingly, that the plasmon resonance plays a key role in relation with the laser frequency. As long as the laser frequency is far from the plasmon frequency, the electronic response exhibits a typical off resonant behavior: the dipole response exactly follows the laser pulse and ionization is comparatively small. On the contrary, when the plasmon frequency is close to the laser frequency, one observes a resonant effect: both the dipole response and ionization are strongly enhanced and the dipole oscillations survive long after the laser has been switched off. As long as the laser pulse is sufficiently short (below a few tens of fs in the case of sodium) [166], these effects remain purely of electronic nature and reflect the existence of the plasmon frequency in the system [167].

In the case of “femtosecond” lasers, the excitation typically takes place around tens of fs. It should be noted that this time is directly comparable to the time characteristics of the valence electron cloud. Not surprisingly, the cluster response (a large collection of atoms forming nanohillocks in our case) will thus be primarily of electronic nature. This response is characterized by a direct emission of electrons and a collective oscillation of the electron cloud with respect to the ionic background (Mie plasmon). The time scales are here typically of order 1-10 fs. In a second stage, the collective oscillations are damped and the electron cloud starts to relax its initial excitation energy into intrinsic (thermal) excitation energy by electron-electron collisions. The time scales associated to these two effects depend both on cluster size and deposited excitation energy (electron electron collisions, around 10–100 fs [167]).

Comparing results of Al with Si and CaF<sub>2</sub> it is obvious that threshold fluence for the nanoripple-formation for the semiconductor is higher than for the metal or for the dielectric. Nanoripples formed on a Si surface have been observed with 10 succeeding pulses, whereas in case of Al and CaF<sub>2</sub> these features have been observed with a single shot irradiation.

### ***(b) Moderate fluence regime***

Figure 3.35 (a-h) (scan area 20  $\mu\text{m} \times 20 \mu\text{m}$ ) shows topographical images of Al after the exposure for increasing laser fluences under UHV conditions. On the left hand side a 2D-image and on the RHS corresponding 3D images are presented. The image in figure 3.34 (a & b) reveals the surface topography where an existence of nanohillocks is almost vanished and bumps-formation is encountered at a fluence of 0.25 J.cm<sup>-2</sup> for 20 succeeding pulses. Two kinds of bumps are observed: bigger bumps with a typical diameter of 1-1.2 $\mu\text{m}$  and of height 50-80 nm; smaller bumps of diameter 50-80 nm with an average height of 10 nm.



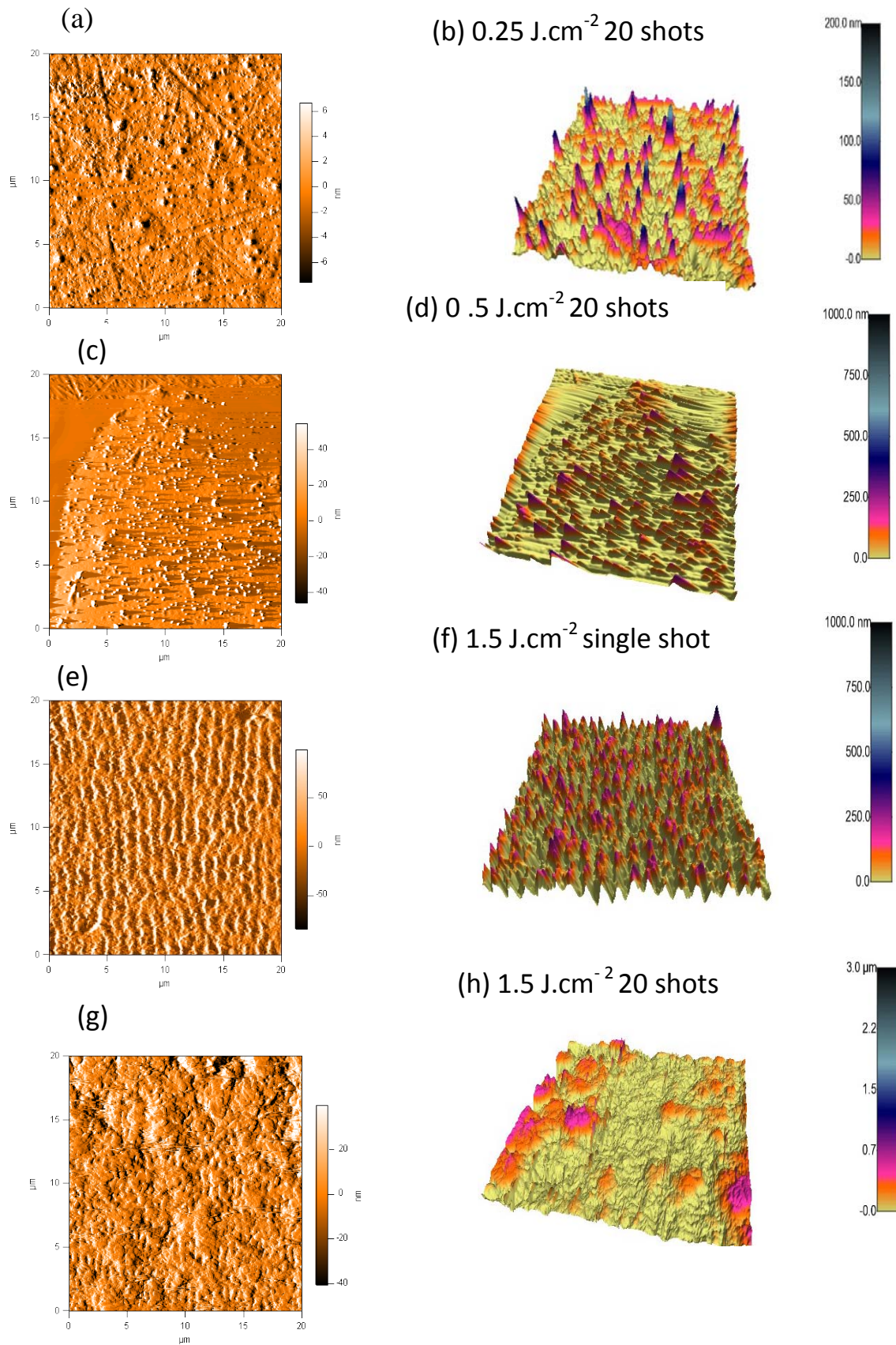


Figure 3.35: Topographical images of an Al after its exposure to increasing laser fluences (at moderate fluence regime) under UHV condition. LHS 2D and RHS corresponding 3-D images (a & b) 0.5 J.cm<sup>-2</sup> for single shot (c & d) 1 J.cm<sup>-2</sup> for 20 shots (e & f) 1.5 J.cm<sup>-2</sup> for single shot (g & h) 1.5 J.cm<sup>-2</sup> for 20 shots.

These smaller bumps have dimensions close to nanohillocks (diameter 50-150 nm and heights 10-20 nm) which imply that two processes (CE and UFM) are superimposed in this fluence regime. The other remarkable feature observed in this figure is an appearance of nanopores on the metallic surface. The typical diameter of these pores is 100-150 nm with an average depth of 1-3 nm.

The surface topography shown in figure 3.35 (c & d) demonstrates the coexistence of bump-formation with an appearance of surface ripples on an Al surface after exposing it to a fluence of  $0.5 \text{ J.cm}^{-2}$  for 20 shots. These bumps are non-symmetrical in their shapes and appear with an average size of 250 nm with an average height of 50 nm. Its magnified view is clearly seen in the figure 3.36 (a) (scan area  $1\mu\text{m}\times 1\mu\text{m}$ ). The top of these bumps is covered with ripples whose enlarged view is presented in figure 3.36 (b) (scan area  $160 \text{ nm} \times 160 \text{ nm}$ ) with its corresponding cross section profile (figure 3.36 c). The average periodicity of these nanoripples is 40 nm and an average height is 2 nm.

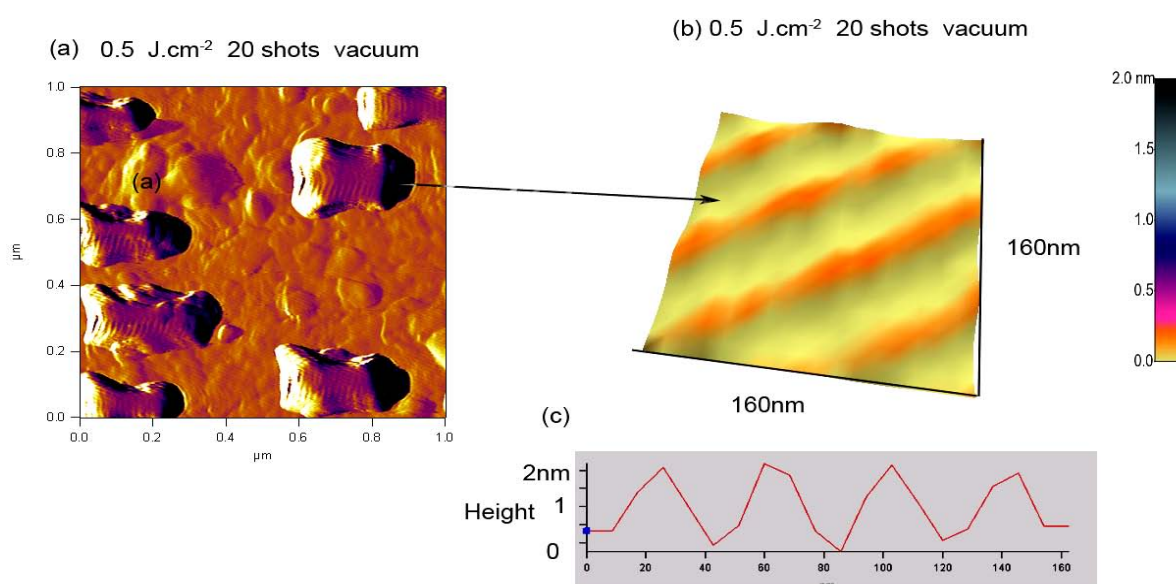


Figure 3.36: Magnified view of figure 3.35 (c & d) (a) Bump-formation on an Al surface at a fluence of  $0.5 \text{ J.cm}^{-2}$  under UHV condition with 20 shots (b) Nanoripple-formation on the top of bumps (c) A section profile of figure 3.38(b).

For an increasing fluence of  $1.5 \text{ J.cm}^{-2}$  with single shot irradiation, classical ripples (LIPSS) are formed on an Al surface shown in figure 3.35 (e & f) as 2D & 3D images. The average periodicity of these ripples is  $1.1 \mu\text{m}$  and an average height of 500 nm. We call these ripples as classical ripples because their periodicity is larger than laser wavelength.

Figure 3.37 (a-c) also shows topographical images of an Al surface after its exposure to a same fluence ( $1.5 \text{ J.cm}^{-2}$ ) as figure 3.35 (e & f) but with a different scan area. The

observations of figures (3.37 a-c) suggest that the appearance of nanoripples at the periphery of classical ripples have not been observed as in case of Si and CaF<sub>2</sub>. Magnified 2D and 3D images of classical ripples (scan area 5 $\mu\text{m}\times 5\mu\text{m}$ ) are shown in figure 3.37 (d & e) with the corresponding section profile in figure 3.37 (f). A detailed AFM analysis yields direct evidence that two kinds of ripples are also formed on the irradiated surface: classical ripples

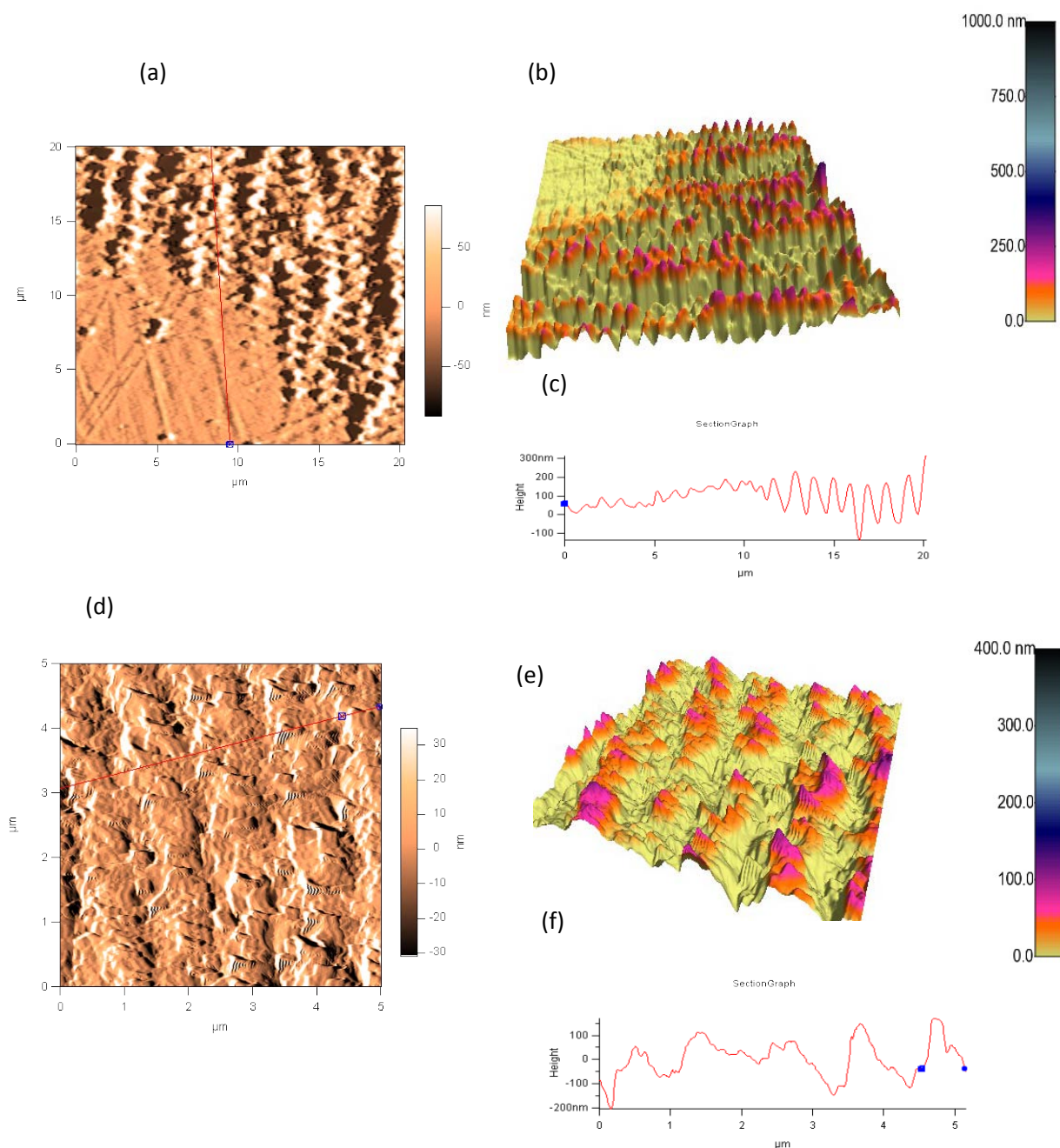


Figure 3.37: Topographical images of an Al surface after its exposure to a fluence of 1.5 J.cm<sup>-2</sup> for a single shot irradiation under UHV condition. (a & b) different scan area (periphery of figure 3.35 e & f ), (c) Cross-section profiles of a, (d) A magnified 2D view of classical ripples, (e) 3D image of d , (f) A section profile of d.



with periodicity of  $1.1\ \mu\text{m}$  and nanoripples which can be observed at the top of an each bump having a periodicity of  $100\ \text{nm}$ .

For a same fluence of  $1.5\ \text{J}\cdot\text{cm}^{-2}$  as used in figure 3.35 (e & f) and figure 3.37, another scan area is shown in figure 3.38 (a-c). Figure 3.38 (a) is a 2-D image of an Al surface with a scan area  $20\ \mu\text{m} \times 20\ \mu\text{m}$ . A debris formation can clearly be identified in this image. The height of the debris is  $1.5\ \mu\text{m}$ . At the top of the debris nanoripples are observed. An enlarged view of these nanoripples is presented in figure 3.38 (b) (scan area  $1\ \mu\text{m} \times 1\ \mu\text{m}$ ) with its corresponding cross-section profile in figure 3.38 (c). The average periodicity of these ripples is of  $200\ \text{nm}$  with an average height of  $50\ \text{nm}$ .

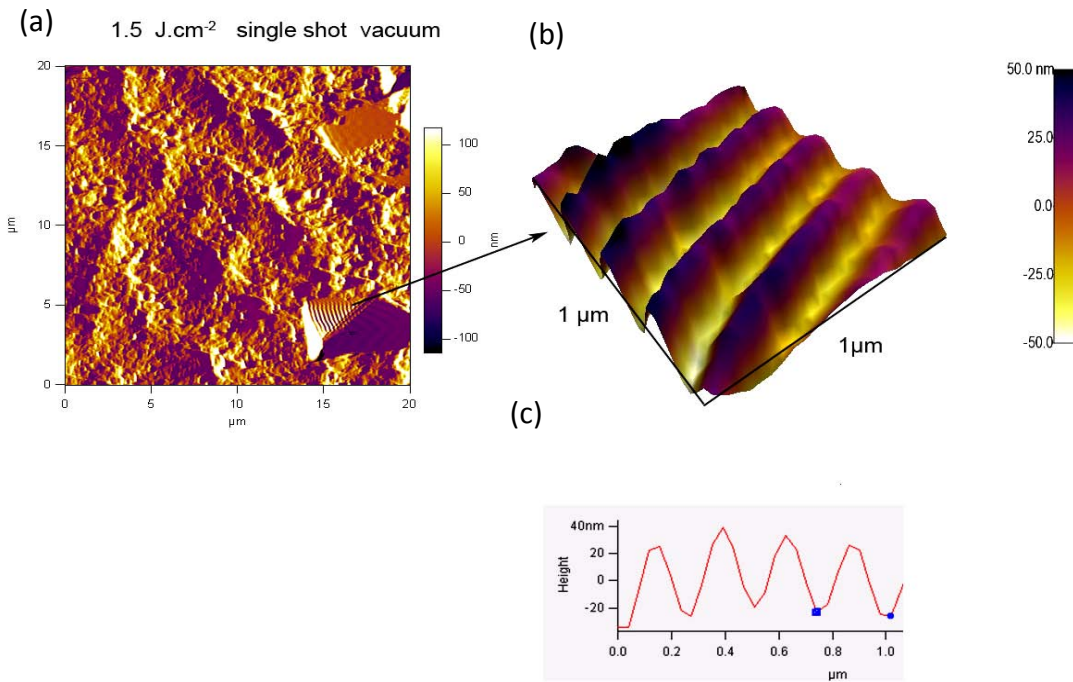


Figure 3.38: (a) A scan area with a debris at an Al surface after irradiating with a single shot at a fluence of  $1.5\ \text{J}\cdot\text{cm}^{-2}$  under UHV condition (scan area  $20\ \mu\text{m} \times 20\ \mu\text{m}$ ), (b) Nanoripple-formation on the top of debris (scan area  $1\ \mu\text{m} \times 1\ \mu\text{m}$ ), (c) A section profile of b.

Figure 3.35 (g & h) is the surface topography of an Al after its exposure to a same fluence of  $1.5\ \text{J}\cdot\text{cm}^{-2}$  but with 20 succeeding pulses. The periodicity is completely disturbed and chaotic surface structures are formed in this fluence regime due to high energy deposition.

The variation in the periodicity of nanogratings (for Al) with the laser fluence is presented by a graph in figure 3.39. This graph reveals that the periodicity of nanoripples increases with the increasing laser fluence.



The salient features from illustrated results are summarized as follows: For all materials (dielectrics, semiconductors and metals), self-organized nanoripples of periodicity much smaller than the laser wavelength are formed. These nanoripples are observed around the ablation threshold or for intensities slightly higher than the ablation threshold (within the lower fluence regime).

For fluences well above the ablation threshold, classical ripples of periodicity  $1\mu\text{m}$  or higher have been observed (at a moderate fluence regime).

Interspacing of ripples depends upon the material, the laser fluence and ambient conditions. For lower laser fluences the spacing of the patterned nanostructure has the tendency to be smaller (see figure 3.39).

For a dielectric and semiconductor these nanoripples have been observed at the periphery of ablated area for fluences well above the ablation threshold. Since the laser beam spatial profile is Gaussian, the appearance of these nanoripples in the periphery of the laser beam profile (typical Gaussian) is a consequence of the lower intensity of the laser beam in these regions. The appearance of nanoripples has not been observed at the periphery of the ablated

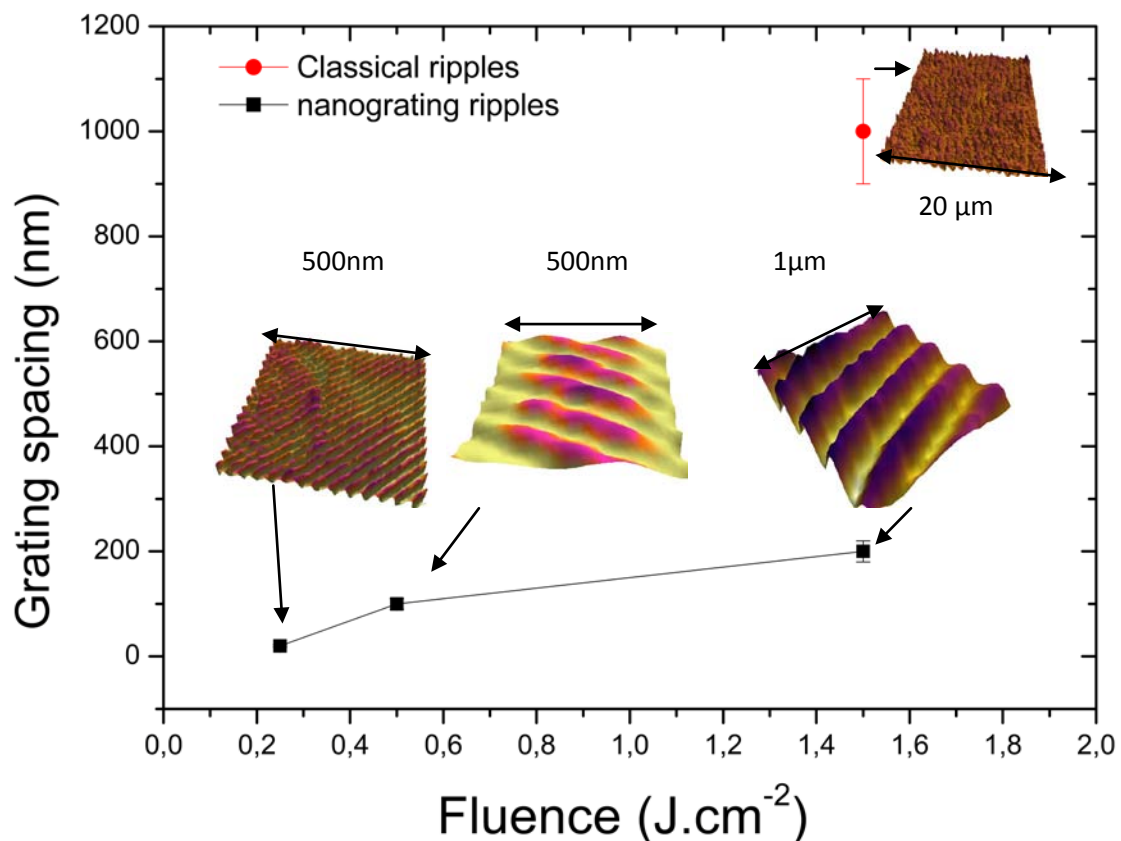


Figure 3.39: The dependence of interspaces of grating structures produced by femtosecond laser pulses on the laser fluence

areas for higher fluences in case of a metal. This can be attributed to lower melting threshold (eV/atom) of a metal as compared for a dielectric or a semiconductor. However, an appearance of nanoripples has been observed at the top of the bumps, with a periodicity ranging from 40 nm-200 nm. These results suggest that surfaces which are substantially non uniform (bump or debris-formation) can show high defect densities in the near-surface region and subsequent overlapping irradiation of pulses produces a gradually increasing buildup of defects and electric field enhancement in these regions. Laser waves can be scattered by rough sites on the surface. These scattered waves coupled with the nearby incident waves and will produce positive feedback and then propagate onto the surface causing self-organized subwavelength ripples in these regions. The formation of LIPSS in different materials by laser-irradiation is a complex process and the exact nature of the interaction is specific to the material and dependent upon the parameters like laser fluence and number of pulses used.

Generally, the laser energy is considered as deposited into the material faster than it can be dissipated by the classical channels of relaxation, i.e., thermal or mechanical, and an overheating of the system is realized with the consequent development of critical pressure gradients. Furthermore, at certain conditions, the laser energy can cause direct bond breaking, and ejection of single atoms, molecules or clusters. Depending on the processing conditions, a specific mechanism can be considered as dominant, but in a more general description of the process the contributions of different mechanisms, such as heterogeneous decomposition, liquid phase ejection and fragmentation, homogeneous nucleation and spinodal decomposition must be accounted for [168].

Addressing the peculiarities of femtosecond laser ablation of dielectric, semiconducting and metallic materials in the moderate fluence regime bump-formation is a commonly observed ablation process. This bump-formation is attributed either to ultrafast melting (plasma formation ) or is related to local volume increase caused due to buildup of stresses [16, 89] by fast laser heating. The relaxation of these compressive stresses, diffusion, transformation and aggregation of primary defects can be considered as responsible for the formation of these micro-bumps (photomechanical effects).

The main differences which have been observed are the explosion like features, which are prominently observed in case of  $\text{CaF}_2$  and have not been observed in case of Si and Al and are attributed to nonlinear absorption of the laser energy by the material through multi-photon [63] and avalanche [43] photoionization process, resulting in optical breakdown and the formation of a high-density plasma.

The bump-shape is nonsymmetrical in case of Al whereas highly symmetrical bumps have been observed in case of Si and CaF<sub>2</sub>.

**(c) High fluence regime**

Figure 3.40 (a-f) presents topographical images of an Al surface after its exposure to a high laser fluence ( $2.5 \text{ J.cm}^{-2}$  for 20 shots) under UHV condition. In figure 3.40 (a-b), a 2D and corresponding 3D image for scan area  $20 \mu\text{m} \times 20 \mu\text{m}$  are shown. Figure 3.40 (c-d) shows an enlarged view for scan area  $5 \mu\text{m} \times 5 \mu\text{m}$  with 2D and corresponding 3D images. In addition to this highly disturbed surface, the other remarkable features observed in these images are larger bumps of a typical dimensions of  $200 \times 400 \text{ nm}$  with an average height of  $100 \text{ nm}$  shown in figure 3.40 (e & f).

Figure 3.41 (a-d) presents topographical images of an Al surface after its exposure to higher laser fluences ( $3.5 \text{ J.cm}^{-2}$  for 20 shots) under UHV condition. In figure 3.41 (a-b) a 2D and corresponding 3D image for scan area  $20 \mu\text{m} \times 20 \mu\text{m}$  are shown respectively. Figure 3.41 (c-d) is an enlarged view with scan area  $5 \mu\text{m} \times 5 \mu\text{m}$  showing 2D and 3D images respectively. These images are representing a highly disturbed and chaotic surface of Al after its exposure to a fluence significantly higher than ablation threshold. This may be attributed to thermal ablation with high temperature rise at the surface. In addition to this highly disturbed surface, the other remarkable features are rectangular shaped bumps of typical dimensions of  $800 \times 900 \text{ nm}$  and an average height of  $100 \text{ nm}$ . At the top of each bump two or three nanobead-like structures can be seen (an enlarged view is shown in figure 3.41 (e)).

These images show a highly disturbed and chaotic surface of Al after its exposure to a fluence significantly higher than ablation threshold. This may be attributed to thermal ablation with high temperature rise at the surface. These nonsymmetrical shapes can be attributed to inhomogeneous nucleation, cluster formation and resolidification of a metallic surface after melting.

The surface topography of an irradiated Al surface with a fluence of  $3.5 \text{ J.cm}^{-2}$  for 20 shots in air is shown in figure 3.42 (a, c). The image is clearly demonstrating the following features. (1) Larger bumps with a diameter ranging from  $600 \text{ nm}$ - $1 \mu\text{m}$  and heights ranging from  $15$ - $35 \text{ nm}$ . (2) Smaller bumps with an average diameter of  $150 \text{ nm}$  and an average height of  $10 \text{ nm}$ . (3) Round-shaped nanocraters or crests with an average diameter of  $600 \text{ nm}$  and an average depth of  $20 \text{ nm}$ . A magnified view of one of this crater is shown in figure 3.42 (e). A large number of pores are also seen in this image.

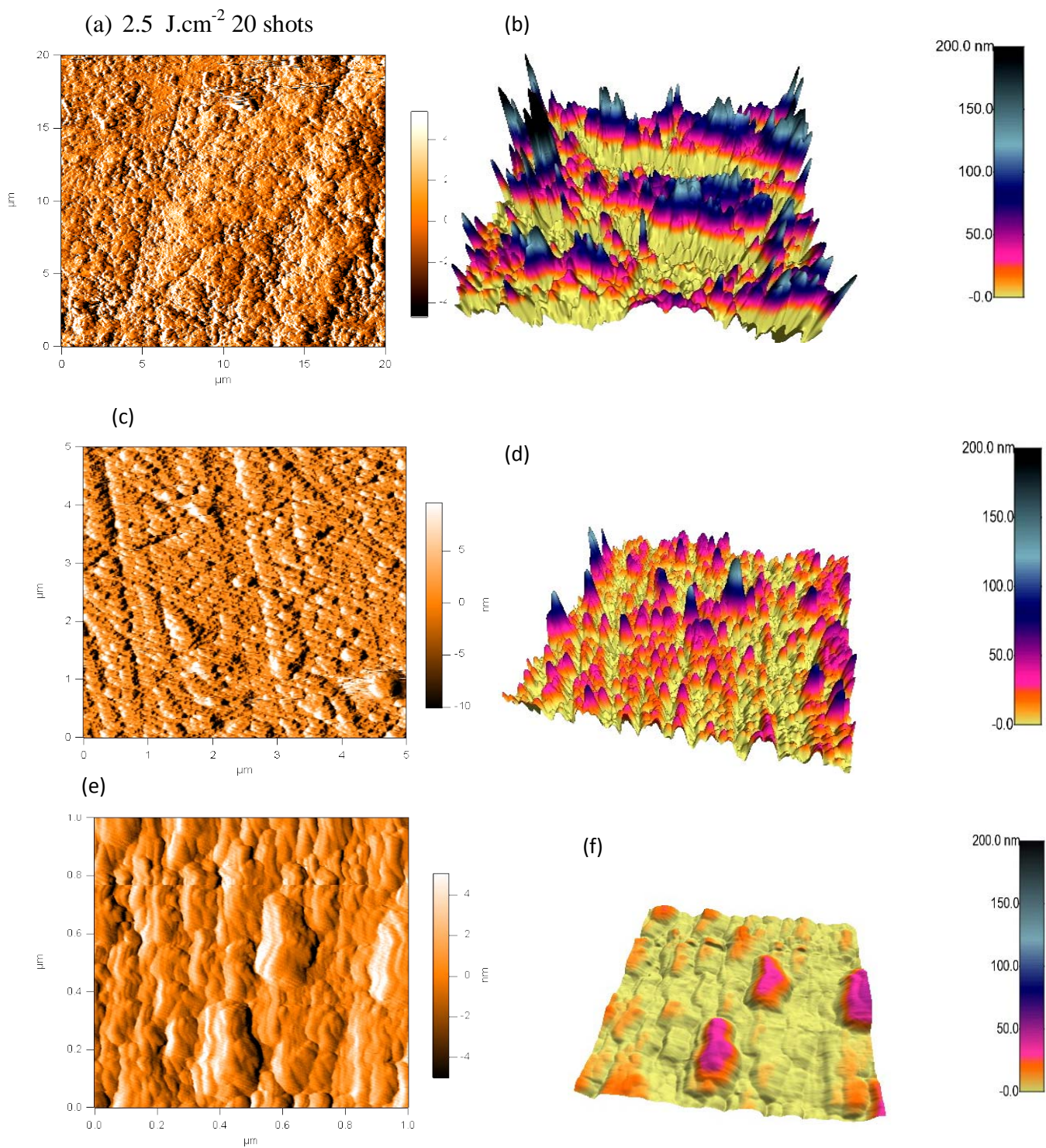


Figure 3.40: Topographical images of an Al surface after its exposure to laser pulses of a high fluence of  $2.5 \text{ J.cm}^{-2}$  for 20 shots under UHV condition (a & b) (scan area  $20 \mu\text{m} \times 20 \mu\text{m}$ ), (c & d) Magnified view of image a & b with scan area  $5 \mu\text{m} \times 5 \mu\text{m}$ , (e & f) Magnified view of image c & d with scan area  $1 \mu\text{m} \times 1 \mu\text{m}$ .



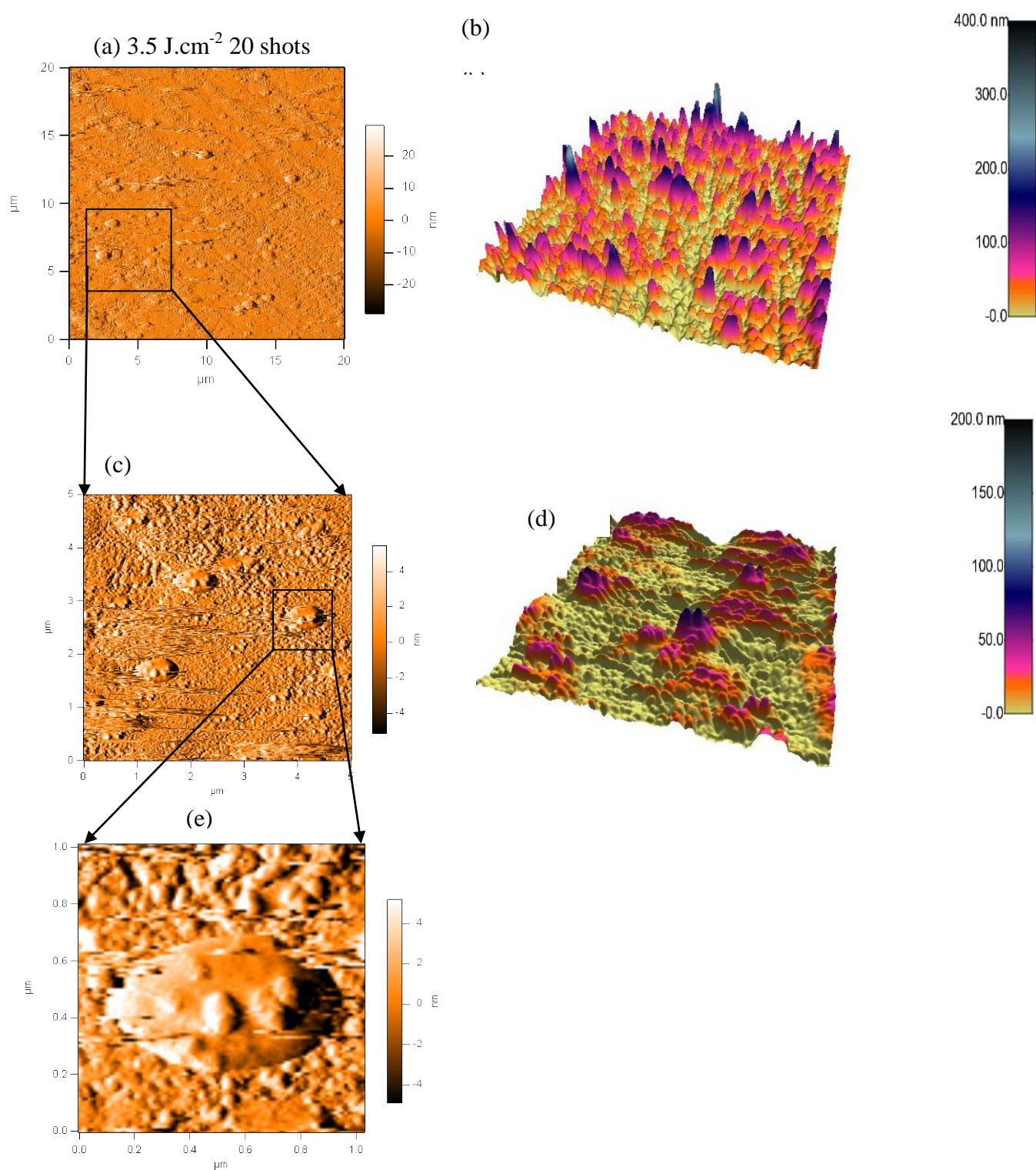


Figure 3.41: Topographical images of an Al surface after its exposure to high fluence under UHV condition (a & b)  $3.5 \text{ J.cm}^{-2}$  for 20 shots (scan area  $20 \mu\text{m} \times 20 \mu\text{m}$ ), (c & d)  $3.5 \text{ J.cm}^{-2}$  for 20 shots (scan area  $5 \mu\text{m} \times 5 \mu\text{m}$ ), (e) Enlarged view of a bump with nanobeaded structures at the top (scan area  $1 \mu\text{m} \times 1 \mu\text{m}$ ).

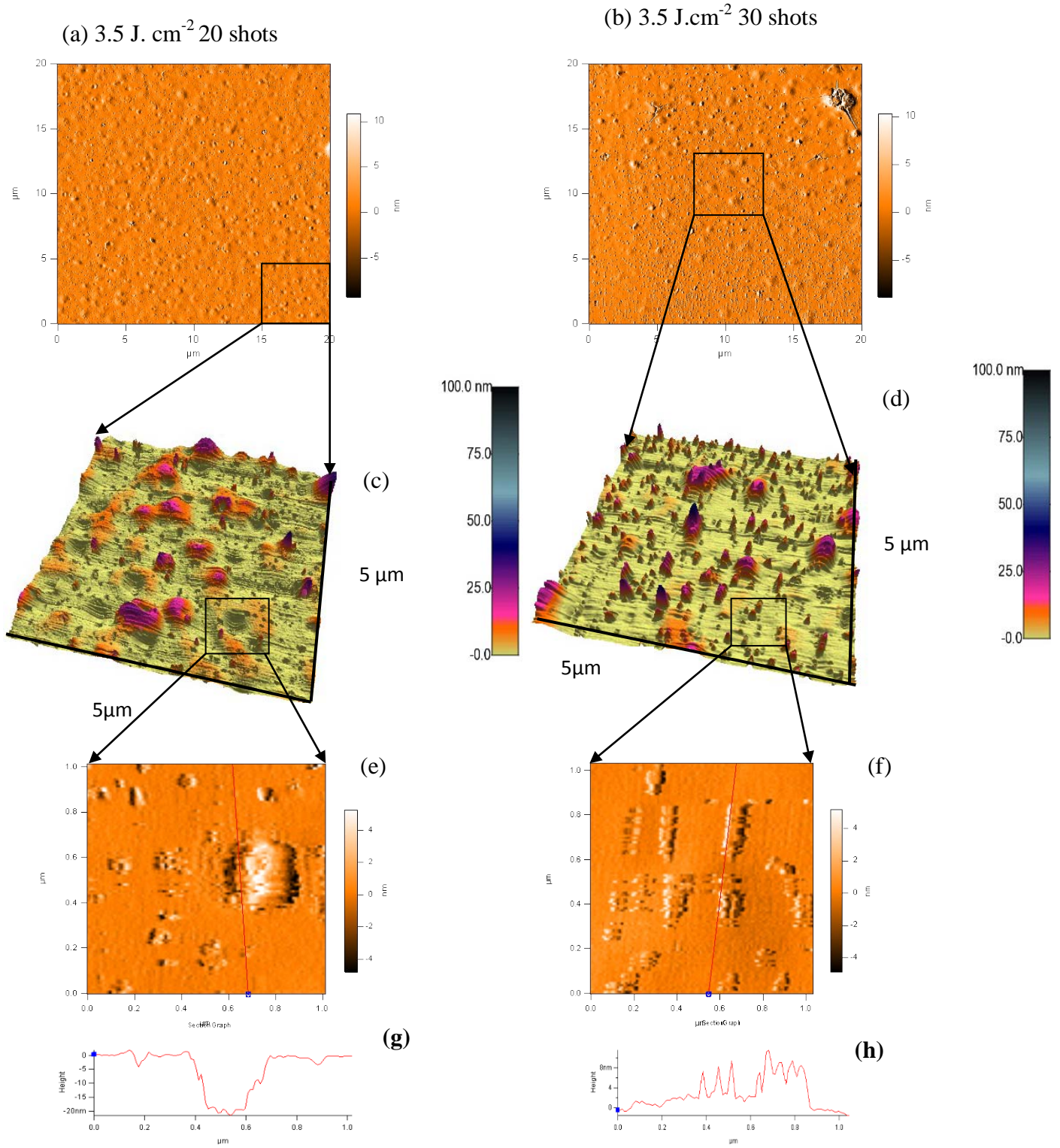


Figure 3.42: Topographical images of an Al surface after its exposure to high fluence of  $3.5 \text{ J.cm}^{-2}$  under ambient condition (a) for 20 shots (scan area  $20 \mu\text{m} \times 20 \mu\text{m}$ ), (b) for 30 shots (scan area  $20 \mu\text{m} \times 20 \mu\text{m}$ ), (c) for 20 shots (scan area  $5 \mu\text{m} \times 5 \mu\text{m}$ ), (d) for 30 shots (scan area  $5 \mu\text{m} \times 5 \mu\text{m}$ ), (e & g) for 20 shots (scan area  $1 \mu\text{m} \times 1 \mu\text{m}$ ), (f & h) for 30 shots (scan area  $1 \mu\text{m} \times 1 \mu\text{m}$ ).

The diameter of these pores is in the range of 50-150 nm whereas depth varies from 5-10 nm. Figure 3.42 (b, d & f) is presenting features after irradiation of Al with a fluence of  $3.5 \text{ J.cm}^{-2}$  for 30 shots in air. Larger bumps with an average diameter of 600 nm and an average height of 30 nm are clearly seen. The second remarkable feature evident in this image is the formation of smaller bumps with a typical diameter of 150 nm and a height of 10 nm. Pores and craters are not identified in this fluence regime.

Ripple-formation is common in both figures. These ripples are observed on the whole irradiated surface even at the tops of bumps (see figures 3.42 f & h) and bottoms of craters (see figure 3.42 e & g). It is discussed already that the formation of bumps is related to local volume increase caused due to buildup of stresses [16, 89] by fast laser heating. Laser-induced stresses are the combination of the hydrostatic pressure and the response to the shearing deformation. According to hydrodynamic simulations for Al and Cu ablation by femtosecond laser irradiation in the intensity range of  $10^{12}$ - $10^{14} \text{ W cm}^{-2}$  [164], the metal surface can be heated to a maximum temperature of 2950 K, 30 ps after the irradiation. Due to electron heating, an electronic compression wave appears at the end of the laser pulse. The electron-ion energy exchange results in a significant increase in the ionic pressure, which propagates inside the metal. High fluences accelerate the energy transfer from the electrons to the lattice and results in higher compression (maximum pressure rise 12-14 GPa at 200 ps) [164]. The relaxation of the compressive stresses generated under conditions of the inertial stress confinement has been interpreted as the main driving force responsible for the acceleration of a transiently melted region of the irradiated target [16].

Under the action of an ultrashort pulse with duration  $\tau < 1 \text{ ps}$  the heated layer  $dT$  is formed for the time less than the acoustic time  $ts = dT/c_s$ , where  $c_s$  is a sound speed. Thus the ultrashort heating  $\tau < ts$  can be considered as an isochoric process. It gives rise to the stress confinement, which is a distinctive feature of the ultrashort laser heating. For fluences in the vicinity of the ablation threshold  $\sim F_a$ , the time evolution may be divided into two consecutive stages: two-temperature (2T) and one-temperature (1T) stage [8]. In the beginning of the 2T stage the electron thermal energy  $E_e$  is much larger than ion energy  $E_i$  within the heated layer. As the thermal wave penetrates into the target, the electron temperature decreases and ion temperature increases. The 2T stage is completed when the electron and ion temperatures are equal. After that the 1T stage starts. The transition between 2T and 1T stages in Al occurs within the time slice 2-5 ps [169].

The graph in figure 3.43 shows the calculated value for the deposited energy (eV/atom) and the corresponding pressure rise (GPa) at different laser fluences for Al. Since both, the

pressure and the deposited energy increase linearly with a laser fluence, the pressure rises at a fluence of  $3.5 \text{ J.cm}^{-2}$  up to a value of 360 GPa which is considerably larger than the Young modulus of Al (75GPa) and is capable of producing bumps, pores and explosions. The transient pressures of many gigapascals [170] is already reported by ultrashort laser interaction.

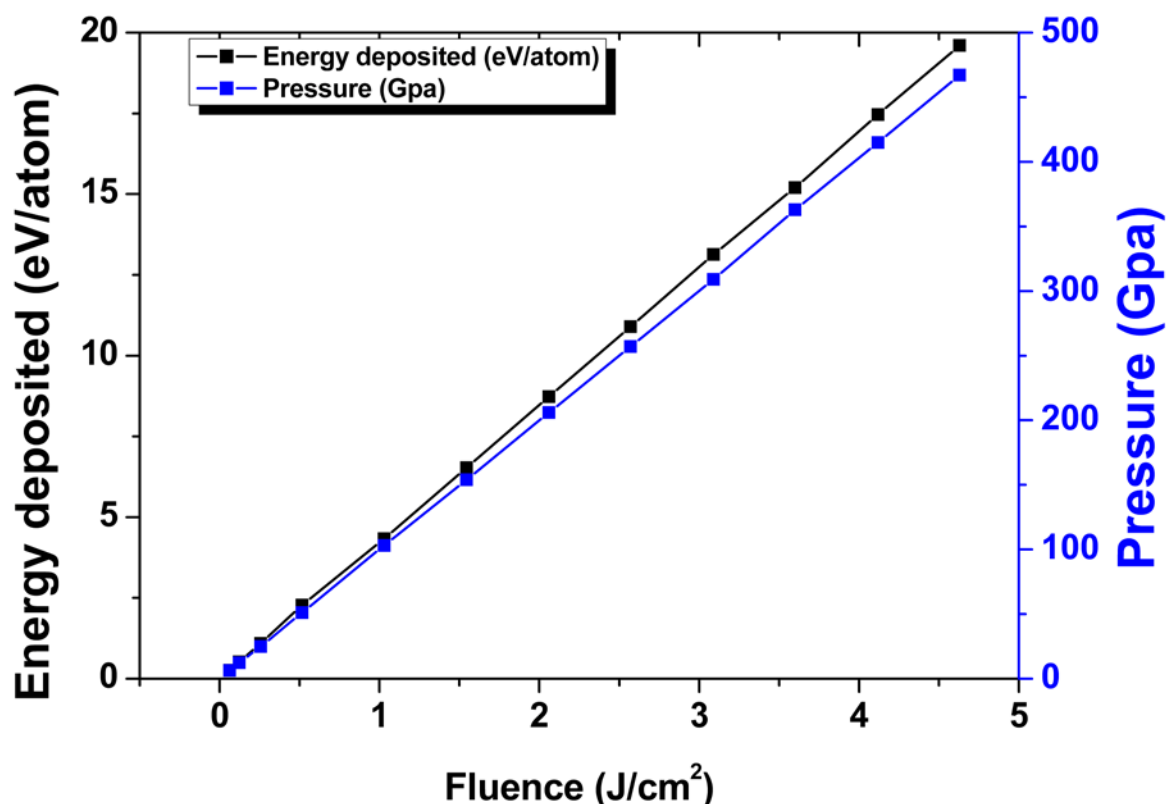


Figure 3.43: Energy deposited (eV/atom) and developed pressure (GPa) Vs different laser fluences for Al.

The presence of the metal and oxide layers can be responsible for significantly different defects like bumps, pores and craters due to their different degrees of thermal expansions within the same irradiated material [171]. The topography of bumps and pores can be explained on the basis of initial non-uniform laser energy deposition indicating a nanoscale material relocation to an adjacent site. The spatial nonuniformity in the deposited laser energy can produce a melt at localized nanoscale sites within the irradiated spot. Once the localized nanoscale melt has been formed, a high radial temperature gradient in a nanomelt can induce a radial surface temperature gradient that expels the liquid to the periphery of the nanomelt. This will lead to the formation of nanocavities and nanoprotusions due to fast freezing of the expelled liquid on the boundary with the solid state material. These initially induced surface



random nanostructures enhance the absorption of laser light [172] and facilitate further growth of surface defects with increasing number of laser shots due to the increased spatial non-uniform energy absorption. When laser fluence is sufficiently high to produce ablation, particles will be ejected from the nanomelts and produce a recoil pressure that squirts the liquid metal outside the nanomelt. It should be noted that for multi-pulse ablation, the repeating vaporization and re-deposition of nanoparticles back onto the surface can also promote the surface nanostructuring [173]. The force impelling the redeposition is presumably caused by a pressure difference between the areas above and below the liquid layer, which is generated during the rapid ejection.

The pores observed at the irradiated Al surface can be explained on the basis of physical model [174] in which it is assumed that the subsurface solid's volume contains spherical micro- and nano-sized pores of probable size ranging from 0.1 to 1  $\mu\text{m}$ . Laser-induced heating can initiate thermal and hydrodynamic processes in the subsurface layers of a metal and an intensive gas desorption takes place. Thus a high pressure develops which could result in the surface destruction. The destruction can occur in the solid state when the gas pressure in the pores exceeds the damage threshold of the material or in the liquid state as a result of gas bubbles growth. For several materials this happens in the temperature range above 2000 K but below the boiling point. These phenomena were observed for certain metals such as Cu and Al at the early stage of laser irradiation before reaching the evaporation threshold [174].

(a)  $8 \text{ J.cm}^{-2}$  10K shots

(b)

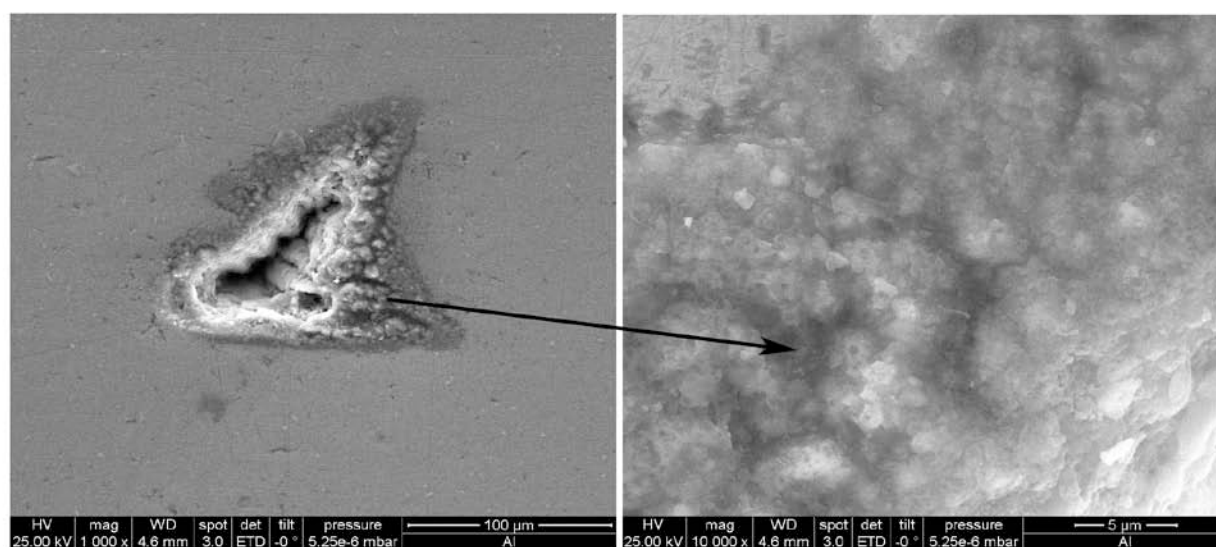


Figure 3.44: SEM images of an irradiated Al surface with a very high laser fluence of  $8 \text{ J.cm}^{-2}$  (a) A Crater –formation with melting (b) An enlarged view of the crater boundary.

For higher fluences ( $3.5 \text{ J.cm}^{-2}$  for 30 shots in air figure 3.40 (d & e) and for 20 shots in UHV figure 3.39 (a & d) no pores are observed. This is due to the fact, that during the explosion, the phase of relaxation is less effective and shock-liquidized material refills the cavities initially formed by explosion [118]. It is also speculated [128] that the effect of shock wave at higher fluence may lead to migration of part of the atoms and result in the disappearance of some dislocations and causing collapse of the nanopores.

At the highest fluence used in experiments i.e.  $8 \text{ J.cm}^{-2}$ , nanostructures are not present over most of the irradiated area and a dominant morphological feature is the crater formation of a typical size of  $100 \mu\text{m}$  due to melt ejection with the appearance of surface microroughness at the periphery. No nanoripples have been observed on the periphery of the ablated spot, where the Gaussian beam intensity is low enough for nonstructural formation. An example of these surface structural modifications is shown in figure 3.44 (SEM image) for a fluence of  $8 \text{ J.cm}^{-2}$ . A big area surrounding the crater is affected thermally. Some redeposited molten droplets, debris, small holes (pores) with localized bursting of the surface are visible around the produced crater shown in figure 3.44 (b).

In case of exposing Al under UHV conditions, the main features observed are irregular shaped bumps along with highly disturbed and chaotic surface structures. The appearance of nanobeaded structures can also be seen at the top of bumps. In case of its exposure under ambient condition, bumps, pores, ripples and craters have been observed. All these structure are attributed to thermal stress wave propagation, inhomogeneous nucleation, cluster formation and resolidification of a metallic surface after melting. Some redeposited molten droplets, debris, and small holes (pores) have been observed in the periphery of the ablated area (around the crater) instead of ripple-formation observed in case of a Si for a fluence of  $8 \text{ J.cm}^{-2}$  (see figure 3.25 and 3.44 ).

The Raman spectroscopy of the Al could not be performed because of the difficulty faced in the measurements which is explained as follows:

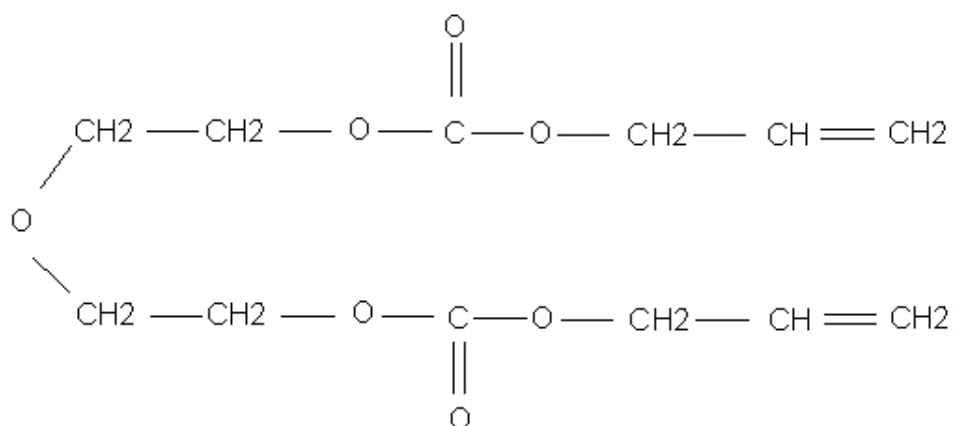
The Raman spectroscopy of a material can be performed only if it has a Raman cross-section. A necessary condition for material to have a Raman cross-section is the existence of a non-zero polarizability. Raman spectroscopy of an Al could not be performed due to the fact that metals usually show zero polarizability, therefore their Raman cross-section is zero and it is not possible to detect any Raman signal.

A change in the molecular polarization potential or amount of deformation of the electron cloud with respect to the vibrational coordinate is required for a molecule to exhibit a Raman effect. The amount of the polarizability change will determine the Raman scattering intensity.

The pattern of shifted frequencies is determined by the rotational and vibration states of the sample. However Surface Enhanced Raman Spectroscopy, or Surface Enhanced Raman Scattering, often abbreviated SERS, is a surface sensitive technique that results in the enhancement of Raman Scattering by molecules adsorbed on rough metal surfaces. The enhancement factor can be as much as  $10^{14}$ - $10^{15}$ , which allows the technique to be sensitive enough to detect single molecules. Given that Raman intensities are proportional to the electric field, there is large increase in the measured signal. This method has been tried but in that case it was difficult to detect and explore the exact location of irradiated area.

### 3.5. Results for Polymers (CR-39)

CR-39 is one of the most popular polymers, which is known as an excellent material for a number of industrial, medical and optical applications. It has good optical transparency and structural stability. It is extensively used in various experiments in fusion research, nuclear science and astrophysics [83, 84]. A CR-39 nuclear track detector has been well demonstrated to have an excellent track registration property and used widely in various fields by many authors [83, 85, 86]. Very few studies, however, have been performed to obtain the fundamental information on laser irradiation effects on this detector (material) [82, 87]. Its chemical name is Allyl diglycol carbonate with the following chemical formula



#### 3.5.1 AFM Measurements

##### (a) *Low fluence regime*

After observing nanohillocks in dielectrics, semiconductors and metals the next step was to explore and identify these nanostructures in a polymer to explain ultrashort-laser ablation for fluences around the ablation threshold. In figure 3.45 the surface topography of CR-39 for

increasing laser fluence is shown after exposing the target under UHV condition. The appearance of nanohillocks produced by localized laser energy deposition after a single shot irradiation on CR-39 surfaces provides a clue that similar kind of nonthermal process (Coulomb Explosion) is responsible as have already been discussed for the previously investigated materials. AFM analysis of irradiated target suggests that an appearance of nanohillocks at the polymer surface has been observed at the same fluence (around ablation threshold) and exactly in the same manner as those for  $\text{CaF}_2$ , Si and Al. Starting from the threshold fluence i.e.  $0.06 \text{ J.cm}^{-2}$ , figure 3.45 (a) is AFM topographical image of nanohillock-formation on a CR-39 surface with an average height of 5 nm and a typical diameter of 40 nm. Figure 3.45 (b) shows that at a fluence of  $0.12 \text{ J.cm}^{-2}$  a larger number of hillocks as

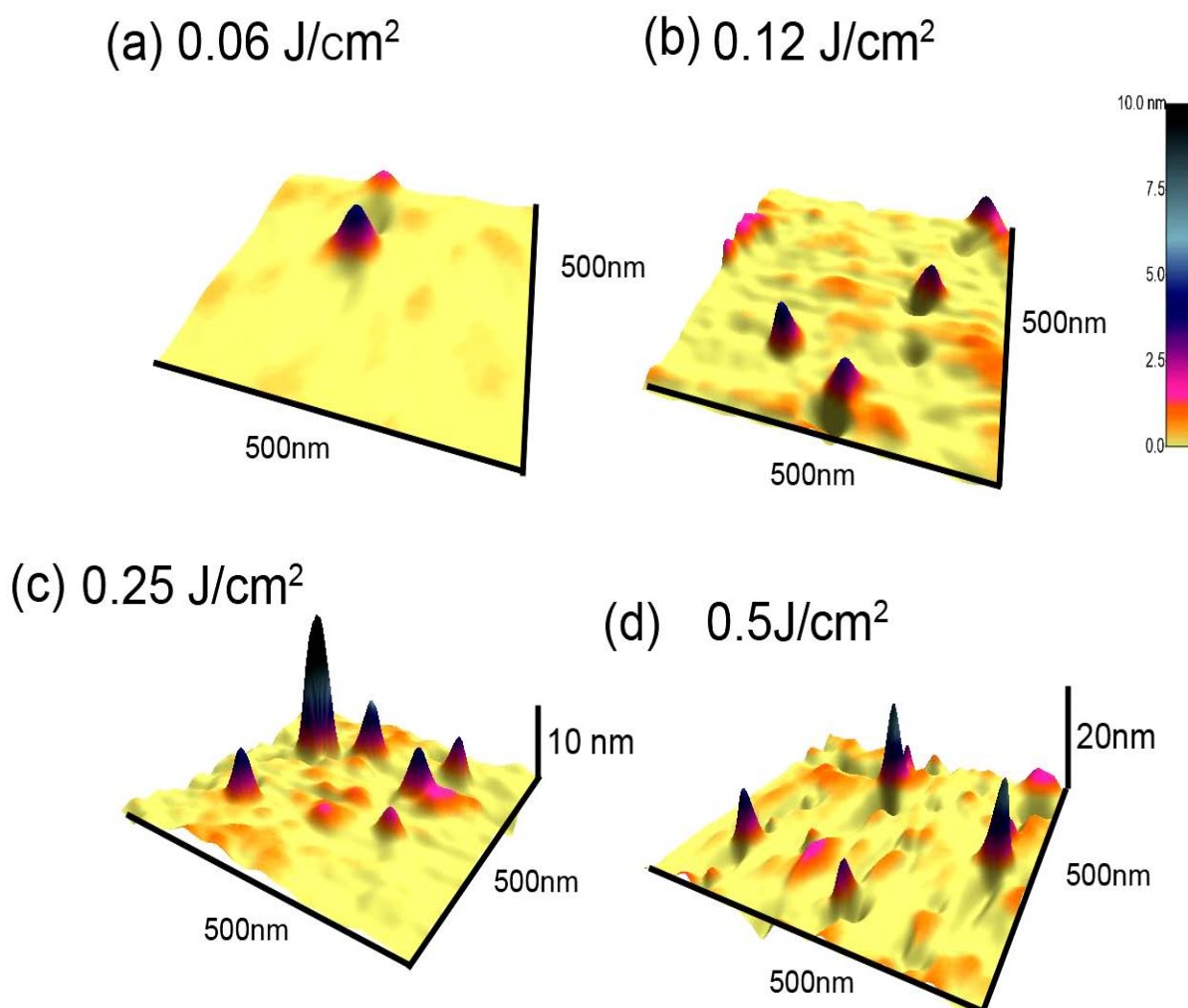


Figure 3.45: AFM Topographic images of nanohillock-formation on the CR-39 surface (scan area  $500 \text{ nm} \times 500 \text{ nm}$ ) as a result of  $25\text{fs}$  laser irradiation in UHV condition at the fluence (a)  $0.06 \text{ J.cm}^{-2}$  (b)  $0.12 \text{ J.cm}^{-2}$  (c)  $0.25 \text{ J.cm}^{-2}$  (d)  $0.5 \text{ J.cm}^{-2}$ .

compared to (a) appears with almost same heights and diameters. Furthermore, at  $0.12 \text{ J.cm}^{-2}$  fluence energy deposited per atom for CR-39 is equivalent to approximately  $0.5 \text{ eV/atom}$  and this is basically the same value as for  $\text{CaF}_2$ . A corresponding surface topography for the laser fluence of  $0.25 \text{ J.cm}^{-2}$  is shown in figure 3.45 (c). The resulting hillock heights range from 2-10 nm with an average diameter of 50 nm. Finally, if the laser energy increases above  $0.5 \text{ J.cm}^{-2}$  (3.45d), the hillocks become broader and the surface is rendered highly disturbed. It makes no sense to speak of localized, isolated nanohillocks anymore. In case of exposing the polymer target under ambient conditions, a similar kind of structures has been observed as in the case found for dielectric, semiconductor and metals (fluences ranging from  $0.25 \text{ J.cm}^{-2}$  to  $2.5 \text{ J.cm}^{-2}$ ). The diameter of these hillocks ranges from 20 nm-70 nm with a typical height of 3-8 nm. The heights of nanohillocks and the onset of these non-localized surface disturbances is more pronounced in CR-39 than for  $\text{CaF}_2$  in spite of approximately same deposited energy per atom. It can be due to the smaller binding energy (3-4 eV) for CR-39 as compared to  $\text{CaF}_2$  (10 eV).

Figure 3.45 (a-c) and 3.46 (a-d) show features (hillocks) of an extremely localized laser energy deposition mechanism in the polymer around the ablation threshold. Keeping in view evidences of previous measurements for dielectrics, semiconductors and metals, the existence of Coulomb explosion is proposed as one possible mechanism for ultra-short-laser ablation [13, 14, 68] implying that molecules or their ions are ablated from the surface without thermal melting. Coulomb explosion in polymers is well accepted [175]. The intense laser can ionize the elements instantaneously by non-resonant multiphoton ionization or optical-field ionization (barrier-suppression ionization) and can produce elemental ions, creating a situation where Coulomb explosions is likely to happen resulting in the emission of energetic ions. The optical field ionization and the Coulomb explosion by an intense laser field have been investigated on diatomic molecules and clusters and the studies of these phenomena have recently been extended to polyatomic molecules. Cornaggia and his co-workers studied the Coulomb explosion of small molecules and several hydrocarbons [176, 177]. The generation of ions from laser-matter interaction can be identified in the energy distribution of ions emitted during a specific process. When the element changes to a plasma as a result of laser irradiation, it expands adiabatically (the laser pulse is too short to be isothermal), and the emitted ions generally exhibit a Maxwellian distributions of energies [175]. The energy deposition into the electronic system by ultrashort- laser pulses seems to initiate similar or identical processes observed for bombardment with highly charged ions, where a substantial part of the kinetic energy of the ions is deposited as an inelastic energy [15]. Coulomb

explosion (CE) mechanism is suggested to explain the atomic displacement via the electronic excitation.

The electric field is accompanied by a laser field, and forces electrons in the molecule to oscillate more vigorously at higher laser intensity. This effect is due to the ponderomotive potential induced by the laser light. The potential is the average kinetic energy of an electron in the laser field, and is given by [178].

$$\phi_{pon} = \frac{e^2 \epsilon^2}{4\pi m^2} = 9.33 \times 10^{-14} I \lambda^2 \quad 3.18$$

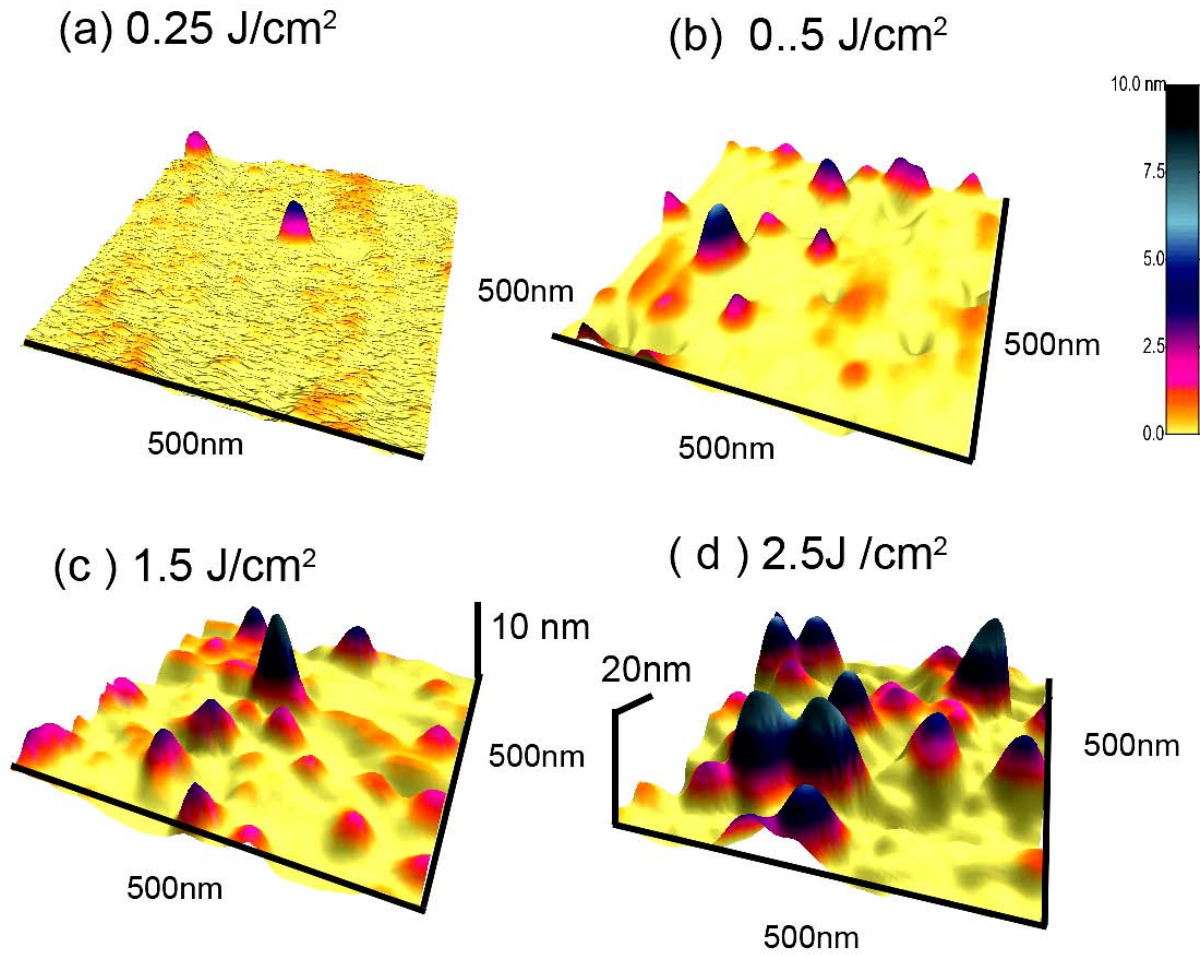


Figure 3.46: AFM Topographic images of nanohillock-formation on the CR-39 surface (scan area 500 nm × 500 nm) as result of 25fs laser irradiation in air at fluences (a) 0.25 J.cm<sup>-2</sup> (b) 0.5 J.cm<sup>-2</sup> (c) 1.5 J.cm<sup>-2</sup> (d) 2.5 J.cm<sup>-2</sup>.

Where  $\varepsilon$  is the electric field strength,  $I$  ( $\text{W cm}^{-2}$ ) is the laser intensity, and  $\lambda$  ( $\mu\text{m}$ ) is the wavelength. The ponder motive potential can reach several hundreds eV at  $10^{16} \text{ W cm}^{-2}$  and is far above the binding energy of valence electrons of a molecule [178]. Femtosecond laser radiation initially transfers its energy to the electronic system of the target, leading to a region of strong electronic excitation. In localized nanometer sized areas within the laser spot the energy deposition and creation of a hot electron density takes place. These hot electrons drift out resulting in positively charged small volumes, where the charging can lead to Coulomb explosion.

The effect of laser fluence on the geometrical size (diameter and height) of these nanohillocks after exposing the target in air and under UHV condition is plotted in figure 3.47. For the targets exposed in air and under UHV condition, both the average diameter and height of hillocks increase with increasing laser energy and can be ascribed to an increased energy deposition.

From figures 3.45 - 3.47 it is inferred that the threshold energy for hillock-formation in air is higher than in UHV condition and shows a similar trend as observed for other materials.

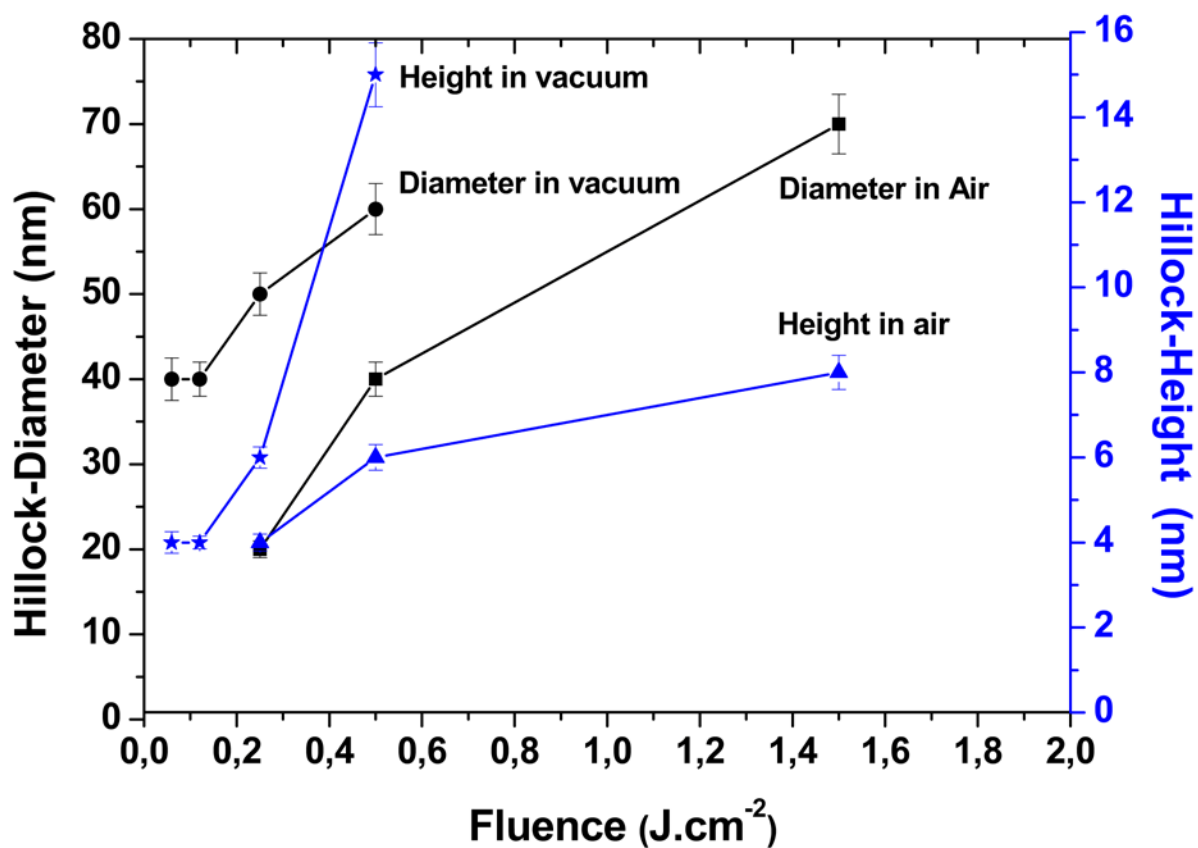


Figure 3.47: Average diameter and height of the nanohillocks formed on the CR-39 surface versus laser fluence after its exposure to 25fs laser pulses in air and under UHV condition.

### ***(b) Moderate fluence regime***

Figure 3.48 presents AFM topographic images ( $2\mu\text{m} \times 2\mu\text{m}$  with different heights) of ultra short laser irradiated CR-39 at a moderate fluence regime of (a)  $0.25\text{ Jcm}^{-2}$  (b)  $0.5\text{ Jcm}^{-2}$  (c & d)  $1.5\text{ Jcm}^{-2}$  for 20 succeeding pulses. This is the fluence regime where nanohillocks have vanished and localized nanostructures in the form of bumps are clearly seen on the irradiated surface. Heights and diameters of these bumps range from 5-20 nm and 100-300 nm, respectively. A trend to increased diameters and number density of these bumps is observed with increasing laser fluences from  $0.2\text{ Jcm}^{-2}$  to  $1.5\text{ Jcm}^{-2}$ . Dependence of geometric characteristics (diameters and heights) and number of bumps can be quantitatively obtained from AFM images (figure 3.48 a-d) for various laser fluences. At a laser fluence of  $1.5\text{ Jcm}^{-2}$ , in addition to these bumps, bubbles-like structures or nanocavities generated by explosion have also been observed. These cavities have been formed at the top of bumps (3.48 d) with diameter ranging from 50-100 nm and depths 1-5 nm. The formation of nanocavities (figure 3.48 d) can be explained on the basis of thermo-elastically induced tensile stresses caused by laser induced heating within the material. For higher fluences, beyond certain threshold value, the stresses become so high that violent expulsion of the material takes place. However, thermo-elastic stresses caused by the temperature rise stay confined in the focal volume leading to a maximum pressure rise [111]. This pressure, confined to a small volume at irradiation site, may exceed the Young modulus of CR-39 and cause rupturing and phase explosion and provides a possible physical reason for melt ejection [179, 180]. The numerous fragments are ejected explosively creating nanopores (bubbles like structures) or nanocavities at the polymer surface. Similar kinds of nanopores (holes) on the tops of the bumps have been observed during ablation experiments on polyimide with femtosecond laser pulses by Kautek and coworker [181] and have been attributed to shielding and diffraction effects induced by impurities in the sample.

Due to the interaction of a laser with solid at fluence above the ionization threshold, a strong shock wave is generated in the interaction region and propagates into the surrounding cold material. The shock wave propagation is accompanied by compression of the solid material at the wave front followed by the decompression, which leads to the formation of an ablation crater on the sample surface. Because of the heat accumulation effect, with the increasing pulse number, the temperature in the focal volume would rise accordingly. As a consequence the thermal energy diffuses from the focal spot to the surrounding and the heated region begins to melt and expand. The circular structure with high refractive index emerges between



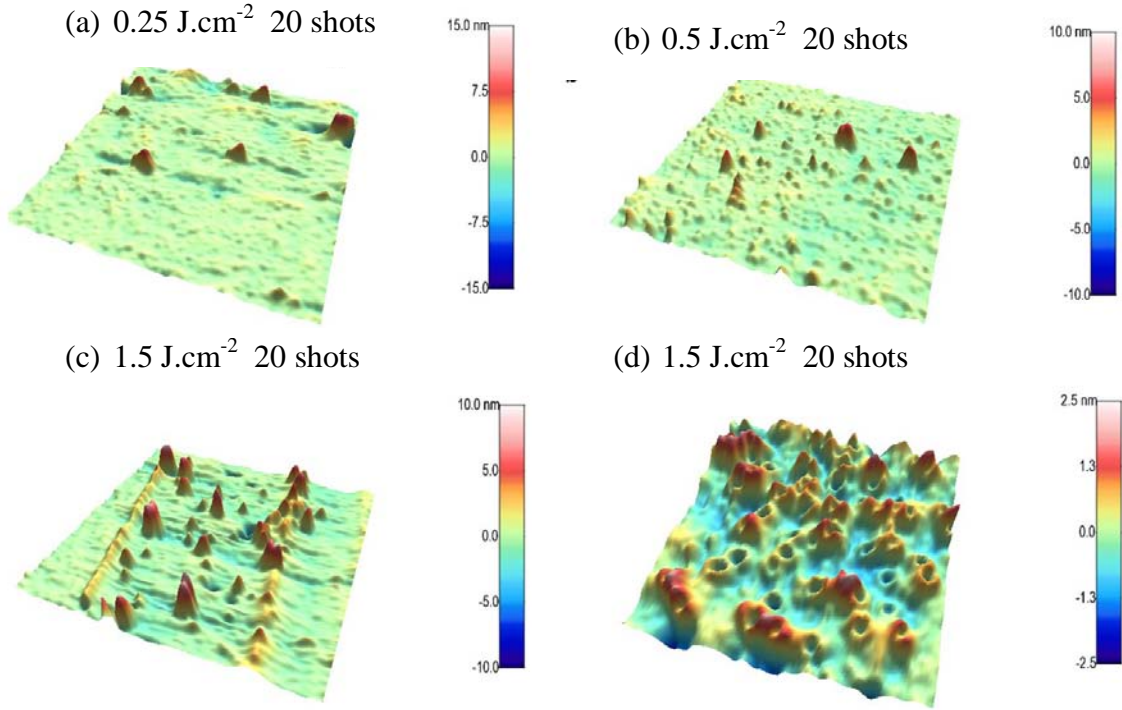


Figure 3.48: AFM topographic images ( $2\mu\text{m} \times 2\mu\text{m}$  with different heights) of femtosecond laser (800nm, 25fs) irradiated CR-39 with 20 succeeding pulses at a fluence of (a)  $0.25\text{ Jcm}^{-2}$ , (b)  $0.5\text{ Jcm}^{-2}$  (c)  $1.5\text{ Jcm}^{-2}$  (bumps are prominent) (d)  $1.5\text{ Jcm}^{-2}$  (nanocavities are prominent).

the expanding region and the unheated one. The laser-matter interaction process is usually split into a sequence of interconnected problems: the absorption of laser light, the ionization and energy transfer from electrons to ions, the heat conduction, and hydrodynamic expansion. Extremely high pressure and temperature with high heating and cooling rates are created in the energy deposition region that may result in formation of new states of matter. The local temperature rise resulting from energy accumulation eventually saturates as the energy inflow from the laser is balanced by heat conduction. The energy density rises above the ablation threshold due to energy accumulation when a few hundred thousand pulses hit the same spot. This is accompanied by a marked change in the interaction physics from a laser-solid to a laser-plasma interaction. The plasma generated in the focal region increases the absorption coefficient and produces a fast energy release in a very small volume. The total deposited energy builds up the pressure that drives the shock wave. The shock wave propagates into the surrounding cold material. The compressed material behind the shock wave can then be transformed to another phase state in such a high pressure condition. After unloading the shock-affected material undergoes transformation into a final state at normal pressure. The final state may possess properties different from those in the initial state. We consider in

succession the stages of compression and phase transformation, pressure release, and material transformation into a postshock state [182].

Laser-induced surface structures were first reported by Dyer et al [183] during etching of polyimide using XeCl (308 nm) excimer laser. Laser-interaction can result in high temperatures on the polymer surface. At such high temperatures, carbon atoms from polymer chains are released due to polymer disintegration and they can move freely on the surface to establish carbon clusters with nanometer size. Afterwards, the agglomerates of carbon particles can act as nucleation sites for cone-like microstructures. Based on this model, laser pulses can induce a large molten layer underneath the ablation layer. A low solidification rate of the molten layer can induce the motion of carbon particles inside the molten layer. For the first ablation shot, the carbon particles of micrometer size are free to move randomly on the ablated surface and therefore, agglomerate to surface clusters. Meanwhile, carbon clusters of nanometer size diffuse into the large molten layer. If the surface carbon clusters reach a temperature higher than the surrounding polymer matrix, thermal diffusion tends to promote a flux of carbon particles towards the surface to create larger carbon clusters, *i.e.*, the random surface diffusion of the micrometer particles leads to carbon depletion outside the molten layers. Each agglomerate of carbon particles acts as a nucleation site for the conical microstructure. The large carbon nucleation sites and the melt of the microstructure skin after each laser shot can finally create a conical microstructure at subsequent pulses. The growth mechanism of the large conical structures then follows to aggregate small conical microstructures in the molten layer upon repeated laser irradiation [184].

The results described above are comparable with the bump-formation in other investigated materials (CaF<sub>2</sub>, Si and Al) under a moderate fluence irradiation. The explosions and nanocavities formed at the top of bumps are comparable with explosions of CaF<sub>2</sub> and can be attributed to nonlinear absorption in transparent materials.

### ***(c) High fluence regime***

Figure 3.49 presents AFM topographic images (2  $\mu\text{m} \times 2 \mu\text{m}$  with different heights) of ultra short laser irradiated CR-39 at a high fluence of (a) 2.5 J.cm<sup>-2</sup> and (b) 3.6 J.cm<sup>-2</sup> for 20 overlapping pulses. The geometric size (diameters and heights) and number of bumps have been observed to be increased significantly after increasing a fluence from moderate regime 1.5 J.cm<sup>-2</sup> to higher fluence regime 2.5 J.cm<sup>-2</sup> (figure 3.49a). The increase in number and size of bumps with increasing laser fluence is due to the higher energy deposition in the irradiated area and increased thermal stresses. With increasing fluence from 2.5 J.cm<sup>-2</sup> to 3.5 J.cm<sup>-2</sup> for

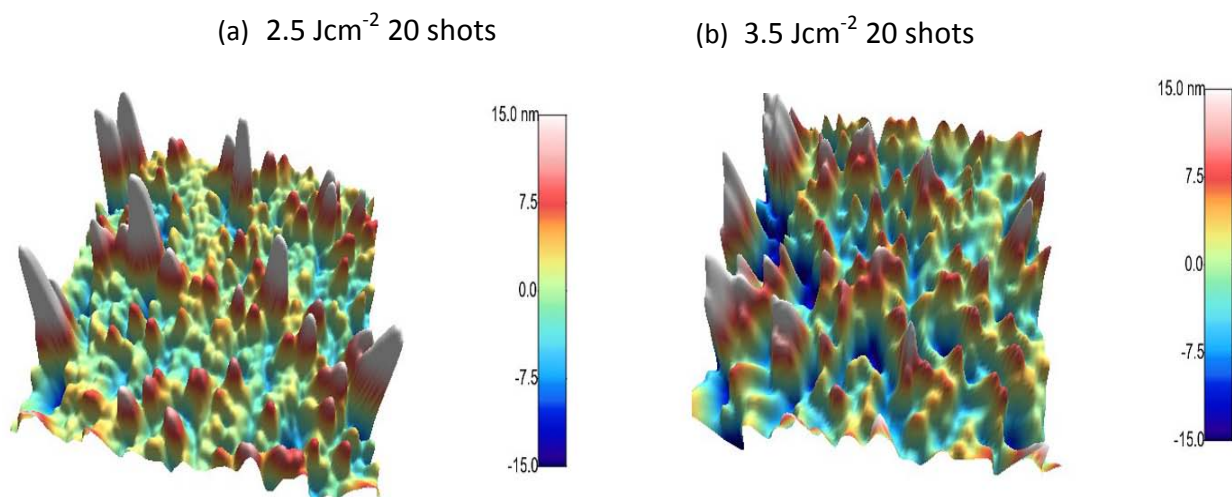


Figure 3.49: AFM topographic images ( $2\mu\text{m} \times 2\mu\text{m}$ ) of irradiated CR-39 at a fluence of (a)  $2.5\text{ J.cm}^{-2}$  (b) and  $3.6\text{ J.cm}^{-2}$  for 20 shots.

20 shots, the formation of these bumps is almost negligible rather there is a setting up of material ejections (figure 3.49 b). This fluence is assumed to be sufficiently high enough to cause melting resulting in crater-formation.

The nature of melting and crater-formation in case of a polymer irradiated with a high fluence (in the range of  $2.5\text{--}3.5\text{ J.cm}^{-2}$ ) differ considerably from those for  $\text{CaF}_2$  (swelling, bulges and rupturing of the crystal associated with larger hump-formation), Si (island formation), Al (chaotic and highly disturbed surface with rectangular bump-formation). This difference is due to the soft nature of the polymer as compared to other materials ( $\text{CaF}_2$ , Si and Al).

### 3.5.2 Raman Spectroscopy

Photo thermal and photochemical decomposition of the organic polymeric molecules can take place by vibrational or rotational excitation due to absorption of near infrared photons [185]. These processes are responsible for spatially inhomogeneous internal stresses, local volume increase, formation of new bonds, cross-linking, bond breaking and marked structural modifications in the polymer [186]. In order to characterize single and multiple shot laser ablation of CR-39, Raman spectroscopy measurements have been performed with the primary intention to correlate the different structural and chemical changes (bond breaking, bond weakening, crosslinking, polymerization, appearance of new disorder bands) with features observed on the surface by AFM. The development of nanostructures for different laser fluences can be correlated with Raman spectroscopy where the transition from electronic processes (nanoablation) to thermal processes takes place with an appearance of a more and more disturbed polymer surface.

*(a) Low fluence regime*

Figure 3.50 and 3.51 show Raman spectra of the pristine and single pulse irradiated CR-39 for different laser fluences under UHV condition and in air respectively. In the pristine CR-39 target all identified peaks (at 1287, 1451, 1643, 1737, 2913 and 2958  $\text{cm}^{-1}$ ) are confirming its fundamental monomer structure [187]. Two peaks observed at the wave numbers around 2913  $\text{cm}^{-1}$  and 2958  $\text{cm}^{-1}$  corresponds to the  $-\text{CH}_2-$  symmetric and asymmetric stretching modes of unexposed CR-39, respectively, which is in good agreement with results by Sharma et al [187]. The decrease in the intensity of these two peaks in the spectra, both in UHV condition and in air, is indicative of a decrease in the  $-\text{CH}_2-$  group density. This decrease saturates with laser intensity and is caused by the lack of hydrogen [188]. This can be due to fact that surface becomes more and more hydrogen deficient resulting in the saturation effect. Decrease in a  $-\text{CH}_2-$  group density in CR-39 after ions and proton irradiation has already been

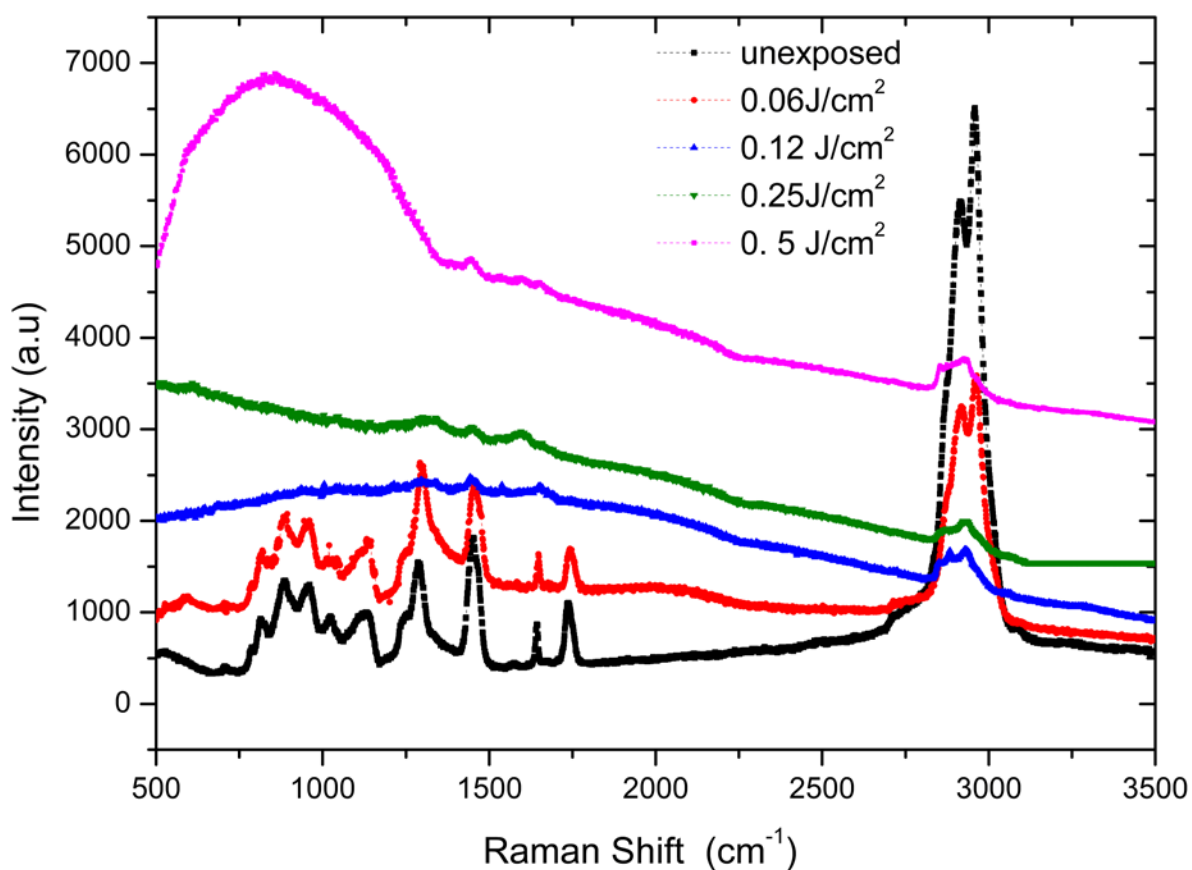


Figure 3.50: Raman spectra of the pristine and single pulse irradiated CR-39 under UHV condition for different fluences 0.06  $\text{J.cm}^{-2}$ , 0.12  $\text{J.cm}^{-2}$ , 0.25  $\text{J.cm}^{-2}$ , and 0.5  $\text{J.cm}^{-2}$ .

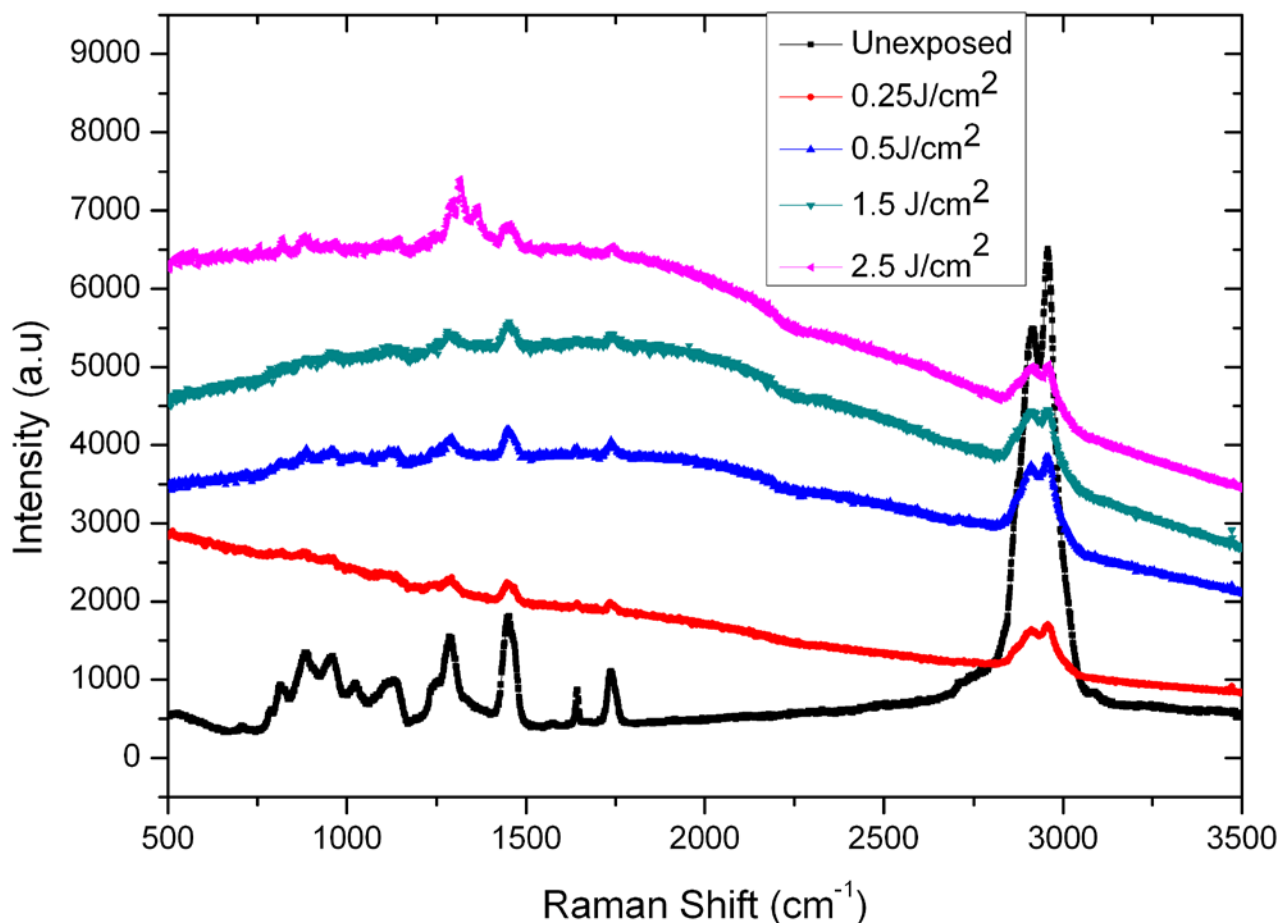


Figure 3.51: Raman spectra of the pristine and single pulse irradiated CR-39 in air for different fluences  $0.25 \text{ J.cm}^{-2}$ ,  $0.5 \text{ J.cm}^{-2}$ ,  $1.5 \text{ J.cm}^{-2}$  and  $2.5 \text{ J.cm}^{-2}$ .

observed [187]. Such dehydrogenation caused by irradiation may lead to the formation of the unsaturated bonds and hence, increase the polar components [189]. No Raman shift is observed in these stretching modes in case of ablation under UHV condition at a laser fluence of  $0.06 \text{ J.cm}^{-2}$  and for all laser fluences in case of air. On the other hand, it is found that for higher fluences there is not only a change in the shape of peaks but also a Raman shift have also been observed in these stretching modes. At a laser fluence of  $0.12 \text{ J.cm}^{-2}$  the original peaks (at  $2958$  and  $2913 \text{ cm}^{-1}$ ) shift to  $2932$  and  $2851 \text{ cm}^{-1}$  with the appearance of a third peak at  $2883 \text{ cm}^{-1}$ . The appearance of a new peak and Raman shifting is attributed to photo-induced modifications of the polymer bands due to intra- and inter-chain energy transfer [190]. Further increase in the laser fluence (from  $0.25 \text{ J.cm}^{-2}$  to  $0.5 \text{ J.cm}^{-2}$ ), results in two new peaks appearing around  $2857$  and  $2932 \text{ cm}^{-1}$  whereas, the peak at  $2883 \text{ cm}^{-1}$  has completely disappeared. The perturbation due to a disordered environment after bond scissions and formation of new bonds (cross linking) results in these Raman shifts. Broadening in the peaks is also observed as a consequence of irradiation. This broadening is due to the decrease in

phonon lifetime as a result of scattering from radiation-induced defects [191]. In electrical insulating solids, it is believed that point defects affect the lattice vibrations and cause scattering for phonons owing to mass differences (mass fluctuation size) and inter atomic coupling force differences (field fluctuations) [192] which will shorten the mean free path of the phonon [193]. The intensity of one of the peaks appearing at  $1735\text{ cm}^{-1}$  corresponding to C=O band reduces significantly after exposure for laser fluences between  $0.25\text{ J.cm}^{-2}$  -  $1.5\text{ J.cm}^{-2}$  in case of air (figure 3.51) and  $0.06\text{ J.cm}^{-2}$  in case of UHV condition (figure 3.50) but without Raman shift. In case of UHV condition this band completely disappears for the higher laser fluences ranging from  $0.12\text{ J.cm}^{-2}$  to  $0.5\text{ J.cm}^{-2}$ . It is a indication of carbonyl bond breaking and is in agreement with degradation of polymers observed by swift heavy ion irradiation [194].

The C=C band at  $1643\text{ cm}^{-1}$  has decreased in its intensity significantly after exposure in air. In case of UHV condition, the intensity of this C=C band reduces after exposure for fluences  $0.06\text{ J.cm}^{-2}$  and  $0.12\text{ J.cm}^{-2}$  and again disappears completely for the higher fluences of  $0.25\text{ J.cm}^{-2}$  and  $0.5\text{ J.cm}^{-2}$ . The decrease in the density of the C=C and C=O bond after exposure suggests that the carbonate ester bonds in CR-39 are destroyed. When a monomer is polymerized to form a polymer there is always the loss of double bonds. The reduced intensity of these double bands can be attributed to a lower degree of polymerization. For higher fluences ( $0.25$  and  $0.5\text{ J.cm}^{-2}$  for UHV condition) the complete disappearance of the bands of the carbon double bonds is observed which can be attributed to high degree of polymerization and degradation of CR-39 involving carbonyl C=C bond-breaking [86] and folding of chains [191]. These results show that the degree of polymerization after exposing the polymer under UHV condition is higher than in air.

The band at  $1451\text{ cm}^{-1}$  originates from the -C-H- bending mode. In case of under UHV condition, only the reduced intensity is observed for all four laser fluences. In case of target exposure in air, Raman shift of  $4\text{ cm}^{-1}$  (from  $1451$  to  $1447\text{ cm}^{-1}$ ) with reduced intensity and broadening is observed for all laser fluences. This can be attributed to breaking and weakening of the -C-H- bonds in the polymer structure after laser irradiation [189]. All other bands have disappeared in case of UHV condition. For higher fluence ( $1.5\text{ J.cm}^{-2}$ ), all these bands are unresolved and would have been merged under the disorder band. This disorder band appears where transition from electronic processes (nanoablation) to thermal processes takes place with the appearance of more disturbed polymer surface. It appears that for the fluence suitable for the electronic processes as described in the AFM images, the bond

breaking or bond scission (from Raman) indicated by the shift, broadening, reduced or complete removal of the various peaks is related with the electronic processes. In case of air, two additional peaks identified at 1314 and 1363  $\text{cm}^{-1}$  at laser fluence of 2.5  $\text{J.cm}^{-2}$ , indicate that the underlying material has accumulated a sufficiently high density of defects due to cross linking of polymer macromolecules to initiate the “ultrafast melting” resulting in a highly disturbed surface as described by the AFM images.

It can be inferred from above discussion that an ultrashort laser-induced electronic excitation in the low intensity regime both in air and under UHV condition results in nanohillock-formation associated with structural and chemical changes. The structural changes are due to the modified photochemistry of the polymer around the ablation threshold where nanohillocks are formed by cross-linking, polymerization and chain scission, both in case of air and UHV condition. It has important implications for the potential of fs ablation for nanoprocessing of transparent materials, where highly efficient and localized laser energy deposition in the target overcomes the limitations of processing with conventional thermal ablation.

#### ***(b) Moderate and high fluence regime***

Raman spectra of an unexposed and exposed CR-39 for moderate and higher fluences (0.25 - 3.5  $\text{J.cm}^{-2}$ ) with 20 succeeding pulses are shown in figure 3.52. The spectra show that the density of  $-\text{CH}_2-$  groups is reduced significantly after exposure at laser fluences of 0.25 and 0.5  $\text{J.cm}^{-2}$  and is almost negligible at laser fluences of 1.5, 2.5 and 3.6  $\text{J.cm}^{-2}$ . This is attributed to the reduction of hydrogen content in the irradiated target for lower laser fluences and its complete disappearance for higher fluences [188]. At laser fluences of 0.25 and 0.5  $\text{J.cm}^{-2}$  broadening of these bands is also observed with a Raman shift of 4  $\text{cm}^{-1}$  in symmetric stretching mode. Raman shift at these fluences can be attributed to strains developed by radiation induced heating [195].

The observed broadening in the peaks is due to the decrease in phonon lifetime as a result of scattering from radiation-induced defects [191]. In electrical-insulating solids, it is believed that point defects affect the lattice vibrations and cause scattering of phonons due to mass differences (mass fluctuation size) and inter atomic coupling force differences (strain field fluctuations) [192] which will shorten the mean free path of the phonon [193]. For higher laser fluence (1.5, 2.5 and 3.6  $\text{J.cm}^{-2}$ ), no peaks are identified for these  $-\text{CH}_2-$  stretching bonds, which is ascribed to complete destruction of these bands. Two peaks are observed at 1737  $\text{cm}^{-1}$  and 1643  $\text{cm}^{-1}$  corresponds to C=O and C=C bands, respectively. The intensity of peaks



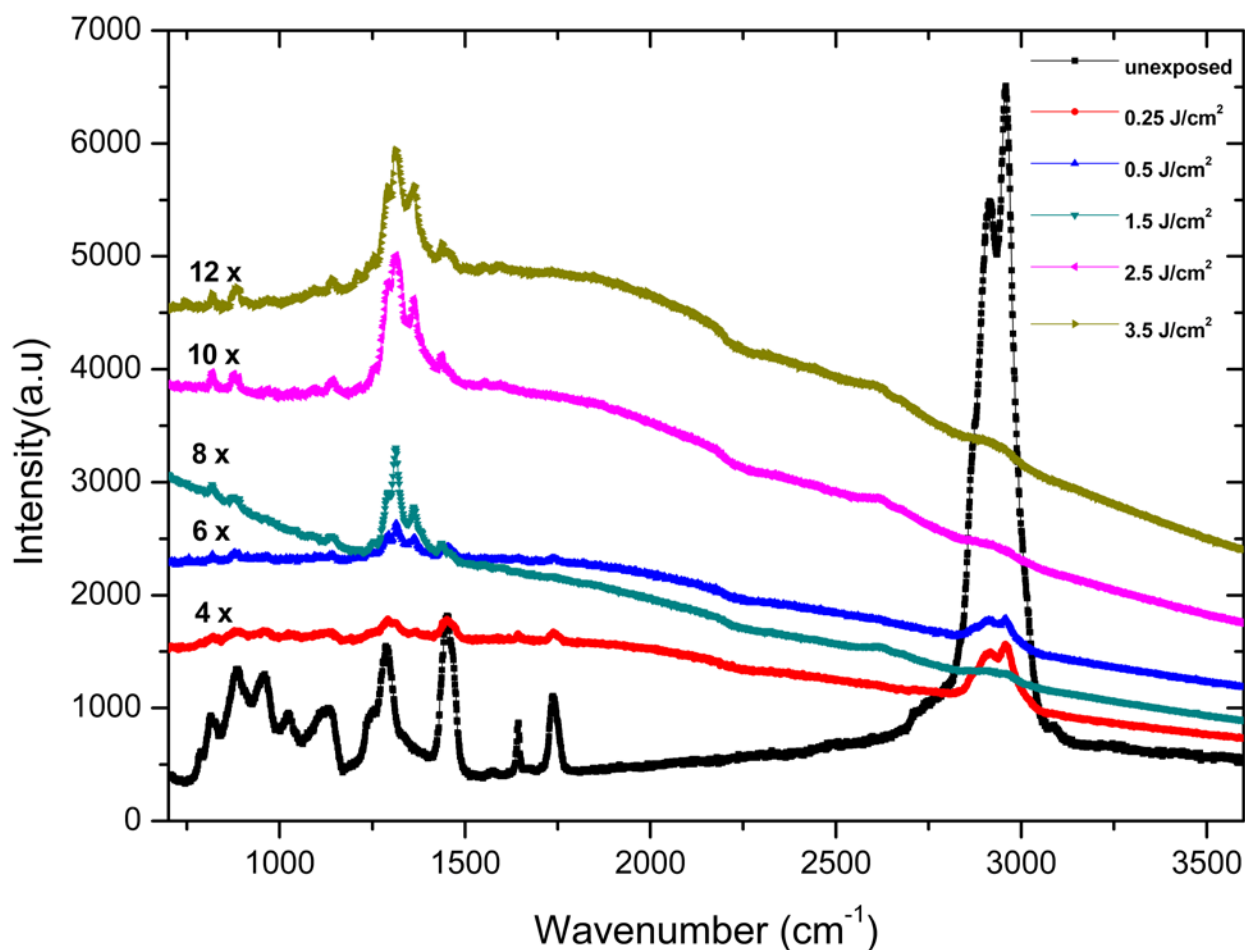


Figure 3.52: Raman spectra of the virgin and laser irradiated CR-39 in air for different fluences  $0.25 \text{ J.cm}^{-2}$ ,  $0.5 \text{ J.cm}^{-2}$ ,  $1.5 \text{ J.cm}^{-2}$ ,  $2.5 \text{ J.cm}^{-2}$  and  $3.6 \text{ J.cm}^{-2}$ .

for these bands is reduced after exposure at a laser fluence of  $0.25 \text{ J.cm}^{-2}$ . For higher laser fluences ranging from  $0.5$ – $3.6 \text{ J.cm}^{-2}$  these bands are completely disappeared exhibiting the destruction of carbonate ester bonds [196] and degradation of CR-39 involving carbonyl C=O bond-breaking and folding of chains [191]. The band at  $1451 \text{ cm}^{-1}$  originates from the –C–H– bending mode. For this band, reduced intensity and broadening without shift in the peak is observed for two lower laser fluences i.e.  $0.25$  and  $0.5 \text{ J.cm}^{-2}$ . This is due to breaking and weakening of –C–H– bonds. When the laser fluence is enhanced to the range of  $1.5$ – $3.6 \text{ J.cm}^{-2}$ , a new peak at  $1436 \text{ cm}^{-1}$  appears. This new band frequency corresponds to symmetric  $\text{CO}_2$  – stretching mode. It has already been reported that  $\text{CO}_2$  molecules are produced in CR-39 when it is irradiated by high energy ionizing radiation [197–199]. The production of  $\text{CO}_2$  can be due to the destruction of main chain of CR-39 by irradiation and is attributed to the break-up of the content of carbonate groups in the vicinity of  $1737 \text{ cm}^{-1}$ , which



structural changes explored by Raman spectroscopy. At low fluence regime, Raman spectroscopy for dielectric ( $\text{CaF}_2$ ) and semiconductor (Si) is indicative of only surface roughness enhancement due to the localized energy deposition without bulk melting and decomposition which favors the dominance of electronic processes or gentle ablation. Whereas, structural changes in CR-39 are due to the modified photochemistry of the polymer around the ablation threshold at which nanohillocks are formed by crosslinking, polymerization and chain scission.

Important features, like bumps, explosions, periodic surface structures, etc. formed at moderate fluence regime (slightly higher than ablation threshold) appear on the surfaces of all materials due to the dominance of ultrafast melting or plasma formation at a time scale of a few hundreds of fs. The bump formation and explosions like features are consequence of relaxation of compressive stresses, diffusion, transformation and aggregation of primary defects. The existence of periodic surface structures is a result of surface plasmon waves.

At a high fluence regime (significantly higher than ablation threshold), there is occurrence of a transition from these ultrafast electronic processes (fs time regime) or gentle ablation to large class of thermal processes, or strong ablation (in ps time scale) where electron-phonon coupling comes into play. These thermal processes are reflected in non-localized large scale disturbances. These disturbances in the form of larger elevations, craters and island like structures are dominant features exhibited at the surface of all materials in this fluence regime. The features are ascribed to melting, vaporization and phase transformation.

At moderate and higher fluence regimes Raman spectroscopy reveals the existence of compressive and tensile stresses and accumulation of larger number of defect aggregates (thermal decomposition) indicated by the shifting and identification of new peaks in case of  $\text{CaF}_2$ . Additional identified peaks are also related to diffusion and transformation, typical features of thermal processes leading to the growth of larger bump-and explosion like defect. For Si irradiated at higher fluence, where the thermal processes are dominant, polycrystallization and amorphization phases are present which are due to surface melting and re-solidification.

Another correlation in case of CR-39 comprising of non linear absorption and the surface features reveals that multiphoton absorption is strongly influenced by surface modifications, structural and chemical changes induced by an ultra short laser irradiation. Three photon absorption is found to be dominant process in pristine CR-39. However, the occurrence of both three and two photon absorption processes is probable for irradiated target. The enhanced nonlinear absorption with the increase in the laser fluences is the cause of gradual

sufficient to overcome the band gap (3.6 eV indirect and 4.2 eV direct) of CR-39 [83]. Our results of three photon absorption (fitting curve in figure 3.53 (a)) strongly prove that by the simultaneous absorption of at least three photons, a sufficient amount of energy is provided to overcome the band gap of CR-39.

Figure 3.53 (b) shows a Z-scan measurement of ultra short laser irradiated CR-39 for different laser fluences. It is evident that nonlinear absorption of the polymer increases with increasing laser fluence. For the fluence of  $0.2 \text{ Jcm}^{-2}$  no significant change in the nonlinear absorption was observed. For CR-39 exposed at a fluence  $0.5 \text{ Jcm}^{-2}$  the absorption is 50% and it enhances to 80 % when target is exposed at a fluence of  $1.5 \text{ Jcm}^{-2}$  whereas it reaches to 90% at a laser fluence of  $3.6 \text{ Jcm}^{-2}$ . Gradual formation of the bumps (figure 3.48 a-d and 3.49 a-b) and changes in chemical structure (figure 3.52) of CR-39 justifies the increase in nonlinear absorption with the increase in the laser fluence. In addition, the increase in the three photon absorption maxima (from  $1.8 \times 10^{-23} \text{ (cm}^3 \cdot \text{W}^{-2})$  to  $26 \times 10^{-23} \text{ (cm}^3 \cdot \text{W}^{-2})$  with the laser fluence in the graph of figure 3.54 favors a three photon process. The optical absorption properties of the polymer are governed by the electronic, vibrational and rotational structure of the molecules. Our AFM and Raman spectra measurements clearly indicate that incident photons have sufficient energy to cause surface and structural modification in the constituent molecules which can bring about significant changes in the absorption properties of CR-39. Intensive laser fluence causes photochemical decomposition in which electronically excited states undergo internal conversion to the vibrationally excited ground state [203]. Consequently, laser-induced photofragmentation can change the binding energies of the neighboring atoms and their coupling to crystal lattice. Mechanism of enhanced density of these vibrationally excited molecules causes a significant enhancement of the multiphoton absorption coefficient of the polymer [204].

The structural destruction of polymer increases the electronic disorder inducing the creation of permitted state in the forbidden (indirect) band or deformation of the valence band [83]. As the interactions of light with valence electrons of the material are responsible for optical properties [205], therefore deformation of valence bands can cause optical modification of the polymer after irradiation. Lasers can induce structural irregularities or defects in the polymer in the form of stress distributions [206], self-trapped exciton, color centers, densification, refractive index change [207], scission of polymer chains [82], formation of free radicals, new bonds and local melting in transparent materials. All these phenomena are responsible for

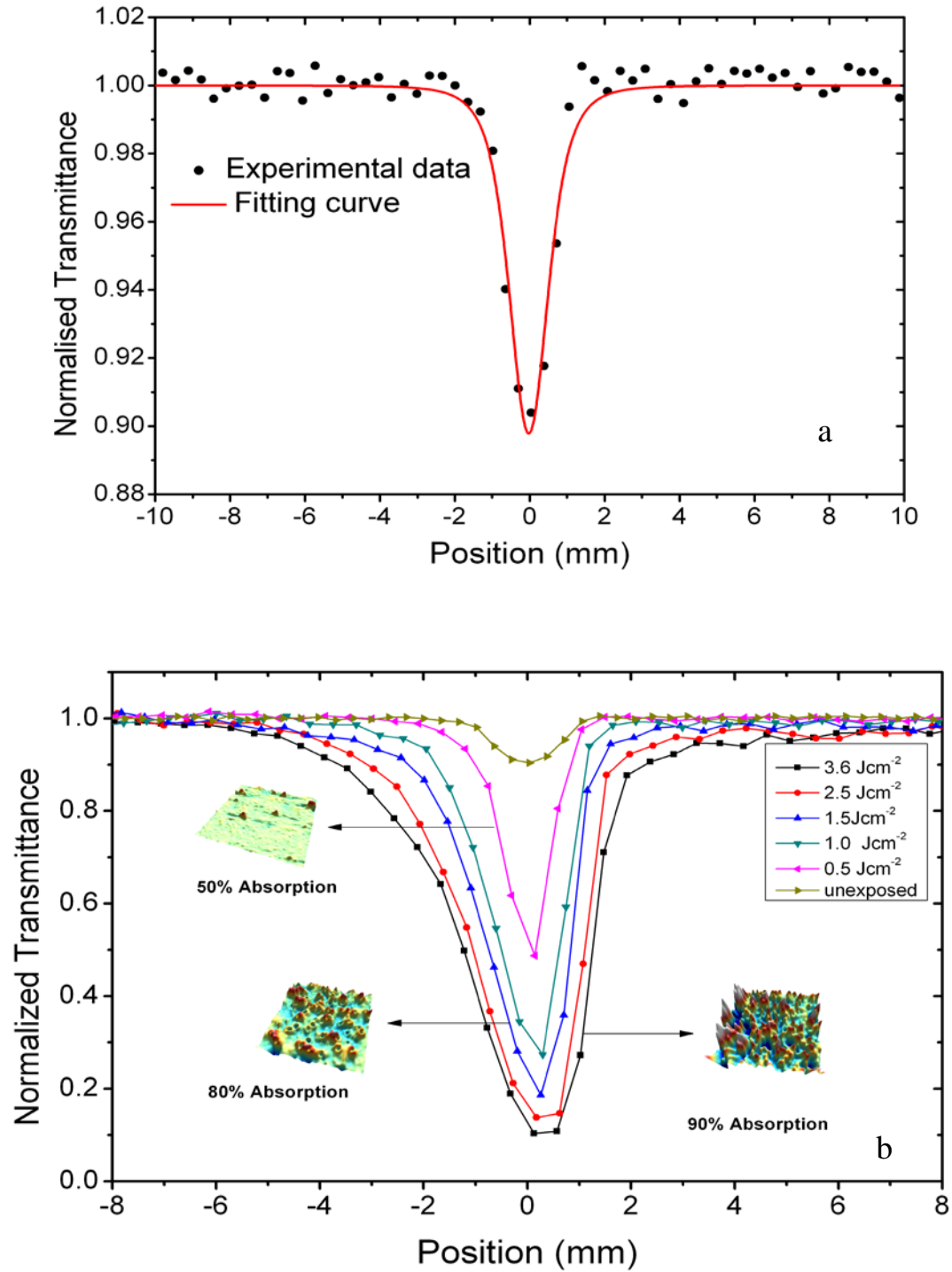


Figure 3.53: (a) Normalized transmittance/absorption measured by Z-scan technique for ultra short laser irradiated CR-39 at different fluences along with surface micrographs pertaining to the respective fluence. (b) Z-scan measurements for an unexposed CR-39 and the corresponding fitting curves obtained from equation 3.21.

a change in the nonlinear absorption of the irradiated material. This change in the nonlinear absorption leads to bumps formation and explosion like features in the irradiated target. However, it is not necessarily true for the irradiated polymer that the whole of the absorption is only due

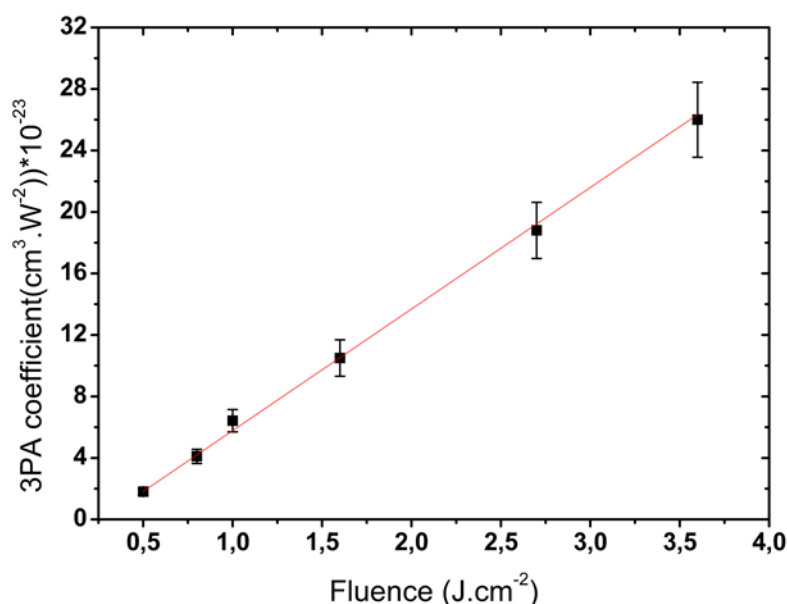


Figure 3.54: Three photon absorption coefficient of femtosecond laser irradiated CR-39 for different

to the three photon because the polymer undergoes several morphological changes and modifications of the polymerization state and important composition changes of the monomer as evidenced from AFM images and Raman measurements. These effect could possibly lead to the formation of absorption centers with changes in band gap energies and an energy cut off lower than the three photon energy and thus to a two photon absorption. Therefore, the occurrence of both two and three photon absorption processes is probable for an irradiated target.

Above results show that multiphoton absorption properties of CR-39 are strongly influenced by surface modifications, structural and chemical changes induced by an ultra short laser irradiation. Three photon absorption is found to be dominant process in pristine CR-39. However the occurrence of both three and two photon absorption processes is probable for irradiated target due to change in band gap energies. The enhanced nonlinear absorption with the increase in the laser fluences is the cause of gradual growth of nanobumps, explosions, nanocavities, etc. formed due to compressive thermal stresses. Bond breaking, cross linking and formation of new bonds by energy deposited during the ultra short laser irradiation is also a major cause of significant increase in the nonlinear absorption of CR-39.

# Chapter 4

## Conclusions

---

Materials when irradiated with ultrashort laser pulses undergo ultrafast electronic and slow thermal processes. A flow chart of the processes governing the ultra short laser matter ablation is given in figure 4.1. The main aim of the work was to identify these processes by surface topographical investigations.

Ultra short laser irradiation effects on the surface modification of  $\text{CaF}_2$ , CR-39 (insulators), Si (semiconductor) and Al (metal) as a function of laser fluence have been investigated using an Atomic Force Microscope (AFM) and Raman Scattering technique. Three different modification regimes depending upon the applied laser fluence are clearly identified: A very low fluence regime (around the ablation threshold), a moderate fluence regime (slightly higher than the ablation threshold), and a high fluence regime (significantly higher than the ablation threshold). The appearance of topographical features like nanohillocks due to localized energy deposition reflect the occurrence of ultrafast Coulomb Explosion (CE) (sub 100 fs) or Surface Optical Rectification (SOR) in the low fluence regime. The existence of these localized nanostructures is a typical characteristic feature for all materials ( $\text{CaF}_2$ , CR-39, Si and Al) at a lower fluence. It is remarkable, that hillocks have been formed for all investigated materials around the ablation threshold exactly under same conditions (laser energy, pulse duration and UHV condition) for which a substantial part of the ejected particles have kinetic energies of several eV. Even more importantly by applying a pump-probe technique (previous measurements [13, 14]) we have been able to establish a very characteristic correlation between the yield of particles with specific energies and the timescale, on which the laser energy is deposited into the material. This again is not a feature of a particular material, but has a quite general validity for all materials. Fast electronic processes responsible for the emission of high energy particles as a result of energy deposition on a timescale of typically 20-200 fs are considered to be responsible for the formation nanohillocks. The transfer of energy stored in the hot electrons into kinetic energy of ablated particles or dislocated target surface atoms is a complicated process. Since many mechanisms can and will contribute, a conclusive answer, which one is actually taking place, is difficult.

Based on several experimental observations, it is postulated that Coulomb explosion is a highly probable explanation for the formation of nanohillocks on the surfaces of all the materials under consideration. In our opinion, however, in particular the short timescale, in which the energy has to be deposited, favors a Coulomb-like process or surface optical rectification (in metals).

Surface topographical features of the irradiated materials are well correlated with the

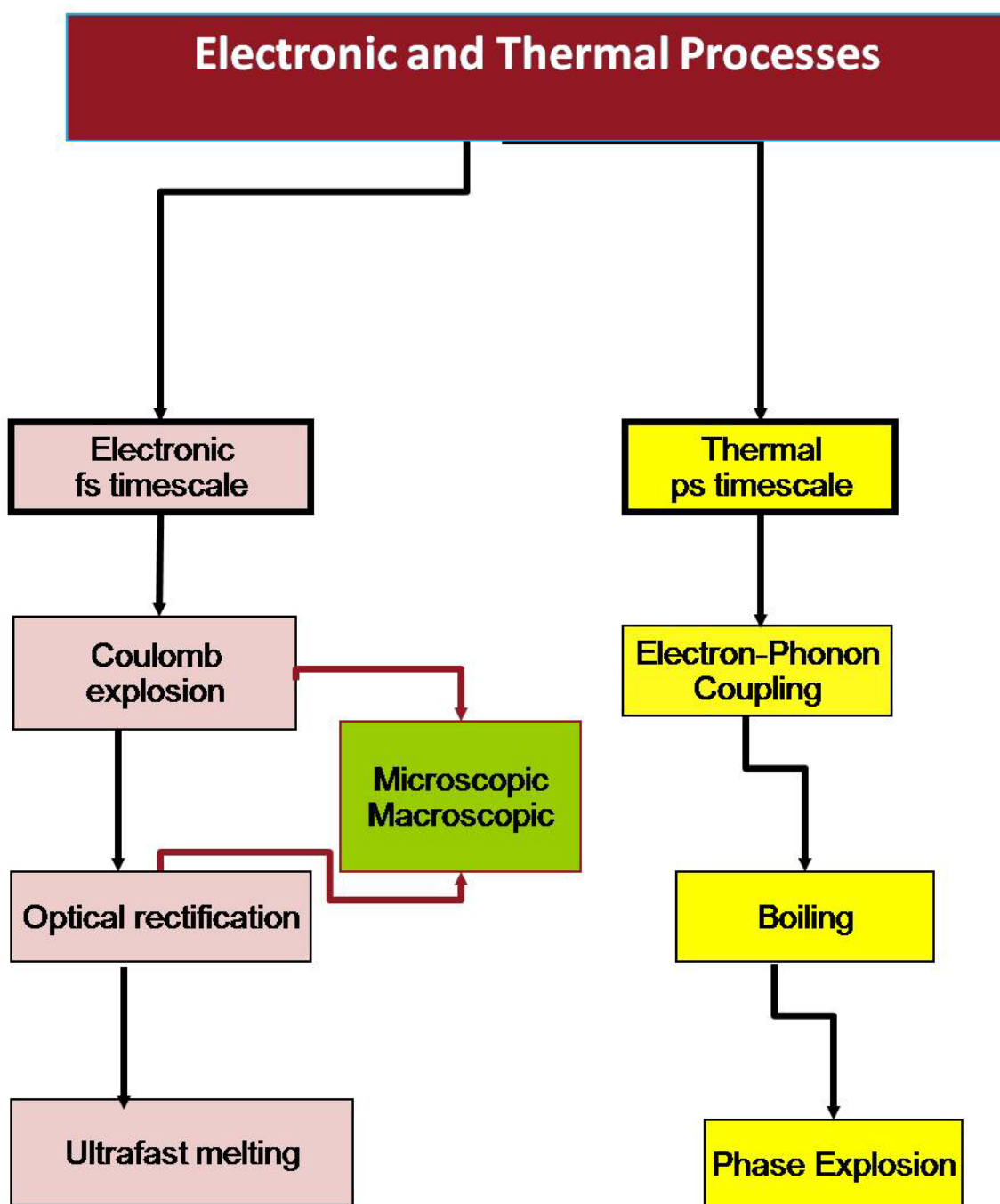


Figure 4.1: Ultrafast electronic and slow thermal processes governing the interaction of ultrashort laser radiation with matter.

structural changes explored by Raman spectroscopy. At low fluence regime, Raman spectroscopy for dielectric ( $\text{CaF}_2$ ) and semiconductor (Si) is indicative of only surface roughness enhancement due to the localized energy deposition without bulk melting and decomposition which favors the dominance of electronic processes or gentle ablation. Whereas, structural changes in CR-39 are due to the modified photochemistry of the polymer around the ablation threshold at which nanohillocks are formed by crosslinking, polymerization and chain scission.

Important features, like bumps, explosions, periodic surface structures, etc. formed at moderate fluence regime (slightly higher than ablation threshold) appear on the surfaces of all materials due to the dominance of ultrafast melting or plasma formation at a time scale of a few hundreds of fs. The bump formation and explosions like features are consequence of relaxation of compressive stresses, diffusion, transformation and aggregation of primary defects. The existence of periodic surface structures is a result of surface plasmon waves.

At a high fluence regime (significantly higher than ablation threshold), there is occurrence of a transition from these ultrafast electronic processes (fs time regime) or gentle ablation to large class of thermal processes, or strong ablation (in ps time scale) where electron-phonon coupling comes into play. These thermal processes are reflected in non-localized large scale disturbances. These disturbances in the form of larger elevations, craters and island like structures are dominant features exhibited at the surface of all materials in this fluence regime. The features are ascribed to melting, vaporization and phase transformation.

At moderate and higher fluence regimes Raman spectroscopy reveals the existence of compressive and tensile stresses and accumulation of larger number of defect aggregates (thermal decomposition) indicated by the shifting and identification of new peaks in case of  $\text{CaF}_2$ . Additional identified peaks are also related to diffusion and transformation, typical features of thermal processes leading to the growth of larger bump-and explosion like defect. For Si irradiated at higher fluence, where the thermal processes are dominant, polycrystalization and amorphization phases are present which are due to surface melting and re-solidification.

Another correlation in case of CR-39 comprising of non linear absorption and the surface features reveals that multiphoton absorption is strongly influenced by surface modifications, structural and chemical changes induced by an ultra short laser irradiation. Three photon absorption is found to be dominant process in pristine CR-39. However, the occurrence of both three and two photon absorption processes is probable for irradiated target. The enhanced nonlinear absorption with the increase in the laser fluences is the cause of gradual

growth of bumps, explosions, nanocavities, etc. formed due to compressive thermal stresses. Bond breaking, cross linking and formation of new bonds by energy deposited during the ultra short laser irradiation is also a major cause of significant increase in the non linear absorption of CR-39.

Figure 4.2 summarizes the observed topographical features corresponding to various physical processes on surfaces of dielectric, semiconducting, metallic and polymeric materials as a result of ultrashort laser irradiation.

In this overview some aspects of interaction of ultra-short laser radiation with solids are discussed. AFM investigations of the surface topography along with the characteristics of ejected particles by laser analytical methods yield coherent information and have widened the understanding of the processes involved. The results shown here are definitely a first step and have a large potential for further investigations.

There are some open questions like, what will be the influence of the pulse-shape and width on the surface topography of irradiated materials? Will it be possible to obtain nanohillock-like features if the pulse width is stretched up to few hundred fs-ps time scale? This is still a subject of investigation in future. The answer to this question might be achievable by analyzing the surface structures formed with irradiation of the materials by varying the pulse width keeping the fluence around the ablation threshold where appearance of nanohillocks has been observed.

Ultrafast time-resolved pump-probe shadowgraphy is another important technique which could enable us to explore the time- and space-resolved measurements of expansion dynamics. This imaging analysis at fs and ps time scale can provide information about the development of melt ejections by ultrashort laser irradiation.

Correlation of pump-probe time of flight measurements (the time behavior of the energy deposition, the composition and energy of the emitted particles), with pump-probe shadowgraphy imaging (time-and space-resolved expansion dynamics) and with corresponding surface topography measurements as a function of fluence and pulse-width will enhance the understanding of the energy deposition and material ejection mechanism.



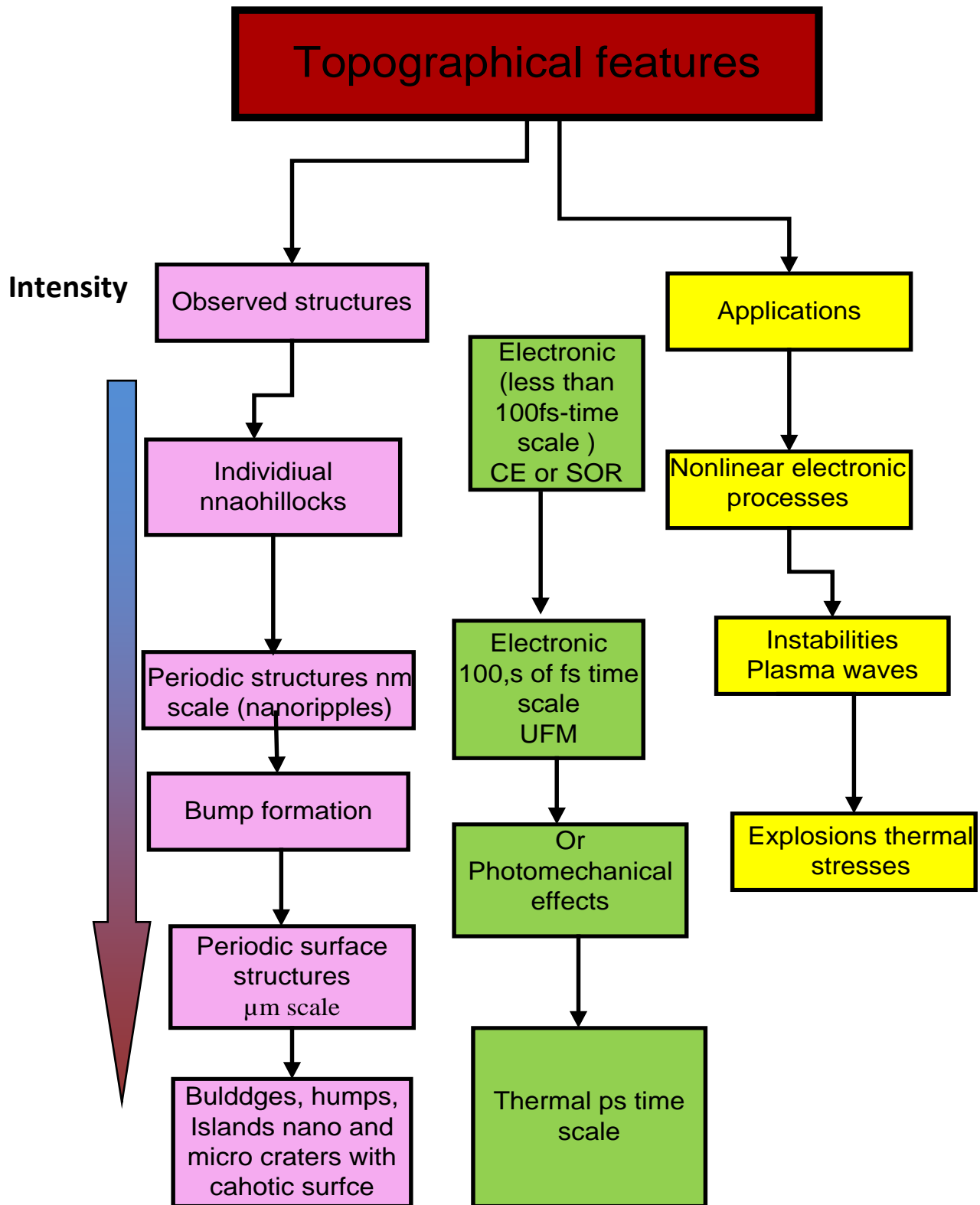


Figure 4.2: Observed topographical features on surfaces of dielectric, semiconducting, metallic and polymeric materials as a result of ultrashort laser irradiation corresponding to different involved physical processes.

## References

- [1] M. Kumar, R. M. Mehra, and S. Y. Choi, *Current Applied Physics* **9**, 737 (2009).
- [2] L. Láska, J. Krása, A. Velyhan, K. Jungwirth, E. Krouský, D. Margarone, M. Pfeifer, K. Rohlena, L. Ryc, J. Skála, L. Torrisi, and J. Ullschmied, *Laser and Particle Beams* **27**, 137 (2009).
- [3] Y. Godwal, M. T. Taschuk, S. L. Lui, Y. Y. Tsui, and R. Fedosejevs, *Laser and Particle Beams* **26**, 95 (2008).
- [4] N. G. Borisenko *et al.*, *Laser and Particle Beams* **26**, 537 (2008).
- [5] B. M. Mirdan, H. A. Jawad, D. Batani, V. Conte, T. Desai, and R. Jafer, *Laser and Particle Beams* **27**, 103 (2009).
- [6] O. Beyer, D. Maxein, K. Buse, B. Sturman, H. T. Hsieh, and D. Psaltis, *Physical Review E - Statistical, Nonlinear, and Soft Matter Physics* **71** 1(2005).
- [7] N. Belhadj, Y. Park, S. LaRochelle, K. Dossou, and J. Azaña, *Optics Express* **16**, 8727 (2008).
- [8] T. Y. Hwang, A. Y. Vorobyev, and C. Guo, *Physical Review B - Condensed Matter and Materials Physics* **79** (8), 085425 (2009).
- [9] A. Plech, V. Kotaidis, M. Lorenc, and J. Boneberg, *Nature Physics* **2**, 44 (2006).
- [10] E. Stratakis, V. Zorba, M. Barberoglou, C. Fotakis, and G. A. Shafeev, *Applied Surface Science* **255**, 5346 (2009).
- [11] F. Costache, S. Eckert, and J. Reif, *Applied Surface Science* **252**, 4416 (2006).
- [12] H. Dachraoui, and W. Husinsky, *Physical Review Letters* **97**10, 7601 (2006).
- [13] H. Dachraoui, and W. Husinsky, *Applied Physics Letters* **89**, 104102 (2006).
- [14] H. Dachraoui, W. Husinsky, and G. Betz, *Applied Physics A-Materials Science & Processing* **83**, 333 (2006).
- [15] A. S. El-Said, Heller, R., Meissl, W., Ritter, R., Facsko, S., Lemell, C., Solleder, B., Gebeshuber, I. C., Betz, G., Toulemonde, M., Möller, W., Burgdörfer, J., Aumayr, F., *Physical Review Letters* **100**, 237601 (2008).
- [16] D. S. Ivanov, B. Rethfeld, G. M. O'Connor, T. J. Glynn, A. N. Volkov, and L. V. Zhigilei, *Applied Physics A: Materials Science and Processing* **92**, 791 (2008).
- [17] W. Husinsky, R. Bruckmüller, P. Blum, F. Viehböck, D. Hammer, and E. Benes, *Journal of Applied Physics* **48**, 4734 (1977).
- [18] A. Vella, B. Deconihout, L. Marrucci, and E. Santamato, *Physical Review Letters* **99**, 046103 (2007).

- [19] W. Marine, N. M. Bulgakova, L. Patrone, and I. Ozerov, *Applied Physics A: Materials Science and Processing* **79**, 771 (2004).
- [20] N. M. Bulgakova, Stoian, R., Rosenfeld, A., Hertel, I. V., Campbell, E. E. B., *Physical Review B - Condensed Matter and Materials Physics* **69**, 541021 (2004).
- [21] N. M. Bulgakova, R. Stoian, A. Rosenfeld, I. V. Hertel, W. Marine, and E. E. B. Campbell, *Applied Physics A-Materials Science & Processing* **81**, 345 (2005).
- [22] B. Rethfeld, K. Sokolowski-Tinten, D. Von der Linde, and S. I. Anisimov, *Physical Review B - Condensed Matter and Materials Physics* **65**, 921031 (2002).
- [23] B. Rethfeld, *Physical Review Letters* **92**, 187401 (2004).
- [24] A. Kaiser, E. Rethfeld, M. Vicanek, and G. Simon, *Physical Review B - Condensed Matter and Materials Physics* **61**, 11437 (2000).
- [25] E. G. Gamaly, A. V. Rode, B. Luther-Davies, and V. T. Tikhonchuk, *Physics of Plasmas* **9**, 949 (2002).
- [26] P. B. Allen, *Physical Review Letters* **59**, 1460 (1987).
- [27] R. H. M. Groeneveld, R. Sprik, and A. Lagendijk, *Physical Review B* **51**, 11433 (1995).
- [28] W. S. Fann, R. Storz, H. W. K. Tom, and J. Bokor, *Physical Review B* **46**, 13592 (1992).
- [29] B. Rethfeld, A. Kaiser, M. Vicanek, and G. Simon, *Applied Physics A: Materials Science and Processing* **69**, S109 (1999).
- [30] B. Rethfeld, A. Kaiser, M. Vicanek, and G. Simon, *Physical Review B - Condensed Matter and Materials Physics* **65**, 2143031 (2002).
- [31] D. Von Der Linde, K. Sokolowski-Tinten, and J. Bialkowski, *Applied Surface Science* **109-110**, 1 (1997).
- [32] R. Stoian, A. Rosenfeld, D. Ashkenasi, I. V. Hertel, N. M. Bulgakova, and E. E. B. Campbell, *Physical Review Letters* **88**, 976031 (2002).
- [33] M. Huang, F. Zhao, Y. Cheng, N. Xu, and Z. Xu, *Physical Review B - Condensed Matter and Materials Physics* **79**, 125436 (2009).
- [34] S. Tokita, S. Inoue, S. Masuno, M. Hashida, and S. Sakabe, *Applied Physics Letters* **95** (2009).
- [35] R. Stoian, D. Ashkenasi, A. Rosenfeld, and E. E. B. Campbell, *Physical Review B - Condensed Matter and Materials Physics* **62**, 13167 (2000).
- [36] J. Reif, F. Costache, S. Eckert, and M. Henyk, *Applied Physics A-Materials Science & Processing* **79**, 1229 (2004).

- [37] W. G. Roeterdink, L. B. F. Juurlink, O. P. H. Vaughan, J. Dura Diez, M. Bonn, and A. W. Kley, *Applied Physics Letters* **82**, 4190 (2003).
- [38] A. A. Rukhadze, K. Z. Rukhadze, and V. P. Tarakanov, *Technical Physics* **53**, 264 (2008).
- [39] V. Y. Bychenkov, and V. F. Kovalev, *Plasma Physics Reports* **32**, 973 (2006).
- [40] N. M. Bulgakova, I. M. Burakov, Y. P. Messhcheryakov, R. Stoian, A. Rosenfeld and I. V. Hertel *JLMN-Journal of Laser Micro/Nanoengineering* **2** (1) 77 (2007).
- [41] S. Sakabe, M. Hashida, S. Tokita, S. Namba, and K. Okamuro, *Physical Review B - Condensed Matter and Materials Physics* **79**(3) 033409 (2009).
- [42] R. Stoian, Rosenfeld, A., Ashkenasi, D., Hertel, I. V., Bulgakova, N. M., Campbell, E. E. B., *Physical Review Letters* **88**, 097603 (2002).
- [43] B. C. Stuart, Feit, M. D., Rubenchik, A. M., Shore, B. W., Perry, M. D., *Physical Review Letters* **74**, 2248 (1995).
- [44] V. Schmidt, W. Husinsky, and G. Betz, *Applied Surface Science* **197**, 145 (2002).
- [45] C. Guo, G. Rodriguez, A. Lobad, and A. J. Taylor, *Physical Review Letters* **84**, 4493 (2000).
- [46] C. Guo, and A. J. Taylor, *Physical Review B - Condensed Matter and Materials Physics* **62**, R11921 (2000).
- [47] M. Weber, and A. Liebsch, *Physical Review B* **35**, 7411 (1987).
- [48] A. Vella, M. Gilbert, A. Hideur, F. Vurpillot, and B. Deconihout, *Applied Physics Letters* **89**, 251903 (2006).
- [49] K. Sokolowski-Tinten, J. Bialkowski, and D. Von Der Linde, *Physical Review B* **51**, 14186 (1995).
- [50] K. Sokolowski-Tinten, C. Blome, C. Dietrich, A. Tarasevitch, M. Horn Von Hoegen, D. Von Der Linde, A. Cavalleri, J. Squier, and M. Kammler, *Physical Review Letters* **87**, 225701 (2001).
- [51] A. Plech, P. Leiderer, and J. Boneberg, *Laser & Photonics Reviews* **3**, 435 (2009).
- [52] A. Cavalleri, Sokolowski-Tinten, K., Bialkowski, J., Schreiner, M., Von Der Linde, D., *Journal of Applied Physics* **85**, 3301 (1999).
- [53] H. O. Jeschke, M. E. Garcia, M. Lenzner, J. Bonse, J. Krüger, and W. Kautek, *Applied Surface Science* **197-198**, 839 (2002).
- [54] K. Sokolowski-Tinten, and D. Von Der Linde, *Physical Review B - Condensed Matter and Materials Physics* **61**, 2643 (2000).

- [55] D. P. Korfiatis, K. A. T. Thoma, and J. C. Vardaxoglou, *Applied Surface Science* **255**, 7605 (2009).
- [56] B. C. Stuart, M. D. Feit, S. Herman, A. M. Rubenchik, B. W. Shore, and M. D. Perry, *Journal of the Optical Society of America B: Optical Physics* **13**, 459 (1996).
- [57] D. S. Ivanov, and B. Rethfeld, *Applied Surface Science* **255**, 9724 (2009).
- [58] Y. Hirayama, and M. Obara, *Applied Surface Science* **197-198**, 741 (2002).
- [59] N. M. Bulgakova, and I. M. Bourakov, *Applied Surface Science* **197-198**, 41 (2002).
- [60] A. Miotello, and R. Kelly, *Applied Physics A: Materials Science and Processing* **69**, S67 (1999).
- [61] B. C. Stuart, M. D. Feit, A. M. Rubenchik, B. W. Shore, and M. D. Perry, *Physical Review Letters* **74**, 2248 (1995).
- [62] D. Ashkenasi, H. Varel, A. Rosenfeld, F. Noack, and E. E. B. Campbell, *Applied Physics A: Materials Science and Processing* **63**, 103 (1997).
- [63] M. Lenzner, J. Krüger, Sartania, S., Cheng, Z., Spielmann, Ch., Mourou, G., Kautek, W., Krausz, F., *Physical Review Letters* **80**, 4076 (1998).
- [64] A. Heltzel, A. Battula, J. R. Howell, and S. Chen, *Journal of Heat Transfer* **129**, 53 (2007).
- [65] N. Itoh, and K. Tanimura, *Journal of Physics and Chemistry of Solids* **51**, 717 (1990).
- [66] T. Q. Jia, X. X. Li, D. H. Feng, C. F. Cheng, R. X. Li, H. Chen, and Z. Z. Xu, *Applied Physics A: Materials Science and Processing* **81**, 645 (2005).
- [67] J. C. Miller, R.F.Haglund,Jr., *Laser Ablation and Desorption* (Acamedic Press USA, 1998).
- [68] V. Schmidt, W. Husinsky, and G. Betz, *Physical Review Letters* **85 (16)**, 3516 (2000).
- [69] E. Vanagas, I. Kudryashov, D. Tuzhilin, S. Juodkazis, S. Matsuo, and H. Misawa, *Applied Physics Letters* **82**, 2901 (2003).
- [70] M. Lenner, Kaplan, A., Huchon, Ch., and Palmer, R.E., *Physical Review B - Condensed Matter and Materials Physics* **79** 184105 (2009).
- [71] Y. P. Meshcheryakov, and N. M. Bulgakova, *Applied Physics A: Materials Science and Processing* **82**, 363 (2006).
- [72] O. Varlamova, F. Costache, J. Reif, and M. Bestehorn, *Applied Surface Science* **252**, 4702 (2006).
- [73] G. Binnig, C. F. Quate, Ch. Gerber, *Phys. Rev. Lett.* **56**, 930 (1986).
- [74] J. Ralston, I. Larson, M. W. Rutland, A.A. Feiler, M.Kleijn, *Pure Appl. Chem.* **77 (12)** 2149 (2005).

- [75] J. Bonse, K. W. Brzezinka, and A. J. Meixner, *Applied Surface Science* **221**, 215 (2004).
- [76] T. Yamauchi, S. Takada, H. Ichijo, and K. Oda, *Radiation Measurements* **34**, X69 (2001).
- [77] J. Wasyluk, D. Adley, T. S. Perova, A. M. Rodin, J. Callaghan, and N. Brennan, *Applied Surface Science* **255**, 5546 (2009).
- [78] M. Sheik-Bahae, A. A. Said, T.-H. Wei, D. J. Hagan, and E. W. Van Stryland, *IEEE Journal of Quantum Electronics* **26**, 760 (1990).
- [79] A. Ajami, M. S. Rafique, N. Pucher, S. Bashir, W. Husinsky, R. Liska, R. Inführ, H. Lichtenegger, J. Stampfl, and St. Lüftenegger, in *Proc. SPIE* **7027**, pp. 70271H.
- [80] T. Q. Jia *et al.*, *Physical Review B - Condensed Matter and Materials Physics* **73**, 1 (2006).
- [81] K. Tanimura, *Physical Review B - Condensed Matter and Materials Physics* **63**, 1843031 (2001).
- [82] S. Bashir, M. S. Rafique, and F. Ul-Haq, *Laser and Particle Beams* **25**, 181 (2007).
- [83] M. F. Zaki, *Journal of Physics D-Applied Physics* **41**, 75404 (2008).
- [84] T. Yamauchi, Y. Mori, K. Oda, N. Yasuda, H. Kitamura, and B. Rémi, *Japanese Journal of Applied Physics, Part 1: Regular Papers and Short Notes and Review Papers* **47**, 3606 (2008).
- [85] S. Kodaira, N. Yasuda, H. Tawara, K. Ogura, T. Doke, N. Hasebe, and T. Yamauchi, *Nuclear Instruments and Methods in Physics Research, Section B: Beam Interactions with Materials and Atoms* **267**, 1817 (2009).
- [86] T. Yamauchi, S. Watanabe, A. Seto, K. Oda, N. Yasuda, and R. Barillon, *Radiation Measurements* **43**, S106 (2008).
- [87] F. Abu-Jarad, S. M. A. Durrani, and M. A. Islam, *Nuclear Inst. and Methods in Physics Research, B* **74**, 419 (1993).
- [88] S. Juodkazis, H. Okuno, N. Kujime, S. Matsuo, and H. Misawa, *Applied Physics A: Materials Science and Processing* **79**, 1555 (2004).
- [89] D. Bäuerle, *Laser processing and Chemistry* (Springer-Verlag Berlin New York, 2000).
- [90] V. R. Bhardwaj, E. Simova, P. P. Rajeev, C. Hnatovsky, R. S. Taylor, D. M. Rayner, and P. B. Corkum, *Physical Review Letters* **96**, 057404 (2006).
- [91] C. Kittel, *Introduction to Solid State physics* (John Wiley and Sons Inc New York 1996).

- [92] A. Chettah, Z. G. Wang, M. Kac, H. Kucal, A. Meftah, and M. Toulemonde, Nuclear Instruments and Methods in Physics Research, Section B: Beam Interactions with Materials and Atoms **245**, 150 (2006).
- [93] D. Kovac̆, G. Otto, and G. Hobler, Nuclear Instruments and Methods in Physics Research, Section B: Beam Interactions with Materials and Atoms **228**, 226 (2005).
- [94] A. S. El-Said *et al.*, Nuclear Instruments & Methods in Physics Research Section B-Beam Interactions with Materials and Atoms **258**, 167 (2007).
- [95] G. Schiwietz, K. Czerski, R. Hellhammer, M. Roth, F. Staufenbiel, R. C. Fadanelli, and P. L. Grande, Nuclear Instruments and Methods in Physics Research, Section B: Beam Interactions with Materials and Atoms **266**, 1287 (2008).
- [96] M. Terasawa, Vacuum **81**, 142 (2006).
- [97] M. Terasawa, Z. A. Insepov, T. Sekioka, A. A. Valuev, and T. Mitamura, Nuclear Instruments and Methods in Physics Research, Section B: Beam Interactions with Materials and Atoms **212**, 436 (2003).
- [98] D. Boschetto, E. G. Gamaly, A. V. Rode, B. Luther-Davies, D. Glijer, T. Garl, O. Albert, A. Rousse, and J. Etchepare, Physical Review Letters **1008** (2), 027404 (2008).
- [99] Y. Dong, and P. Molian, Applied Physics Letters **84**, 10 (2004).
- [100] M. Henyk, N. Vogel, D. Wolfframm, A. Tempel, and J. Reif, Applied Physics A: Materials Science and Processing **69**, S355 (1999).
- [101] R. Bennewitz, D. Smith, and M. Reichling, Physical Review B - Condensed Matter and Materials Physics **59**, 8237 (1999).
- [102] R. Wagner, J. Gottmann, A. Horn, and E. W. Kreutz, Applied Surface Science **252**, 8576 (2006).
- [103] J. Reif, O. Varlamova, and F. Costache, Applied Physics A: Materials Science and Processing **92**, 1019 (2008).
- [104] G. Miyaji, and K. Miyazaki, Optics Express **16**, 16265 (2008).
- [105] G. Miyaji, and K. Miyazaki, Applied Physics Letters **91** (2007).
- [106] T. Otobe, M. Yamagiwa, J. I. Iwata, K. Yabana, T. Nakatsukasa, and G. F. Bertsch, Physical Review B - Condensed Matter and Materials Physics **77**, 165104 (2008).
- [107] G. K. Giust, and T. W. Sigmon, Applied Physics Letters **70**, 767 (1997).
- [108] T. H. R. Crawford, J. Yamanaka, G. A. Botton, and H. K. Haugen, Journal of Applied Physics **103** (2008).
- [109] J. Bonse, S. Baudach, J. Krüger, W. Kautek, and M. Lenzner, Applied Physics A: Materials Science and Processing **74**, 19 (2002).

- [110] A. Rosenfeld, M. Lorenz, D. Ashkenasi, P. Rudolph, J. Krüger, and W. Kautek, *Applied Physics A: Materials Science and Processing* **69**, S759 (1999).
- [111] A. Vogel, and V. Venugopalan, *Chemical Reviews* **103**, 577 (2003).
- [112] B. Poumellec, L. Sudrie, M. Franco, B. Prade, and A. Mysyrowicz, *Optics Express* **11**, 1070 (2003).
- [113] S. Gaspard, M. Oujja, R. de Nalda, C. Abrusci, F. Catalina, L. Bañares, S. Lazare, and M. Castillejo, *Applied Surface Science* **254**, 1179 (2007).
- [114] S. Lazare, V. Tokarev, A. Sionkowska, and M. Wiśniewski, *Applied Physics A: Materials Science and Processing* **81**, 465 (2005).
- [115] A. Mermillod-Blondin, I. M. Burakov, Y. P. Meshcheryakov, N. M. Bulgakova, E. Audouard, A. Rosenfeld, A. Husakou, I. V. Hertel, and R. Stoian, *Physical Review B* **77**, 4205 (2008).
- [116] E. G. Gamaly, S. Juodkasis, K. Nishimura, H. Misawa, B. Luther-Davies, L. Hallo, P. Nicolai, and V. T. Tikhonchuk, *Physical Review B - Condensed Matter and Materials Physics* **73**, 214101 (2006).
- [117] S. Juodkasis, K. Nishimura, S. Tanaka, H. Misawa, E. G. Gamaly, B. Luther-Davies, L. Hallo, P. Nicolai, and V. T. Tikhonchuk, *Physical Review Letters* **96**, 6101 (2006).
- [118] T. Hashimoto, S. Juodkasis, and H. Misawa, *New Journal of Physics* **9** (2007).
- [119] M. S. R. A. Ajami, N. Pucher, S. Bashir, W. Husinsky, R. Liska, R. Inführ, H. Lichtenegger, J. Stampfl, and St. Lüftenegger, (*Proceedings SPIE 7027*, 2008), pp. 7027.
- [120] S. Bashir, M. S. Rafique, and W. Husinsky, *Applied Surface Science* (In Press) (2009).
- [121] X. R. Zhang, X. Xu, and A. M. Rubenchik, *Applied Physics A: Materials Science and Processing* **79**, 945 (2004).
- [122] F. Korte, J. Koch, and B. N. Chichkov, *Applied Physics A: Materials Science and Processing* **79**, 879 (2004).
- [123] A. Mermillod-Blondin, I. M. Burakov, Y. P. Meshcheryakov, N. M. Bulgakova, E. Audouard, A. Rosenfeld, A. Husakou, I. V. Hertel, and R. Stoian, *Physical Review B - Condensed Matter and Materials Physics* **77** (2008).
- [124] W. Watanabe, and K. Itoh, *Optics Express* **10**, 603 (2002).
- [125] C. B. Schaffer, N. Nishimura, E. N. Glezer, A. M. T. Kim, and E. Mazur, *Optics Express* **10**, 196 (2002).



- [126] S. Juodkazis, H. Misawa, T. Hashimoto, E. G. Gamaly, and B. Luther-Davies, *Applied Physics Letters* **88** (2006).
- [127] L. Hallo, A. Bourgeade, C. Mézel, G. Travaille, D. Hébert, B. Chimier, G. Schurtz, and V. T. Tikhonchuk, *Applied Physics A: Materials Science and Processing* **92**, 837 (2008).
- [128] B. Qian, Song, J., Dong, G., Su, L., Zhu, B., Liu, X., Sun, S., Zhang, Q., and Qiu, J., *Optical Express* **17**, 8552 (2009).
- [129] H. Tsuda, and J. Arends, *Advances in dental research* **11**, 539 (1997).
- [130] L. Su, J. Xu, W. Yang, X. Jiang, Z. Zhao, G. Zhou, H. Li, and J. Si, *Solid State Communications* **132**, 757 (2004).
- [131] C. Wurster, K. Lassmann, and W. Eisenmenger, *Physical Review Letters* **70**, 3451 (1993).
- [132] B. W. Bozlee, G. J. Exarhos, and R. W. Teel, *Proceedings of SPIE - The International Society for Optical Engineering* **3578**, 533 (1999).
- [133] T. Suzuki, K. Tanimura, and N. Itoh, *Physical Review B* **48**, 9298 (1993).
- [134] M. Bauer, M. Bischoff, S. Jukresch, T. Häfslensbusch, A. Matern, A. Gortler, R. W. Stark, A. Chuvilin, and U. Kaiser, *Optics Express* **17**, 8253 (2009).
- [135] K. Nakamota, *Infrared and Raman Spectra of Inorganic and Coordinate Compounds part a* (John Wiley and sons ,Inc New Jersey, 2009).
- [136] M. M. Tlili, M. B. Amor, C. Gabrielli, S. Joiret, G. Maurin, and P. Rousseau, *Journal of Raman Spectroscopy* **33**, 10 (2002).
- [137] S. C. Ke, *Physical Review B - Condensed Matter and Materials Physics* **62**, 4194 (2000).
- [138] F. S.Parker, *Applications of Infrared, Raman and Resonance Raman Spectroscopy in Biochemistry*  
(<http://books.google.at/books?hl=de&lr=&id=kd2RT4uSWE0C&oi=fnd&pg=PT6&dq=%22Parker%22+%22Applications+of+Infrared,+Raman,+and+Resonance+Raman+...%22+&ots=OONUeqwPah&sig=6wpeRGNbgTiXvdT7-VLsEP0-iNA#PPA4,M1>, 1983).
- [139] G. Wysocki, R. Denk, K. Piglmayer, N. Arnold, and D. Bäuerle, *Applied Physics Letters* **82**, 692 (2003).
- [140] R. Le Harzic, H. Schuck, D. Sauer, T. Anhut, I. Riemann, and K. Köhnig, *Optics Express* **13**, 6651 (2005).

- [141] K. Venkatakrishnan, and B. Tan, *Journal of Micromechanics and Microengineering* **16**, 1587 (2006).
- [142] F. Costache, S. Kouteva-Arguirova, and J. Reif, *Applied Physics A: Materials Science and Processing* **79**, 1429 (2004).
- [143] Y. F. Lu, W. K. Choi, Y. Aoyagi, A. Kinomura, and K. Fujii, *Journal of Applied Physics* **80**, 7052 (1996).
- [144] M. S. Trtica, B. M. Gakovic, D. Maravic, D. Batani, T. Desai, and R. Redaelli, *Applied Surface Science* **253**, 9315 (2007).
- [145] A. J. Pedraza, J. D. Fowlkes, and Y. F. Guan, *Applied Physics A: Materials Science and Processing* **77**, 277 (2003).
- [146] Z. Guosheng, P. M. Fauchet, and A. E. Siegman, *Physical Review B* **26**, 5366 (1982).
- [147] I. W. Boyd, S. C. Moss, T. F. Boggess, and A. L. Smirl, *Applied Physics Letters* **45**, 80 (1984).
- [148] M. Y. Shen, C. H. Crouch, J. E. Carey, R. Younkin, E. Mazur, M. Sheehy, and C. M. Friend, *Applied Physics Letters* **82**, 1715 (2003).
- [149] T. H. Her, R. J. Finlay, C. Wu, and E. Mazur, *Applied Physics A: Materials Science and Processing* **70**, 383 (2000).
- [150] A. J. Pedraza, J. D. Fowlkes, and D. H. Lowndes, *Applied Physics Letters* **74**, 2322 (1999).
- [151] S. I. Dolgaev, S. V. Lavrishev, A. A. Lyalin, A. V. Simakin, V. V. Voronov, and G. A. Shafeev, *Applied Physics A: Materials Science and Processing* **73**, 177 (2001).
- [152] M. S. Trtica, B. M. Gakovic, B. B. Radak, D. Batani, T. Desai, and M. Bussoli, *Applied Surface Science* **254**, 1377 (2007).
- [153] J. E. Sipe, J. F. Young, J. S. Preston, and H. M. Van Driel, *Physical Review B* **27**, 1141 (1983).
- [154] D. K. Fork, G. B. Anderson, J. B. Boyce, R. I. Johnson, and P. Mei, *Applied Physics Letters* **68**, 2138 (1996).
- [155] T. Oba, Y. Kido, and Y. Nagasaka, *International Journal of Thermophysics* **25**, 1461 (2004).
- [156] V. N. Popok, and E. E. B. Campbell, *Reviews on Advanced Materials Science* **11**, 19 (2006).
- [157] A. Borowiec, M. Mackenzie, G. C. Weatherly, and H. K. Haugen, *Applied Physics A: Materials Science and Processing* **76**, 201 (2003).
- [158] J. Jia, M. Li, and C. V. Thompson, *Applied Physics Letters* **84**, 3205 (2004).

- [159] A. I. Ryazanov, S. A. Pavlov, E. V. Metelkin, and A. V. Zhemerev, Journal of Experimental and Theoretical Physics **101**, 120 (2005).
- [160] A. Vella, B. Deconihout, L. Marrucci, and E. Santamato, Physical Review Letters **99** 046103 (2007).
- [161] A. Vella, J. Houard, F. Vurpillot, and B. Deconihout, Applied Surface Science **255**, 5154 (2009).
- [162] Ch.Lemell, Private Communication , Vienna University of Technology Austria (2008).
- [163] J. Krüger, P. Meja, M. Autric, and W. Kautek, Applied Surface Science **186**, 374 (2002).
- [164] J. P. Colombier, P. Combis, F. Bonneau, R. Le Harzic, and E. Audouard, Physical Review B - Condensed Matter and Materials Physics **71**, 1 (2005).
- [165] A. Gloskovskii, D. Valdaitsev, S. A. Nepijko, G. Schonhense, and B. Rethfeld, Surface Science **601**, 4706 (2007).
- [166] E. Suraud, and P. G. Reinhard, Physical Review Letters **85**, 2296 (2000).
- [167] P. G. Reinhard, and E. Suraud, Laser Physics **11**, 566 (2001).
- [168] S. Amoruso, R. Bruzzese, M. Vitiello, N. N. Nedialkov, and P. A. Atanasov, Journal of Applied Physics **98**, 044907 (2005).
- [169] V. Zhakhovskii, N. Inogamov , and K. Nishihara, Journal of Physics: Conference Series **112**, 042080 (2008).
- [170] R. Evans *et al.*, Physical Review Letters **77**, 3359 (1996).
- [171] T. H. R. Crawford, J. Yamanaka, E. M. Hsu, G. A. Botton, and H. K. Haugen, Applied Physics A: Materials Science and Processing **91**, 473 (2008).
- [172] A. Y. Vorobyev, and C. Guo, Physical Review B - Condensed Matter and Materials Physics **72**, 1 (2005).
- [173] A. Y. Vorobyev, and C. Guo, Applied Surface Science **253**, 7272 (2007).
- [174] Y. Chivel, M. Petrushina, and I. Smurov, Applied Surface Science **254**, 816 (2007).
- [175] M. Hashida, H. Mishima, S. Tokita, and S. Sakabe, Optics Express **17**, 13116 (2009).
- [176] C. Cornaggia, M. Schmidt, and D. Normand, Physical Review A **51**, 1431 (1995).
- [177] C. Cornaggia, Laser Physics **19**, 1660 (2009).
- [178] S. Shimizu, J. Kou, S. Kawato, K. Shimizu, S. Sakabe, and N. Nakashima, Chemical Physics Letters **317**, 609 (2000).

- [179] V. Koubassov, J. F. Laprise, F. Théberge, E. Förster, R. Sauerbrey, B. Müller, U. Glatzel, and S. L. Chin, *Applied Physics A: Materials Science and Processing* **79**, 499 (2004).
- [180] S. Baudach, J. Bonse, J. Krüger, and W. Kautek, *Applied Surface Science* **154**, 555 (2000).
- [181] S. Baudach, J. Bonse, and W. Kautek, *Applied Physics A: Materials Science and Processing* **69**, S395 (1999).
- [182] H. Ma, G. Guo, J. Yang, Y. Guo, and N. Ma, *Nuclear Instruments and Methods in Physics Research, Section B: Beam Interactions with Materials and Atoms* **264**, 61 (2007).
- [183] P. E. Dyer, S. D. Jenkins, and J. Sidhu, *Applied Physics Letters* **49**, 453 (1986).
- [184] H. R. Zangeneh, P. Parvin, Z. Zamanipour, B. Jaleh, S. Jelvani, and M. Taheri, *Radiation Effects and Defects in Solids* **163**, 863 (2008).
- [185] A. A. Serafetinides, M. Makropoulou, E. Fabrikesi, E. Spyratou, C. Bacharis, R. R. Thomson, and A. K. Kar, *Applied Physics A: Materials Science and Processing* **93**, 111 (2008).
- [186] J. Vanderschueren, G. Yianakopoulos, J. Niezette, C. Chatry, and J. Gasiot, *Journal of Applied Polymer Science* **44**, 1027 (1992).
- [187] T. Sharma, S. Aggarwal, A. Sharma, S. Kumar, D. Kanjilal, S. K. Deshpande, and P. S. Goyal, *Journal of Applied Physics* **102** (2007).
- [188] J. S. Chen, S. P. Lau, Z. Sun, B. K. Tay, G. Q. Yu, F. Y. Zhu, D. Z. Zhu, and H. J. Xu, *Surface and Coatings Technology* **138**, 33 (2001).
- [189] J. S. Chen, Z. Sun, P. S. Guo, Z. B. Zhang, D. Z. Zhu, and H. J. Xu, *Journal of Applied Physics* **93**, 5103 (2003).
- [190] Y. V. Romanovskii, H. Bässler, and U. Scherf, *Chemical Physics Letters* **383**, 89 (2004).
- [191] B. Mallick, R. C. Behera, T. N. Tiwari, S. Panigrahi, and S. K. Samal, *Radiation Effects and Defects in Solids* **163**, 161 (2008).
- [192] X. Shi, L. Chen, J. Yang, and G. P. Meisner, *Applied Physics Letters* **84**, 2301 (2004).
- [193] C. L. Wan, W. Pan, Q. Xu, Y. X. Qin, J. D. Wang, Z. X. Qu, and M. H. Fang, *Physical Review B - Condensed Matter and Materials Physics* **74** (2006).
- [194] J. M. Costantini, J. P. Salvetat, F. Couvreur, and S. Bouffard, *Nuclear Instruments and Methods in Physics Research, Section B: Beam Interactions with Materials and Atoms* **234**, 458 (2005).

- [195] R. J. Young, and W. Y. Yeh, *Polymer* **35**, 3844 (1994).
- [196] Y. Mori, T. Ikeda, T. Yamauchi, A. Sakamoto, H. Chikada, Y. Honda, and K. Oda, *Radiation Measurements* (2009).
- [197] C. S. Chong, I. Ishak, R. H. Mahat, and Y. M. Amin, *Radiation Measurements* **28**, 119 (1997).
- [198] A. F. Saad, S. T. Atwa, R. Yokota, and M. Fujii, *Radiation Measurements* **40**, 780 (2005).
- [199] M. A. Malek, and C. S. Chong, *Radiation Measurements* **35**, X203 (2002).
- [200] M. A. Malek, and C. S. Chong, *Vibrational spectroscopy* **24**, 181 (2000).
- [201] T. Yamauchi, *Radiation Measurements* **36**, 73 (2003).
- [202] C. Wochowski, Y. Hanada, Y. Cheng, S. Metev, F. Vollertsen, K. Sugioka, and K. Midorikawa, *Journal of Applied Polymer Science* **100**, 1229 (2006).
- [203] B. Jaleh, P. Parvin, K. Mirabaszadeh, and M. Katouzi, *Radiation Measurements* **38**, 173 (2004).
- [204] W. W. Duley, *U.V lasers effects and applications in material science* (Cambridge University Press UK, 1996).
- [205] R.E.Hummel, *Electronic Properties of Materials* (Springer-Verlag Berlin USA, 1993).
- [206] A. A. Serafetinides, M. I. Makropoulou, C. D. Skordoulis, and A. K. Kar, *Applied Surface Science* **180**, 42 (2001).
- [207] C. W. Ponader, J. F. Schroeder, and A. M. Streltsov, *Journal of Applied Physics* **103**, 063516 (2008).